Universitat Autònoma de Barcelona

Theoretical Investigations of H_2 Formation on Interstellar Silicates Surfaces

Javier Navarro Ruiz

Tesi Doctoral

Estudi de Doctorat en Química

Directors:

Mariona Sodupe Roure

Albert Rimola Gibert

Departament de Química

Facultat de Ciències

2015

Universitat Autònoma de Barcelona
Departament de Química
Unitat de Química Física

Memòria presentada per aspirar al Grau de Doctor per Javier Navarro Ruiz,

Javier Navarro Ruiz

Vist i plau,

Mariona Sodupe Roure **Albert Rimola Gibert**

Bellaterra, 29 d'octubre de 2015

Als meus pares i germà

Preface

Among the molecules in space, H_2 is one of the most relevant of the universe. It is the most abundant one in the interstellar medium and is a key intermediate for the formation of bigger molecules. Its formation is complex, but due to its inherent relevance understanding its interaction and its formation can be considered as a paradigm of the astrophysical process.

The present thesis is structured in four chapters. Chapter 1 introduces the astrochemical framework in which the thesis is located, pointing out the presence of interstellar hydrogen in the interstellar medium and where it takes place, in the interstellar dust grains around. After presenting the goals this thesis aims, Chapter 2 overviews the general theoretical aspects behind it, such as electronic structure, density functional methods, solids modelling and tunnelling effects, providing finally the computational details entailed. Chapter 3 corresponds to results and discussion and is divided into different sections. Section 3.1 presents some physicochemical properties of the crystalline bulk structure and the corresponding surfaces of Mg_2SiO_4 forsterite and of the Fe-containing $Mg_{1.5}Fe_{0.5}SiO_4$ olivine systems. Section 3.2 reports the adsorption of H atoms and their recombination to form a H_2 molecule on the crystalline Mg_2SiO_4 forsterite (010) surface and Section 3.3 analyses the relevance of surface morphology by considering the H_2 formation on the crystalline Mg_2SiO_4 forsterite (001) and (110) surfaces. Finally, Section 3.4 investigates the influence of Fe^{2+} atoms by modelling the physisorption/chemisorption of H atom on the Fe-containing (010) surface, subsequently taking place the formation of H_2. Chapter 4 addresses the general conclusions of the present thesis and possible future perspectives, Chapter 5 includes the references cited and Appendix A and B supports the information given in Chapter 3.

Additionally, at the beginning of this work, a list of abbreviations of some terms used throughout the text is appended.

Acknowledgements

Primer de tot m'agradaria donar les gràcies als meus directors, sense ells aquesta tesi doctoral no hauria estat possible. He tingut el privilegi d'haver estat tutelat per persones tan extraordinàries com la Prof. Mariona Sodupe i el Dr. Albert Rimola, sota els quals he après profundament i perfeccionat moltes de les tècniques computacionals que ara conec i que s'analitzen detalladament en aquesta tesis. Expressar el meu agraïment a l'Agència de Gestió d'Ajuts Universitaris i de Recerca (AGAUR) de la Generalitat de Catalunya i a la Universitat Autònoma de Barcelona (UAB) pel suport financer concedit gràcies al Programa d'Ajuts per a la Contractació de Personal Investigador Novell (FI-DGR, NÚM. EXPEDIENT: *2015FI_B 00953* i *2015FI_B2 00083*). Gràcies també al meu grup de recerca "Computational Studies of (Bio)inorganic Systems" (GETAB Group) i a les subvencions que ha rebut a través dels projectes del Ministeri de Ciència i Innovació (*CTQ2011-24847/BQU*, *CTQ2013-40347-ERC*, *CTQ2014-59544-P* i *CTQ2014-60119-P*) i de la Generalitat de Catalunya (*2009SGR-638* i *2014SGR-482*), molts dels congressos als quals he pogut assistir com a doctorand van ser possibles. També estic agraït al Consorci de Serveis Universitaris de Catalunya (CSUC) pels recursos computacionals proporcionats per l'assoliment d'aquesta tesi. Agraeixo especialment a Angelos Michaelides el haver-me donat la oportunitat de pertànyer al seu grup de recerca "Interfaces: Catalytic and Environmental" (ICE Group) i el seu suport durant la meva estada predoctoral al London Centre for Nanotechnology de la University College London (UCL) i al Thomas Young Centre a Londres, Regne Unit. També vull agrair al nostre estimat col·laborador des de fa temps i coautor de diversos treballs plegats, el Prof. Piero Ugliengo de la Università degli Studi di Torino, les seves valuoses contribucions als diversos treballs presentats en aquesta tesi. Estic en deute amb els excel·lents doctorands i professors amb els què he compartit moltes estones entranyables i he treballat en els darrers anys, per les nombroses aportacions que aquí es presenten i per tot el què m'han ensenyat i, en general, a tot el personal de la Unitat de Química Física. Finalment, però no per això menys important, paraules de gratitud vers la meva família i amics, un pilar fonamental durant tots aquests anys, el seu recolzament ha estat molt gratificant.

Javier Navarro Ruiz

Bellaterra, Octubre del 2015

List of Abbreviations

Abbreviation	Meaning
AGB	Asymptotic Giant Branch
AGN	Active Galactic Nuclei
AIMD	Ab Initio Molecular Dynamics
BSSE	Basis Set Superposition Error
CC	Coupled Cluster method
CI	Configuration Interaction method
CO	Crystalline Orbital
cr	Cosmic Ray
DFT	Density Functional Theory
DRC	Distinguished Reaction Coordinate
ECP	Effective Core Potential
EPM	Electrostatic Potential Map
ER	Eley–Rideal
FUSE	Far Ultraviolet Spectroscopic Explorer
GGA	Generalized Gradient Approximation
GPW	Gaussian and Plane Waves method
GTBF	Gaussian-type Bloch Functions
GTF	Gaussian-type Functions
HA	Hot Atom
HF	Hartree–Fock
HK	Hohenberg–Kohn
IR	Infrared light
ISM	Interstellar Medium
KS	Kohn–Sham
LCAO	Linear Combination of Atomic Orbitals
LDA	Local Density Approximation
LSDA	Local Spin Density Approximation
LH	Langmuir–Hinshelwood
MBPT	Many Body Perturbation Theory
PAH	Polycyclic Aromatic Hydrocarbon

PAW	Plane Augmented Wave
PDR	Photon–Dominated Region
PP	Pseudopotential
PW	Plane Wave
SCF	Self–Consistent Field
TPD	Temperature–Programmed Desorption
TST	Transition State Theory
UV	Ultraviolet light
VIS	Visible light
YSO	Young Stellar Object
ZPE	Zero-Point Energy

Contents

1. Introduction

We live in a molecular Universe; that is, a Universe where molecules are abundant and widespread; a Universe with a rich organic inventory, particularly in regions of star and planet formation; a Universe where the formation of stars and the evolution of galaxies is driven in many ways by the presence of molecules; a Universe where prebiotic interstellar molecules may represent the first steps towards life; a Universe where molecules can be used as "dye" to trace important processes in the interstellar medium; a Universe where molecules provide unique information on the physical conditions of a wide variety of regions; and a Universe where molecules can work together to form such complex species.

Our knowledge on cosmic matter, particularly on the ice, dust and gas of the interstellar medium, has actually progressed by merging results from observations, laboratory experiments and numerical astrochemical models. However, these approaches do not provide detailed atomistic views of neither of them nor the role of the gas-grain interactions accounting for their electronic structure features, which is essential to deeply understand their physicochemical properties and the role they play in the increment of the chemical complexity in the Universe. This can be improved by adding a fourth level of investigation grounded on rigorous quantum mechanical methods. The present thesis investigates the H_2 formation and the role of silicates by means of this fourth approach.

1.1. Interstellar Medium

The Milky Way is largely empty. At first glance, the outer space seems to be constituted uniquely of stars separated by great distances (around 10^{13} km in the solar neighbourhood) with a complete vacuum between them. Observations with telescopes have shown that this is not the case; there are regions that contain considerable material, although by earthly standards such regions still constitute a pretty good vacuum. For example, whereas the best man-made vacuum is about 10^{12} atoms per cubic centimetre and a cubic centimetre of the air in the room has about 10^{19} atoms in it, on average the "typical" gas density in space is one atom per cubic centimetre. However, the space is not uniform in density and it can have densities up to a thousand or a million atoms per cubic centimetre.

The stuff out of which stars are made, namely the gas and dust that is present throughout the Galaxy, is collectively known as the interstellar medium (ISM), the material between the stars. The interstellar medium plays a central role in the evolution of galaxies. It is the repository of the ashes of previous generations of stars enriched by the nucleosynthetic products of the fiery cauldrons in the stellar interiors. These are injected either with a bang, in a supernova explosion of massive stars, or with a whimper, in the much slower-moving winds of low-mass stars during the asymptotic giant branch (AGB) phase of stellar evolution (see Figure 1.1). In this way, the abundances of heavy elements in the ISM slowly increase. This is part of the stars cycle of life, because the ISM itself is where future generations of stars will be created. It is this constant recycling and its associated enrichment that drives the evolution of galaxies, both physically and in their emission characteristics [1].

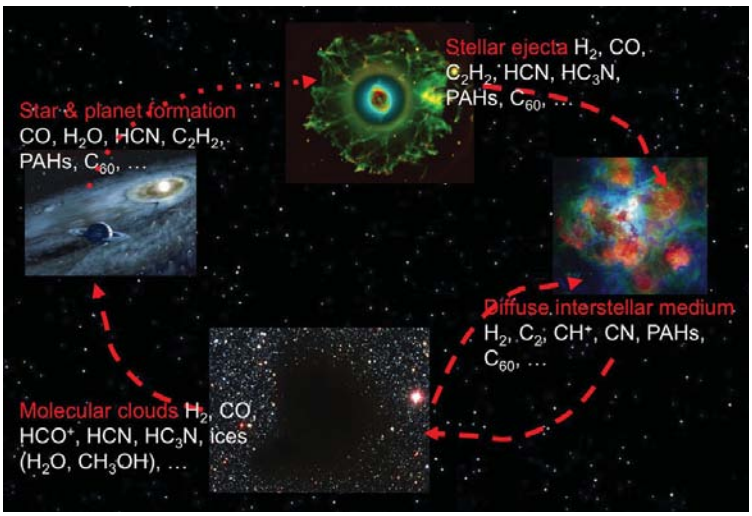

Figure 1.1 The life cycle of the interstellar medium (ISM), taken from Tielens [1]. It starts with the injection of material from stars either in the form of wind or in an explosion. In the interstellar medium, material circulates rapidly, and often between more diffuse phases and molecular clouds. Molecular clouds can become gravitationally unstable and form new stars and associated planetary systems. The central star eventually evolves and in its death throes ejects much of its gas back into the ISM. The whole life cycle from old star to new star takes a few billion years.

Dust outside our local group of galaxies is still surprisingly poorly understood, especially given its fundamental importance to our understanding of the history of star-formation, its effects on the formation of early stars, and its role in the formation of planets and hence life. From observations, we know that dust must have been formed on short timescales in the early Universe, simply because significant dust is observed from epochs previous to about one billion years after the Big Bang. In the present Universe the long-lived stars

seem to be the main dust producers (although this may not have been thus early on). One possibility is that intermediate-mass stars, the high-mass end of the AGB, may have contributed very substantially to dust mass at early times. It remains, however, very uncertain how much dust could have been formed from these high-mass AGB stars, and whether enough intermediate mass stars could have been produced from metal-free and metal-poor stars. Indeed, very little is firmly known about the production and destruction of dust in the high-mass end of late stage stellar evolution compared to the low-mass end [2], as well as about effectiveness of these high-mass AGB stars in injecting dust into the ISM at different metallicities (in astronomy and physical cosmology the metallicity of an object is the proportion of its matter consisting of chemical elements other than hydrogen and helium). An extensive detail about the interstellar dust is provided in Section 1.3.

Stardust grains with enriched isotopic compositions in Earth crust's compounds have been isolated from meteorites. Meteorites offer a unique window on the *solar nebula* – the disk-shaped nest of gas and dust that enveloped the early Sun some ~4.57 billion years ago – from which planetesimals and planets accreted [3]. Minuscule presolar grains have been found in some meteorites, providing an opportunity to analyse directly the chemistry of interstellar matter. Even so, some of these tiny grains provide constraints on our understanding of how elements were forged inside stars before the Sun's birth (a portrait of star-forming region can be appreciated in Figure 1.2). Once formed, these grains were released to the interstellar medium, where dust cycles occur many times from diffuse to dense cloud phases and vice versa (see Figure 1.1). An interstellar cloud is an aggregation of gas and dust in the ISM containing large quantities of atoms, molecules and dust, with a typical mass ratio of 100 and with temperatures ranging from 10 to 100 K [4]. The dust in these regions is typically cold and thus, can be detected through its thermal emission at submillimetre and millimetre wavelength.

The interstellar chemistry is rich and diverse as shown in Table 1.1, where all the gas-phase molecules identified in the ISM are reported. The interstellar medium is filled primarily by diffuse gases, mostly hydrogen and helium, but with oxygen, carbon, and nitrogen contributing about 1% by mass and all the other elements mostly in micrometre-size dust motes. Molecules, in addition, are present in all different phases of this life cycle (see Figure 1.1). About 170 molecules have been identified through their rotational (millimetre, $\sim 10^{-3}$ m), rotational-vibrational (infrared, $\sim 10^{-3} - 10^{-6}$ m), and/or

electronic (ultraviolet or visible, $\sim 10^{-6} - 10^{-8}$ m) transitions (see Table 1.1). We recognize simple hydrides such as H_2, H_2O, and NH_3, a diverse array of hydrocarbon chain species such as the cyanopolyynes (*e.g.*, HC_3N), but also cyclic species including possibly benzene, common simple organics such as alcohols and aldehydes, highly reactive species such as ions and radicals, and very stable species such as the C_{60} and C_{70} fullerenes. Besides these specific molecules it has also been shown that, as a class of molecules, polycyclic aromatic hydrocarbons (PAHs) are the most abundant polyatomic species in space [5].

Figure 1.2 Celestial Valentine. Generations of stars can be seen in this infrared portrait from NASA's Spitzer Space Telescope. In this wispy star-forming region, called W5, the oldest stars can be seen as blue dots in the centers of the two hollow cavities (other blue dots are background and foreground stars not associated with the region). Younger stars line the rims of the cavities, and some can be seen as pink dots at the tips of the elephant-trunk-like pillars. The white knotty areas are where the youngest stars are forming. Red shows heated dust that pervades the region's cavities, while green highlights dense clouds. *Image Credit: NASA/JPL-Caltech/Harvard-Smithsonian*

Roughly speaking there are two kinds of interstellar clouds in the ISM, diffuse and dense clouds (for a definitive study of the classification of interstellar clouds see Snow and McCall [5]). Diffuse clouds constitute the first step in the evolutionary pathway from low-density atomic hydrogen clouds to the molecular Universe. They are transitions between the atomic and molecular phases of the interstellar medium, and provide a relatively simple laboratory for the study of fundamental chemical processes. Diffuse interstellar clouds are regions of relatively low density, roughly 100–300 particles cm^{-3}, and are characterized by an average temperature of ~100 K corresponding to a thermal pressure of 4000 K cm^{-3}. Typical sizes and masses of diffuse clouds are $\sim 10^{14}$ km and $\sim 10^{33}$ kg but actually diffuse clouds show a broad mass and size distribution which joins quite smoothly into those of molecular clouds [6]. They are quite transparent to the ambient interstellar radiation field.

Hence, UV radiation field of approximately ~10^8 photons s^{-1} cm^{-2} plays an important role in their physics and chemistry, such as preventing the formation of larger molecules.

Table 1.1 *Identified interstellar and circumstellar molecules*

Simple hydrides, oxides, sulphides, halogens				
H_2 (IR, UV)	CO	NH_3	CS	HCl
O_2	H_2O_2	PO	CO_2 (IR)	NaCl*
H_2O	SO_2	OCS	H_2S	KCl*
PN	SiO	SiH_4* (IR)	SiS	AlCl*
N_2O	CH_4 (IR)	HSCN	HF	AlF*
HONC	HNCO	AlOH		
Nitriles and acetylene derivatives				
C_2 (IR)	HCN	CH_3CN	HNC	C_2H_4* (IR)
C_3 (IR, UV)	HC_3N	CH_3C_3N	HNCO	C_2H_2 (IR)
C_5* (IR)	HC_5N	CH_3C_5N	HNCS	C_6H_2 (IR)
C_3O	HC_7N	CH_3C_2H	HNCCC	C_3H_6
C_3S	HC_9N	CH_3C_4H	CH_3NC	C_3H_7CH
C_4Si*	$HC_{11}N$	CH_3C_6H	HCCNC	H_2C_4
HC_2CHO	CH_2CHCN	CH_2CCHCN		
Aldehydes, alcohols, ethers, ketones, amides				
H_2CO	CH_3OH	HCOOH	HCOCH	CH_3CH_2CN
CH_3CHO	CH_3CH_2OH	$HCOOCH_3$	CH_3NH_2	NH_2CH_2CN
CH_3CH_2CHO	CH_2CCHOH	CH_3COOH	CH_3CONH_2	NH_2CN
NH_2CHO	$(CH_2OH)_2$	$(CH_3)_2O$	H_2CCO	CH_2CHCN
CH_2OHCHO	$(CH_3)_2CO$	H_2CS	C_2H_5OCHO	CH_3SH
Cyclic molecules				
C_3H_2	SiC_2	c-C_3H	CH_2OCH_2	C_6H_6 (IR) ?
c-SiC_3	H_2C_3O	C_2H_4O		
Molecular cations				
CH^+	CO^+	$HCNH^+$	OH^+	HN_2^+
CH_3^+	HCO^+	HC_3NH^+	H_2O^+	H_3^+ (IR)
HS^+	HOC^+	H_2COH^+	H_3O^+	SO^+
HCS^+	$HOCO^+$	CF^+		

		Molecular anions		
C_4H^-	C_6H^-	C_8H^-	CN^-	C_3N^-
C_5N^-				
		Radicals		
OH	C_2H	CN	C_2O	C_2S
CH	C_3H	C_3N	NO	NS
CH_2	C_4H	HCCN*	SO	SiC*
NH (UV)	C_5H	CH_2CN	HCO	SiN*
NH_2	C_6H	CH_2N	C_5N*	CP*
SH	C_7H	NaCN	KCN	MgCN
C_3H_2	C_8H	MgNC	FeCN	C_4H_2
HNO	H_2CN	HNC_3	HO_2	C_6H_2
AlNC	SiNC	C_4Si	SiCN	HCP
CCP	AlO			
		Fullerenes		
C_{60} (IR)	C_{70}* (IR)	C_{60}^+ (VIS) ?		

Species denoted with * have been detected only in the circumstellar envelope of carbon-rich stars. Most molecules have been detected at ratio and millimetre wavelengths, unless otherwise indicated (IR, VIS, or UV). Species labelled with a question mark await confirmation.

The known molecular content of diffuse clouds in interstellar space consists primarily of simple diatomic molecules – only a few polyatomic species have been identified to date – particularly simple hydrides. Initially, such studies were limited to the visible and near-UV wavelength ranges and, hence, focused on transitions of species with low-lying electronic states (*e.g.*, radicals and ions). The first interstellar molecules, CH, CN neutrals and CH ions, were discovered this way in the late 1930s and early 1940s of the previous century [7] but they have now also been observed through millimetre and submillimetre adsorption lines [8]. However, spectroscopic surveys lead to the discovery of new molecules with filled electronic shells, and many more molecules have been detected in the photon-dominated diffuse medium, although at lower abundances than found in dense clouds. The detected species include the most abundant molecular species, H_2, as well as a slew of others like HD, CO, OH, CH_2, H_2O, C_2, and recently C_2H and c-C_3H_2 molecules in several extragalactic diffuse clouds. The simple carbon chains, C_2 and C_3, have also been observed in the visible and far-IR wavelength ranges [9], [10]. The C_2H abundance varies little from

diffuse to dense clouds whereas the c-C_3H_2 abundance is markedly higher in dense clouds [8]. Over the last decade, the emission from molecules in diffuse clouds has been studied through their rotational transitions at submillimetre wavelengths (*e.g.*, CO, HCO^+). Rotational–vibrational transitions of the important H_3^+ ion have also been discovered in the near-IR (~3.7 μm) [11]. Besides these simple species, reactions of the neutral molecules CH and CH_2 molecules with C ions leading to the formation and build-up of large polycyclic aromatic hydrocarbons in the diffuse ISM have been postulated due to the strong IR emission bands that dominate the near- and mid-IR emission spectrum [12]. However, the presence of large carbon-bearing species is strongly dependent on their formation and survival rate because the diffuse medium is controlled by photochemistry. The larger carbonaceous molecules that enter the diffuse interstellar gas are detected in circumstellar envelopes around late-type stars. Finally highlight SiC and SiO molecules, precursors of silicates and silicon carbides that form the core of dust.

Dense clouds, also referred to as *cloud cores* or *dense cores*, differ in a number of important aspects from the diffuse clouds. They tend to contain a dense condensation up to a few tens of solar masses of material, and gas densities can reach 10^3 to 10^6 particles cm^{-3}, high values according to interstellar standards. As a result, the intensity of the dissociating far-UV radiation field (in the wavelength range 912–2000 Å) is lower and gas-phase chemistry in these clouds is primarily driven by cosmic-ray ionization [13]. These dense clouds are also much cooler than diffuse clouds, temperatures around ~10 K, so that interstellar grains become coated in ices.

Much of the chemistry in the ISM occurs within relatively dense clouds [14], [15]. Reactions between ice mantles and gas molecules produced organic compounds that can be extracted from meteorites and identified by their bizarre isotopic compositions [16]. In fact, the interaction between the gas phase and the solid state becomes one of the driving forces of molecular diversity in dense clouds. A final difference with diffuse clouds is the importance of self-gravity in dense clouds. New stars are only formed in dense clouds and such embedded protostars can influence their environment through shocks driven by their powerful outflows. Protostars will also heat the surrounding dust and this energy is coupled to the gas through gas-grain collisions [17]. This heating of the dust can evaporate previously accreted ice mantles when the temperature is raised above the sublimation temperature [18], [19]. Many dust grains were undoubtedly destroyed in the ISM, but some

hardy survivors were incorporated into the nebula when the dense cloud collapsed, and thence were accreted into meteorites.

Over the last three decades, rotational spectroscopy in the millimetre wavelength region has revealed that dense clouds contain a large variety of molecules (see Table **1.1**). In fact, most of the over 140 molecules (out of ~170) discovered to date in space are found in dense clouds. Given the overabundance of hydrogen in the ISM, one might expect the molecular composition to be dominated by saturated hydrides such as H_2O [20], NH_3 [21], and CH_4. Simple hydrides and oxides are indeed present in dense clouds (see Table 1.1). However, interstellar clouds also contain a variety of unsaturated radicals and ions [22]. These species are very reactive under terrestrial laboratory conditions and indeed some were discovered in space before they were even identified in the laboratory. The degree of unsaturation is particularly remarkable, attesting to the importance of kinetics over thermodynamics in interstellar molecular clouds. Except for molecular hydrogen formation, much of the chemistry occurs in the gas phase and is driven by penetrating far-UV photons and cosmic rays [23], [24]. Molecular species do accrete onto dust grains where they can undergo further reactions. In this way an ice mantle is formed. Evidently, other chemical routes have opened up under these conditions [25]. This is generally attributed to the chemistry of ice molecules evaporating into the warm gas through the heating action of the protostar [26].

In the denser media, gas-phase species can accrete onto grains forming a mantle. In diffuse clouds, the accreted species may be predominantly bound by chemisorbed forces, partly because physisorbed species will be rapidly photodesorbed by the high flux of far-UV photons. In dense clouds, the accretion process leads to the formation of an icy mantle consisting of simple molecules such as H_2O, CO, CO_2, and CH_3OH [27]. These ices may be processed by UV photons and high-energy cosmic rays into larger, more complex species, which could be more tightly bound to the cores. While there is compelling experimental evidence for these processes [28], their importance in an interstellar setting is more controversial and, presently, there is little direct observational support. Coagulation, the mechanism by which dust grains grow into larger entities in the ISM and protoplanetary disks, may also play a role in increasing the grain size inside diffuse and dense clouds.

Analogous gas and grain chemistry can be expected to produce a wide range of complex organic species. The six biogenic elements required to build such structures on our planet include some of the most common elements: H, O, C, N, S and P. Phosphorous, although about 1000 times less abundant than carbon, is critical in the transition from prebiotic to biotic chemistry. Only the two most abundant elements (hydrogen and oxygen) are required to produce water. Four elements (H, O, C, and N) are sufficient to form all of the nucleic acids (with phosphorous) and eighteen of the twenty amino acids commonly found in biological structures. Remaining two amino acids, cysteine and methionine, require the availability of sulphur. Thus, with five elements (H, O, C, N, and S) a prebiotic system could form in an appropriate solvent (water), take on shape (structural proteins, lipoproteins, and polysaccharides), and facilitate chemical reactions (enzymatic proteins).

Star formation occurs within cloud cores. The combination of high densities, heating by young embedded stars, and illumination by nearby sources of hard radiation drives the chemical evolution in these regions. Here, one can expect enhancement of both gas-phase chemical reactions and grain-surface chemistry [29]. The higher temperatures open many chemical pathways, which are kinetically hindered at lower temperatures. High densities increase the rate of collisions of chemically interacting partners. Penetrating X-rays and UV radiation ionize atomic and molecular species, thereby greatly increasing their chemical interaction cross-sections. This radiation may also dissociate larger molecules and thus provide additional chemical pathways for producing smaller molecules.

Hard radiation also creates radicals on grain surfaces, which – combined with the mobility due to elevated grain temperatures – leads to enhanced chemical processing. If grain reactions are sufficiently exothermic, the resulting molecules will be directly released from the grain surface. If not released at their creation, they could leave the surface later when the grain temperature is sufficiently high. Alternatively, the molecules could become part of the grain's molecular coating, influencing its optical properties [30], could help coagulating with other grains to produce larger particles (a necessary step towards planet formation), or simply be present and participate in the creation of more complex species.

To conclude, the interstellar medium is vitally important to the evolution of galaxies, the formation of planets and the origin of life. Interstellar dust is an important constituent of these galaxies and is crucial for interstellar chemistry by reducing the UV radiation which

causes molecular dissociations and providing the site of the formation of the most abundant interstellar molecule, H_2.

1.2. Interstellar Hydrogen

In the first moments after the Big Bang, the Universe was extremely hot and dense. As the Universe cooled, conditions became just right to give rise to the building blocks of matter – the quarks and electrons of which we are all made. A few millionths of a second later, quarks aggregated to produce protons and neutrons. Within minutes, these protons and neutrons combined into nuclei. As the Universe continued to expand and cool, things began to happen more slowly. It took 380,000 years for electrons to be trapped in orbits around nuclei, forming the first atoms. These were mainly hydrogen and helium, which are still by far the most abundant elements in the Universe. 1.6 million years later, gravity began to form stars and galaxies from clouds of gas. Heavier atoms such as carbon, oxygen and iron, have since been continuously produced in the hearts of stars and catapulted throughout the Universe in spectacular stellar explosions called supernovae.

1.2.1. Relevance

Molecular hydrogen, besides being the most abundant molecule in the Universe – comprises approximately 90% of the matter of the Universe by number density and about 75% of the Universe by mass [4] – plays a fundamental role in many astrophysical and astrochemical contexts [31]. It is found in all regions where the shielding of the UV photons, responsible for its photo-dissociation, is sufficiently large. The spectral lines of hydrogen are prominent in a great variety of astronomical objects and the role of hydrogen in astrochemistry has been a subject of much study. Astronomers have discovered spectral lines from H^+, H-atoms, H_2 molecules, H_2^+ and H_3^+ in vast clouds of gas and dust in the interstellar medium [32]. H_2 makes up the bulk of the mass of the dense gas in galaxies and could represent a significant fraction of the total Universe's baryonic mass (that is, excluding so-called dark matter and dark energy).

Further on, H_2 plays two main roles that render it key for our understanding of the interstellar medium, in particular of the processes regulating star formation and the

evolution of galaxies. Firstly, H_2 is recognized as a major contributor to the cooling of astrophysical media. In interstellar clouds, collisions will excite hydrogen molecules to higher levels, and they will eventually de-excite returning to a lower energy state through photon emission, which will carry the energy out of the region cooling the cloud, so that gases could begin to collapse under gravity to form the first stars (metal-free stars) and galaxies. Cooling mechanisms are essential to allow gravitational collapse because the pressure of hot gas resists further contraction unless heat can be emitted in the form of radiation, both in the early Universe and in the ISM. H_2 is also an effective coolant for gases at T~100 K, where collisions result in rotational excitation, followed by emission; hence H_2 cooling mechanisms also take place in the ISM and remain of great importance to the present day. H_2 has also specific radiative and collision properties that make it a diagnostic probe of unique capability. Many competing mechanisms could contribute to its excitation and H_2 can serve as probe of a wide range of physical environments. Thus, as we understand reasonably well its radiative and collision properties, we can construct realistic models of the response of H_2 to its surroundings. Secondly, the formation of H_2 on grains initiates the chemistry of interstellar gas due to the $H_2 \rightarrow H_3^+$ source of protonation (as it is discussed in section 1.2.5).

1.2.2. Spectroscopic Detection

Molecular hydrogen has always been expected to be abundant in diffuse clouds [33] but, despite its importance, it is also the most difficult species to observe directly. The reason is that H_2 is a simple, highly symmetric and homonuclear molecule. As it consists of two atoms of identical mass, the centre of mass and the centre of charge of the molecule coincide, resulting in no permanent dipole moment. With no dipole moment, only quadrupole rotational transitions can occur. This means that only the $\Delta J=0$ and $\Delta J=\pm 2$ rotational transitions occur, while the $\Delta J=\pm 1$ (dipole) rotational transitions are strictly forbidden. Thus, the most abundant molecule in the ISM, carrying most of the mass and playing a key role in excitation, thermal balance, and gas-phase chemistry, is virtually invisible to direct observation. This means that unlike other molecules, H_2 emits no long-wavelength rotational lines.

The only directly observable probes of H_2 in the diffuse ISM are:

1. Absorption at far-UV wavelengths in the diffuse ISM (towards nearby stars) by electronic transitions in the Lyman and Werner bands lying below 0.112 μm [34], [35]. These lines arise in both cold and warm H_2.
2. Emission by IR rotational-vibrational transitions in the electronic ground state of H_2 at wavelengths between 1 and 28 μm in relatively warm regions [36], [37]. The molecular gas must be warm (500–2000 K), excited either by shocks, outflows, or UV fluorescence from nearby stars.

However, the gas in the interstellar clouds is generally too much cold to populate even the lowest rotational-vibrational levels (a few 10 K compared to level energies corresponding to temperatures of more than 6000 K even for the lowest rotational-vibrational levels). Temperature-promoted population of the highly excited states, thus giving rise to emission of the H_2 lines, is hampered. Nevertheless, other mechanisms leading to this population are possible. The excitation mechanisms of H_2 are observed in photon-dominated regions (PDRs) where the excitation of rotational-vibrational and high rotational levels within the electronic ground state dominates. Observations with *Copernicus* and FUSE (Far Ultraviolet Spectroscopic Explorer) show that in most diffuse clouds – where this pumping is important [38] – there is a substantial population of H_2 in rotational levels up to about J=6 [5].

The mechanisms for populating H_2 in the ISM, often called pumping mechanisms, are mainly *via* collisional excitation and UV radiation (the H_2 pumping diagram is shown in Figure 1.3). Inelastic collisions are the dominant excitation mechanism if the gas density and temperature (typically of order 2000–3000 K) are high enough, at least for the lower energy levels [39], [40]. Therefore, by collisions with other H_2 molecules, atoms or electrons the rotational-vibrational levels are populated. These thermal collisions are particularly important in dense PDRs ($n_H > 10^4$ cm^{-3}) and shocked regions of the ISM, such as molecular outflows [41], where collisions maintain the lowest rotational levels in thermal equilibrium. In another excitation mechanism, the molecule absorbs ultraviolet photons (as is observed) and is radiatively pumped into its electronically excited states, the above mentioned Lyman and Werner bands. As it decays back into the electronic ground state, it populates the high vibrational levels *via* quadrupole transitions, and the subsequent cascade to ν=0 gives rise to optical and IR fluorescent emission, and a characteristic distribution of level populations [42], [43]. In 10–15% of UV absorption events, the

molecule will dissociate [44]. Other H_2 pumping mechanisms also occur in the ISM. For example, H_2 formation in excited states can also contribute to the excitation of the molecule. Finally, in environments such as active galactic nuclei (AGNs) or X-ray emitting young stellar objects (YSOs), where hard X-rays are capable to penetrate deeply into zones that are opaque to UV photons, H_2 excitation can be dominated by X-rays [45].

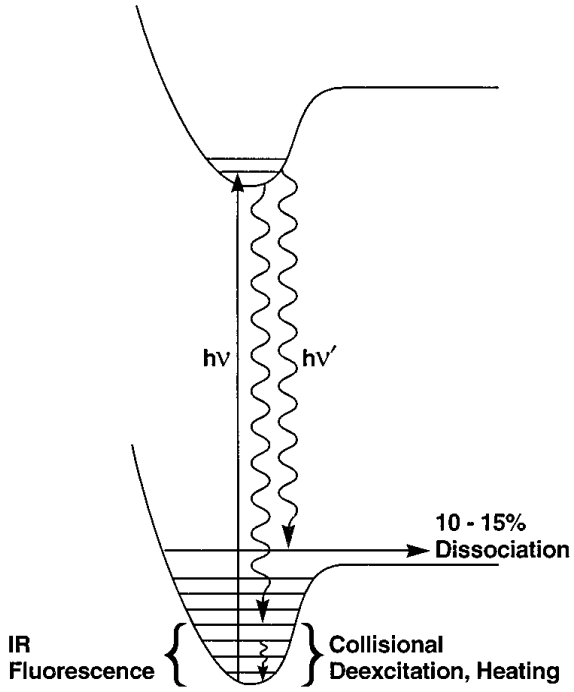

Figure 1.3 The schematic diagram of the H_2 pumping, taken from Hollenbach and Tielens [44].

Similar to the existing direct methods to observe the abundance of H_2 in the ISM, indirect observations also exist. In fact, most of what we know about interstellar molecules comes from observations of so-called *tracer* species [4], [46]. The CO, which is observed in its J=1–0 rotational transition at λ=2.6 mm, is commonly used as a tracer of molecular gas in the Galaxy. H_2 is thought to be the dominant molecular species, with a H_2/CO ratio of 10^4–10^5 [4], [47], consistent with expectations based on diffuse cloud gas-phase chemistry models. Since the formation of molecular species like CO occurs under conditions favourable for H_2 formation, the amounts of H_2 can be estimated from the observed amount of CO with the assistance of a few simplified assumptions.

1.2.3. Formation

It was determined that a H_2 molecule in a diffuse cloud has a lifetime of ~1000 years, which is very short in an astrophysical timescale [48]. Thus, there must be an efficient mechanism for the formation of H_2 in the ISM to account for the high abundance. There is no good way to produce molecular hydrogen through gas-phase reactions. Even so, there are two primary ways that H_2 can be formed in the gas phase. The first is Radiative Association in which two H atoms collide to form H_2 followed by radiation of the excess 4.5 eV reaction energy as photons:

$$H^0 + H^0 \rightarrow H_2 + h\nu$$

After the H^0–H^0 collision the reaction energy is converted into internal energy (excitation of rotational-vibrational levels of the ground state) and must be released because the newly-formed H_2 molecule is stable. Because radiative transitions in a homonuclear molecule are highly forbidden, the radiation of the reaction energy is very inefficient and the molecule is much more likely to dissociate before it relaxes. The rate coefficient for radiative attachment is $< 10^{-23}$ cm^3 s^{-1}, so this mechanism is too slow and inefficient to form H_2 in sufficient quantities to be important in the ISM [49]. Three-body processes, in which three H^0 atoms collide and the third H^0 atom carries off the excess reaction energy, are similarly unlikely at ISM densities (important only at high density, $n_H > 10^{15}$ particles cm^{-3}) [4], though they have been proposed as a way to form H_2 in protoplanetary disks.

The second gas-phase mechanism to form molecular hydrogen is Associative Detachment and can also be formed through the H^- ion, which in turn is formed through the radiative association reaction:

$$H^0 + e^- \rightarrow H^- + h\nu$$

$$H^- + H^0 \rightarrow H_2 + e^-$$

The first step is slow, having a temperature-dependent rate coefficient of $\sim 10^{-18}$ T cm^3 s^{-1} [48]. The second step is much faster, with a nearly temperature-independent rate coefficient of $\sim 1.3 \times 10^{-9}$ cm^3 s^{-1}, and competes with photodissociation of H^-, which has a rate of $\sim 2.4 \times 10^{-7}$ s^{-1} for diffuse clouds. Overall, this mechanism is also very inefficient at forming H_2 in the ISM, especially at low temperatures (though it is about an order of magnitude faster than direct radiative attachment). While it is too slow to explain the

observed abundances of H_2 in the present-day ISM, it may be important in the first generation of stars in the early Universe, when no dust grains exist and copious electrons were present from partial ionization of H^0. In cold neutral clouds, and comparing the rates of these two gas-phase routes, none of these processes is nearly fast enough to account for the formation of H_2 and justify the observed H_2 abundances, so it is clear that there has to be an efficient alternative.

Because of the difficulty of forming H_2 in the gas-phase, it is now generally accepted that the currently favoured H_2 formation mechanism in the ISM proceeds on the surfaces of interstellar dust grains through a grain-surface heterogeneous catalysis [33], [49]–[69]. This formation channel was suggested by van de Hulst in 1948 [70], first described by McCrea & McNally in 1960 [71] and then first modelled giving its classic treatment by Gould & Salpeter in 1963 [50]. This formation mechanism is thought to be highly efficient, in such a way that almost all H-atoms adsorbed onto a dust grain leave as part of a H_2 molecule [33], [50]. But due to our limited understanding of the relevant properties of interstellar grains (composition, structure and hydrogen coverage) and hence of grain surface reactions, the H_2 formation mechanism is not fully understood yet.

At the low temperatures of the ISM, an H atom colliding with a dust grain will have a certain probability of sticking to the surface, provided that it is not moving too fast and that the grains themselves are not too hot, which makes the surfaces energetically less "sticky" [52], [60]. Once the H atom has been adsorbed by the grain surface, it will migrate around until it reaches a site on the grain surface where it is more tightly bound by either chemisorption (*i.e.*, bound covalently with surface materials) or physisorption (*i.e.*, bound by intermolecular van der Waals forces). The adsorbed hydrogen atom can move around the surface *via* thermal hopping or quantum tunnelling [58] as shown by Figure 1.4, although such sites act as "sinks" for H atoms. It is while trapped in this site that the atom is likely to encounter another H atom, and the two can react to form H_2. Upon formation, the 4.5 eV of reaction energy must be distributed into: i) translational or kinetic energy of the molecule (after breaking the bond with the grain surface), ii) heating the dust grain at the formation site, and iii) internal energy of the molecule in the form of excitation of rotational-vibrational states within the electronic ground state. The exact distribution of energy depends on the details of formation that are fundamentally unknown, and so formation excitation is difficult to assess observationally [72].

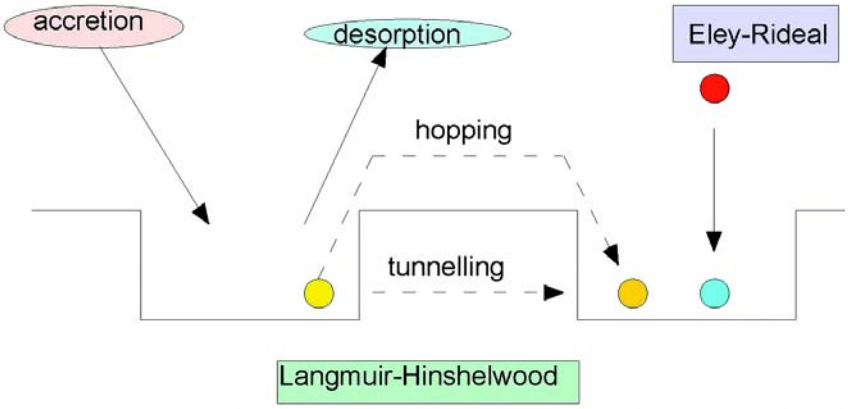

Figure 1.4 The two major mechanisms of surface chemistry following accretion onto a dust grain with lattice sites shown as potential energy minima in one dimension. Diffusion occurs *via* hopping or tunnelling from one lattice site to another. Figure reproduced from S. T. Bromley, T. P. M. Goumans, E. Herbst, A. P. Jones and B. Slater, *Phys. Chem. Chem. Phys*, vol. 16, pp. 18623-18643, 2014.

There are three proposed mechanisms through which molecular hydrogen is thought to be formed at the dust grain surfaces: the Langmuir-Hinshelwood (LH) mechanism, the Eley-Rideal (ER) mechanism and the *hot atom* (HA) mechanism, which are shown in Figure 1.4. In the LH mechanism [73], [74], both reactants first adsorb onto the surface, then react by recombination and finally the reaction product desorbs from the surface (surface diffusion facilitates the interaction between adsorbed molecules):

$$\begin{matrix} H_{(g)} \\ k_H \quad \downarrow\uparrow \quad k'_H \\ H_{(ads)} \end{matrix} + \begin{matrix} H_{(g)} \\ k_H \quad \downarrow\uparrow \quad k'_H \\ H_{(ads)} \end{matrix} \xrightarrow{k} \begin{matrix} H_{2\,(g)} \\ \downarrow\uparrow \\ H_{2\,(ads)} \end{matrix}$$

In the ER mechanism [75], [76], only one of the reactant adsorbs onto the surface, after which the other reactant interacts with the adsorbed species directly from the gas phase, followed by the desorption of the reaction product:

$$\begin{matrix} H_{(g)} \\ k_H \quad \downarrow\uparrow \quad k'_H \\ H_{(ads)} \end{matrix} + H_{(g)} \xrightarrow{k} H$$

The previous two mechanisms represent the extremes in terms of coverage. However, Harris and Kasemo [77] considered the case where one of the reactants is adsorbed while the other one has a high translational energy to reach to the surface, losing part of its energy by diffusion, and reacting with the pre-adsorbed atom. This is the *hot precursor* or *hot atom* (HA) mechanism. All three of these mechanisms have been studied theoretically

[52], [60]–[63], [65]–[69], [78], with most work done on the ER mechanism as it is the easiest one to model. However, in interstellar conditions, the LH mechanism is thought to dominate, since at such low pressures, there will be very low coverage of H-atoms. There will be so few adsorbed atoms on the surface that it is unlikely that a gas phase atom will collide with a pre-adsorbed atom on impact with the dust grain.

1.2.4. Previous Astrochemical Modelling and Experimental Studies

As aforementioned, Gould and Salpeter [50] developed the first astrochemical model of H_2 formation in the ISM in 1963, modelling a "dirty-ice" surface between temperatures of 10–20 K, and Hollenbach and Salpeter [33], [79] extended the treatment to model dust grains as irregular surfaces below a critical temperature of 40–50 K and to include H-atoms bound to defects.

Cazaux and Tielens [57], [58] found that H_2 can form efficiently on dust at T=6–300 K. It was found that physisorbed H-atom recombines efficiently with a chemisorbed H-atom up to ~100 K. At higher temperatures, the residence time of physisorbed atoms on the surface was too short to react and form H_2; hence at high temperature regions of the ISM, two chemisorbed H-atoms are required to form molecular hydrogen. The reaction between two chemisorbed H-atoms was found to be less efficient than the reaction between a physisorbed and a chemisorbed atom [57].

These astrochemical studies considered dust particles as "ideal" grains, and this will affect the applicability of these modelling results to astrophysical regions in the ISM and also to any laboratory experiments considered. Nevertheless, the general conclusion from the above astrochemical studies is that the formation of H_2 on a dust grain surface is efficient, and that nascent molecules may exhibit significant vibrational and rotational excitation.

Laboratory investigations into H_2 formation have produced a variety of results, being the group of Pirronello, Vidali and coworkers [51], [53]–[56] some of the most important. They carried out temperature-programmed desorption (TPD) studies of H_2 formation on various surfaces of astrophysical relevance, such as silicate surfaces by using olivine as the dust grain analogue, amorphous carbon surfaces and amorphous water-ice surfaces. On olivine, the Pirronello group found that the recombination efficiency was lower than

seminal model-based estimates [54]. However, it could be improved with estimates of the recombination efficiency from astrophysical observations and more developed models, in which dust grains are taken to be coarser and larger. By studying HD formation on olivine as a function of surface temperature, Pirronello *et al.* [53] concluded that at low surface temperatures there are two main regimes of surface coverage by H-atoms that are of astronomical importance. The most important result is for the high coverage regime, which indicates that the H_2 formation nascent energy (~4.5 eV) will not cause the molecule to be desorbed directly into the gas phase, but that the surface may act as a reservoir for a significant amount of energy. In a further study, the Pirronello group also found that the recombination of H_2 is efficient for olivine held at a range of temperatures from 6 to 10 K and for carbon surfaces held at a range of temperatures from 10 to 20 K [55].

The Pirronello group also investigated H_2 formation on amorphous ice on top of an inert surface [56], using both low and high density amorphous solid water (ASW). Low density ASW is microporous and has a higher surface area to volume ratio than high density ice. It was found that H_2 formation was more efficient on low density ASW but also that the efficiency increases at low surface temperatures, at T = 10 K.

1.2.5. Chemical Role of H_2

A good recent perspective about the role of molecular hydrogen and the interstellar chemistry is the work by Herbst [80]. Much of the formation of molecules found in the ISM can be explained using gas-phase chemistry initiated by cosmic rays. Cosmic rays are fast particles, mostly protons, electrons, and helium ions, and they pervade the entire volume of interstellar space. They range widely in energy, but those that interact most effectively with the gas have energies from a few MeV up to a few hundred MeV. Cosmic rays (*c.r.*) of such high energies are obviously capable of ionising all interstellar species and will ionise molecular hydrogen, for which the most likely channel leads to the hydrogen molecular ion (H_2^+). In dense clouds, where much of the hydrogen is molecular due to the negligible photodissociation rate for the galactic UV field, the most likely reaction for the hydrogen molecular ion is with another hydrogen molecule to form protonated molecular hydrogen (H_3^+), a stable molecule of triangular form and the most

fundamental polyatomic molecule [4], whose presence was predicted originally in regions where H_2 is partially ionized, and formed through the reactions [81]:

$$H_2 + \text{c.r.} \rightarrow H_2^+ + e^- + \text{c.r.}$$

$$H_2^+ + H_2 \rightarrow H_3^+ + H$$

H_2 has a rather low proton affinity (*i.e.*, low reaction energy between H_2 and H^+), so H_3^+ once formed readily donates its extra proton to just about any atom or molecule, thereby initiating a network of ion-molecule reactions that is thought to be responsible for the formation of many interstellar species. The ionization state of heavy elements in the diffuse ISM depends on the ionization energy of the atoms in the ground state. For the common elements C, N, O and S, they are likely to be in ionization states of C^+ and S^+, while N and O remains non-ionized. Reactions with atomic oxygen to form water and the OH radical (both are found in high relatively abundance) are:

$$H_3^+ + O \rightarrow OH^+ + H_2$$

$$OH^+ + H_2 \rightarrow H_2O^+ + H$$

$$H_2O^+ + H_2 \rightarrow H_3O^+ + H$$

$$H_3O^+ + e^- \rightarrow OH + H_2 \text{ or } 2H$$

$$\rightarrow H_2O + H$$

Separate from the hydrogen–oxygen chemistry, one of the rare examples in which a radiative association reaction plays an important role in forming molecules in space is the process that initiates the hydrogen–carbon chemistry. Simple hydrocarbons, such as CH_2, can be produced *via*:

$$C^+ + H_2 \rightarrow CH_2^+ + h\nu$$

$$CH_2^+ + H_2 \rightarrow CH_3^+ + H$$

$$CH_3^+ + e^- \rightarrow CH + H_2 \text{ or } 2H$$

$$\rightarrow CH_2 + H$$

where H_2 is needed in the first and second step.

CO is the second most abundant molecule in the ISM. It is of major importance in star formation and at low cloud temperatures (between 10 and 100 K) it is also a very important molecular coolant, radiating excess energy in the millimetre wavelength range. Energetically possible (exothermic) reactions of the products above, OH and CH_3^+, with relatively abundant C^+, O and N, can lead to CO and CN (CN can be produced by similar reactions by replacing O with N in the last two reactions) through the following reactions:

$$C^+ + OH \rightarrow CO^+ + H$$

$$CO^+ + H_2 \rightarrow HCO^+ + H$$

$$CH_3^+ + O \rightarrow HCO^+ + H_2$$

$$HCO^+ + e^- \rightarrow CO + H$$

in which H_2 is consumed in the second step and newly formed in the third one.

Molecular formation in the ISM often proceeds through ion-molecule or neutral-neutral gas-phase reactions. Exothermic ion-molecule reactions, as a rule, occur rather rapidly because the strong polarization-induced interaction potential and can be used to overcome any activation energy involved. They are approximately two orders of magnitude faster than neutral-neutral reactions, even disregarding the activation barriers generally involved in the latter. Thus, a small amount of ionization can be very effective in driving interstellar chemistry. If the ion-molecule reaction involves a neutral species possessing a permanent dipole, then the reaction rate coefficient can be much larger [4].

To sum up, the presence of H_2, which initiates all of the chemistry in the ISM, is essential for the synthesis of larger species like the molecules listed in . Otherwise, none of these molecules would be found in the ISM.

1.3. Interstellar Dust Grains

So far, we have been concerned primarily on the molecular composition of the ISM and the species present in it, as well as on the formation of molecular hydrogen. We now turn our attention to a solid-state component: Interstellar Dust Grains.

Dust grains are small, solid flakes of graphite and/or silicates coated with water ice, found in the interstellar and interplanetary media. They are irregularly shaped with sizes of the order of a fraction of a micron across. Grains, as mentioned above, provide a surface where species can accrete, meet, and react, giving rise to a complex chemistry. Dust grains are also crucial sites of molecule formation, and are thought to be responsible for most of the H_2 in the ISM. They also regulate the gas phase abundances of the elements through accretion and destruction processes. Molecular chemistry is unthinkable without dust grains acting as reaction sites. Additionally, dust is not only the main molecule builder, it might also be thought as one of the principal ingredients of planetary formation, and life.

Thus, dust grains are important components of the interstellar medium [82]. In our Galaxy, the gas-to-dust ratio is about 100:1. Since the ISM is about 10% of the baryonic mass of the Galaxy (stars and atomic gas), dust grains comprise roughly 0.1% of the total. At the same time, they absorb approximately 30-50% of the UV and visible starlight emitted by nearby stars and re-radiate it as far-IR continuum emission, dividing into two main emissions: i) the "Extended Red Emission", a broad featureless emission band peaking between 0.61 and 0.82 μm, and the ii) "Thermal Continuum Radiation", one at wavelengths above 60 μm (far-IR) and the other one at 3-30 μm [83]. Since the IR radiation is of lower energy than the UV and visible ones, the difference goes into heating the dust grain, with typical temperatures of about tens of Kelvin degrees.

However, the manifestation of interstellar dust that first brought it to our attention is its ability to extinguish starlight passing through it. The most dramatic manifestation of interstellar dust is the dark cloud catalogued at the beginning of the 20th century, many of which can be seen with the naked eye in the Milky Way. Dust provides the dominant opacity source in the interstellar medium for non-ionizing photons and therefore controls the spectral energy distribution at all wavelengths longer than 912 Å. Therefore, the presence of dust grains in the ISM is deduced observationally by interaction with starlight.

1.3.1. Composition

Dust grains are solid, microscopic particles expected to consist of abundant dielectric and refractory materials (primarily carbon and/or silicon, among others) and compounds of hydrogen and abundant gases such as oxygen, leading to the formation of high temperature

condensates such as silicates, graphite, and carbides [22]. The grain composition determines the index of refraction needed to determine its optical properties. There is no one single type of "grain", but rather a mixture of different types of grains formed under different physical conditions. The composition of interstellar dust has been widely debated and silicates and carbonaceous materials are generally considered the most important interstellar dust components, with ices of volatile compounds like water or CO_2 condensed on their surfaces (*e.g.*, "ice mantles"). Pure metallic grains (*e.g.*, iron spheres or needles) have also been considered. In general, silicates are expected to provide a substantial fraction of the total mass in dust grains in the ISM, followed by carbonaceous compounds.

The "interstellar silicate" is an ensemble of astrophysical silicates with different types and amounts of contamination, existing as a mixture of crystalline and amorphous forms (~5% crystalline and 95% amorphous in the ISM, although different crystalline fractions have been suggested in other environments like circumstellar dust shells). Interstellar silicates are formed from compounds with Fe and Mg since both elements are astrophysically abundant, although dust grains also lock up a substantial fraction of all heavy elements. The principal forms are Pyroxens ($Mg_xFe_{1-x}SiO_3$, $x = 0 - 1$), including Enstatite ($MgSiO_3$) and Ferrosilite ($FeSiO_3$), and Olivines ($Mg_{2x}Fe_{2-2x}SiO_4$, $x = 0 - 1$), including Fayalite (Fe_2SiO_4) and Forsterite (Mg_2SiO_4). All of these are common in meteorites and spectral signatures of Enstatite and Forsterite have been seen in the dusty shells around AGB stars. Olivine and Forsterite have been observed in comets and in dust grains captured by the Stardust mission.

Carbonaceous dust grains include pure carbon in both crystalline form (*i.e.*, diamond and graphite), and amorphous or glassy form (*i.e.*, composed of a mixture of graphite and diamonds), and hydrocarbons in the form of hydrogenated amorphous carbons, polycyclic aromatic hydrocarbons (PAHs), and aliphatic hydrocarbons. Carbonaceous compounds such as silicon carbide (SiC) and carbonates such as Calcite ($CaCO_3$) and Dolomite ($CaMg(CO_3)_2$) are also present, but are rare ($< 5\%$ of all forms of carbonaceous grains).

1.3.2. Formation

The primary breeding ground for solid particles to become interstellar dust grains is thought to have started during the mass-loss of lower mass stars in the late stages of stellar

evolution (*i.e.*, the AGB stage). Observationally, it appears that most dust grains that are essential for the formation of planetary system are formed in the dense outflowing winds of cool AGB and Red Giant stars, in old planetary nebulae and in the cooling envelopes of novae, rather than in the ISM itself. In these atmospheres we find the ideal conditions for dust formation: sufficient high densities (~10^9 particles cm^{-3}) for grain growth coupled with moderate gas kinetic temperatures close to the condensation temperatures of many heavy elements (1000–2000 K), high supersaturation pressure needed for nucleation directly from the gas phase and limited dust destruction by evaporation, sputtering and/or shocks [84].

When dust grains in a protostellar disk begin to coagulate into larger grains, these lead to planetesimals and eventually to planets. However, once formed, the grains can be broken into smaller units by a combination of sputtering and grain-grain collisions. For more massive stars, in the warm neutral and ionized intercloud media, dust is processed by a combination of photoerosion by UV light and strong shocks driven by supernova explosions if the conditions are not too harsh. The hot gases in the shock can sputter atoms from the grains. Also, high velocity collisions among grains can lead to vaporization, melting, phase transformation, and shattering of the projectile and target. In any scenario, dust production will only be possible for a relative short period of stellar evolution, on time scales of a few to a few thousand years.

The source of dust components are divided into two basic classes depending on the relative O/C abundances [85]:

- **O > C (Oxygen Rich):** The atmosphere of the Sun and the diffuse ISM are oxygen rich. The principal dust components are silicates and not carbonaceous solids as most of the C is as CO. Observations show that the dusty outflows from O-rich stars have very strong 10 and 18 μm silicate features in their spectra.
- **O < C (Carbon Rich):** This occurs in Carbon Stars where nucleosynthesis has raised the atmospheric C abundances very high. The principal dust components are carbonaceous solids like graphite and amorphous carbon. The 10 μm silicate feature is notably absent in the mid-IR spectra of carbon stars, but some show a weak 11.3 μm SiC emission feature.

Spherical grains are usually considered because they permit straightforward analytic solutions. The reality, however, is that grains are not spheres (see Figure 1.5). Indeed, the observed polarization of starlight passing through dust grains demands that the grains are non-spherical. One way to approach the intrinsic size distribution of grains is to consider a model in which grains grow by steady accretion; *i.e.*, two small grains collide and stick to form a bigger grain, which collides with interstellar atoms and stick to grains and so forth. The treatment originally considered was simple atomic accretion, without grain-grain sticking [86].

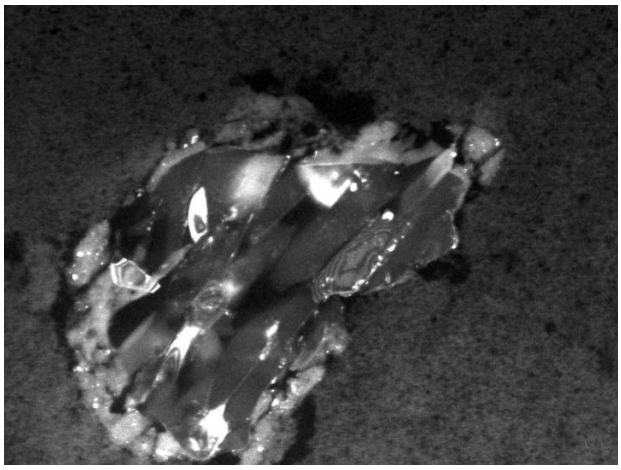

Figure 1.5 A grain of Forsterite from Comet 81P/Wild 2, captured by the NASA spacecraft Stardust and brought back to Earth. The particle is about 2 micrometres across.
Image Credit: NASA/JPL-Caltech/University of Washington

1.3.3. Olivines

Olivines ($Mg_{2x}Fe_{(2-2x)}SiO_4$) are one of the most abundant silicate groups in the Earth's upper mantle. These silicate groups are mostly found in a crystalline state. Cosmic olivines, however, are mainly present as amorphous materials [87], although crystalline forms have also been detected [88]. Crystalline olivines present an orthorhombic structure with space group *Pbnm* (a=4.746 Å, b=10.18 Å, c=5.976 Å) [89] and consist of distorted SiO_4 tetrahedra and MgO_6/FeO_6 octahedra, in which the tetrahedra and the octahedra share the vertices. Half of the available octahedral voids are occupied by the divalent cations, as it can appreciate in Figure 1.6. There are two symmetry-independent Mg atoms [90]: one of them shares edges forming rods parallel to the crystallographic *c* axis; the other one are

laterally linked to these rods through the corresponding edges (we will discuss more this symmetry in Section 3.1).

Both on Earth and in space, crystalline olivines appear to be richer in magnesium than in iron [88], [91]. A typical sample of the mineral olivine contains approximately 10% Fe ($Mg_{1.8}Fe_{0.2}SiO_4$). Even so, it is worth mentioning that different studies indicate that the Fe-containing solid solutions are more stable in the high-spin state than in the low-spin one at normal conditions (*i.e.*, each Fe^{2+} cation (d^6) in a quintet electronic state) [92]–[94].

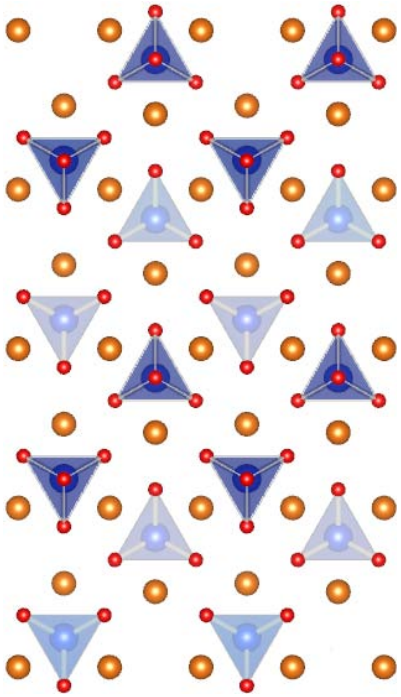

Figure 1.6 View of the bulk geometry of olivine material such as forsterite or fayalite along the crystallographic *z* axis. O, red; Mg or Fe, gold; Si, blue; SiO_4 units shown as tetrahedral are emphasized.

As mentioned before, silicate dust grains emit thermal radiation at IR and millimetre wavelengths, and their mid-IR spectral features give information on both the chemical composition and the size of dust grains [87]. Amorphous silicates generally show two single broad IR bands at about 9.7 and 18 μm, corresponding to the Si–O stretching and O–Si–O bending vibrations, respectively. The amorphous character of the interstellar silicates results in broad bands due to the random distribution of bond lengths and angles characteristic of this amorphous nature. In contrast, crystalline silicates exhibit a wealth of narrow bands, dividing the spectrum generally into three main spectral regions: i) between 9.0–12.5 μm, corresponding to different asymmetric and symmetric stretching vibrations of the SiO_4 tetrahedra; ii) between 14–22 μm, due to bending vibrations of the SiO_4

tetrahedra; and iii) beyond 22 μm, attributed to translational motions of the metal cations. These spectral "fingerprints" help the identification of silicate minerals in space.

1.4. Previous Theoretical Works

1.4.1. Formation, Structure and Modelling of Olivines

Silicates are present throughout circumstellar and interstellar space; however, the processes that lead to their formation are poorly understood. Being SiO the dominant silicon bearing molecule in stellar outflows, Reber *et al.* [95] combined experiments in beams with theoretical investigations to examine mechanisms for the agglomeration of SiO to form silica as a limit case of O-rich silicate. In addition, Goumans and Bromley [96] added the presence of Mg to these nucleation processes, showing that pure SiO nucleation is unfeasible, while heteromolecular nucleation of Mg, Si, and O is a plausible mechanism to form magnesium silicates under stellar outflow conditions.

Atomic-scale simulations of solid state surfaces are useful techniques to understand the physicochemical properties of olivines, as they provide structural atomistic details (*e.g.*, the presence and nature of surface defects) [97], [98], one-electron properties (*e.g.*, charge distribution, electrostatic potentials, and spin densities) or spectroscopic properties (*e.g.*, vibrational features, infrared signatures, and dielectric tensors) [99], [100]. Forsterite surfaces are by far the most studied olivine surfaces with different atomistic simulation techniques, by means of periodic treatments using classical shell-ion model potentials [101], [102] and using density functional methods [103], in order to evaluate the structures and stabilities of their low-indexes surfaces.

The large variability of oxygen sub-lattice in the forsterite mineral results in a complex set of crystal planes. For instance, there are already 7 different planes characterized by the smallest Miller indexes due to the crystal's orthorhombic symmetry ({100}, {010}, {001}, {110}, {101}, {011}, {111} crystal forms) whose structural modelling is rather difficult, since electroneutrality should be enforced by complex chemical reconstruction. If surfaces with plane indexes of up to 2 are included, the total number of structurally unique orientations increases to 19. Normally, slab models are modelled by cutting out the bulk crystal at the Mg–O bonds rather than the Si–O ones to keep the SiO_4 units intact, as

previous calculations have indicated that the breaking of the Si–O interaction always results in less stable surfaces [101]. Moreover, both polar and nonpolar surface slabs can be obtained, depending on the edge layers and the thickness of the slab model.

Table 1.2 summarizes the surface energies of the seven most common crystallographic forms of forsterite reported by different previous studies (for a more details see Section 2.4.2.2 of Chapter 2). There is a good agreement between them, and the small differences are due to the electronic structure method used. The faces with the lowest and highest surface energies, in all the cases, are the (010) and (110), respectively. Additionally, the nonpolar (010) forsterite surface – the most stable one in dry conditions according to these previous calculations – is the major cleavage plane. Then, the following stability order of the surfaces is: (010) < (120) < (001) < (101) ≈ (111) < (021) < (110).

Table 1.2 *Surface energies γ (J m^{-2}) of the main crystal faces of forsterite*

Face	Watson *et al.* [101]	de Leeuw *et al.* [102]	Bruno *et al.* [103]
(010)	1.28	1.28	1.22
(101)	1.81	1.88	1.78
(111)	1.80	1.81	1.84
(001)	1.61	1.74	1.78
(110)	2.28	1.96	2.18
(120)	1.56	1.56	1.36
(021)	1.95	1.94	1.90

All these surface energy values determine the equilibrium morphology of a crystal, and also the related growth rate of the various surfaces, providing a measure of the relative stabilities of the surfaces. Therefore, considering the surface energy values listed in Table 1.2 it is possible to draw the equilibrium morphology of a forsterite crystal in vacuum. As an example, Figure 1.7 shows a common experimental morphology of forsterite.

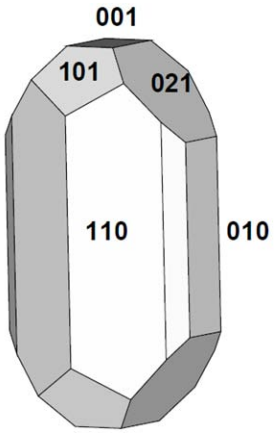

Figure 1.7 Experimental equilibrium morphology of forsterite, taken from de Leeuw *et al.* [102].

1.4.2. Surface Molecular Hydrogen Formation

Several theoretical studies focusing on the H_2 formation on carbonaceous surface models (*i.e.* coronene clusters and C(0001) surfaces) have been published [60]–[69], generally predicting a high reaction probability and significant rotation-vibration populations in nascent molecules, in agreement with the experimental findings [104]. Usually, effects due to the presence of porous and point defects were not accounted for.

Few quantum mechanical-based studies dealt with the H adsorption and the H_2 formation on silicate surfaces, in which the latter is simulated either by nano-clusters or by periodic approaches using crystalline surfaces. The studies of Bromley and coworkers [105], [106] belong to the first category, in which $(MgO)_6((SiO)_2)_3$ and $Mg_4Si_4O_{12}$ silicate nano-clusters were adopted as dust models and both H adsorption and recombination were studied using density functional theory (DFT) methods and Gaussian type basis sets. Garcia-Gil *et al.* [107] exhaustively explored different H adsorption sites on the Mg_2SiO_4 (010) surface by means of periodic calculations at the PBE level with core pseudopotentials and triple-zeta polarized localized basis sets as encoded in the SIESTA program, showing that the most favourable physisorption site is on the Mg atom and the chemisorption one on the neighbouring O atom. Downing *et al.* [108] studied the H adsorption on the (010) crystal termination of both forsterite and fayalite using a PBE functional and plane wave basis set as encoded in the VASP program, finding chemisorption on both Mg and O sites.

An embedded (QM/MM) approach was adopted by Goumans *et al.* [109], in which a cluster model of the (010) crystalline forsterite surface containing 55 atoms was treated quantum mechanically with the mPWB1K functional and Gaussian basis set of polarized double zeta quality, which was embedded in a large array of point charges providing the long range Coulomb contribution. They found that the simultaneous H adsorption on the Mg and O surface sites yields the formation of a hydride (H^-) and a proton (H^+), respectively, the recombination of which was found to be energetically very favourable. This point was essential to establish a route to the formation of molecular H_2 through chemisorbed H atoms, which is operative at relatively high temperature (diffuse clouds, $T = 100\ K$) at which the H physisorbed state would be unstable.

On the other hand, interaction of molecular hydrogen with MgO surfaces has been largely studied. It was demonstrated that the H_2 molecule dissociates heterolytically on stepped MgO surfaces [110], [111], with formation of H^+ bound to a low-coordinated O^{2-} anions (OH groups) and H^- ions bound to Mg cations (MgH groups). Homolytic splitting, with formation of a pair of OH groups per adsorbed H_2 molecule, is only possible in special conditions, like for polar MgO(111) surfaces or under irradiation due to the generation of O^- radicals. Two theoretical relevant works are from Pisani and coworkers [110] and Pacchioni and coworkers [111]. The former one simulated the hydrogen interaction with an oxygen vacancy at the MgO(001) surface, correlating the heterolytically dissociation of hydrogen found with the defective MgO surface. And the latter one demonstrated that homolytic splitting of H_2 is the thermodynamically most favoured dissociation mode if MgO(001) films of a few atomic layers are deposited on a metal support.

1.5. Objectives

As aforementioned, the available theoretical works only addressed H_2 formation on the most stable surfaces and consider only the reactant paths starting from the H atoms accommodated on the most stable sites, while the reaction channels that connect one adsorption state to another one (*i.e.*, H hopping) have not been fully characterized. This is an important issue because at the very low temperatures at which these processes occur the inter-conversion between two adsorption sites could be kinetically hampered.

Moreover, atomistic details of the surface structure of dust grains, including the presence of Fe^{2+}, are still largely missing. The large number of studies on forsterite contrasts with the limited works focused on Fe-containing olivine surfaces, the available theoretical works being limited to the bulk and the (010) surface of fayalite [112]–[115]. This lack of theoretical studies is partly due to the large compositional variability in these minerals that can tolerate various isomorphic substitutions and to the fact that the treatment of Fe-containing minerals bears additional difficulties due to the possible presence of strong correlations effects. Therefore, the physicochemical properties of Fe-bearing olivine surfaces are poorly understood. Understanding these systems is of significant importance because they serve as an important source for electrons in redox reactions in various geochemical environments [116]–[119]. Moreover, the change of the Fe oxidation state may have a profound impact on the electronic structure of the surfaces of these minerals, such as in their adsorption properties and chemical activity.

Therefore, the aim of this thesis is the characterization of the bare forsterite surfaces and their role in the H_2 formation by using *ab initio* calculations based on Density Functional Theory methods adopting a periodic approach. In particular, main goals are:

1. Providing a detailed description of different physicochemical features of the bulk and (010) surface (the main cleavage crystallographic plane of forsterite) of Mg_2SiO_4 and $Mg_{1.5}Fe_{0.5}SiO_4$ (25% of Fe^{2+} substitution), as well as the (001) and the (110) surfaces of forsterite, as examples of systems with an intermediate and a high surface energy, respectively. In particular, analysis of the surface structures and electronic (electrostatic potentials and spin density maps, and Fe^{2+} electronic states), vibrational (infrared spectra) and dielectric (reflectance spectra) properties.
2. Describing the H adsorption and H_2 formation on the (010), (001) and (110) crystalline faces of forsterite (Mg_2SiO_4) represented by a slab model of finite thickness. This includes: i) characterization of different adsorption sites and of the corresponding interconversion paths; and ii) characterization of different reactive channels adopting both Langmuir–Hinshelwood and Eley-Rideal mechanisms that led to the H_2 formation. Differences on these aspects due to the different surface morphology and stability are also evaluated.
3. Extending the H adsorption and H_2 formation study on the (010) crystalline surface of $Mg_{1.5}Fe_{0.5}SiO_4$, to assess possible electronic structure effects exerted by Fe^{2+}.

2. Methodology

Theoretical chemistry applies the basic principles of physics to understand chemistry at the molecular level. While theoretical chemistry is concerned with providing the conceptual and mathematical tools to solve the many-electron problem represented by a molecular system, computational chemistry transforms these tools into efficient numerical algorithms that allow, through the use of computers, the study of systems and chemical processes. At the same time, quantum mechanics and statistical mechanics set the basics for our understanding of the properties of matter.

In this chapter we first review the general concepts on electronic structure calculation through the many-body Hamiltonian of electrons and nuclei. This leads naturally to the introduction of wave function-based methods and Density Functional Theory (DFT), one of the most popular methods for the solution of the many-body problem. Furthermore, since the present thesis employs silicate surface models, the quantum mechanical treatment of periodic systems is also provided. Finally, we will discuss *ab initio* molecular dynamics since it has been used throughout our study of gas/solid interface.

2.1. General Concepts on Electronic Structure Calculation

One of the central problems of quantum chemistry is the description of the motion of electrons in a system of interacting electrons and nuclei. Given a system of N_α nuclei and N electrons, the problem to solve is the time-independent, non-relativistic Schrödinger equation, $\widehat{\boldsymbol{H}}\boldsymbol{\Psi} = \boldsymbol{E}\boldsymbol{\Psi}$, where $\widehat{H}$ is the Hamiltonian operator for this system in the absence of electromagnetic fields and can be expressed as the sum of the kinetic terms of the nuclei ($\hat{T}_n$) and of the electrons ($\hat{T}_e$) and the potential terms for interactions between electrons and nuclei ($\hat{V}_{ne}$), electrons between each other ($\hat{V}_{ee}$) and between nuclei ($\hat{V}_{nn}$). If we adopt atomic units, the Hamiltonian $\widehat{H}$ can be written as:

$$\widehat{H} = -\frac{1}{2}\sum_{\alpha}\frac{1}{M_\alpha}\nabla_\alpha^2 - \frac{1}{2}\sum_{i}\nabla_i^2 - \sum_{\alpha}\sum_{i}\frac{Z_\alpha}{r_{\alpha i}} + \sum_{i}\sum_{j>i}\frac{1}{r_{ij}} + \sum_{\alpha}\sum_{\beta>\alpha}\frac{Z_\alpha Z_\beta}{R_{\alpha\beta}} \tag{2.1}$$

$$\widehat{H} = \hat{T}_n + \hat{T}_e + \hat{V}_{ne} + \hat{V}_{ee} + \hat{V}_{nn} \tag{2.2}$$

where α and β subscripts refer to the nuclei with charge Z and mass M, i and j subscripts refer to the electrons and e and n subscripts refer to electrons and nuclei, respectively.

To obtain an approximate solution the Born-Oppenheimer approximation [120] is introduced. Since the nuclei are so much more massive than the electrons (at least 1840 times in the case of the hydrogen atom) they must accordingly have much smaller velocities. In the Born-Oppenheimer approximation it is assumed that both movements are decoupled, thus it is plausible that on the typical time-scale of the nuclear motion, the electrons will very rapidly relax to the instantaneous nuclei configuration [121]. Within this approximation, the first term of eq. (2.1), the kinetic energy of the nuclei, can be neglected and the last term of eq. (2.1), the repulsion between the nuclei, can be considered to be constant. As a result, in order to solve the time-independent Schrödinger equation resulting from the Hamiltonian in eq. (2.1), we can assume that the nuclei are fixed and solve for the electronic ground-state first:

$$\hat{H}_e \Psi_e(\vec{r};\vec{R}) = (\hat{T}_e + \hat{V}_{ne} + \hat{V}_{ee})\Psi_e(\vec{r};\vec{R}) = E_e(\vec{R})\Psi_e(\vec{r};\vec{R}) \tag{2.3}$$

where $\Psi_e(\vec{r};\vec{R})$ is the electronic wave function, which describes the motion of the electrons and *explicitly* depends on the electronic coordinates but depends *parametrically* on the nuclear coordinates, as does the electronic energy, $E_e(\vec{R})$. Finally, one can calculate the energy of the system in that configuration and solve for the nuclear motion. The total energy $U(\vec{R})$, defined as the potential energy acting on the nuclei, is then the sum of $E_e(\vec{R})$ and the constant nuclear repulsion term, $V_{nn}(\vec{R})$:

$$U(\vec{R}) = E_e(\vec{R}) + V_{nn}(\vec{R}) = E_e(\vec{R}) + \sum_{\alpha}\sum_{\beta>\alpha}\frac{Z_\alpha Z_\beta}{R_{\alpha\beta}} \tag{2.4}$$

The exact solution to eq. (2.3) is limited to the H_2^+ molecule-ion. For larger systems, methods to obtain approximate solutions to eq. (2.3) have been developed (see *e.g.* Ref. [122] for a review). In the following section we provide an introduction to two of the most popular electronic structure methods: wave function-based methods and Density Functional methods.

2.2. Wave Function-Based Methods

The first applications of quantum mechanics to the chemical bond came very shortly after the simplest electronic system, the hydrogen atom, had been solved. To overcome the impossibility of exactly solving the Schrödinger equation for many electron systems, in 1930 Hartree and Fock proposed the origin of the current *ab initio* methods.

2.2.1. Hartree-Fock Approximation

The simplest approximation for the electronic wave function for a system with *N* electrons is known as the *Hartree product*, the product of *N*-orthonormal one-electron wave functions (spin-orbitals, χ_i), which in turn are defined by the product of a spatial function $\phi_i(\vec{r})$ and a spin function $\alpha(s)$ or $\beta(s)$. However, the Hartree product cannot describe properly the multi-electron wave function because it is not antisymmetric with respect to the exchange of the coordinates of any pair of particles. A proper antisymmetric wave function which ensures this property is obtained from these products organized in a *Slater determinant*. When a single Slater determinant is used to approximate the electronic wave function, the solution of the Schrödinger equation is achieved by the variational Hartree-Fock method (a complete description of such technique can be found in Ref. [121]–[123]).

The Slater determinant that generates the lowest possible energy value is obtained by minimizing the energy with respect to the spin-orbitals, under the condition that they remain orthonormal during minimization. The resulting equations are the Hartree-Fock equations, which are in *N* equations where each electron moves in an average field. To solve them, Roothaan [124] and Hall [125] proposed to express each molecular orbital as a linear combination of atomic orbitals (LCAO), which are those that constitute the basis set functions. The weights in the combination should be determined by the variational principle, by means of an iterative process known as Self Consistent Field (SCF) method.

2.2.2. *Post* Hartree-Fock Methods

The Hartree-Fock (HF) method is the first and simplest approach to describe quantum mechanically most of the chemical systems. A principal drawback is that it considers electrons as independent particles that move in an average field, thus hampering their

movements to be correlated. That is, the HF approximation has a lack of electron correlation. In order to include this quantum-mechanical phenomenon one can expand the wave function including more Slater determinants representing different electron configurations [122]. The conventional methods for including it start with the HF function and are referred to as *post* Hartree-Fock methods. Among these methods, the most important are: the variational method of configuration interaction (CI) [126], the many body perturbation theory (MBPT) [127], [128] and the coupled cluster method (CC) [129]–[131].

i) CI methods define the wave function (Ψ_{CI}) as a linear combination of Slater determinants representing different electronic configurations (Ψ_I), $\Psi_{CI} = \sum_I c_I \Psi_I$. Among the *post*-Hartree-Fock methods, CI is conceptually the simplest one, since it consists in solving the eigenvalue equation of the system once the matrix representation of the Hamiltonian has been expressed on the basis of the configurations of the determinants. However, a Slater determinant is not always an eigenfunction of $\hat{S}^2$ and therefore, when working with determinants, it should be taken into account that the spin-adapted configurations frequently include more than one determinant and that in order to preserve the space and symmetry properties of the wave function, the complete configuration has to be included in the expansion.

ii) MBPT can be applied to systems whose Hamiltonian can be expressed by the sum of two contributions: the zeroth-order Hamiltonian, $\widehat{H}_0$, whose eigenvalues and eigenfunctions are known, and the perturbation, $\hat{V}$. The exact energy and the wave function can be expanded in an infinite series whose elements are the zeroth-order energy and wave function and the successive corrections, expressed through increasing powers of the perturbation operator, $\hat{V}$. If the partition between the zeroth-order Hamiltonian and the perturbation is appropriate, the energy correction series converges and the estimation of the exact energy is acceptable with a limited expansion. It should be taken into account, however, that the results are not variational and accordingly it is easy to overestimate the energy corrections when the system has almost degenerate energies between the excited and the reference configurations.

iii) CC theory introduced the concept of wave operator as an operator that transforms the reference wave function into the exact one. Hence, an exponential expression of the wave function is proposed:

$$\Psi_{CC} = e^{\hat{T}}\Psi_0 \tag{2.5}$$

where Ψ_0 is the reference wave function and $\hat{T}$ is the *cluster operator*, which can be expanded as a sum of cluster operators for each excitation degree:

$$\hat{T} = \hat{T}_1 + \hat{T}_2 + \hat{T}_3 + \ ... \tag{2.6}$$

Expanding the exponential in a Taylor series:

$$e^{\hat{T}} = \hat{1} + \hat{T} + \frac{1}{2!}\hat{T}^2 + \frac{1}{3!}\hat{T}^3 + \ ... \tag{2.7}$$

and equalling the terms with the same excitation level, the degree-of-excitation relations are obtained. In these expressions two types of contributions can be observed: $\hat{T}_i$ is the so-called *linked* or *connected* cluster component of the *i*-th excitation degree, and the other terms, all products of two operators or more, are the *disconnected* components, which reach the same degree of excitation from products of lower excitation operators.

The first level of approximation in CC methods consists of truncating the cluster expansion at the double excitations: $\hat{T} = \hat{T}_1 + \hat{T}_2$, leading to the CCSD approximation [132]. Nowadays there are different methods that go beyond double excitations and include the effect of the triple excitations, in the exact, as CCSDT, or approximate form, such as CCSD(T) [130]. The CC methods have the undoubted advantage that they lead to correct fragment separability. But similar to the configuration and perturbative methods, they need a reference wave function Ψ_0; that is, the determinant formed from the first *N* basis functions φ_i (*i.e.*, occupied orbitals).

2.3. Density Functional Methods

Density Functional Theory [133] is an alternative way to wave function-based *ab initio* methods to introduce the effects of electron correlation in solving the electronic Schrödinger equation (see eq. (2.3)). The low computational cost, combined with reasonable accuracy, has made DFT a standard technique in most branches of chemistry and materials science [134]. According to the DFT, the ground-state energy of a many-electron system can be expressed from the electron density and indeed the use of the electron density rather than the wave function for the calculation of the energy forms the foundation of DFT. Unfortunately, the exact mathematical formula relating energy to the electron density is not known and it is necessary to use approximate expressions. In the following sections the fundamentals and the practical formulation of DFT are discussed.

2.3.1. The Foundations of DFT

DFT has its conceptual roots in the Thomas–Fermi model of a uniform electron gas [135], [136] and the Slater local exchange approximation [137]. A formalistic proof for the correctness of the Thomas–Fermi model was provided by the Hohenberg–Kohn (HK) theorems [138], [139], which along with the Kohn–Sham formalism [140] constitute the two core elements of DFT. The former is mainly conceptual, but *via* the second the most common implementations of DFT have been done.

The first HK theorem states that any observable of a stationary non-degenerate ground state can be calculated, in principle exactly, from the electron density of the ground state $\rho_0(r)$; that is, any observable can be written as a function of the electron density of the ground state. Quoting directly from the Hohenberg/Kohn paper, this first theorem states that *"the external potential $V_{ext}(\vec{r})$ is (to within a constant) a unique functional of $\rho(r)$; since, in turn $V_{ext}(\vec{r})$ fixes $\hat{H}$ we see that the full many particle ground state is a unique functional of $\rho(r)$"*. There is a one-to-one mapping between the ground-state density $\rho_0(r)$ and the corresponding ground-state wave function $\Psi_0(r_1, r_2, \dots, r_N)$ and, accordingly, any ground-state property of a system can be obtained from the density. The second HK theorem provides the variational principle for $E[\rho]$ and states that the electron density of a non-degenerate ground state $\rho_0(r)$ can in principle be calculated, determining the density that minimizes the energy of the ground state E_0 [141]. Thus, the ground-state energy E_0

can be obtained from the minimization of this functional at the ground-state density $\rho_0(r)$, namely:

$$E_0 = E[\rho_0(r)] \leq E[\rho(r)] \tag{2.8}$$

A successful minimization of the energy functional $E[\rho(r)]$ will yield the ground-state density $\rho_0(r)$ and thus, all other ground-state observables. The first and second Hohenberg–Kohn theorems together attempt to find a solution to the many-body problem in terms of $\rho(r)$ alone instead of the much more complicated many-body wave function that depends on $3N$ degrees of freedom. A practical scheme for calculating ground-state properties from electron density was provided by the Kohn–Sham approach [140] considered in the next section.

2.3.2. The Kohn–Sham Method

In 1965, Kohn and Sham developed, with the introduction of atomic orbitals, a formalism that yields a practical way to solve the HK theorem for a set of interacting electrons, starting from a virtual system of non-interacting electrons that have an overall ground-state density equal to the density of the real system where electrons do interact. The main problem behind initial DFT formalisms was the difficulty in representing the kinetic energy of the system. The central premise in the Kohn–Sham (KS) approach is that the kinetic energy functional of a system can be split into two parts: one part that can be calculated exactly and that considers electrons as non-interacting particles and a small correction term accounting for electron-electron interaction. Following the KS formalism, within an orbital formulation, the electronic energy of the ground state of a system comprising *N* electrons can be written as:

$$E[\rho] = T_s[\rho] + V_s[\rho] + V_{ee}[\rho] \tag{2.9}$$

where $T_s[\rho]$ represents the kinetic energy of the non-interacting electrons, $V_s[\rho]$ accounts for the nuclear-electron interactions and $V_{ee}[\rho]$ is the electron-electron interaction, composed of two terms:

$$V_{ee}[\rho] = J[\rho] + E_{XC}[\rho] = \frac{1}{2}\iint \frac{\rho(r_1)\rho(r_2)}{|r_1 - r_2|} dr_1 dr_2 + E_{XC}[\rho] \tag{2.10}$$

where the first term $J[\rho]$ correspond to the Coulombic repulsions between the total charge distributions at r_1 and r_2, and the second term $E_{XC}[\rho]$, known as exchange-correlation, accounts for all quantum mechanical terms not included in $J[\rho]$: the correction to the kinetic energy arising from the interacting nature of the electrons and all non-classic corrections to the electron-electron interactions (*i.e.*, exchange and Coulomb correlations and the correction to the unphysical self-interaction contribution). The most challenging aspect of DFT is the description of this term.

The ground-state electron density $\rho(r)$ at a location *r* can be written as a set of one-electron orbitals (the KS orbitals, $\chi_i(r)$), given by:

$$\rho(r) = \sum_{i=1}^{Noc} |\chi_i(r)|^2 \tag{2.11}$$

The KS orbitals are determined by solving the KS equations. These can be derived by applying the variational principle to the electronic energy $E[\rho]$, with the charge density given by eq. (2.11):

$$\hat{h}_{KS}\chi_i(r) = \varepsilon_i\chi_i(r) \tag{2.12}$$

In this equation $\hat{h}_{KS}$ represents the KS Hamiltonian and ε_i is the KS orbital energy associated. The KS Hamiltonian can be written as:

$$\hat{h}_{KS} = -\frac{1}{2}\nabla^2 + V_{eff}(r) \tag{2.13}$$

where the first term describes the kinetic energy of the non-interacting *i*-electron and the second one, $V_{eff}(r)$, is the effective potential which transforms a virtual system of non-interacting electrons into one that has the ground-state electron density equal to that of the target system and that accomplish eq. (2.11). $V_{eff}(r)$ depends on the density as:

$$V_{eff}(r) = V_n(r) + \int \frac{\rho(r_2)}{|r_1 - r_2|} dr_2 + V_{XC}(r) \tag{2.14}$$

and must be used in the one-electron eq. (2.12) to determine the KS orbitals. $V_{XC}(r)$ in eq. (2.14) is the functional derivative of the exchange-correlation energy, given by:

$$V_{XC}(r) = \frac{\delta E_{XC}[\rho]}{\delta \rho(r)} \tag{2.15}$$

Once $E_{XC}[\rho]$ is known, $V_{XC}(r)$ can be readily obtained. The resolution of the KS equation is processed in a self-consistent fashion, starting from a set of initial guess molecular orbitals, $\{\chi_i(r)\}$, in which the electron density is determined using eq. (2.11). This density in turn serves to obtain $V_{eff}(r)$ from eq. (2.14) and then solve eq. (2.12) of eigenvalues and eigenfunctions. This process is repeated until convergence.

The exchange-correlation energy $E_{XC}[\rho]$ is generally divided into two separate terms, an exchange term $E_X[\rho]$ and a correlation term $E_C[\rho]$:

$$E_{XC}[\rho] = E_X[\rho] + E_C[\rho] \tag{2.16}$$

The exchange term is normally associated with the interactions between electrons of the same spin, whereas the correlation term essentially represents those between electrons of opposite spin. These two terms are themselves also functionals of the electron density and the corresponding functionals are known as the exchange functional and the correlation functional, respectively. Both components can be of two distinct types: local functionals, depending only on the electron density ρ, and gradient corrected, which depend on both ρ and its gradient $\nabla\rho$. These are discussed in the next section [142]. Despite the progress in the field, it is important to note that the main source of inaccuracy in DFT is normally a result of the approximate nature of the exchange-correlation functional.

2.3.3. Approximations to the Exchange–Correlation Potential

The local density approximation (LDA) constitutes the simplest approach to represent the exchange-correlation functional. The first LDA approximation to the exchange energy was proposed by Dirac [143] and uses a model of electron gas of homogeneous and constant density $\rho(r)$:

$$E_X^{LDA}[\rho] = -\frac{3}{4}\left(\frac{3}{\pi}\right)^{1/3} \int \rho^{4/3}(r)dr \tag{2.17}$$

In LDA, the correlation energy $E_C[\rho]$ is difficult to obtain separately from the exchange energy. There are several possibilities for the correlation energy; one of these is the analytical expression of Vosko, Wilk and Nusair, known as Vosko-Wilk-Nusair or VWN [144], which was developed from interpolation of a set of correlation energy values obtained by Ceperley and Alder from Monte Carlo calculations [145].

In solid-state chemistry, the LDA provides surprisingly good results for metallic solids with delocalized electrons, *i.e.* those that most closely resemble the uniform electron gas. However, LDA presents well-known disadvantages for solids. It reveals systematic shortcomings in the description of systems with localized electrons and accordingly shows underestimation of bond distances and overestimation of binding energies. Furthermore, as a rule, LDA calculations compute too small bandgaps.

The local spin density approximation (LSDA), initially proposed by Slater [146], represents a more general application of LDA, which introduces spin dependence into the functionals. Within the LSDA approach, the exchange functional is given by:

$$E_X^{LSDA}[\rho] = \frac{3}{4}\left(\frac{6}{\pi}\right)^{1/3} \int \left[\rho_\alpha^{4/3}(r) + \rho_\beta^{4/3}(r)\right] dr \tag{2.18}$$

where α and β stand for spin up and spin down densities, respectively. For closed-shell systems, α and β are equal and LSDA becomes virtually identical to LDA.

The LDA approximation assumes that the exchange-correlation effects are local and depend only on the value of the electron density at each point. Generalized gradient approximation methods (GGAs) introduce the density gradients $\nabla\rho(r)$ in the description of the exchange-correlation effects, taking into account the value of the density $\rho(r)$ at each point and how this density varies around each point. The main source of error of GGA methods is in the exchange energy, which is often underestimated by about 10-15%.

There are different non-local corrections for both the exchange part and the correlation part. While for the exchange the most commonly corrections used are the Becke86 (B86) [147] and Becke88 (B88) [148], for the correlation part the most applied are those of Perdew86 (P) [149] and the extremely popular Lee-Yang-Parr (LYP) [150], which is constructed from the Colle-Salvetti correlation energy formula. The geometries, the frequencies and the LDA charge densities improve with GGA corrections, since in

thermochemical tests the obtained average errors are of 6 kcal mol^{-1}, and for systems with hydrogen bonds GGA works reasonably well, although they still fail to describe van der Waals complexes.

More recently, a new class of DFT functionals based on the GGA was developed by including additional semi-local information beyond the first-order density gradient contained in the GGAs. These methods, termed as meta-GGA (M-GGA), depend explicitly on higher order density gradients $\nabla^2\rho(r)$, or typically on the kinetic energy density $\tau(r)$, which involves derivatives of the occupied KS orbitals.

Hybrid density functional (H-GGA) methods combine the exchange-correlation of a conventional GGA method with a percentage of exact (or Hartree-Fock) exchange. In fact, the amount of exact exchange cannot be assigned in general from first-principles and therefore is fitted semiempirically. Hybrid functionals have allowed a significant improvement over GGAs for many molecular properties. Currently, the most popular hybrid functional is the Becke's 3-parameters method (B3LYP), which uses the B88 exchange functional and the LYP correlation functional [150] with a 20% of exact exchange. However, different authors [151], [152] proposed empirical parameter-free hybrid functionals of the general form, like the PBE0 [153], in which the amount of exact exchange has been derived as 25% from theoretical reasoning through a perturbation theory argument, showing a promising performance for all important properties and being competitive with the most reliable, empirically parameterized current functionals.

Hybrid-meta GGA methods (HM-GGA) represent the newest class of density functionals. Based on a similar concept to the M-GGA functionals, the difference lies in the fact that they start from M-GGAs instead of standard GGAs. Hence, these methods depend on the exact exchange, the electron density, and its gradient and the kinetic energy density. Some functionals belonging to this category are the Minnesota M06 family developed by Truhlar [154]. These methods represent an improvement over the previous formalisms, particularly in the determination of barrier heights and atomization energies.

2.3.4. Some Difficult Cases for DFT

In general, DFT methods provide high-quality geometries, good dipole moments, excellent vibrational frequencies and a good estimation of the thermochemistry and of reaction barriers with a cost similar to that of HF, thereby introducing electron correlation at a much reduced cost. However, there exist some difficult cases for which DFT cannot provide the desired accuracy. These systems are incorrectly, in general, with weak interactions, charge transfer processes, and open-shell systems.

i) Systems with weak interactions such as van der Waals complexes. DFT functionals are incapable of properly describing London dispersion forces, which derive entirely from electron correlation at "long range". Adding exact exchange to the DFT functional cannot entirely alleviate this problem, since the Hartree-Fock level of theory, while non-local, does not account in any way for opposite-spin electron correlation. For van der Waals interactions, explicit parameterizations have been developed. A particular approach was done by Stefan Grimme [155], who used experimental data and included damped atom-pairwise corrections (referred to as DFT-D) of the form $C_6 R^{-6}$ to take dispersion into account. In DFT-D calculations, the total energy of a collection of atoms calculated with DFT, E_{DFT}, is augmented as follows:

$$E_{DFT-D} = E_{DFT} - S_6 \sum_{i \neq j} \frac{C_6^{ij}}{R_{ij}^6} f_{damp}(R_{ij}) \tag{2.19}$$

Here, R_{ij} is the distance between atoms i and j, C_6^{ij} is a dispersion coefficient for atoms i and j, which can be calculated directly from tabulated properties of the individual atoms, and $f_{damp}(R_{ij})$ is a damping function to avoid unphysical behaviour of the dispersion term for small distances. The only empirical parameter in this expression is S_6, a scaling factor that is applied uniformly to all pairs of atoms. In applications of DFT-D, this scaling factor has been estimated separately for each functional by optimizing its value with respect to collections of molecular complexes in which dispersion interactions are important. DFT-D2 energy correction considers all pairs of atoms while DFT-D3 also considers triplets of atoms to account for three-body effects.

ii) Intermolecular complexes by charge transfer interactions. Modern DFT functionals tend to predict these interactions stronger than they should be. Including exact exchange in the functional alleviates the problem to some extent, but only by cancellation of errors, since Hartree-Fock theory incorrectly predicts the interactions between these complexes are generally underestimated. Dative bonds have also been found to be problematic for many functionals. Standard functionals underestimate dissociation energies and the inclusion of a substantial fraction of exact exchange is required to improve them.

iii) Open-shell systems such as complexes with different spin states (*e.g.* transition metal complexes) and radical complexes. The bad description of these systems is due to partly a bad cancellation of the self-interaction part of the exchange functional. This causes and over-stabilization of spin density delocalized situations [156], [157]. Hartree-Fock tends to be inaccurate for such systems in the opposite direction. Thus, hybrid functionals tend to show improved performance to the relative stability by an offsetting of errors.

2.4. Modelling Solids and Surfaces

A crystal is a macroscopic entity formed by a large number of atoms. Neglecting impurities, defects and other irregularities, a crystal can be considered as a periodic structure where a unit is repeated in the three directions of space (see Figure 2.1a). The large number of atoms in a crystal makes that the study of the electronic structure of these systems and the properties can only be addressed through the use of models that represent the real system. This chapter addresses the key ideas in the modelling of surfaces and solids.

2.4.1. Cluster Approach

One choice for representing a solid system consists of reducing it into a small number of atoms that characterize, more or less properly, the desired region of the solid, ignoring the rest of the system. This is the basis of the finite model or *cluster* model (see Figure 2.1b). This choice has *pros* and *cons*. An indisputable advantage of finite models is that any

method of quantum chemistry, irrespective of wave function-based or DFT methods can be used. However, the major difficulty arises in the construction of finite models, since the finite nature may have potentially adverse effects due to the limited size of the clusters, which is reflected by edge effects.

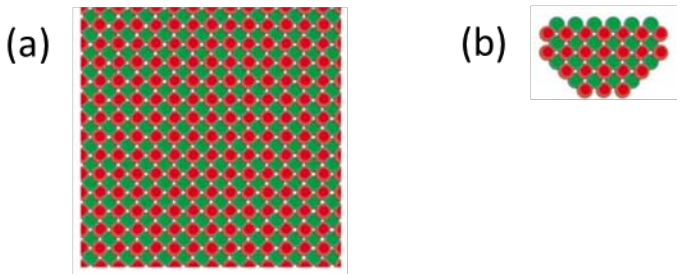

Figure 2.1 Geometries used to simulate surfaces of crystals, taken from Starrost and Carter [158]. (a): bulk and (b): *cluster* geometries (shown here for the zincblende crystal and suppressing the dimension normal to the page).

This limitation has moved on developing a number of *embedding* techniques with the aim of introducing the effect of the rest of the crystal. Depending on the type of system, different embedding strategies are available, such as the ONIOM [159]–[161] (our own *n*-layered integrated molecular orbital and molecular mechanics) approach and the QM-Pot scheme developed by Sierka and Sauer [162], [163]. The basic idea of both methods is to divide the whole system in two parts: the local part, which is described at an accurate level of theory, and the long-range effects, which are evaluated at a lower level with periodic conditions.

2.4.2. Periodic Approach

The use of a finite model only takes advantage of the stiffness of the solid and not its long-range order or periodicity. However, the existence of long-range order and its exploitation as a particular translational element of symmetry allows the consideration of a full solid and study some properties that are not local, but are based precisely on the nature of the system as a macroscopic entity [164]. The use of translational symmetry or periodicity results in periodic methods. In the following sections the basic concepts of the infinite model approach from a quantum mechanical point of view are introduced.

2.4.2.1. The Bloch Theorem

A crystalline solid consists of the orderly repetition of atoms or groups of atoms in the three directions according to its Bravais lattice. The repeating units that can generate the solid by translation, $\vec{T} = n_1\overrightarrow{a_1} + n_2\overrightarrow{a_2} + n_3\overrightarrow{a_3}$, where $\overrightarrow{a_i}$ are elementary translations, are called unit cells. In addition, those with the least volume are called primitive cells. There are basically two ways to construct these cells:

i) Linking equivalent points of the solid (lattice points) by periodicity, leading to unit cells formed by parallelepipeds.
ii) Connecting each lattice point to its nearest neighbours and tracing the planes normal to these segments through their midpoints, leading to the so-called Wigner-Seitz unit cells.

If $\vec{T}$ is a vector of the direct lattice, the reciprocal lattice is defined by $\vec{K} = m_1\overrightarrow{b_1} + m_2\overrightarrow{b_2} + m_3\overrightarrow{b_3}$, where $\overrightarrow{a_i} \cdot \overrightarrow{b_j} = 2\pi\delta_{ij}$. The components of the $\vec{T}$ and $\vec{K}$ vectors, from direct and reciprocal lattice, are integers (*i.e.*, correspond to lattice points). The unit cell of the reciprocal lattice obtained using the Wigner-Seitz construction is called the first Brillouin Zone and it is of great importance in periodic calculations [165].

At this point it is of great importance to introduce the Bloch's Theorem, since it defines Bloch functions adapted to the crystal symmetry [166]. This theorem derives from the assumption that in the one-electron Hamiltonian of a crystal the potential is periodic, that is $V(\vec{r}) = V(\vec{r} + \vec{T})$, and so it is the Hamiltonian as a whole, *i.e.*, $\hat{H}(\vec{r}) = \hat{H}(\vec{r} + \vec{T})$. Therefore, the Bloch theorem can be written as:

$$\hat{T}\varphi^{\vec{k}}(\vec{r}) = \varphi^{\vec{k}}(\vec{r} + \vec{T}) = e^{i\vec{k}\vec{T}}\varphi^{\vec{k}}(\vec{r}) \tag{2.20}$$

where $\vec{k}$ argument has been included to index the φ function. $\varphi^{\vec{k}}(\vec{r})$ is called Bloch's function and is adapted to the symmetry of the crystal, in the sense that it is eigenfunction of their translation operators [167]. The number of $\vec{k}$ vectors is infinite, but if $\overrightarrow{k'} = \vec{k} + \vec{K}$, where $\vec{K}$ is a vector of integer components in reciprocal space, as $e^{i\vec{K}\vec{T}} = 1$, we have that $e^{i\vec{k}\vec{T}} = e^{i\overrightarrow{k'}\vec{T}}$, and hence $\vec{k}$ and $\overrightarrow{k'}$ are redundant and it will be sufficient to consider those vectors belonging to Brillouin cell, the uniquely defined primitive cell in reciprocal space.

Furthermore, to avoid an infinite system, the Born-Von Karman periodic boundary conditions are introduced. Accordingly, the crystal is considered finite with N_1, N_2 and N_3 cells in each dimension, so a translation $\vec{T}$ returns to the original point. Thus, it must be complied that:

$$k_j = \frac{n_j}{N_j}, \text{with } j = 1, 2, 3 \text{ and } n_j = 0, 1, 2, 3, \dots, N_j \tag{2.21}$$

where N_j is the total number of cells considered and n_j is a natural number. Possible values of $\vec{k}$ (in the Brillouin zone) are no longer infinite, but their number is equal to the cells of the crystal.

The Schrödinger equation of periodic systems is obtained by replacing the Bloch function in the one-electron Schrödinger equation and taking into account the periodic potential $V(\vec{r})$, obtaining the following expression:

$$\hat{H}(\vec{r})\varphi^{\vec{k}}(\vec{r}) = \left[-\frac{1}{2}\nabla^2 + V(\vec{r})\right]\varphi^{\vec{k}}(\vec{r}) = E^{\vec{k}}\varphi^{\vec{k}}(\vec{r}) \tag{2.22}$$

where $V(\vec{r})$ and $\varphi^{\vec{k}}(\vec{r})$ have the same periodicity. Thus, the eigenvalue problem for the solid has been transformed from an infinite set to a set of discretely spaced eigenvalues, $E^{\vec{k}}$.

The one-electron crystalline orbitals (CO), similar to the molecular orbitals (MO) in a molecular calculation, are linear combinations of basis set functions $[\phi_\mu^{\vec{k}}(\vec{r})]$:

$$\varphi_n^{\vec{k}}(\vec{r}) = \sum_\mu c_{\mu n}^{\vec{k}} \phi_\mu^{\vec{k}}(\vec{r}) \tag{2.23}$$

where the coefficients $c_{\mu n}^{\vec{k}}$ are determined using the variational principle by solving the equation:

$$H^{\vec{k}}\, C^{\vec{k}} = S^{\vec{k}}\, C^{\vec{k}}\, E^{\vec{k}} \tag{2.24}$$

assuming one-electron Hamiltonian type. As a result, we obtain the crystalline orbitals and the corresponding one-electron energies. The problem is solved for different values of $\vec{k}$. As Bloch functions are irreducible representations of the group of translations, the matrix

elements for different $\vec{k}$ are zero. Thus an infinite problem becomes *N* (number of cells of the crystal) problems of size *M* (basis functions of unit cell). Although *N* is very large, the fact that the eigenvalues of the energy vary continuously with $\vec{k}$, allows the problem to be resolved in a small number of points by making the necessary interpolations.

The problem of efficiently evaluating the integrals defined in reciprocal space, over the possible values of $\vec{k}$ in the Brillouin zone, has been widely developed by Monkhorst and Pack [168]. This method generates sets of special points in the Brillouin zone, which provides an efficient means of integrating the periodic functions. In practise, to choose how many *k* points are used in each direction in reciprocal space it is necessary to numerically well converge all calculations at each *k* point, when from a given *k* point the total energy is seen to be (almost) independent of the number of *k* points. Otherwise, for smaller numbers of *k* points, the energy varies considerably and the number of *k* points is insufficient to give a well-converged result. In addition, periodic calculations can take full advantage of the symmetry that exists in a perfect solid, meaning that the integrals in reciprocal space do not need to be evaluated using the entire Brillouin zone, but they can just be evaluated in a reduced portion of the zone. This reduced region in *k* space is called the *irreducible Brillouin zone*.

2.4.2.2. Surface Models

A periodic model describing a surface is called *slab* model and consists of a number of atomic layers parallel to a given (*hkl*) crystalline plane. The two atomic layers that finish the *slab* are those simulating the surface. A model of this type can be two-dimensional, where the translational symmetry is maintained only in the two directions that define the surface, thus preveting a gap above and below the surface (see Figure 2.2a and Figure 2.2b), or three-dimensional, which consists of a series of equidistant *slabs* normal to the surface plane and separated by empty zones, so that the layers do not interact with each other, called *super-cell slab* (see Figure 2.2c). Because of their different nature, centred-atoms Gaussian functions can work with purely two-dimensional *slab* models, while the plane-wave functions are limited to *super-cell slab*.

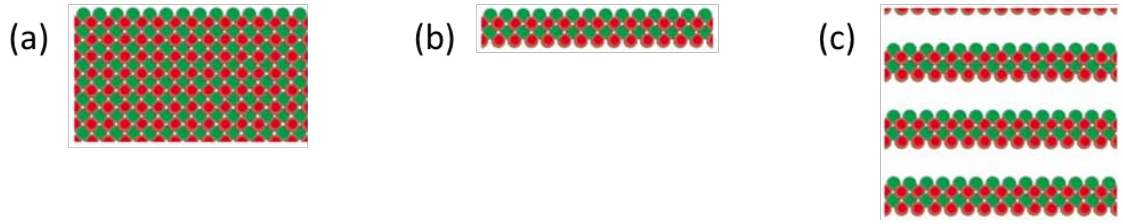

Figure 2.2 Geometries used to simulate surfaces of crystals, taken from Starrost and Carter [158]. (a): 4-layered 2D slab, (b): single 2D slab and (c): super-cell 3D slab (shown here for the zincblende crystal and suppressing the dimension normal to the page).

In surface modelling, one must be careful when building the surface. For example, a pure solid metal has a homogeneous composition (all atoms are equal) and, therefore, the modelling of their surfaces is relatively easy due to the absence of a particular bonds or group of atoms that cannot be separated. Instead, the modelling of ionic, covalent or mixed metal (as an alloy) surfaces is more difficult because of their heterogeneity.

One way to evaluate energetically different crystalline surfaces of a given solid is computing the specific surface energy [169]. The surface energy is a measure of the thermodynamic stability of the surface and is defined as the energy cost per unit area required forming the surface from the bulk crystal. The surface energy can be computed as:

$$\gamma = \lim_{n\to\infty} E_s(n) = \lim_{n\to\infty} \frac{E(n)_{slab} - nE_{bulk}}{2A} \tag{2.25}$$

where E(n) is the energy of an n-layer slab, E_{bulk} is the energy of the bulk, A is the area of the surface unit cell, and the factor of 2 in the denominator accounts for the upper and lower surfaces of the slab model. As more layers are added in the calculation ($n\to\infty$), $E_s(n)$ converges to the surface energy per unit area (γ).

Ideally a surface, built from cutting the bulk, must be nonpolar (*i.e.*, the dipole moment normal to the surface should be 0) to avoid stability problems arising from the surface polarity. However, modifications at atomic level, reconstructions of the surfaces and rearrangements of the electronic structure can induce a polarising electric field in the system.

2.4.2.3. Basis Sets

As mentioned, crystalline orbitals are expanded in terms of basis set functions. Two types of basis set are currently used in electronic-structure calculations of periodic systems: localized Gaussian-type functions (GTF) and plane waves (PW). Gaussian functions, attributed to the atom A with coordinate $\overrightarrow{r_A}$ in the reference unit cell, are formally associated with all translationally equivalent atoms in the crystal occupying positions $\overrightarrow{r_A} + \vec{T}$ ($\vec{T}$ is the direct lattice translation vector). Because in the periodic systems these basis sets must be chosen in such a way that they satisfy the Bloch theorem, GTFs are expressed as Gaussian-type Bloch functions (GTBFs) centred at atomic nuclei and constructed according to:

$$\phi_{\mu}^{\vec{k}_{BZ}}(\vec{r}) = \sum_{\vec{T}} e^{i\vec{k}\vec{T}} \varphi_{\mu}\left(\vec{r} - \overrightarrow{r_A} - \vec{T}\right) \tag{2.26}$$

At the same time Gaussian-type basis functions are expanded as a linear combination (contraction) of individually normalized Gaussian primitives $g_j\left(\vec{r} - \overrightarrow{r_A} - \vec{T}\right)$ characterized by the same centre but with different exponents:

$$\varphi_{\mu}\left(\vec{r} - \overrightarrow{r_A} - \vec{T}\right) = \sum_{j=1}^{N} d_j g_j\left(\vec{r} - \overrightarrow{r_A} - \vec{T}\right), \qquad g_j\left(\vec{r} - \overrightarrow{r_A} - \vec{T}\right) = g\left(\vec{r} - \overrightarrow{r_A} - \vec{T}; \alpha_j\right) \tag{2.27}$$

where N is the length of the contraction, α_j the contraction exponents and d_j the contraction coefficients.

Gaussian functions have the advantage that the number of basis-set functions depends on the number of atoms included in the crystalline cell but not on the dimension or shape of the cell. However, the basis-set functions in solids are modulated over the infinite lattice: any attempt to use large uncontracted molecular or atomic basis sets with very diffuse functions can result in problems of linear dependence [170]. Therefore, exponents and contraction coefficients in the molecular and periodic systems are generally rather different and, with some exceptions, molecular basis sets are not directly transferable to the study of crystalline solids. Because of the use of a limited number of basis-set functions, the so-called basis set superposition error (BSSE) is entailed; *i.e.*, a spurious stabilizing contribution arising from the improved description of a fragment in a complex due to the

assistance of the basis sets of the other fragments. This error is normally corrected *a posteriori*, at the uncorrected geometries, with the Counterpoise method [171].

Plane wave basis sets are more common as a basis set for expanding the crystalline orbitals [172]. Using the Bloch theorem the single-electron wave function $\psi_n(\vec{r})$ can be written as a product of a wave-like part and a cell-periodic part. Due to its periodicity the latter can be expanded as a set of PWs. Thus, in the PW basis the single-electron wave function can be written as a linear combination of PWs:

$$\psi_n^{\vec{k}}(\vec{r}) = e^{i\vec{k}\vec{r}} \sum_K c_{n,K}\, e^{i\vec{K}\vec{r}} = \sum_K c_{n,K}\, e^{i(\vec{k}+\vec{K})\vec{r}} \tag{2.28}$$

where the periodic function is a discrete set of PWs with wave vector $\vec{K}$ equal to a reciprocal lattice vector of the crystal.

PWs are orthonormal and form a complete set. Thus, any continuous and standardisable function can expand on this base. The use of PWs simplifies algebraic manipulations and calculations are usually performed in reciprocal space. Furthermore, the PW basis set is universal, in the sense that it does not depend on the positions of the atoms in the unit cell or its nature. Contrarily to GTFs, one does not have to construct a new basis set for every atom nor modify them in different materials, and the basis can be made better (and more expensive) or worse (and cheaper) by varying a single parameter: the *cutoff* energy value. Moreover, plane-wave calculations do not suffer from the basis-set superposition error (BSSE).

Energy and gradient calculations for GGA functionals are more efficient with PWs than with GTFs. On the contrary, the calculation of the exact exchange using PWs is very expensive compared to GTFs, hampering the use of hybrid functionals, which, in some occasions, are more accurate than standard GGA functionals. Another disadvantage of PW basis sets is that calculations are intrinsically periodic in three dimensions (3D) and this 3D box is uniformly filled with plane waves, regardless of the dimensionality of the system. Lastly, one of the difficulties of PWs is that to properly describe atomic cores the expansion must be very large. In practice, one must use a finite set of PWs, but this in fact means that well-localized core electrons cannot be described in this manner. This makes it essential to augment the basis set with additional functions (as in linear combination of

Augmented Plane Waves scheme, PAW), or use pseudopotentials (PP, through the first-principles Effective Core Potential, ECP).

Combining the best of each of these two basis sets, the Gaussian and plane waves (GPW) method is obtained, which is part of the program package CP2K along with its implementation in Quickstep [173]. The GPW method allows for accurate density functional calculations in gas and condensed phases and can be effectively used for molecular dynamics simulations. The derivatives of the GPW energy functional, namely forces and the Kohn–Sham matrix can be computed in a consistent way and the computational cost of computing the total energy and the Kohn–Sham matrix is linearly scaled with the system size, resulting in an efficient and accurate method. Wave function optimization with the orbital transformation technique leads to good parallel performance and outperforms traditional diagonalization methods.

2.5. Molecular Dynamics Approach

Molecular dynamics (MD) is a well-established numerical simulation technique that allows accounting for temperature effects [174]. For a general *N*-particle system, Newton's second law for particle *i* takes the form:

$$m_i \frac{d^2 \boldsymbol{r}_i}{dt^2} = \boldsymbol{F}_i \left(\boldsymbol{r}_1, \ldots, \boldsymbol{r}_N, \frac{d\boldsymbol{r}_i}{dt} \right) \tag{2.29}$$

where m_i is the mass of the object, $\boldsymbol{r}_i$ its position, $\boldsymbol{v}_i = d\boldsymbol{r}_i/dt$ its velocity, $\boldsymbol{a}_i = d^2\boldsymbol{r}_i/dt^2$ its acceleration, and $\boldsymbol{F}_i$ the force experimenting the *i*-th object due to all of the other particles in the system (and possibly the velocity of the particle as well). These equations are referred to as the classical *equations of motion* of the system. Unfortunately, the interparticle forces are highly nonlinear functions of the *N* particle positions so that eqn. 2.29 possesses enormous dynamical complexity and obtaining an analytical solution is hopeless. Thus, numerical methods to solve the classical equations of motion are used.

At the same time, the generated trajectories are used to extract macroscopic thermodynamic and dynamic observables for a wide variety of systems and they can be useful as a guide toward understanding the mechanisms underlying a given chemical

process. MD also permits direct "visualization" of the detailed motions of individual atoms in a system, thereby providing a "window" into the microscopic world. Many of these applications address important problems in biology, such as protein and nucleic acid folding, in materials science, such as surface diffusion, catalysis, and structure and dynamics of glasses and their melts, as well as in nanotechnology, such as the behaviour of self-assembled monolayers and the formation of molecular devices.

One of the major milestones in molecular dynamics is the technique known as *ab initio* or first-principles molecular dynamics within the Born-Oppenheimer approximation (here simply AIMD) [175]. In AIMD simulations, the interatomic interactions are computed directly from the electronic structure "on the fly" as the simulation proceeds, thereby allowing to treat explicitly the breaking and formation of chemical bonds. Even though the computational overhead of solving the electronic Schrödinger equation using widely employed approximation schemes is considerable, the field of molecular dynamics is an exciting and rapidly evolving one and nowadays the methodology is capable of performing many different types of MD calculations.

2.5.1. Ensembles in Molecular Dynamics

The simplest and most fundamental of the equilibrium ensembles is a system isolated from any surroundings characterized by fixed values of the N identical particles in a container of volume V with a total internal energy E. This ensemble is known as the *microcanonical ensemble* (NVE) and provides the starting point from which all other equilibrium ensembles are derived. The variables N, V and E are all macroscopic thermodynamic quantities referred to as *control variables*. Control variables are simply quantities that characterize the ensemble and that determine other thermodynamic properties of the system. Different choices of these variables lead to different system properties. Suppose, further that given an infinite amount of time, the system with energy E is able to visit all configurations on the constant energy hypersurface. A system with this property is said to be *ergodic* and can be used to generate a microcanonical ensemble. This assumption is especially of paramount importance in the molecular dynamics approach. In general, it is not possible to prove the ergodicity or lack thereof in a system with many degrees of

freedom, although clearly it will not hold for a system whose potential energy $U(\boldsymbol{r})$ possesses high barriers, *i.e.* regions where $U(\boldsymbol{r}) > E$.

The main disadvantage of the microcanonical ensemble is that conditions of constant total energy are not those under which experiments are performed. Therefore, it is important to develop ensembles that have different sets of thermodynamic control variables in order to reflect more common experimental setups. The *canonical ensemble* (NVT) is a good example. Its thermodynamic control variables are constant particle number *N*, constant volume *V* and constant temperature *T*, which characterize a system in thermal contact with an infinite heat source. Additionally, the canonical ensemble forms the basis for the *NPT* (isothermal-isobaric) and μVT (grand canonical) ensembles. Especially for large systems, also so-called thermodynamic limit, results from the canonical ensemble will not deviate much from results of the other ensembles.

The treatment of the canonical ensemble naturally raises the question of how molecular dynamics simulations can be performed under the external conditions of this ensemble. By leading the conditions of the canonical ensemble it is clear that the energy is not conserved; however, when a system is in thermal contact with an infinite external heat source, its energy will fluctuate in such a way that its temperature remains fixed. Although these energy fluctuations vanish in the thermodynamic limit, most simulations are performed far enough from this limit that the fluctuations cannot be neglected. In order to generate these fluctuations in a molecular dynamics simulation, it is necessary to mimic the effect of the thermal reservoir. Various methods to achieve this have been proposed [176]–[178], being the Nosé Hamiltonian in 1984 the first one originally introduced [176]. An additional "agent" is introduced into a system that "checks" whether the instantaneous kinetic energy is higher or lower than the desired temperature and then scales the velocities accordingly. In 1985, Hoover [177] introduced a reformulation of the Nosé dynamics that has become one of the staples of molecular dynamics, appearing an additional term that acts as a kind of friction term (their evolution is driven by the difference in the instantaneous value of the kinetic energy and its canonical average). However, the Nosé–Hoover equations fail because they do not contain a sufficient number of variables to offset the restriction caused by multiple conservation laws. For this reason, the *Nosé-Hoover chain equations* were developed [178]. By adding new thermostat variable pairs and rewriting the equations of motion 2.29, these new equations ensure the correct distribution.

2.5.2. Free Energy Calculations

Free energy is a quantity of particular significance in statistical mechanics through which other thermodynamic quantities are obtained via differentiation. Indeed, we are often interested in the free energy *difference* between two thermodynamic states, showing for example whether a chemical reaction occurs spontaneously or requires input of work.

There are several widely used techniques that have been developed for calculating Helmholtz free energy differences ΔA [179]. One of them is the *thermodynamic integration* formulation [180]. Given an initial state *A* and a final state *B*, an adiabatic path is one along which the system is relaxed at each point of the reaction path. In order to perform the transformation from one state to the other, it is common to introduce an "external" variable λ in order to parameterize the adiabatic path. The mechanism is one in which the system starts in state *A* ($\lambda = 0$), switches off the potential U_A while simultaneously switching on the potential U_B, and completing the process when $\lambda = 1$. Computing the derivative of *A* with respect to λ and reorganizing, the free energy difference ΔA_{AB} can be obtained from the relation:

$$\Delta A_{AB} = A_B - A_A = \int_0^1 \langle \frac{\partial U}{\partial \lambda} \rangle_\lambda \, d\lambda \tag{2.30}$$

where $\langle \partial U/\partial \lambda \rangle_\lambda$ denotes an average over the canonical ensemble with λ fixed at a particular value. In practice, the thermodynamic integration formula is implemented as follows: a set of M values of λ is chosen from the interval [0,1] and at each chosen value λ_k a full MD calculation is carried out in order to generate the average $\langle \partial U/\partial \lambda_k \rangle_{\lambda_k}$. The resulting values of $\langle \partial U/\partial \lambda_k \rangle_{\lambda_k}$, $k = 1, \dots, M$, are then substituted in eq. (2.30) and the result is integrated numerically to produce the free energy difference ΔA_{AB} (the selected values $\{\lambda_k\}$ can be evenly spaced).

2.6. Tunnelling Calculations

Classically, any reaction with a sizeable energy barrier $\Delta G^\ddagger$ will be dramatically slow at the low temperatures, owing to the exponential behaviour of the Eyring equation in the classical formulation of the transition state theory (TST):

$$k^{TST} = \left(\frac{k_B T}{h}\right) e^{-\frac{\Delta G^{\ddagger}}{k_B T}} \tag{2.31}$$

However, quantum tunnelling, a purely quantum mechanical effect, can play a significant role, thus allowing chemical reactions to occur at significant rates at low temperatures, which classically would have negligible rates [181]. Tunnelling effects are also pronounced for reactions involving reduced masses along the reaction coordinate; mainly, light nuclei transfer, such as proton or hydrogen transfer reactions. The probability for a given system to tunnel through a reaction barrier depends primarily on the curvature of the barrier, which is controlled by the transition vibrational frequency and, to a lower degree, on the height of the barrier. Most notably, because of the strong tunnelling path-length dependence, which in turn depends on the adiabatic energy surface (*i.e.*, including the zero-point energy corrections, ZPE), it could be more efficient if a shorter tunnelling path is traversed, even if that is at a higher energy cost. Thus, the most efficient tunnelling path at a given temperature depends on the entire adiabatic energy surface around the barrier.

The importance of tunnelling for a specific reaction can be estimated by employing the tunnelling crossover temperature T_X, which can be calculated using the formula by Fermann and Auerbach [182]:

$$T_X = \frac{h\nu^{\ddagger}\Delta U_0^{\ddagger}/k_B}{2\pi\Delta U_0^{\ddagger} - h\nu^{\ddagger}\ln 2} \tag{2.32}$$

with $\nu^{\ddagger}$ the absolute value of the imaginary frequency of the transition mode, h the Plank's constant, $\Delta U_0^{\ddagger}$ the zero-point energy-corrected barrier and k_B the Boltzmann's constant. T_X generally marks the temperature below which tunnelling becomes dominant and above which tunnelling becomes negligible.

For small tunnelling effects the semi-classical approximation often provides sufficient accuracy. In this case, tunnelling contributions are accounted for by introducing the transmission coefficient ($\kappa(T)$) into the classical Eyring rate constant (k^{TST}):

$$k^{SC-TST} = \kappa(T) \times k^{TST} \tag{2.33}$$

There are simple and one-dimensional models to calculate $\kappa(T)$ and adequately correct k^{TST} rates [183]. A seminal correction is that of Wigner [184], which takes:

$$\kappa(T) = 1 + \frac{1}{24}\left(\frac{h\nu^{\ddagger}i}{k_B T}\right)^2 \tag{2.34}$$

where $\nu^{\ddagger}$ is the imaginary frequency associated with the reaction coordinate. The Wigner correction works well when $h\nu^{\ddagger}i \ll k_B T$, so at very low temperatures it fails. More robust approximations to $\kappa(T)$ were provided by Skodje and Truhlar [185]:

$$\kappa(T) = \frac{\beta\pi/\alpha}{\sin(\beta\pi/\alpha)} - \frac{\beta}{\alpha - \beta} e^{\left[(\beta-\alpha)\Delta U_0{}^{\ddagger}\right]} \quad \text{for } \beta \leq \alpha \tag{2.35}$$

$$\kappa(T) = \frac{\beta}{\beta - \alpha}\left\{e^{\left[(\beta-\alpha)\Delta U_0{}^{\ddagger}\right]} - 1\right\} \quad \text{for } \alpha \leq \beta \tag{2.36}$$

where $\alpha = \frac{2\pi}{h\nu^{\ddagger}i}$, $\beta = \frac{1}{k_B T}$ and $\Delta U_0{}^{\ddagger}$ is the ZPE-corrected barrier; and by Fermann and Auerbach [182]:

$$\kappa(T) = e^{\Delta U_0{}^{\ddagger}/k_B T} e^{-2\pi\Delta U_0{}^{\ddagger}/h\nu^{\ddagger}i}\left(1 + \frac{2\pi k_B T}{h\nu^{\ddagger}i}\right) \tag{2.37}$$

However, when tunnelling starts to dominate over-the-barrier reactivity, such as astrochemical reactions due to the very low temperatures they occur, more accurate models are necessary to adequately deal with tunnelling. Previous studies of activated astrochemical reactions [186]–[191] have employed harmonic quantum transition state theory (HQTST) [192], in which the tunnelling path is fully optimised in all dimensions of the reacting system. This theory is a reformulation of instanton theory [193], [194], which allows one to find the most efficient tunnelling path by employing quantum statistics through Feynman path (FP) integrals. Here the focus is on finding the quantum analogue of the saddle point on the MEP (usually referred to as transition state, TS) by locating the highest point on the minimum action path (MAP) [195], which is denoted as a quantum transition state (qTS). Although HQTST is essentially a semi-classical approximation, it performs remarkably well at very low temperature, although generally slightly overestimates reaction rates near T_X [191].

2.7. Computational Details

In this last section of Chapter 2, the computational details entailed in the present thesis are provided and it is divided into two different subsections: electronic structure calculations with the CRYSTAL09 code and molecular dynamics simulations with the CP2K/QUICKSTEP package (v2.5).

2.7.1. Electronic Structure Calculations with CRYSTAL09

All periodic calculations have been performed with the *ab initio* CRYSTAL09 code [170], [196]. This code implements the Hartree−Fock and Kohn−Sham self-consistent field method based on localized Gaussian Type Orbitals (GTO) for periodic systems [197]. Surface models computed by CRYSTAL09 are true 2D systems, at variance to plane wave-based codes, in which the slab is artificially replicated through infinity also in the direction perpendicular to the slab by including a large amount of empty space.

The SCF calculations and geometry optimizations were performed with different density functional methods depending on the section. Results of section 3.1 were obtained with the B3LYP functional [150], [198], which has been demonstrated to be accurate enough for the bulk. Results of section 3.2 and section 3.3 with the B3LYP-D2* functional, which includes an empirical *a posteriori* correction term proposed by Grimme [155] to account for dispersion forces (missed in the pure B3LYP method), but whose initial parametrization (D2) was modified for extended systems (D2*) [199], to provide accurate results for the calculations of cohesive energies of molecular crystals and of adsorption processes within a periodic treatment [200]–[202], due to the presence of species adsorbed on the surface of systems. Moreover, in some selected cases, for the adsorption of one H atom on (010) forsterite surface, single point energy calculations using the PBE [203], BLYP [148], [150] and BHLYP [204] density functional methods at the B3LYP-D2* optimized geometries have also been performed in order to check the influence of the method on the computed adsorption energies. Results of section 3.4 were obtained with the BHLYP functional [204], because it better describes the electronic structure of Fe-containing systems, as it is shown in the beginning of the section with a calibration study (see section 3.4.1). Transition state (TS) search has been performed using the distinguished

reaction coordinate (DRC) technique as implemented in CRYSTAL09, which has been proven to be robust and efficient enough for the proton jump of non-hydrated and hydrated acidic zeolites [205]. The activated complex structures corresponding to the TS have been checked by ensuring that only one imaginary frequency resulted by the Hessian matrix diagonalization. All calculations involving one H or Fe^{2+} atom have been run as open-shell systems based on the unrestricted formalism. Geometry optimizations of the bulk systems have been performed in *Pbnm* space symmetry, whereas those of the surface models in the *P1* group symmetry (no symmetry), in order to ensure the maximum degrees of freedom during the optimization. Net charges and electron spin densities on the atoms were derived from the Mulliken population analysis.

The multi-electron wave function is described by linear combination of crystalline orbitals, which in turn are expanded in terms of GTO basis sets. Two different Gaussian basis sets have been adopted: (i) a B1 basis set described by the following all-electron contractions: (8s)–(831sp)–(1d) for Si; (6s)–(31sp)–(1d) for O; (6s)–(631sp)–(1d) for the top-layer Mg atoms (standard 6-31G(d,p) Pople basis set); (8s)–(61sp)–(1d) for the remaining Mg atoms; and (6s)–(6631sp)–(31d)–(1f) for Fe; and (ii) a B2 basis set described by the larger all-electron contractions: (8s)–(6311sp)–(1d) for Si; (8s)–(411sp)–(1d) for O; (631111s)–(42111p)–(1d) for the top-layer Mg atoms (standard 6-311G(d,p) Pople basis set); (8s)–(511sp)–(1d) for the remaining Mg atoms; and (62111111s)–(331111p)–(311d) for Fe; these basis functions were already used in previous works focused on the forsterite [99], [100], [206] and fayalite [114] bulk properties. For all calculations, a TZP basis set from Ahlrichs and co-workers [207] has been used for the H atoms. For the characterization of the minerals (Section 3.1), all the calculations were employed at B2 basis set, while for the H_2 formation processes (Sections 3.2 to 3.4), all the geometry optimizations have been carried out using the B1 basis sets and the energy is refined with single point energy calculations at B2 onto the optimized B1 geometries (hereafter referred as B2//B1). Specifically, in Section 3.2 different optimizations have been carried out using both the B1 and B2 basis sets in order to compare the obtained results.

We set the shrinking factor of the reciprocal space net, defining the mesh of *k* points in the irreducible Brillouin zone [168], to 5 and 20 for B1 and B2 calculations, respectively, requiring the diagonalization of the Hamiltonian matrix in 3 and 6 *k* points, respectively. The accuracy of both Coulomb and exchange series was set to values of overlap integrals

of 10^{-6} and 10^{-16} for both B1 and B2. A pruned (75, 974) grid (CRYSTAL09 keyword XLGRID) has been used for the Gauss–Legendre and Lebedev quadrature schemes in the evaluation of functionals [170], [208]. The condition to achieve SCF convergence between two subsequent cycles was set to 10^{-7} Hartree. Relaxations of both the internal atomic coordinates and the unit cell parameters for the bulk structures, on the one hand, and relaxations of only the internal atomic coordinates keeping the lattice parameters fixed at the bulk values for the rest of the calculations, on the other hand, were carried out within the same run by means of analytical energy gradients [209] using a quasi-Newton algorithm, in which the quadratic step (Broyden−Fletcher−Goldfarb−Shanno Hessian updating scheme, BFGS) [210]–[213] is combined with a linear one as proposed by Schlegel [214].

The adsorption energies (ΔE) per mole of an H atom and per unit cell were computed as:

$$\Delta E = E(SH//SH) - E(S//S) - E_m(H) \tag{2.38}$$

where E(SH//SH) is the energy of the relaxed unitary cell containing the forsterite surface S in interaction with the H atom, E(S//S) is the energy of the relaxed unitary cell of the free forsterite surface, and E_m(H) is the energy of the free H atom (the symbol following the double slash identifies the geometry at which the energy was computed). Because Gaussian basis functions were used, the above ΔE definition suffers from the basis set superposition error (BSSE). The above equation can be easily recast to include the BSSE correction, using the same counterpoise method adopted for intermolecular complexes [215]. The definition of the BSSE-corrected adsorption energy ΔE^C is:

$$\Delta E^C = \Delta E^{*C} + \delta E_S \tag{2.39}$$

$$\Delta E^{*C} = E(SH//SH) - E(S[H]//SH) - E([S]H//SH) \tag{2.40}$$

in which δE_S is the deformation energy of the forsterite surface due to the adsorption of the H atom (note that δE_H is null), E(S[H]//SH) is the energy of the forsterite surface plus the ghost functions of H, and E([S]H//SH) is the energy of the infinite replica of H with the ghost functions of the forsterite surface. For the sake of brevity, we refer to previous work for a complete discussion concerning the calculation of the ΔE^C and the associated BSSE values [215].

CRYSTAL09 computes the zero-point energy (ZPE) corrections and thermodynamic quantities using the standard statistical thermodynamics formulae based on partition functions derived from the harmonic oscillator approximations, which are used to correct the adsorption energy values by temperature effects. The corresponding vibrational frequencies are calculated by obtaining the eigenvalues from diagonalization of the mass-weighted Hessian matrix at Γ point (point $k = 0$ in the first Brillouin zone, called the central zone). The mass-weighted Hessian matrix was obtained by numerical differentiation (central-difference formula) of the analytical first energy derivatives, calculated at geometries obtained by displacing, in turn, each of the 3*N* equilibrium nuclear coordinates by a small amount, $u = 0.003$ Å (*N* is the number of atoms) [216]. For the considered systems in this thesis, building up the full mass-weighted Hessian matrix would have been very expensive, so that only a portion of the dynamical matrix was computed by considering the displacements of a subset of atoms; *i.e.*, the H atoms and the first and second-layer atoms of the surface. Only for the characterization of Mg_2SiO_4 and $(Mg,Fe)_2SiO_4$ systems in Section 3.1, the full mass-weighted Hessian matrix has been performed in order to calculate all the normal modes. The value of the infrared intensity for each normal mode was also computed via the dipole moment variation along the normal mode adopting the set of localized Wannier functions [217]–[219].

Reflectance spectra (R(ν)) of 3D-periodic systems can be simulated with CRYSTAL09 by combining different ingredients available in the code: i) calculation of the vibrational modes, their corresponding intensities and separation of the transverse and longitudinal optical (TO and LO, respectively) modes [216], [220]; ii) calculation of the electronic high frequency components (ε_∞) [221]–[224] contributing to the frequency-dependent complex dielectric function (ε(ν)); and iii) calculation of the mass-weighted effective mode Born charges [225]–[227]. Reflectance spectra of several crystalline mineral systems have successfully been simulated with CRYSTAL09 [100], [114], [206], [228]–[230].

Finally, tunnelling crossover temperature (T_X) and rate constants k^{TST} have been computed by standard TST using partition functions and the $\Delta G^{\ddagger}$ adopting the Eyring formalism. Tunnelling contributions have been accounted for in a semi-classical way by calculating the transmission coefficient, $\kappa(T)$, using the formulae presented in eq. (2.34)–(2.37) (see Section 2.6 of Chapter 2).

2.7.2. Molecular Dynamics Simulations with CP2K

All the results related with MD simulations have been obtained with the CP2K/QUICKSTEP package (v2.5). CP2K/QUICKSTEP [173] employs a mixed Gaussian and plane-wave basis set and norm-conserving pseudopotentials. The electronic structure is computed using the PBE [203] density functional method and including the empirical *a posteriori* D2 correction term [155] missed in the pure PBE exchange-correlation functional. Transition state (TS) structure is optimized with the climbing image-nudged elastic band (CI-NEB) algorithm [231], fully optimizing all atoms for the 19 images in the NEB. The activated complex structure corresponding to the TS has been checked by ensuring that only one imaginary frequency resulted by the full Hessian matrix diagonalization. The spin polarization was enabled throughout all calculations by using the Unrestricted Kohn-Sham formalism.

We used short range molecularly optimized double-ζ valence polarized (m-DZVP) Gaussian basis functions for Mg and molecularly optimized triple-ζ valence polarized (m-TZVP) for Si, O and H. Also a 500 Ry cut-off was used for the plane wave expansion and ten valence electrons for magnesium ($2s^2 2p^6 3s^2$), four for silicon ($3s^2 3p^2$), six for oxygen ($2s^2 2p^4$) and one for hydrogen ($1s^1$).

At variance with the slab models calculated with CRYSTAL, calculations in CP2K have been performed on (2 x 2) orthorhombic cells. In CP2K, the slabs were therefore created fixing the lattice vector normal to the slab and after that with a total thickness of 10 Å plus a vacuum gap between the slab and the next periodic image of 15 Å. At the same time, the slabs have been decoupled from their periodic images along the vacuum according to the method by Martyna and Tuckerman [232]. The condition to achieve SCF convergence between two subsequent cycles was set to 10^{-6} Hartree. Relaxations of the internal atomic coordinates have been carried out by means of analytical energy gradients keeping the lattice parameters fixed at the bulk values. All calculations were performed with the limit memory variant of the Broyden-Fletcher-Goldfarb-Shanno scheme (LBFGS).

The final replica images that define the minimum energy path (MEP) as a result of the CI-NEB procedure were used as initial guesses in the execution of a series of constrained *ab initio* MD simulations. AIMD simulations in the Born-Oppenheimer approximation using the electronic structure set-up described earlier were performed, within the canonical

(NVT) ensemble at a target temperature of 100 K and 10 K. We compute 10-ps long AIMD simulations on the (2 x 2) orthorhombic cell with a MD time-step of 0.5 fs, the first 5 ps of each trajectory are used for equilibration and the remaining 5 ps for analysis. The average forces are well converged after 6000–8000 MD steps. Equilibration has been performed using the Nosé-Hoover chain thermostat [178] to maintain constant average temperature; both the energy and temperature were closely monitored for all simulations to ensure their conservation.

The classical free-energy barrier for this H diffusion path accounting for dynamic effects over the reaction coordinate ξ is obtained, from these series, by employing the *thermodynamic integration* formula [180] shown in Chapter 2 (see Free Energy Calculations, Section 2.5.2).

3. Results and Discussion

The interstellar dust and the chemical reactions that occur on it have traditionally been studied by astronomical observations and experiments and, more recently, using computational techniques. Interstellar silicate dust is mainly Mg-rich, although some fractions also contain iron. Most of the theoretical studies were focused on the adsorption and reactivity of H atoms on the (010) forsterite surface, but the very same processes on other forsterite surfaces and on Fe-containing surfaces have not been investigated. Thus, understanding their behaviour and how they affect the interstellar chemistry activity is crucial.

This chapter is organized as follows. In Section 3.1, some physicochemical properties of the crystalline bulk structure and the corresponding nonpolar (010), (001) and (110) surfaces of Mg_2SiO_4 forsterite, the Mg-pure olivine system, on the one hand, and the crystalline bulk structures and the corresponding nonpolar (010) surfaces of the Fe-containing $Mg_{1.5}Fe_{0.5}SiO_4$ olivine systems, on the other hand, will be studied. In Section 3.2, the adsorption of H atoms and their recombination to form a H_2 molecule on a slab model of the crystalline Mg_2SiO_4 forsterite (010) surface mimicking the interstellar dust particle surface will be reported. In Section 3.3, the relevance of surface morphology on H_2 formation will be analysed by considering the processes on the crystalline Mg_2SiO_4 (001) and (110) surfaces. Results are presented and compared to those previously reported for the most stable (010) surface. Finally, in Section 3.4, the influence of Fe^{2+} atoms will be investigated by simulating the adsorption and recombination of atomic hydrogens on a Fe-containing (010) surface model.

3.1. Physicochemical Properties of Crystalline Olivines and their Relevant Surfaces

3.1.1. Mg_2SiO_4 Bulk: Structure, IR, Dielectric and Reflectance Properties

The bulk crystal structure of forsterite is represented in Figure 3.1. It is made up by distorted SiO_4 tetrahedra and MgO_6 octahedra, in which the tetrahedra and the octahedra share the vertices. Half of the available octahedral voids are occupied by the Mg^{2+} divalent cation. There are two symmetry-independent Mg atoms, named Mg1 and Mg2 [89]. The Mg1-centered octahedra share edges forming rods parallel to the crystallographic *c* axis and the Mg2 octahedra are laterally linked to these rods through the corresponding edges.

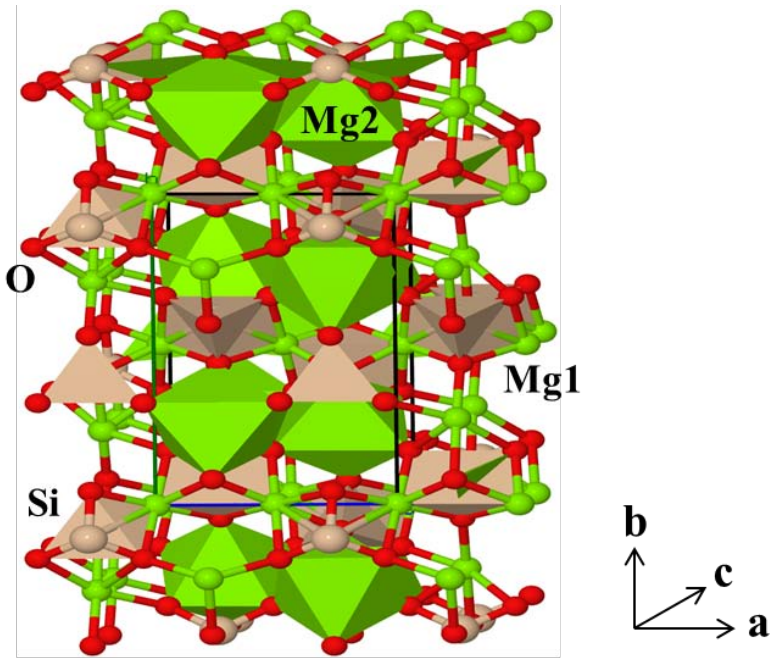

Figure 3.1 View (along the *c* crystallographic axis) of the crystal structure of forsterite.

The optimized structural parameters of the bulk structure of forsterite (see Table 3.1) are in good agreement with experiments. As already reported [99], calculated cell parameters are slightly overestimated (with deviations below 1%), giving a volume variation of 2.2%. Moreover, the experimental Si–O and Mg–O distances are well reproduced, the largest differences being given in the Mg2–O distances (0.024 Å larger, at the most).

Table 3.1 *B3LYP-optimized and experimental bond distance range and cell parameters (in Å) of the bulk structure of forsterite. The volume of the bulk (in Å^3) is also included.*

	This work	**Experimental**
Si–O	1.628–1.673	1.616–1.649
Mg1–O	2.073–2.131	2.069–2.126
Mg2–O	2.062–2.222	2.040–2.166
a	4.789	4.746
b	10.253	10.18
c	6.009	5.976
Volume	295.10	288.73

Bulk forsterite has an orthorhombic structure and presents 28 atoms in the unit cell (four formula units per cell), giving rise to 84 vibrational modes (35 IR active modes, 36 Raman active modes, 10 inactive modes and 3 modes to rigid translations). Vibrational modes in silicates are usually classified in two main categories; i) the internal modes (I), which include the stretching and bending vibrations of the SiO_4 tetrahedra; and ii) the external modes (E), which include rotations and translations of the SiO_4 tetrahedra and translations of the metal cations. In previous works [233]–[239], mode classification and band assignments of olivinic crystals have exhaustively been discussed by means of infrared, Raman and reflectance spectroscopic measurements.

Table 3.2 reports the computed and experimental vibrational frequencies for the bulk forsterite. As already described [100], B3LYP frequencies reproduce very well the experimental values, with a mean average of 4.8 cm^{-1} and a largest deviation of 9 cm^{-1}, corresponding to the peak at 517 (B3LYP, calculated) – 508 (experimental) cm^{-1}. Remarkably, the shortest deviations are associated with the Mg translations modes and the largest deviations are associated with the SiO_4 bending modes.

Table 3.2 *Comparison of the B3LYP vibrations (cm^{-1}) with the experimental ones for the bulk forsterite. Calculated intensities (values in brackets) are in km mol^{-1}. Assignment of the vibrational symmetry is also included.*

	Vibrations			
IR Band	B3LYP	[Intensity]	Experimental	Symmetry
293	291	[673.52]	291	B_{3u}
	294	[806.38]	293	B_{1u}
	295	[223.87]	296	B_{2u}
350	350	[1035.69]	352	B_{3u}
389	389	[1059.96]	383	B_{2u}
	404	[269.18]	397	B_{3u}
416	412	[1288.46]	412	B_{1u}
	420	[985.05]	419	B_{1u}
	421	[31.42]	420	B_{3u}
514	513	[527.73]	505	B_{2u}
	514	[641.76]	506	B_{1u}
	517	[74.45]	508	B_{3u}
614	614	[463.53]	606	B_{2u}
873	870	[1561.67]	873	B_{3u}
	874	[2659.78]	874	B_{1u}
982	982	[1413.29]	978	B_{2u}
	989	[43.58]	987	B_{3u}

As anticipated in the Computational Details 2.7 section, the reflectance spectrum of a given 3D-periodic system (namely, bulk structures) can be simulated with the CRYSTAL09 code. As mentioned, an important ingredient for the construction of the reflectance curves are the static dielectric tensor (ε_0) and its electronic high frequency components (ε_∞), calculated through the coupled-perturbed Kohn–Sham scheme (CPKS) [221]–[224]. The electronic high frequency contributions are almost constant with respect to frequency in the IR range, as electronic transition energies are very large compared to IR transition energies. For bulk forsterite, the calculated ε_0 and ε_∞ values along the *x*, *y* and *z* directions are provided in Table 3.3 (the three cartesian directions correspond to the crystallographic ones, so that the dielectric tensor turns out to be diagonal). ε_0 is nearly

symmetric and its ε_∞ components are about 1/3 of those of ε_0. The *x* and *z* components of ε_0 ($\varepsilon_{0,x}$ and $\varepsilon_{0,z}$) and the *y* and *z* components of ε_∞ ($\varepsilon_{\infty,y}$ and $\varepsilon_{\infty,z}$) are quite similar between them, respectively, whereas the *y* component of ε_0 and the *x* component of ε_∞ ($\varepsilon_{0,y}$ and $\varepsilon_{\infty,x}$, respectively) are both larger with respect their components by about 10%. Differences with respect to the experimental values are negative in both cases and the deviations span the 2.6–3.5% range for ε_0 and the 7.8–9.3% range for ε_∞ (see Table 3.3).

Table 3.3 *B3LYP-calculated static dielectric tensor (ε_0) and electronic high frequency components (ε_∞) of forsterite along the* x, y *and* z *directions. Experimental values for* ε_0 *from Ref.* [240] *and for* ε_∞ *from Ref.* [90] *are also included.*

		B3LYP	Experimental	Deviation (%)
x	ε_0	6.693	6.87	-2.6
	ε_∞	2.575	2.789	-7.7
y	ε_0	7.132	7.39	-3.5
	ε_∞	2.424	2.673	-9.3
z	ε_0	6.565	6.74	-2.6
	ε_∞	2.475	2.726	-9.2

Together with simulated infrared data (wavenumbers and intensities), reflectance spectrum $R(\nu)$ is the primary information from which experimentalists extract IR wavenumbers and intensities, and is defined as follows [241]:

$$R(\nu) = \left| \frac{\sqrt{\epsilon(\nu) - \sin^2(\theta)} - \cos(\theta)}{\sqrt{\epsilon(\nu) - \sin^2(\theta)} + \cos(\theta)} \right|^2 \tag{3.1}$$

where θ is the IR beam incident angle to a sample surface. According to the experimental setup of Ref. [239], the reflectance spectrum has been set employing $\theta = 10°$. The reflectivity is computed through the classical dispersion model of damped oscillator from a complex dielectric function $\epsilon(\nu)$. In the case of orthorhombic systems, $\epsilon(\nu)$ turns out to be a diagonal tensor, with diagonal elements defined as:

$$\epsilon(\nu)_{ii} = \epsilon_{\infty,ii} + \sum_j \frac{f_{j,ii}\nu_j^2}{\nu_j^2 - \nu^2 - i\nu\gamma_j} \tag{3.2}$$

where ε_∞ the dielectric constant representing the contribution from highest wavenumber; f_j the oscillator strength; v_j the resonant wavenumber; and γ_j the damping factor. As the harmonic model is used in the simulations, it is unable to compute the γ_j damping factors. Then, the experimental values γ_j^{exp} are used [239]: 0.0187, 0.0165 and 0.0185 for the three crystallographic axes (*x*, *y*, *z*), respectively. Lastly, the investigated range is 0–1200 cm^{-1} and includes 2400 points for the *x*, *y* and *z* axes, respectively.

There are rich features observed in the reflectance spectra for each crystalline axis of forsterite. The calculated peaks are shown in Table 3.4 and the computed spectra in Figure 3.2. In the present case, 12 peaks in axis *x* (B_{3u}), 11 in axis *y* (B_{2u}) and 7 in axis *z* (B_{1u}) are clearly identified. The features are assigned as Si–O stretching and bending (1000–500 cm^{-1}), SiO_4 rotation (500–400 cm^{-1}) and Mg translation (400–140 cm^{-1}) [234].

Table 3.4 *Comparison of the calculated B3LYP reflectance peaks (cm^{-1}) with the experimental ones* [239] *of the bulk forsterite for each crystalline axis.*

Axis *x* (B_{3u})		Axis *y* (B_{2u})		Axis *z* (B_{1u})	
Calculated	Experimental	Calculated	Experimental	Calculated	Experimental
1020	976	997	984	921	874
964	958	908	872	544	503
836	841	837	838	494	476
634	604	557	527	439	415
547 / 530	501	518	506	423	408
435	402	477	456	300	305
392	379	441	417	---	291
321	320	409	395	278	276
296	294	364	349		
274	275	300	289		
203	201	---	277		
		140	143		

B3LYP frequencies reproduce rather well the experimental reflectance spectra, with largest deviation of 47 cm^{-1}, corresponding to the peak at 921 (calculated) – 874 (experimental) cm^{-1} in the axis *z*. Remarkably, the shortest deviations are associated with the Mg translations modes and the largest deviations are associated with the SiO_4 stretching and

bending modes, in line with the IR spectra. Most calculated values are slightly overestimated; thus, they have been shifted to upper values compared to the experimental ones. The interesting change is the splitting of two peaks at 547 and 530 cm^{-1} in axis *x* with respect to the experimental one at 501 cm^{-1} and the absence of computed peaks at 277 and 291 cm^{-1} in axis *y* and *z*, respectively.

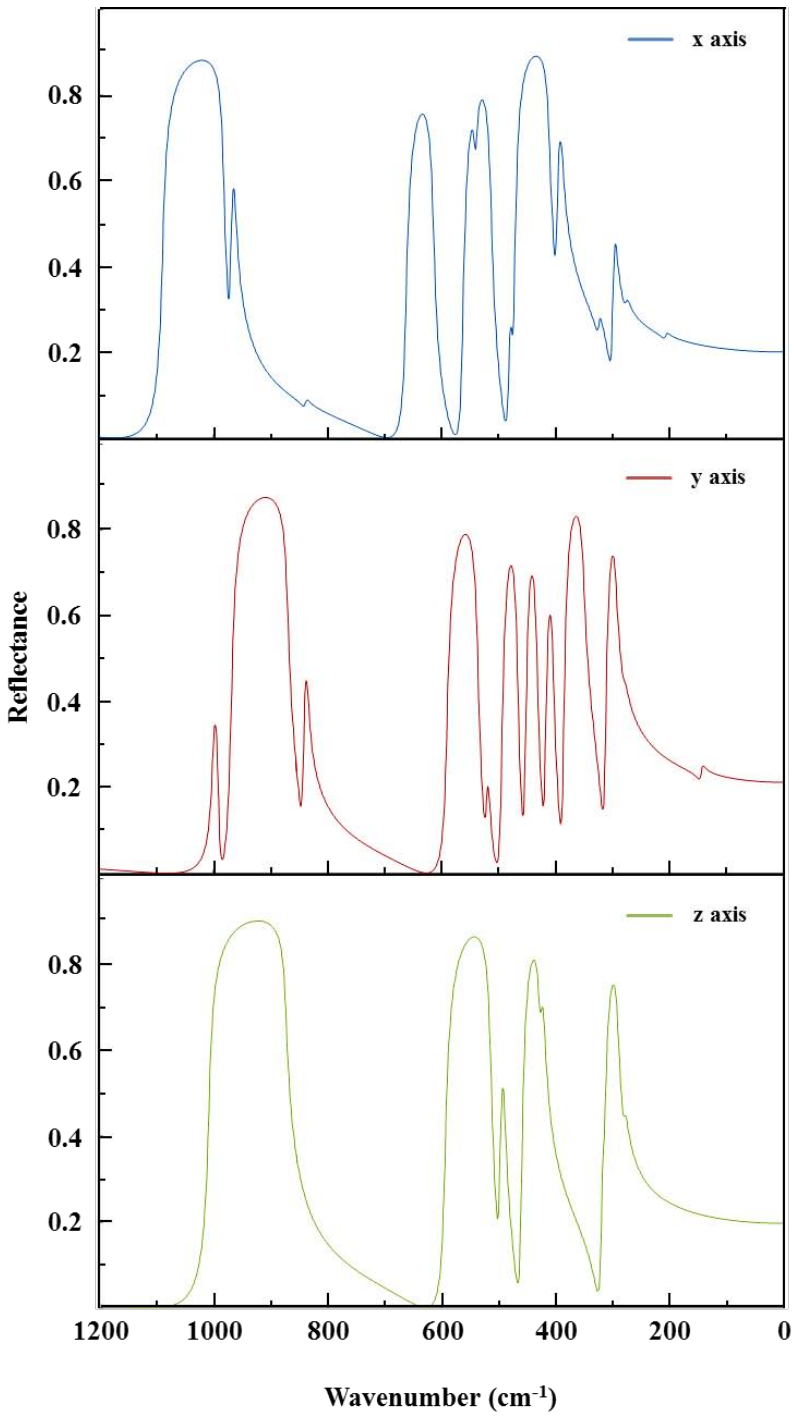

Figure 3.2 B3LYP-simulated reflectance spectra along the three axis of the bulk forsterite structure.

3.1.2. Mg_2SiO_4 Surfaces: Structure, Energy-Related Features, Electrostatic Potential Maps and IR Properties

Crystalline periodic two-dimensional slab models for the nonpolar (010), (001) and (110) forsterite surfaces (hereafter referred to as Fo(010), Fo(001) and Fo(110), respectively) were derived by cutting out the optimized forsterite crystal along the corresponding directions. For the case of the (010) surface, a larger unit cell compared to the primitive cell has been adopted (*i.e.*, the bulk *c* lattice parameter is doubled in the slab). The resulting surface models contain 56 atoms per unit cell and have thicknesses, after geometry relaxation, of about 8.6, 11.8 and 8.0 Å, respectively.

The nonpolar Fo(010) surface (shown in Figure 3.3a) is terminated by edge-layers containing both M2 magnesium ions and oxygen atoms, in which Mg^{2+} cations are unsaturated centres coordinated by three O atoms. The structure of the optimized Fo(001) is shown in Figure 3.3b. Surface relaxation brings about significant changes compared to the initial slab cut, as the outermost Mg atoms move toward the internal structure by 0.4 Å, making the surface more compact, and displace laterally by 0.6 Å to coordinate to four O atoms adopting a seesaw shape. The optimized surface exhibits a tetracoordinated Mg atom and an O corner atom. Finally, Figure 3.3c shows the optimized slab model for the Fo(110) case. Surface reconstruction from the initial slab cut does not result in significant structural changes and the optimized model present two outermost Mg atoms that are tricoordinated by O atoms in a pyramidal geometry.

The calculated equilibrium interatomic distances of Fo(010), Fo(001) and Fo(110) surfaces, the optimized cell parameters and the calculated surface energies are given in Table 3.5. In general, our structural parameters are in agreement with those of Watson and co-workers [101], in which the atomistic simulations of these surfaces were performed using the THB1 interatomic potential. The calculated Fo(010) slab model is almost bulk-terminated surface with slight undulating surface topology. This is in agreement with the experimental study of Hochella [242], in which the forsteritic {010} crystal form was found to be 1x1 surface unit cells with small relaxations using low energy electron diffraction. The internal Si–O and Mg–O distances are very similar to those present in the respective bulk structure, demonstrating the low reconstruction suffered by this surface. However, the outermost Mg–O distance is significantly shorter (about 0.2 Å) because Mg

ion is coordinatively unsaturated. Moreover, the outermost Si–O distances are also shorter (about 0.025 Å) than the internal ones. Even so, the lattice parameters of the surfaces are somewhat larger compared to the corresponding bulk values (*i.e.*, about 1% for *a* and 2.3 % for *c*).

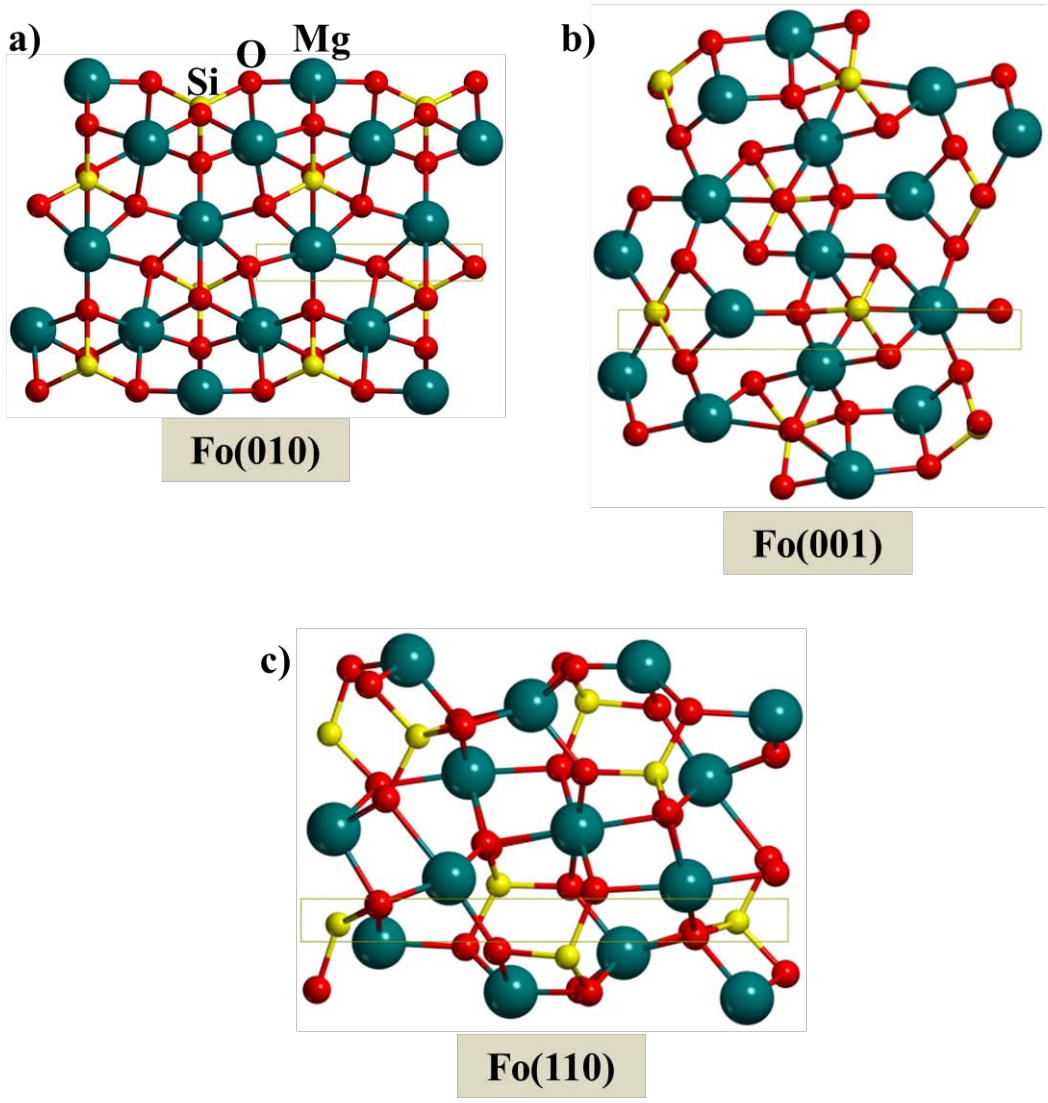

Figure 3.3 Lateral views of the crystalline nonpolar (010) (a), (001) (b) and (110) (c) Mg_2SiO_4 surface models. Unit cells are highlighted in yellow.

Table 3.5 *Si–O and Mg–O range of the B3LYP-optimized bond distances of the Fo(010), Fo(001) and Fo(110) slab models. Bare values correspond to distances involving atoms present in the internal structure of the surfaces, whereas values in italics involve atoms present at the outermost positions of the edge-layers. B3LYP-optimized cell parameters and surface energies of the different slab models.*

	Fo(010)	**Fo(001)**	**Fo(110)**
Si–O (Å)	1.630 – 1.703	1.647 – 1.678	1.631 – 1.670
	1.615 – 1.698	*1.610 – 1.665*	*1.597 – 1.705*
Mg–O (Å)	2.031 – 2.363	1.996 – 2.284	1.986 – 2.366
	1.868 – 1.912	*1.995 – 2.052*	*1.856 – 2.144*
a (Å)	4.831	4.838	5.831
b (Å)	6.141	9.960	11.537
$\widehat{ab}$ **(degrees)**	90.00	92.48	91.46
area (Å^2)	29.67	48.15	67.25
E_{surf} (Jm^{-2})	1.160	1.673	1.788

For the case of Fo(001) and Fo(110), the internal Si−O distances are very similar with respect to the bulk values, the maximum variation belonging to Fo(001) (between 0.6–1.3%). Larger variations, although not dramatic, are observed for the internal Mg–O distances, the maximum one corresponding to Fo(110) (between 4.2–6.5%). These results demonstrate that no important changes are appreciable in the innermost positions of these surfaces during the surface reconstruction. In contrast, more significant variations are observed for those distances involving the outermost atoms. For both slab models, the Mg–O lengths decrease (variations of about 5.8–7.7% in Fo(001) and 3.5–10% in Fo(110)) because they are under coordinated, whereas the changes of the Si–O distances are less pronounced (about 2.3%). The optimized lattice parameters of Fo(001) are very similar to those previously reported [101]–[103] (largest variation of 0.04%), whereas for Fo(110) the variations are more accentuated (about 1.8%), since all the results are converged with respect to the thickness of the slab.

The calculated surface energy (E_{surf}) of Fo(010) is 1.16 Jm^{-2}, implying that the cleavage of the bulk crystal to create this surface is not a highly energetic process. Its stability may be due to the formation of O–Mg–O bridges on the surface, similar to O–Si–O and O–Na–O bridges, which were found to stabilise α-quartz-based surfaces [243]. The presence of alternating O-Si-O and O-Mg-O surface bridge groups gives rise to a surface energy

similar to that for the (010) MgO surface (1.20 Jm^{-2}). The surface energies of Fo(001) and Fo(110) are 1.67 Jm^{-2} and 1.79 Jm^{-2}, confirming the same ranking of surface stability predicted in previous works [101]–[103].

Drawing electrostatic potential maps (EPMs) is useful because they show regions of negative and positive potentials, hence providing clues about the most favourable adsorption sites and of the driving forces involved. Figure 3.4 shows the B3LYP-EPMs for Fo(010), Fo(001) and Fo(110) on a surface enclosing 90% of the electron density. In all cases, EPMs show prominent positive and negative valued regions, which are associated with the outermost Mg and O surface atoms, respectively. This suggests that Mg atoms are the best candidates to interact with electron donor atoms and surface O atoms for H-bonding interactions and electrophilic molecules. Net Mg and O charges obtained by a Mulliken population analysis confirm this trend and the ionic character of the surfaces as they are found to be +1.60|e| and −1.22|e| for the Fo(010), +0.82|e| and −1.01|e| for the Fo(001) and +0.97|e| and −1.01|e| for the Fo(110), respectively.

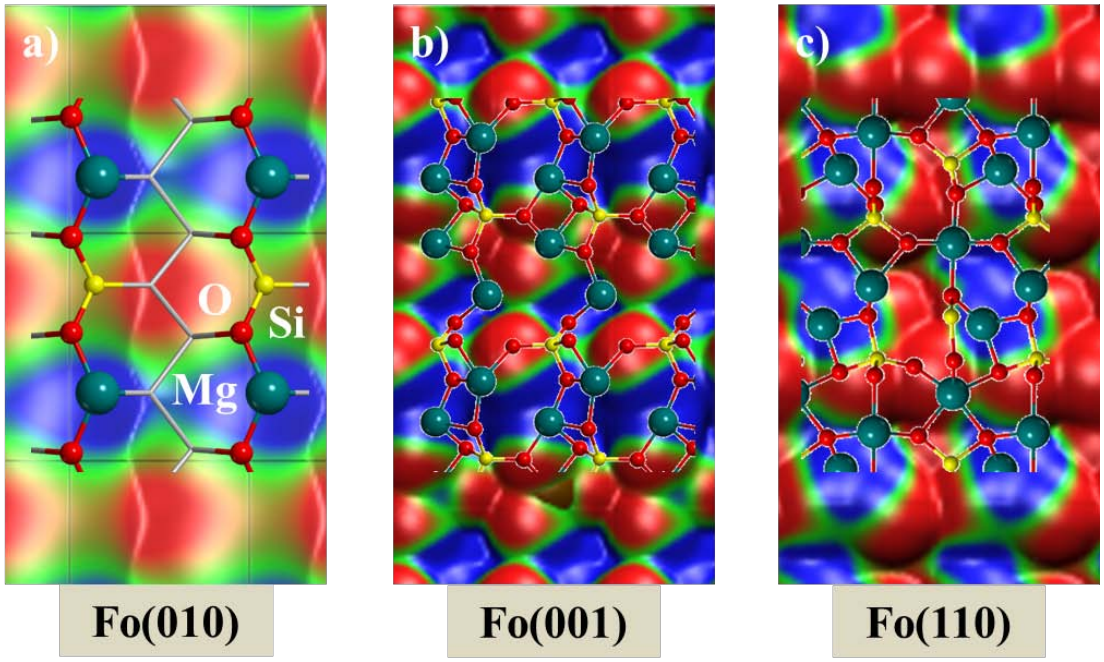

Figure 3.4 Top views of the electrostatic potential maps of the Fo(010) (a), Fo(001) (b) and Fo(110) (c) slab models mapped on surfaces enclosing 90% of the total electron density. Negative values (–0.02 au) coded as red colours; positive values (+0.02 au) coded as blue colours; green colour indicates ~0.00 au electrostatic potential values.

A comparison of the IR spectra between the bulk structure and the corresponding (010), (001) and (110) Mg_2SiO_4 surfaces is presented in Table 3.6 and Figure 3.5. Spectra of the surface slabs have two significant differences: i) they have been shifted to upper values and ii) they present more bands. The hypsochromic shift related to point i) is probably due to the shorter distances of the outermost Si–O and Mg–O bonds because the Mg ions are coordinatively unsaturated centres (*vida supra*). For instance, the peaks at 416 and 873 cm^{-1}, corresponding to the bulk forsterite and belonging to the rotation and stretching of the SiO_4 tetrahedra, respectively, shifts at 420, 474 and 456 cm^{-1} for the rotation and at 945, 902 and 915 cm^{-1} to the stretching for the Fo(010), Fo(001) and Fo(110) case, respectively.

Table 3.6 *B3LYP vibrational bands of the bulk forsterite and nonpolar Mg_2SiO_4 surfaces (in brackets smaller bands associated with the main band). Assignment of the vibrational mode is also included.*

Bulk bands (cm^{-1})	Fo(010) bands (cm^{-1})	Fo(001) bands (cm^{-1})	Fo(110) bands (cm^{-1})	Vibrational Mode
293	287 / (309)	294	251	Translation Mg
350	360	344	395	Translation Mg
389	399	428	---	Rotation SiO_4
416	420	474	456	Rotation SiO_4
(494) / 514	479 / 530	545	497	Bending SiO_4
614	(646) / 668	614	(598) / 644 / (674) / (709)	Bending SiO_4
---	---	764	774 / 824	Stretching SiO_4
(838) / 873	911 / 945	(859) / 902	(864) / 915	Stretching SiO_4
(967) / 982	1017	950 / 981	(1006) / (1030) / 1087	Stretching SiO_4

The presence of more bands in the spectra of the surfaces (point ii)) is due to the splitting of specific broad bands present in the bulk spectra associated with the vibrations of atoms of the outermost positions of the surfaces. For instance, the peak at 293 cm^{-1}, belonging to the translation of the Mg^{2+}, splits into two bands at 287 and 309 cm^{-1} for the Fo(010) case; the peak at 982 cm^{-1} also splits into two bands at 950 and 981 cm^{-1} for the Fo(001) case; and the peak at 614 cm^{-1}, belonging to the bending of the SiO_4, splits into four bands at 598, 644, 674 and 709 cm^{-1} for the Fo(110) case.

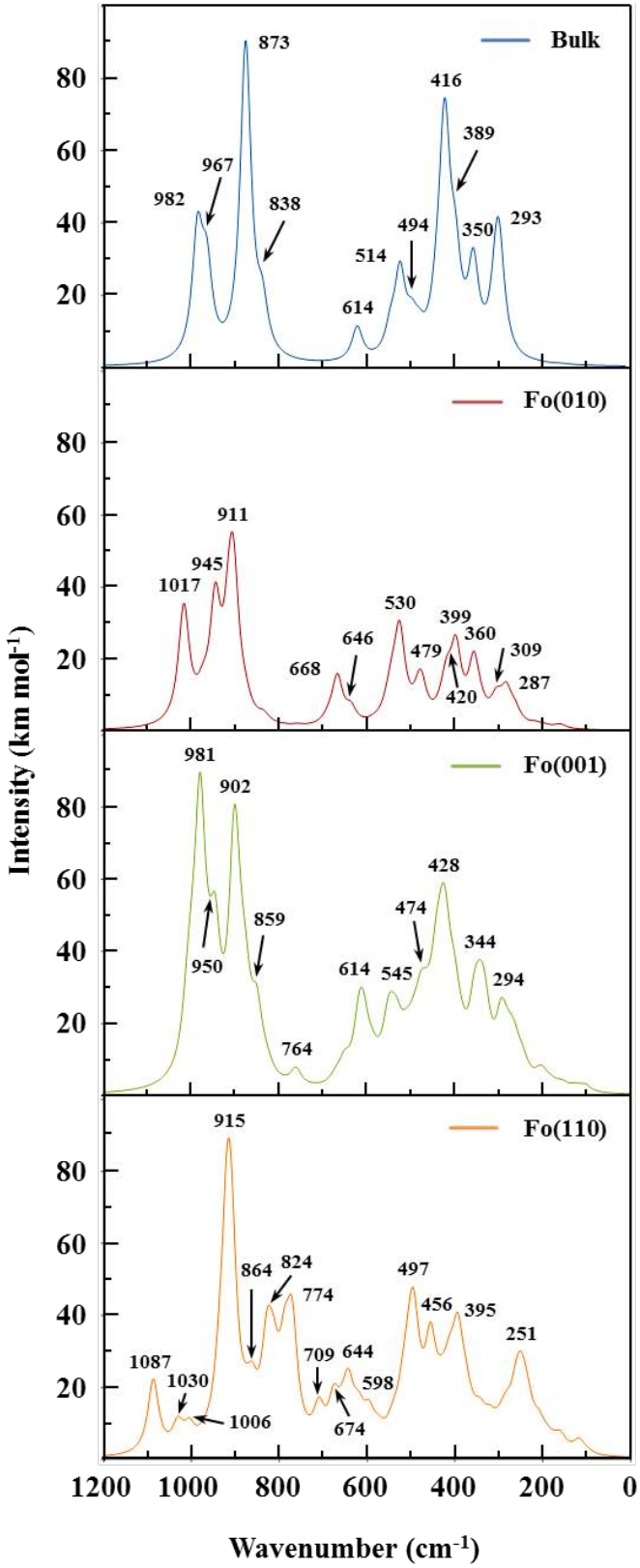

Figure 3.5 B3LYP-simulated infrared spectra of the bulk forsterite structure (in blue) and nonpolar Fo(010) (in red), Fo(001) (in green) and Fo(110) (in orange) surfaces.

Finally, a couple of particular features must be mentioned: i) the peak at 389 cm^{-1} is not present in Fo(110), because it is due to the rotation of an outermost SiO_4 group and Fo(110) does not have this feature; and ii) the peak at 764 cm^{-1} in Fo(001) and a double peak at 774 and 824 cm^{-1} in Fo(110) that are not present neither in the bulk nor in Fo(010), because they are due to a ν(Si–O) stretching of an outermost SiO_4 group, a motif which is only present in Fo(001) and Fo(110).

3.1.3. $(Mg,Fe)_2SiO_4$ Bulk: Structure, Spin State, IR and Reflectance Properties

For the sake of brevity, the Fe-containing ($Mg_{1.5}Fe_{0.5}SiO_4$)-related systems will be hereafter referred to Fo_{75}. The bulk crystal structure of forsterite and Fo_{75} is very similar [89] (see Figure 3.6). A substitution of half of Mg2 by Fe leads to the Fo_{75}^{M2} structure (see Figure 3.6a), whereas substitution of half of Mg1 by Fe yields Fo_{75}^{M1} (see Figure 3.6b). It is worth mentioning that different studies [92]–[94] indicate that the Fe-containing solid solutions are more stable in the high-spin state than in the low-spin one at normal conditions, and accordingly the bulk Fo_{75}^{M2} and Fo_{75}^{M1} systems have been computed in this high-spin state (*i.e.*, each Fe^{2+} cation (d^6) in a quintet electronic state).

The calculated equilibrium geometries of Fo_{75}^{M2} and Fo_{75}^{M1} are given in Table 3.7. Cell parameters are larger than those of forsterite because of the larger ionic radius of Fe^{2+} than Mg^{2+} (0.78 and 0.72 Å, respectively), and accordingly the volume of the two iron containing systems is larger as well. The presence of Fe (irrespective of its position) slightly affects the Mg–O distances by increasing their values compared to the forsterite ones, whereas the Si–O distances are in both systems very similar to those of forsterite.

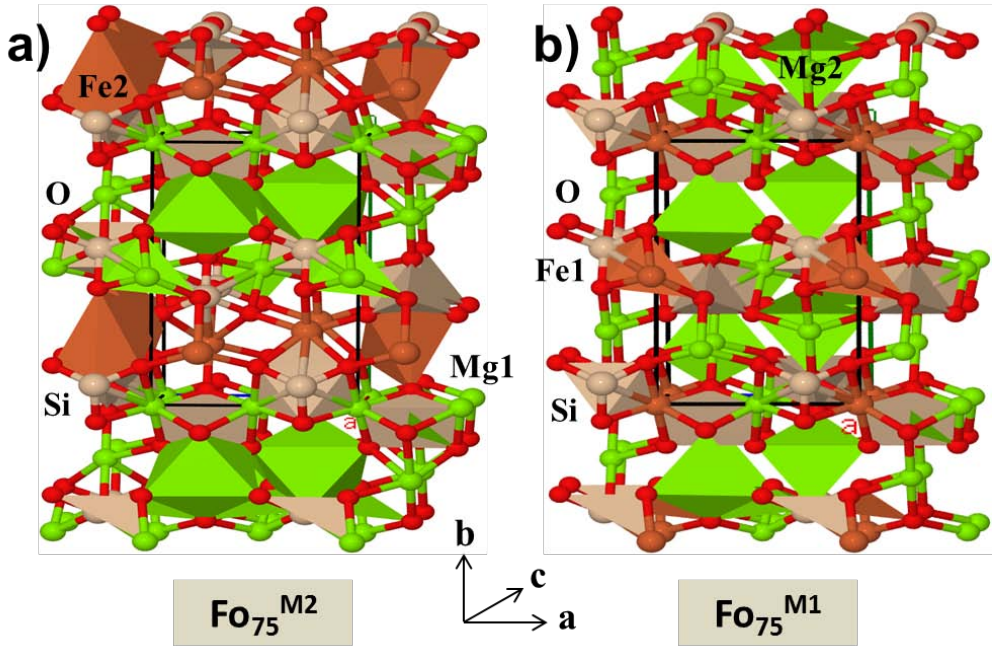

Figure 3.6 View (along the *c* crystallographic axis) of the crystal structure of Fo_{75}.

Table 3.7 *B3LYP-optimized bond distance range and cell parameters (in Å) of the bulk structures of forsterite, Fo_{75}^{M2} and Fo_{75}^{M1}. The volume of the bulks (in $Å^3$) is also included.*

	Forsterite	**Fo_{75}^{M2}**	**Fo_{75}^{M1}**
Si–O	1.628–1.673	1.629–1.672	1.633–1.674
Mg1–O	2.073–2.131	2.064–2.148	2.096–2.134
Mg2–O	2.062–2.222	2.070–2.228	2.066–2.242
Fe1–O	–	–	2.119–2.226
Fe2–O	–	2.085–2.298	–
a	4.789	4.791	4.835
b	10.253	10.369	10.320
c	6.009	6.063	6.021
Volume	295.10	301.28	300.46

Bulk olivine has, like forsterite, an orthorhombic structure and present 28 atoms in the unit cell, giving rise to 84 vibrational modes. Figure 3.7 shows the calculated IR spectra of bulk forsterite and Fo_{75}^{M2}. Both systems present 8 common vibrational frequencies in the 200–1000 cm^{-1} range corresponding to the translation of the metal cations and the rotation, the bending and stretching motions of the SiO_4 tetrahedra. Results show that the overall spectra of Fo_{75}^{M2} are shifted to lower values due to the higher mass of the substituting Fe^{2+}.

Further calculations for forsterite in which the Mg^{2+} ions that are substituted by Fe^{2+} in Fo_{75}^{M2} have the mass of iron (hence reproducing a mass-analogue of Fo_{75}^{M2}), show that the shifts are mainly due to the higher mass of Fe^{2+}. This bathochromic shift is significantly important in those bands where Fe^{2+} is involved; that is, those associated with the metal translation (*i.e.*, from 293 to 276 cm^{-1} and from 350 to 280 cm^{-1}) and those associated with modes of SiO_4 bonded to the metal cations (*e.g.*, from 873 to 855 cm^{-1}). This is in agreement with the experimental measurements [244] and theoretical results [114] that compare the IR features of forsterite with fayalite.

Fo bands (cm^{-1})	**Fo_{75}^{M2} bands (cm^{-1})**	**Vibrational Mode**
293	**276**	**Transl. Mg (+ Fe)**
350	**280**	**Transl. Mg (+ Fe)**
389	**373**	**Rot. SiO_4**
416	**406**	**Rot. SiO_4**
514	**513**	**Bending SiO_4**
614	**603**	**Bending SiO_4**
873	**855**	**Stretching SiO_4**
982	**978**	**Stretching SiO_4**

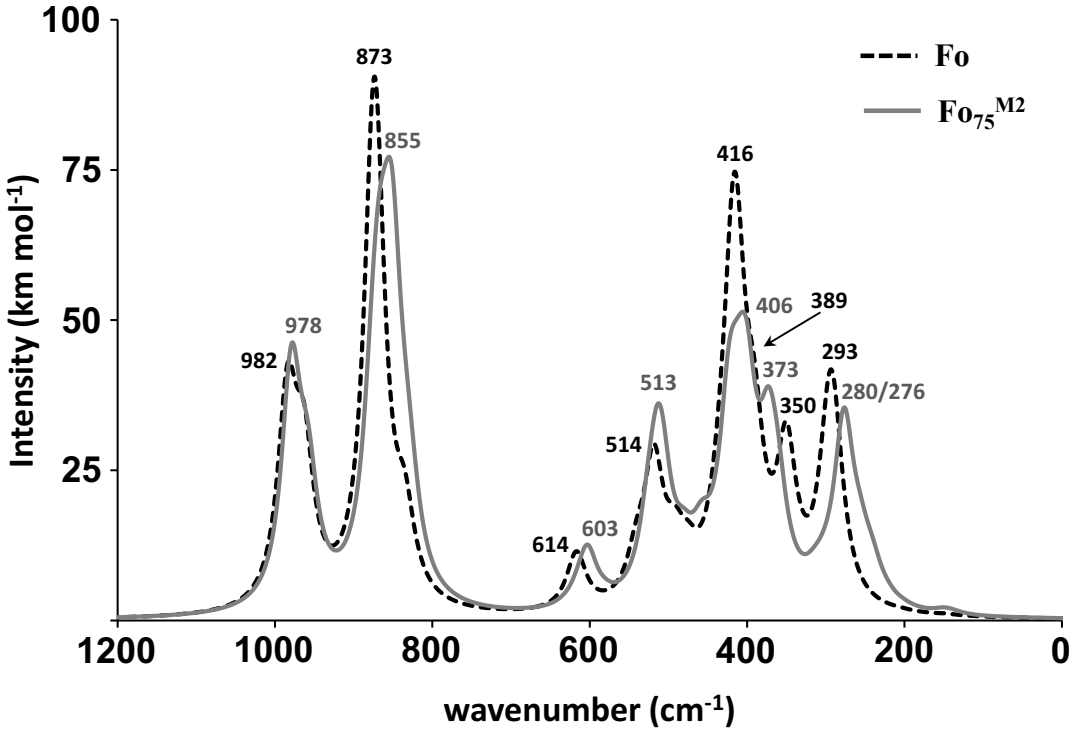

Figure 3.7 B3LYP-simulated infrared spectra of the forsterite (dashed-black) and Fo_{75}^{M2} (solid-grey) bulk structures.

Finally, the reflectance spectra of forsterite and Fo_{75}^{M2} along the *y* direction are shown in Figure 3.8. Due to the fact that these orthorhombic crystalline systems are almost isotropic, they present the same behaviour irrespective the direction in which the light vibrates when passing through the crystal and only one direction is presented. Expectedly, the reflectance spectrum of Fo_{75}^{M2} is shifted to lower wavenumbers compared to the forsterite one in consistency to the higher mass of the substituted iron. Remarkably, such a bathochromic shift was also observed in the comparison of the single-crystal reflectivity of pure Mg_2SiO_4 with the natural $(Mg_{0.86},Fe_{0.14})SiO_4$ [236]. Moreover, the presence of the Fe reduces overall the far-infrared reflectivity of olivine compared to pure forsterite, in agreement with the experimental measurements and caused by the larger refractive index of Fe-containing olivines than the Mg-pure ones.

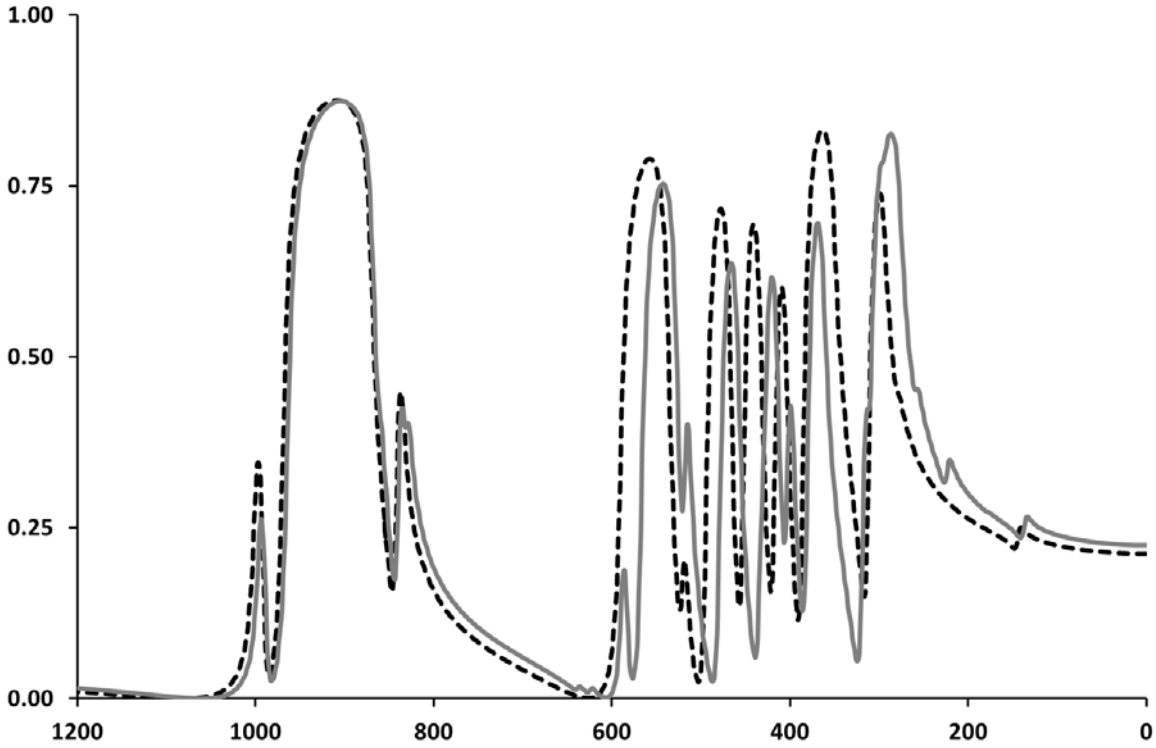

Figure 3.8 B3LYP-simulated reflectance spectra along the *y* axis of the bulk Mg_2SiO_4 and $(Mg,Fe)_2SiO_4$ structures.

3.1.4. $(Mg,Fe)_2SiO_4$ Surfaces: Structure, Energy-Related Features, Spin States, Electrostatic Potential and Spin Density Maps and IR Properties

Crystalline periodic 2D slab model for the nonpolar (010) Fe-containing forsterite surfaces were derived directly from the corresponding optimized olivine-like crystal bulk structure, adopting a larger unit cell compared to the primitive cell (*i.e.*, the bulk *c* lattice parameter is doubled in the slab). For these systems, three different slab models have been designed from the two initial bulk structures; *i.e.*, Fo_{75}^{top} and the Fo_{75}^{int} surfaces from Fo_{75}^{M2}; and Fo_{75}^{mid} from Fo_{75}^{M1}. Fo_{75}^{top} exhibits the Fe^{2+} ions at the outermost positions of the edge-layers of the slab model (see Figure 3.9a) and, similarly to the analogous Mg^{2+} ions in Fo(010), are coordinatively unsaturated centres. In Fo_{75}^{mid}, the Fe ions are placed in the mid-regions of the slab (see Figure 3.9b), whereas in Fo_{75}^{int} they are in the innermost regions (see Figure 3.9c). For these surfaces, the atomic integrated spin density has been evaluated by computing both the quintet, triplet and singlet states per Fe^{2+} ions. Considering that a unit cell contains two Fe^{2+} cations, the overall spin multiplicity for the unit cell is, therefore, nonaplet, quintet and singlet, respectively.

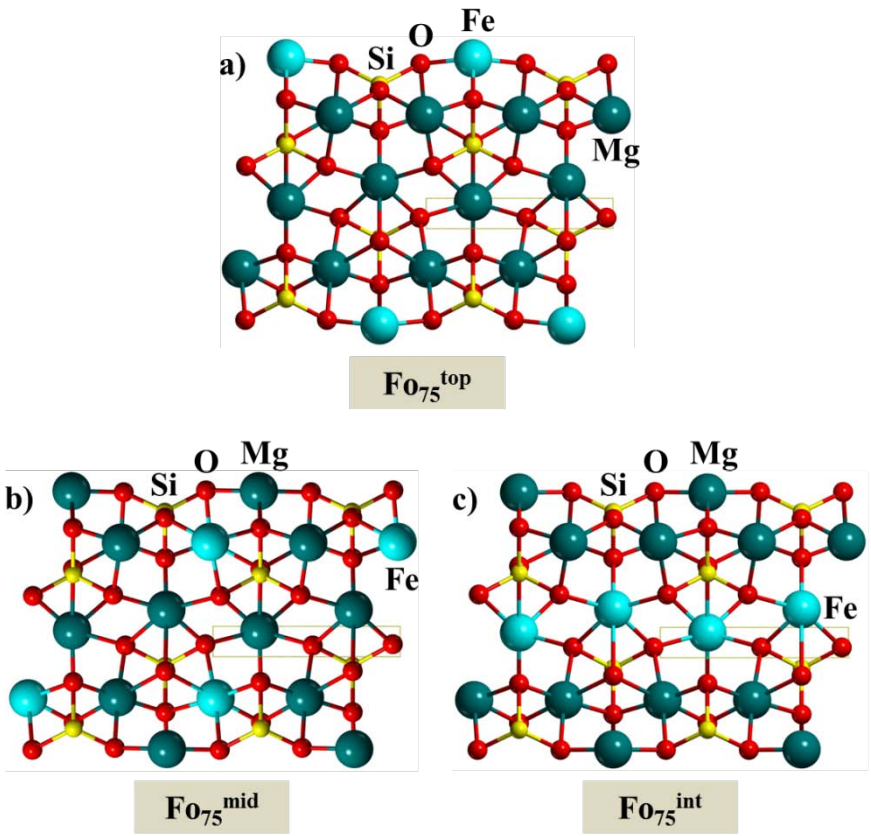

Figure 3.9 Lateral views of the nonpolar (010) surfaces for the Fe-containing olivine surfaces (Fo_{75}^{top}, Fo_{75}^{mid} and Fo_{75}^{int}). Unit cells are highlighted in yellow.

The calculated equilibrium interatomic distances of forsterite and Fo_{75} (010) surfaces are given in Table 3.8 and the optimized cell parameters in Table 3.9. The internal Si–O and metal-oxygen distances are very similar to those present in the respective bulk structures, demonstrating the low reconstruction suffered by these surfaces. However, the outermost Mg–O and Fe–O (for Fo_{75}^{top}) distances are significantly shorter (about 0.2 Å) because these metal ions are coordinatively unsaturated. Moreover, the outermost Si–O distances are also shorter (about 0.025 Å) than the internal ones. Consequently, the lattice parameters of the surfaces are somewhat shorter compared to the corresponding bulk values (*i.e.*, about 1% for *a* and 2.3 % for *c*). On the other hand, for Fo_{75} surfaces, it is observed that the Fe–O distances are larger for Fe^{2+} in the quintet state than in the triplet and the singlet states, and accordingly surface areas decrease with the spin multiplicity. This is due to the larger electronic repulsion between the Fe^{2+} 3d electrons and O^{2-} in the quintet state than in the triplet and singlet ones.

Table 3.8 *Range of the B3LYP-optimized bond distances of Fo(010) and Fe-containing olivine (010) surfaces (Fo_{75}^{top}, Fo_{75}^{mid} and Fo_{75}^{int}) for the different spin state per Fe^{2+} ion (quintet, qt; triplet, tp; singlet, sg). Values in italics correspond to distances involving atoms present at the outermost positions of the edge-layers.*

	Si–O	**Mg1–O**	**Mg2–O**	**Fe1–O**	**Fe2–O**
Fo(010)	1.630–1.703	2.031–2.196	2.052–2.363	–	–
	1.615–1.698	–	*1.868–1.912*	–	–
Fo_{75}^{top}(qt)	1.631–1.703	2.040–2.200	2.071–2.247	–	–
	1.609–1.688	–	–	–	*1.886–1.999*
Fo_{75}^{top}(tp)	1.632–1.703	2.031–2.201	2.061–2.239	–	–
	1.606–1.688	–	–	–	*1.868–1.972*
Fo_{75}^{top}(sg)	1.627–1.705	2.032–2.177	2.070–2.224	–	–
	1.607–1.685	–	–	–	*1.876–1.892*
Fo_{75}^{mid}(qt)	1.638–1.698	2.049–2.178	2.055–2.335	2.062–2.262	–
	1.624–1.696	–	*1.863–1.912*	–	–
Fo_{75}^{mid}(tp)	1.636–1.704	2.025–2.188	2.064–2.398	2.004–2.327	–
	1.627–1.706	–	*1.851–1.915*	–	–
Fo_{75}^{mid}(sg)	1.632–1.698	2.029–2.206	2.063–2.314	2.035–2.173	–
	1.617–1.698	–	*1.863–1.912*	–	–

Fo_{75}^{int}(qt)	1.628–1.701	2.026–2.213	–	–	2.103–2.471
	1.617–1.701	–	*1.874–1.925*	–	–
Fo_{75}^{int}(tp)	1.631–1.703	2.042–2.184	–	–	2.023–2.419
	1.615–1.704	–	*1.873–1.918*	–	–
Fo_{75}^{int}(sg)	1.632–1.699	2.031–2.174	–	–	2.070–2.155
	1.611–1.699	–	*1.864–1.906*	–	–

Table 3.9 *B3LYP-optimized cell parameters of Fo(010) and Fe-containing olivine (010) surfaces (Fo_{75}^{top}, Fo_{75}^{mid} and Fo_{75}^{int}) for the different spin state per Fe^{2+} ion (quintet, qt; triplet, tp; singlet, sg). Surface areas (in $Å^2$) and calculated surface energies (Jm^{-2}) are included.*

	a	**c**	**Area**	**E_{surf}**
Fo(010)	4.831	6.141	29.67	1.160
Fo_{75}^{top}(qt)	4.817	6.153	29.65	0.870
Fo_{75}^{top}(tp)	4.805	6.176	29.68	1.538
Fo_{75}^{top}(sg)	4.809	6.016	28.94	2.201
Fo_{75}^{mid}(qt)	4.875	6.163	30.05	1.111
Fo_{75}^{mid}(tp)	4.830	6.102	29.48	1.644
Fo_{75}^{mid}(sg)	4.813	6.128	29.50	1.709
Fo_{75}^{int}(qt)	4.839	6.203	30.02	1.097
Fo_{75}^{int}(tp)	4.836	6.197	29.97	1.768
Fo_{75}^{int}(sg)	4.807	6.107	29.36	2.039

The calculated surface energy of Fo_{75}^{top}(qt), is 0.87 Jm^{-2}, 0.29 Jm^{-2} lower than Fo(010), meaning that less energy is needed to cut the corresponding bulk system and that the Fo_{75}^{top}(qt) is expected to be less reactive than Fo(010). This lower surface energy of Fo_{75}^{top}(qt) is associated with the high spin of Fe^{2+} (note that triplet and singlet states exhibit higher surface energies), since the loss of Fe–O electrostatic interactions in Fo_{75}^{top}(qt) is partly compensated by a larger decrease of electron repulsion between Fe^{2+} 3d electrons and O^{2-} in this spin state quintet state upon generating the surface.

The relative stability of Fo_{75} (010) surfaces has been calculated considering the electronic state and the position of the Fe^{2+} cations (see Figure 3.10). The most stable surface concerns the Fe^{2+} ions placed at the outermost positions in a quintet spin state (*i.e.*,

hereafter referred to as Fo_{75}^{top}(qt)). Moreover, for the three surfaces, the relative stability of the three spin states considered follow the order qt > tp > sg, *i.e.*, the most stable Fe^{2+} spin configuration is the quintet high spin state, in consistency with what is known for bulk solid solutions. Noteworthy, for the Fe^{2+} in the quintet and triplet spin states, Fo_{75}^{top} surfaces are more stable than Fo_{75}^{mid} and Fo_{75}^{int}, whereas for the singlet state, Fo_{75}^{mid} becomes the most stable surface, in agreement with the fact that saturated coordination environments stabilize low spin versus high spin states. Note that saturated environments induce a larger splitting of 3d orbitals.

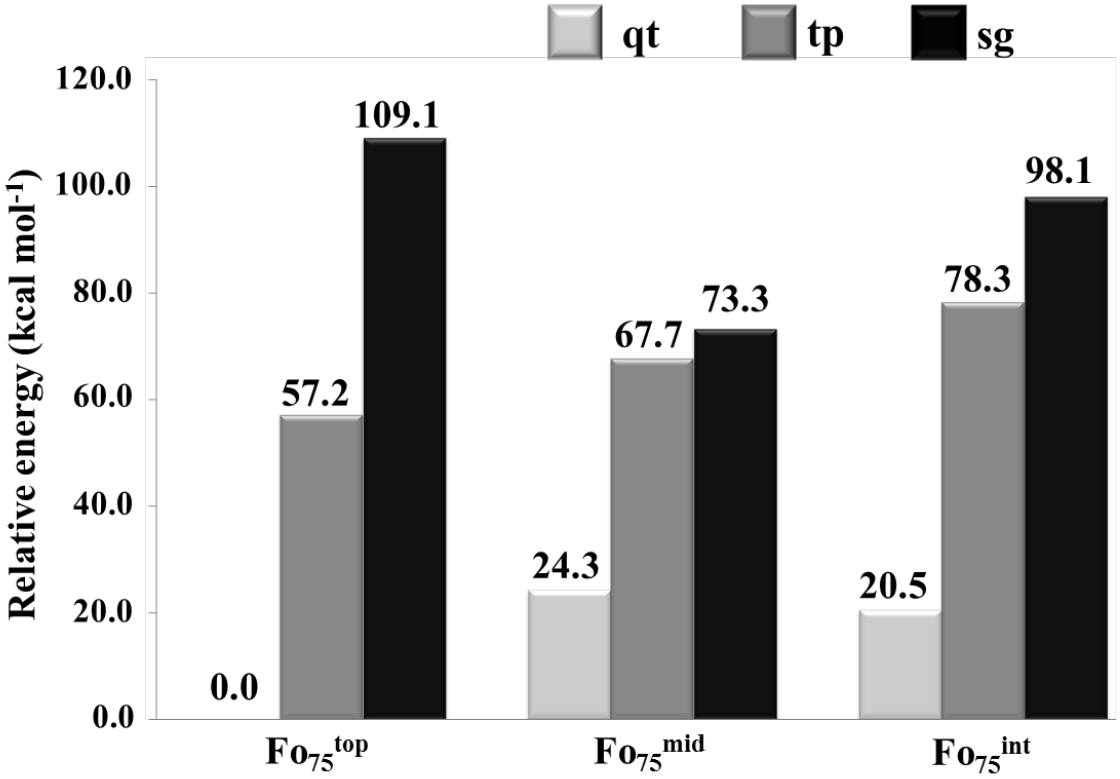

Figure 3.10 Relative stability of the Fe-containing Fo(010) surfaces as a function of the spin configuration per Fe^{2+} ion (quintet, qt; triplet, tp; singlet, sg) and the position of the Fe^{2+} ions in the slab models.

Figure 3.11a shows the B3LYP-EPM for Fo_{75}^{top}(qt) on a surface enclosing 90% of the electron density, showing positive and negative valued regions, which are associated with the outermost Fe and O surface atoms, respectively. This suggests that Fe atoms are the best candidates to interact with electron donor atoms and surface O atoms for H-bonding interactions and electrophilic molecules. It is worth pointing out that these two well-defined potential regions are less pronounced in the Fo_{75}^{top}(qt) surface than in the Fo(010), suggesting that favourable electrostatic interactions are expected to be larger in Fo(010)

rather than in Fo_{75}^{top}(qt). Net charges obtained by a Mulliken population analysis confirms this trend as they are found to be +1.40|e| and -1.19|e| for Fe and O, respectively, in Fo_{75}^{top}(qt).

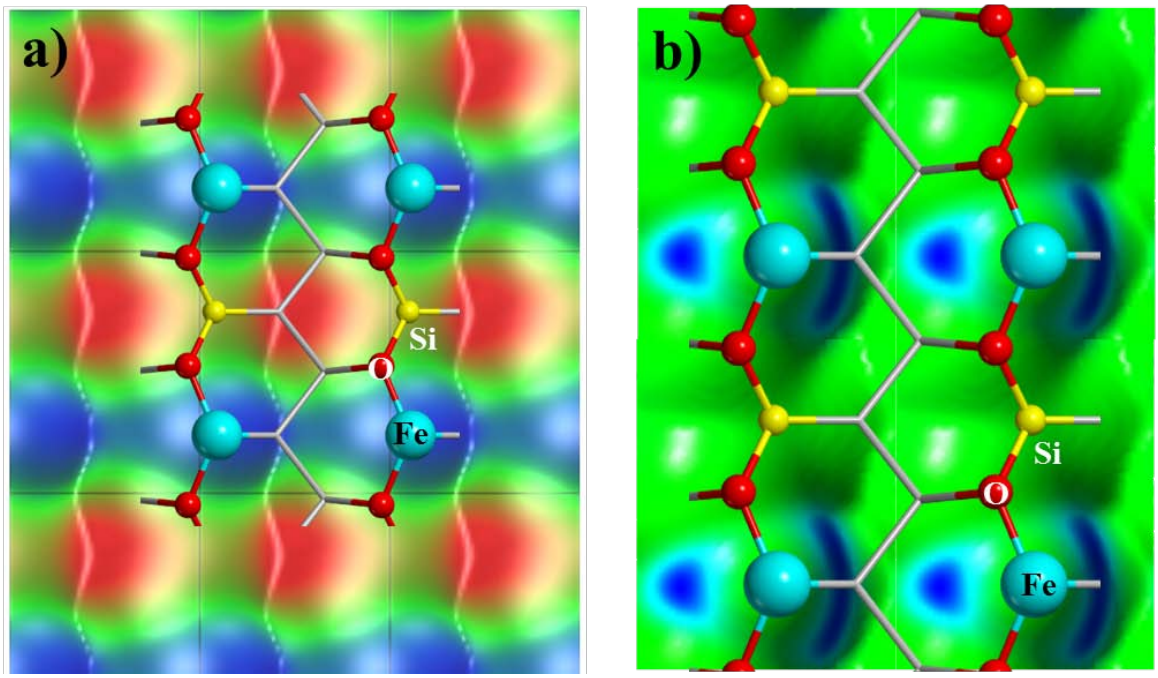

Figure 3.11 Top views of the electrostatic potential maps of the Fo_{75}^{top}(qt) slab model (a) and of the spin density map of the Fo_{75}^{top}(qt) surface (b) mapped on surfaces enclosing 90% of the total electron density. Negative values (-0.02 a.u.) coded as red colors; positive values (+0.02 a.u.) coded as blue colors; green color indicates ≈0.0 a.u. electrostatic potential values or spin density values.

The spin density features have also been analysed through its spin density map (see Figure 3.11b), which shows the spin localization at the surface atoms. The map clearly shows that the spin of Fo_{75}^{top}(qt) lies mainly at the Fe^{2+} cations, in line with the calculated Mulliken atomic integrated spin density for the Fe atom of +3.7|e| (out of +4|e|), and about +0.15|e| of the neighbouring O atoms. This means that, in addition to establish electrostatic interactions with electron donor atoms, Fe^{2+} sites will be active with respect to adsorbed radical species.

Comparison of the IR spectra of Fo(010) with Fo_{75}^{top}(qt) and between the Fe-containing bulk structure and the corresponding (010) surface (Fo_{75}^{M2} *vs* Fo_{75}^{top}(qt)) is presented in Figure 3.12 and Figure 3.13, respectively. The first comparison gives the same differences as when previously comparing bulk systems; that is, the Fe-containing spectrum is globally bathochromic shifted.

Fo^{surf} bands (cm^{-1})	**Fo_{75}^{top}(qt) bands (cm^{-1})**	**Vibrational Mode**
287	**279**	**Transl. Mg**
309	**304**	**Transl. Mg**
360	**348**	**Transl. Mg (+ Fe)**
399	**372**	**Rot. SiO_4**
420	**409**	**Rot. SiO_4**
479	**468**	**Bending SiO_4**
530	**504**	**Bending SiO_4**
668	**624**	**Bending SiO_4**
911	**892**	**Stretching SiO_4**
945	**920**	**Stretching SiO_4**
1017	**1023**	**Stretching SiO_4**

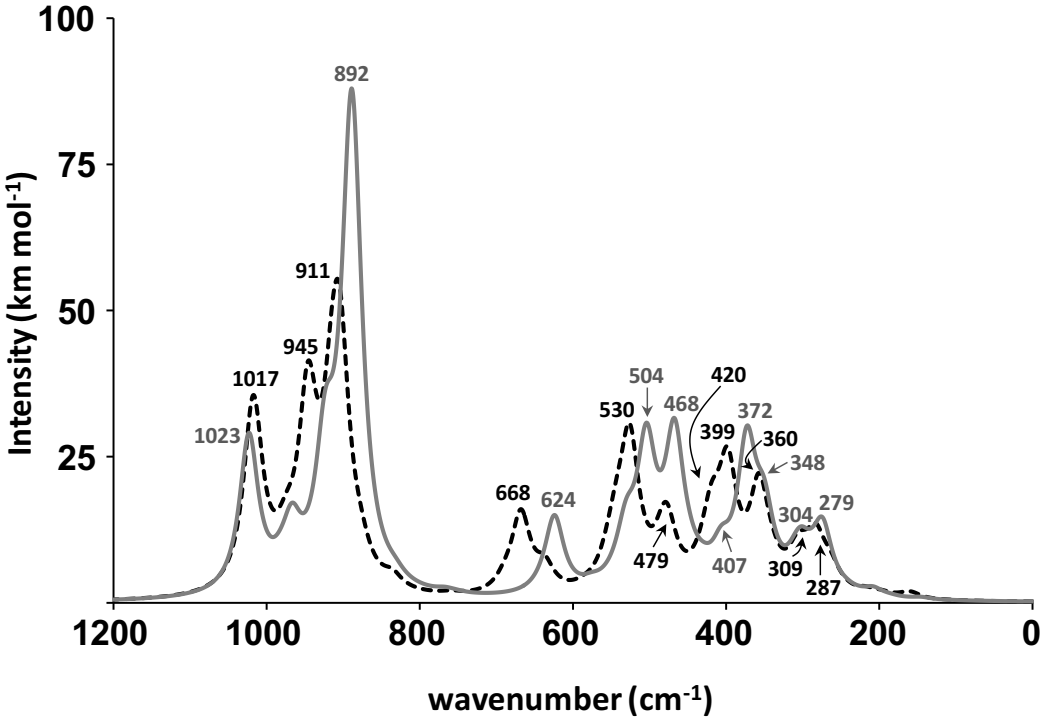

Figure 3.12 B3LYP-simulated infrared spectra of the Fo(010) (dashed-black) and Fo_{75}^{top}(qt) (solid-grey) surface slab models.

Fo_{75}^{M2} bands (cm^{-1})	Fo_{75}^{top}(qt) bands (cm^{-1})	Vibrational Mode
280/276	279/304/348	Transl. Mg (+ Fe)
373/406	372/407	Rot. SiO_4
513/603	468/504/624	Bending SiO_4
855/978	892/920/1023	Stretching SiO_4

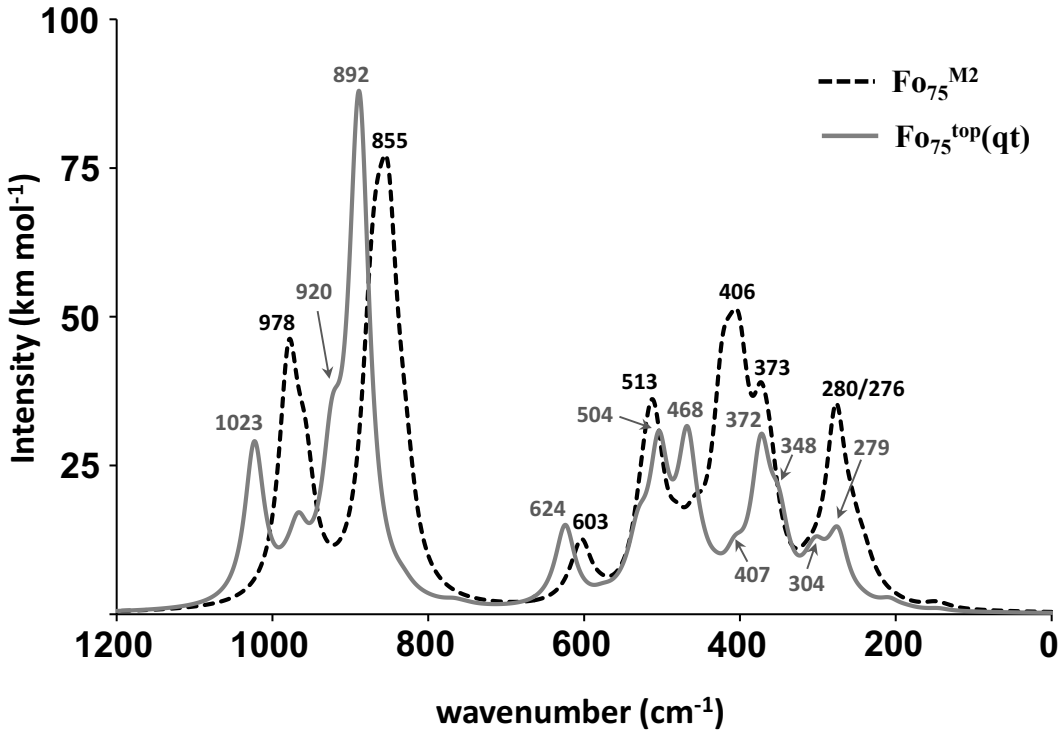

Figure 3.13 B3LYP-simulated infrared spectra of the Fo_{75}^{M2} bulk structure (dashed-black) and Fo_{75}^{top}(qt) nonpolar (010) surface (solid-grey).

The second comparison shows that spectra of the surface slab has two significant differences compared to the bulk one, similarly to what is observed in forsterite systems: i) it has been shifted to upper values; and ii) it presents more bands. The hypsochromic shift related to point i) is probably due to the shorter distances of the outermost Si–O, Mg–O and Fe–O bonds because the metal ions are coordinatively unsaturated centres. The presence of more bands in the spectra of the surfaces (point ii)) is due to the splitting of broad bands present in the bulk spectra associated with the vibrations of atoms of the outermost positions of the surfaces. For instance, the peak at 276 cm^{-1} (Fo_{75}^{M2}) belonging to the translations of the metal cation split into the bands at 279 and 304 cm^{-1} (Fo_{75}^{top}(qt)), or the peak at 855 cm^{-1} (Fo_{75}^{M2}) split into the bands at 892 and 920 cm^{-1} (Fo_{75}^{top}(qt)).

3.1.5. Final Remarks

The bulk forsterite (Mg_2SiO_4) and the corresponding nonpolar (010), (001) and (110) surfaces, and the Fe-containing $Mg_{1.5}Fe_{0.5}SiO_4$ olivinic system (25% of Fe substitution) and the corresponding crystalline nonpolar (010) surfaces have been simulated and their structural, electronic and vibrational features have been analysed in detail. The optimized structural parameters reproduce fairly well the crystallographic data for the bulk forsterite, the calculated cell parameters being slightly overestimated. Reconstruction of all the surfaces is minor and mainly corresponds to the shortening of the outermost Mg–O bond distances because the Mg^{2+} cations at these positions are coordinatively unsaturated centres. There is a good agreement of the calculated IR and reflectance spectra and dielectric values of forsterite bulk with the experimental ones. Comparison of the different IR indicates that: i) IR spectra of the surface slab models are shifted to upper values with respect to the corresponding bulk one as a consequence of the coordinatively unsaturated Mg^{2+} present at the outermost positions of the slab models, which sport shorter Mg–O distances, and ii) bands present in the IR spectra of the bulk systems split in the respective surface ones because of the different vibrational signatures of the Mg and SiO_4 groups present at the slab edge layers. The computed reflectance spectra show a remarkable agreement with the experimental data, characterizing the vast majority of signals.

In the $(Mg,Fe)_2SiO_4$ systems, the Fe^{2+} substitutions induce an overall enlargement of the bulk structure compared to bulk forsterite because of its larger ionic radius. The shortening of the uppermost metal-O bond distances in the surface reconstruction process is slight and mainly due to the coordinatively unsaturated metal centres. Relative energy calculations and the calculated surface energies for different Fe^{2+}-electronic states indicate that the most stable Fe-containing surfaces have the metal cations in the quintet state, followed by the triplet and the singlet states. Moreover, limited to the Fe^{2+}-quintet state, those surfaces with the cations placed at the outermost positions of the slab are more stable than those placed in more internal positions. The simulated IR spectra of the Fe-containing bulk system and the corresponding surfaces present associated bands in agreement with the Mg-pure forsterite systems. Comparison of the different IR features indicates that Fe^{2+}substitution induce an overall bathochromic shift of the spectra compared to the Mg-pure ones because of the larger atomic mass of Fe.

3.2. H Adsorption and H_2 Formation on (010) Mg_2SiO_4 Surface

Once some physicochemical properties of olivinic surfaces have been theoretically characterized [245], here the adsorption of one and two H atoms and their subsequent combination to form molecular hydrogen on the most stable forsterite (010) crystalline surface is studied.

3.2.1. Adsorption of One H Atom

B3LYP-D2* optimized complexes for the adsorption of one H atom on Fo(010) are shown in Figure 3.14. Table 3.10 reports the adsorption energies calculated at the different B1 and B2 basis sets and Table 3.11 the adsorption energies, the charge and spin densities of adducts using different DFT methods.

Three different complexes have been found which, according to the calculated adsorption energies, can be categorized as physisorption (010–Mg1 and 010–Mg2) and chemisorption (010–O1). In 010–Mg1, the H atom is nearly on the bare Mg and on the centre of a triangle defined by three oxygen surface atoms; in 010–Mg2, the H atom is interacting with one coordinatively unsaturated Mg atom; and in 010–O1, the H atom is chemically bonded with an O atom, hence forming a surface silanol (SiOH) group. For 010–Mg1 and 010–Mg2, the spin density is almost entirely localized on the H atom, whereas for 010–O1 is on the unsaturated neighbouring Mg atom, the H atom having a character of H^+ (see Table 3.11 for details). The trend for the calculated B3LYP-D2* adsorption energies is, from more to less favourable: 010–O1 > 010–Mg2 > 010–Mg1 (see Table 3.10). The contribution of the dispersive forces (term $\Delta E_{\mathrm{D2*}}$ of Table 3.10) is larger in 010–Mg1 (by about the 55% of the total adsorption energy) than in 010–Mg2 and 010–O1 (13% and 2%, respectively). The higher dispersion contribution in 010–Mg1 compared to 010–Mg2 is basically due to a higher number of intermolecular contacts between the adsorbed H and the forsterite surface atoms. The inclusion of the zero-point energy (ZPE) corrections is mandatory as it causes a lowering of the adsorption energies by about 30–50%, but thermal and entropic corrections do not affect the adsorption energies because of the very low temperatures ($\Delta U_0^C \approx \Delta G_T^C$).

From a methodological point of view it is worth highlighting that, for a given adsorption state, the calculated adsorption energies at B2 and B2//B1 are very similar (difference of 0.3 kcal mol^{-1}, at the most) and have similar BSSE values, whereas at B1 the BSSE is about twice as large as that at B2. This indicates that calculations at B2//B1 provide accurate results at a reasonable computational cost. Adsorption energies calculated using different DFT methods on the optimized B3LYP-D2* structures (see Table 3.11) vary compared to those obtained using the default B3LYP-D2* method. It results that for the B-LYP family the larger stability of 010–Mg2 with respect to 010–Mg1 decreases with the amount of exact exchange to the point that at BHLYP-D2* 010–Mg2 is less stable than 010–Mg1, *i.e.*, the (010–Mg2)–(010–Mg1) relative energies are −2.0, −1.0 and +0.6 kcal mol^{-1}, at BLYP-D2*, B3LYP-D2* and BHLYP-D2*, respectively. This trend is in agreement with the fact that spin density is more delocalized at 010–Mg2, a situation that is overstabilized with GGA functionals due to the self-interaction error.

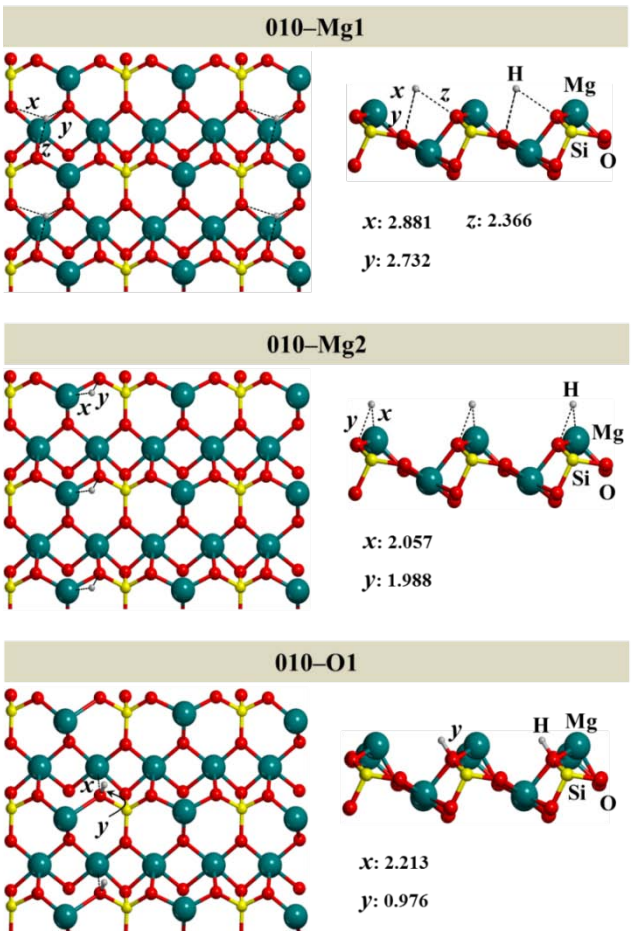

Figure 3.14 B3LYP-D2* optimized geometries (*x*, *y* and *z* distances in Å) of the different complexes for the H adsorption on the (010) Mg_2SiO_4 surface model (010–Mg1, 010–Mg2 and 010–O1). Left: top view of adducts. Right: lateral view of a surface fragment.

Table 3.10 *Computed adsorption energies (in kcal mol^{-1}) of one H atom for the different 010–Mg1, 010–Mg2 and 010–O1 adducts at the B3LYP-D2*/B1, B3LYP-D2*/B2//B3LYP-D2*/B1 and B3LYP-D2*/B2 levels of theory. B3LYP BSSE uncorrected adsorption energy (ΔE_{el}); contribution of dispersion to the adsorption energy (ΔE_{D2^*}); B3LYP-D2* BSSE uncorrected adsorption energy ($\Delta E = \Delta E_{el} + \Delta E_{D2^*}$); BSSE corrected adsorption energy ($\Delta E^C = \Delta E + BSSE$); zero-point energy corrected adsorption energy ($\Delta U_0^C = \Delta E^C + \Delta ZPE$) and corrected adsorption free energy (ΔG_{10K}^C and ΔG_{100K}^C).*

Reaction	Level	ΔE_{el}	ΔE_{D2^*}	ΔE	ΔE^C	ΔU_0^C	ΔG_{10K}^C	ΔG_{100K}^C
Fo(010) + H → 010–Mg1	B1	-1.7	-1.6	-3.3	-1.9	-0.8	-0.8	-0.8
	B2//B1	-1.7	-1.6	-3.3	-2.7	-1.6	-1.6	-1.6
	B2	-1.8	-1.5	-3.4	-2.7	-1.7	-1.7	-1.7
Fo(010) + H → 010–Mg2	B1	-3.8	-0.6	-4.3	-3.2	-1.5	-1.5	-1.5
	B2//B1	-3.7	-0.6	-4.3	-3.8	-2.1	-2.1	-2.1
	B2	-3.6	-0.5	-4.1	-3.7	-1.9	-1.9	-1.9
Fo(010) + H → 010–O1	B1	-15.5	-0.1	-15.6	-12.5	-6.1	-6.1	-6.1
	B2//B1	-16.6	-0.1	-16.7	-15.4	-9.0	-9.0	-9.0
	B2	-16.3	-0.3	-16.5	-15.1	-9.0	-9.0	-9.0

Table 3.11 *BSSE uncorrected adsorption energies (ΔE, in kcal mol^{-1}), net charges and electronic spin densities on the H atom, on the Mg atom closest to H, and the sum of spin density values of the O atoms closest to H for the H/Fo(010) adducts optimized at the B3LYP-D2*/B2//B3LYP-D2*/B1 level.*

			Charge			Spin		
Method	Adduct	Δ*E*	H	Mg	O	H	Mg	O
PBE-D2*	010–Mg1	-4.3	+0.02	+0.83	-1.01	0.86	0.10	0.04
	010–Mg2	-5.0	+0.00	+0.80	-0.97	0.71	0.09	0.20
	010–O1	-18.7	+0.31	+0.33	-0.90	0.03	0.91	0.06
BLYP-D2*	010–Mg1	-3.0	+0.00	+0.88	-1.04	0.84	0.10	0.06
	010–Mg2	-5.0	-0.03	+0.84	-1.00	0.69	0.11	0.20
	010–O1	-15.8	+0.29	+0.38	-0.92	0.03	0.89	0.08
B3LYP-D2*	010–Mg1	-3.3	+0.02	+0.96	-1.10	0.88	0.08	0.04
	010–Mg2	-4.3	-0.01	+0.92	-1.07	0.73	0.07	0.20
	010–O1	-16.7	+0.32	+0.41	-0.98	0.02	0.92	0.06
BHLYP-D2*	010–Mg1	-2.5	+0.02	+1.08	-1.18	0.91	0.06	0.03
	010–Mg2	-1.9	+0.00	+1.03	-1.15	0.78	0.05	0.17
	010–O1	-15.2	+0.34	+0.47	-1.05	0.01	0.95	0.04

Figure 3.15a shows the ZPE-correction energy profiles for the conversion of the 010–Mg1 and 010–Mg2 physisorbed configurations into the 010–O1 chemisorbed state following the 010–Mg1 → 010–Mg2 → 010–O1 path. The conversion from 010–Mg1 to 010–Mg2 involves the diffusion of the H atom on the Mg atom, whereas from 010–Mg2 to 010–O1 it involves the formation of a surface O–H bond at the expense of the partial breaking of the outermost Mg–O bond. As expected, the computed energy barrier of the first step is lower than the second one (4.1 and 6.4 kcal mol^{-1}, respectively) since the latter involves bond breakings and formation. However, the calculated transition structures are higher in energy than the Fo(010) + H asymptote, thus indicating that the jump from one site to another may occur through H desorption–adsorption steps rather than *via* surface diffusion. To delve deeper into this point, localization of transition structures connecting Fo(010) + H with the adsorbed states has been attempted. For 010–Mg1 and 010–Mg2, no transition structures have been found; *i.e.*, calculations show a continuous increase of energy up to a plateau with the increasing Fo(010)–H distance. In contrast, a transition structure for 010–O1 has indeed been found with an energy barrier of 6.0 kcal mol^{-1} (see Figure 3.15b) very close to the value obtained on passing from 010–Mg2 to 010–O1 (see Figure 3.15a).

The barrier computed for passing from the physisorbed 010–Mg2 structure to the chemisorbed state 010–O1 is 6.4 kcal mol^{-1}, significantly higher than the value of 1.7 kcal mol^{-1} computed by Kerkeni and Bromley on the forsterite nanoclusters [105] and of that of 2.4 kcal mol^{-1} reported by Goumans *et al.* [109] for the embedded cluster method. These differences may well be due to the different computational approaches, both in the DFT method adopted (mPWB1K functional) and the way how the surface is modelled.

Any attempt to locate other adsorption sites by starting the optimization process with the H atom closer to a different oxygen atom or on top of Mg ions simply gave 010–Mg1, 010–Mg2 or 010–O1 as final products. This is somehow at variance with the work by Sidis *et al.* [107] in which H was predicted to remain attached to a second less exposed oxygen atom as well as with the results by Downing *et al.* [108], in which H was predicted to chemisorb also at the surface Mg ion. Nevertheless, for both cases the adsorption was much less favourable than for the cases also (and only) found in the present work.

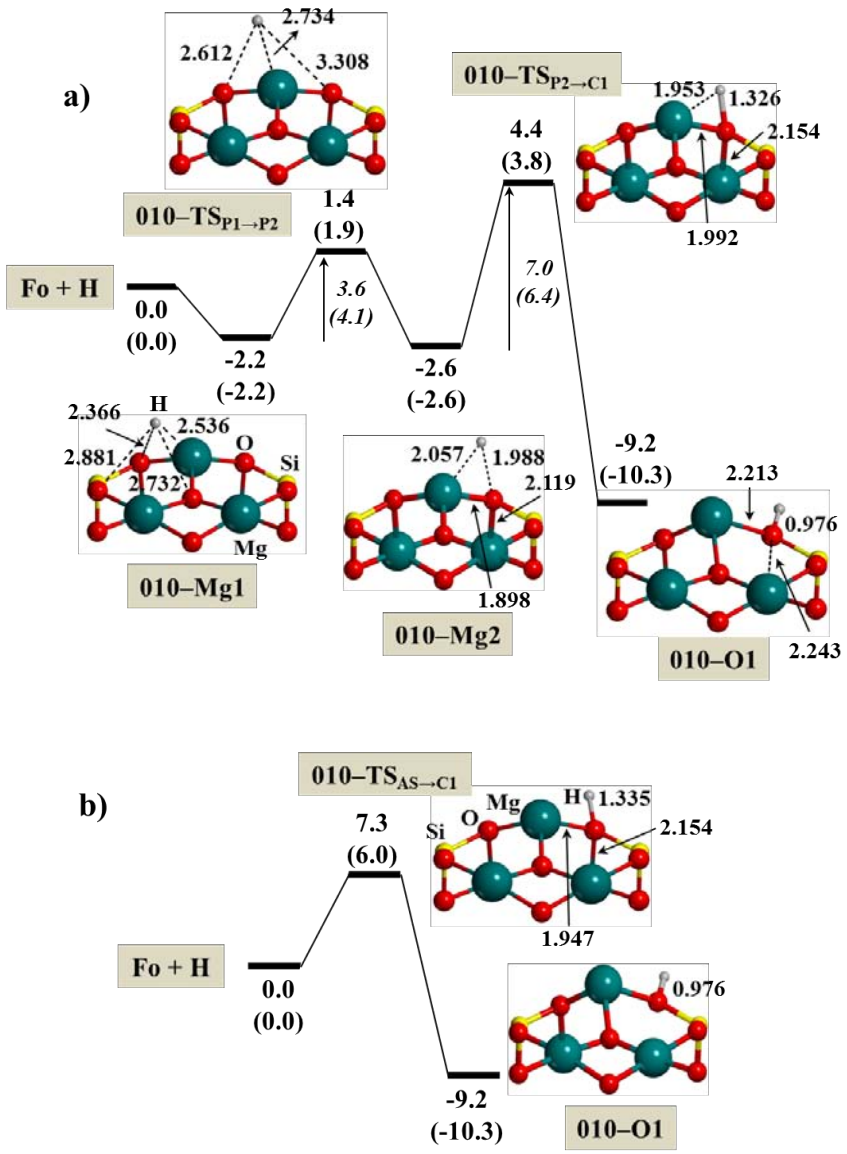

Figure 3.15 B3LYP-D2* energy profiles including zero-point energy corrections for: (a) the inter-conversion between the different adsorption states adopting a 010–Mg1 → 010–Mg2 → 010–O1 sequence; and (b) direct H adsorption to form 010–O1 (bond distances in Å and energies in kcal mol^{-1}). Relative energies are referenced with respect to the Fo(010) + H zero-energy asymptote. Bare values calculated at B1; in parentheses at B2//B1.

Present results can be compared to the experimental measurements reported in the classical work by Vidali and Pirronello [246]. They extracted energy values from thermal desorption experiments (TPD) giving both the physisorbed H desorption energy and the barrier height for H jumping from one site to the next neighbour. As the formal treatment of TPD data corresponds to an Arrhenius equation their desorption energy data E_a should be transformed to enthalpy values before being compared to the computed ones [200]. The experimental and computed enthalpy of desorption ΔH_d are:

$$\Delta H_d = E_a - RT \quad \text{(from experiment)} \tag{3.3}$$

$$\Delta H_d = -\Delta E^C - \Delta E(ZPE) - \Delta E(T) + RT = -\Delta U^C - \Delta E(T) + RT \quad \text{(from theory)} \tag{3.4}$$

in which E_a is the experimental desorption energy resulting from the Arrhenius equation, $-\Delta E^C$ is the purely BSSE-corrected electronic desorption energy, $-\Delta U^C$ is the desorption energy inclusive of zero-point energy correction and $-\Delta E(T)$ is the thermal correction to bring ΔU^C to the actual T (from 10 to 100 K). It can be shown that $-\Delta E(T)$ is less than 0.05 kcal mol^{-1} while RT is 0.02 kcal mol^{-1} at 10 K and ten times higher at T = 100 K. Using data from Table 3.10 we arrive at our best estimate of ΔH_d = 1.8 kcal mol^{-1} (900 K) at the experimental temperature of 10 K. The datum obtained from the experimental TPD measurements [246] is 0.6 kcal mol^{-1} (318 K), three times smaller than our best estimate. Theoretical studies described in Chapter 1 report data which are also higher than the experimental datum. As none of these data have been corrected for ZPE and thermal effects we use our electronic ΔE^C = 2.7 kcal mol^{-1} value for comparison, which corresponds of ΔH_d = 1.8 kcal mol^{-1} discussed above. Goumans *et al.* [109] computed 2.5 kcal mol^{-1}, Sidis *et al.* [107] a value of 3.2 kcal mol^{-1}, Kerkeni and Bromley [105] a range of values between 1.4 and 5.8 kcal mol^{-1} as a function of the adsorption cluster site.

Analysis of the contribution to the physisorption energy reveals that dispersion contribution is in the 0.5–1.6 kcal mol^{-1} range and cannot be ignored. The sensitivity of the physisorption to the adopted functional is addressed in Table 3.11, in which the 010–Mg2 desorption energy (not accounting for BSSE) moves from 1.9 (BHLYP-D2*) up to 5.0 (PBE-D2*) kcal mol^{-1}. To reconcile experimental data with the computed one Goumans *et al.* [109] invoked the possible role of surface hydroxylation in the experiment which heals the active sites of forsterite. While that can be the case, our data show that different functionals may play a significant role in changing the physisorption value, which imposes some caution when using DFT for computing very weak interactions in open-shell systems. The computed value of the kinetic barrier for H jump between physisorbed sites was 4.1 kcal mol^{-1} (see Figure 3.15), much higher than the experimental datum reported by Katz *et al.* [246] of only 0.57 kcal mol^{-1}. Goumans *et al.* [109] computed a value of 1.6 kcal mol^{-1} while Kerkeni and Bromley [105] computed a range between 0.14 and 4.8 kcal mol^{-1} as a function of the considered path on the heterogeneous cluster surface, using both the mPWB1K functional.

3.2.2. Temperature Effects in the Diffusion of Atomic Hydrogen

This section has been developed in collaboration with Prof. Angelos Michaelides at the London Centre for Nanotechnology of the University College London in a predoctoral short visit of three months. The visit aimed to simulate the H diffusion from a physisorption to a chemisorption state on the (010) Mg_2SiO_4 surface taking into account dynamic and tunnelling effects, in order to have a more detailed description of the H hopping process. The main goal of my stay at the laboratory of Prof. Michaelides was to apply Path Integral Molecular Dynamics (PIMD) to incorporate quantum nuclear effects into molecular dynamics simulations using Feynman path integrals with the CP2K code. However, the high computational cost of PIMD, alongside the current technical difficulties with this code to carry out free-energy profiles (including tunnelling effects) using collective variables (such as thermodynamic integration), made this study impossible. Thus, the study was in the end focused on analysing the dynamic effects of this H hopping at different temperatures.

Bearing in mind that the computed potential-energy barrier may be relatively high to account for a proper diffusion of H atom, dynamic effects in the range of temperatures of diffuse clouds (*i.e.*, 100 K and 10 K) were considered to assess the influence of temperature on the free-energy profiles. Thus, different AIMD simulations at these two temperatures have been carried out for the 010–Mg2 → 010–O1 H hopping. The classical free-energy profile along the physisorption–chemisorption path obtained with classical-nucleus AIMD simulations at the two different temperatures adopting the thermodynamic integration approach (see Section 2.5.2) is shown in Figure 3.16. The error bars denote the standard deviation obtained from a block-averaging procedure which eliminates statistical correlations between simulations snapshots.

The calculated free-energy data for the H hopping are provided in Table 3.12. The relative stability (in terms of Helmholtz free energies) of 010–O1 with respect of 010–Mg2 at 100 K is 13.9 kcal mol^{-1} and at 10 K is 13.4 kcal mol^{-1}. By means of static calculations and only taking the ZPE corrections into account[1] the energy difference is 15.2 kcal mol^{-1}. These results indicate that inclusion of dynamic effects reduces the difference of stabilities by about 12 %. The computed free-energy barriers at 100 K and at 10 K are 1.0 and 0.8

[1] The value of 15.2 kcal mol^{-1} was calculated by optimizing both structures within the same methodology, *i.e.*, at PBE-D2 level with CP2K.

kcal mol^{-1}, respectively, which are lower than that computed by static calculations and corrected by ZPE terms (2.1 kcal mol^{-1}). Although the energetic differences are small, dynamic effects at these temperatures are significantly of relevance since such differences decrease the energy barrier up to 62%. This is relatively important when considering classical rate constants, as on finds variations up to two orders of magnitude higher at 100 and 10 K than with static consideration ($k_{100K}^{TST} \approx k_{10K}^{TST} > k_{static}^{TST}$).

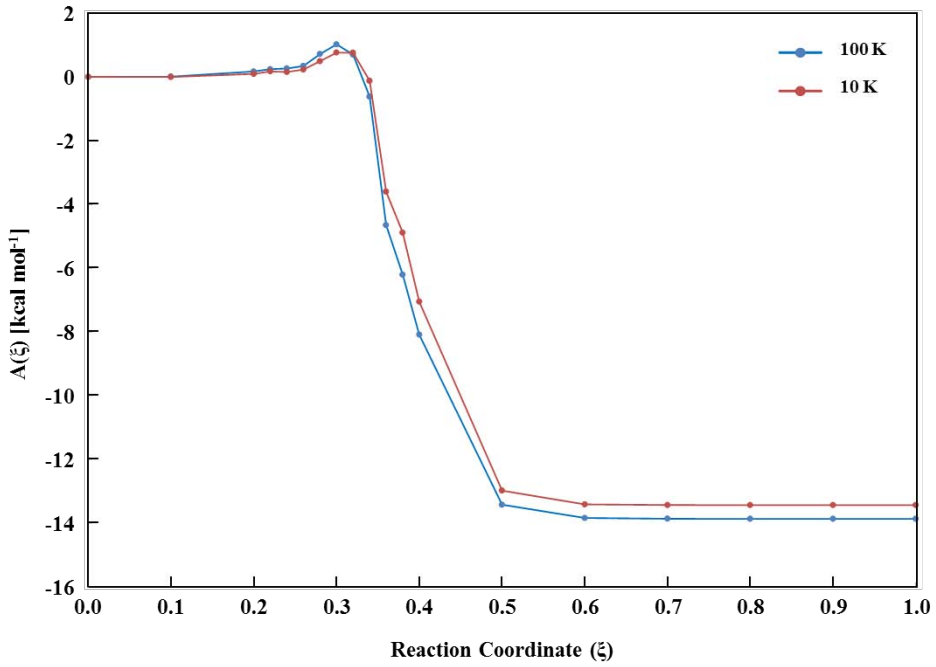

Figure 3.16 Free-energy profiles for H diffusion from 010–Mg2 to 010–O1 adsorption sites.

Table 3.12 *Relative Helmholtz free energies (in kcal mol^{-1}) and the associated relative error (in terms of per 100), computed Helmholtz free-energy barriers (in kcal mol^{-1}) and the associated relative error (in terms of per 100) and rate constant according to the classical formulation of the TST (in s^{-1}) for the different calculations of the H diffusion process.*

T	ΔA_{rel}	$\delta(\Delta A_{rel})$	$\Delta A^{\ddagger}$	$\delta(\Delta A^{\ddagger})$	k_T^{TST}
100	13.9	8.6	1.0	52.4	1.1×10^{11}
10	13.4	11.8	0.8	61.9	2.1×10^{11}
Static	15.2	0	2.1	0	2.7×10^{9}

Finally, it is worth mentioning that AIMD simulations at 300 K without any restriction were also performed. Simulations show a spontaneous conversion from the 010–Mg2 to the 010–O1 state, while at 100 K the process does not occur, indicating that at this temperature both states are stable and the H atom remains around its equilibrium geometry.

3.2.3. Adsorption of a Second H Atom

To simulate the formation of the H_2 molecule on the forsterite surface through a Langmuir–Hinshelwood mechanism, the adsorption of a second H atom onto the 010–Mg1, 010–Mg2 and 010–O1 adducts has firstly been studied. Figure 3.17 shows the B3LYP-D2* optimized adducts and Table 3.13 the calculated reaction energies for the global H adsorption processes.

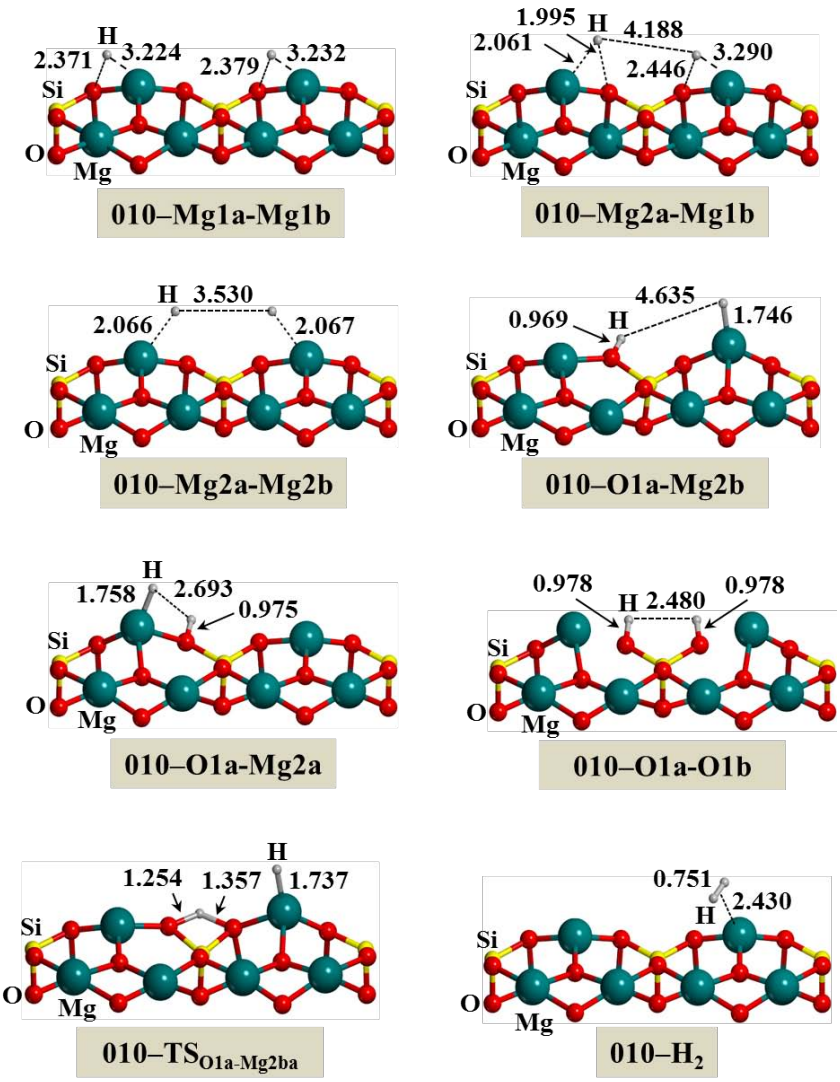

Figure 3.17 B3LYP-D2* optimized geometries of the different complexes derived from a second H adsorption on the (010) Mg_2SiO_4 surface model (010–Mg1a-Mg1b, 010–Mg2a-Mg1b, 010–Mg2a-Mg2b, 010–O1a-Mg2b, 010–O1a-Mg2a and 010–O1a-O1b), for the adsorption of a H_2 molecule (010–H_2) and for the transition state converting 010–O1a-Mg2b into 010–O1a-Mg2a (010–$TS_{O1a–Mg2ba}$). Bond distances are in Å.

Since the adopted unit cell includes two equivalent but symmetry independent "Mg–O_3" moieties (*a* and *b* depending on the considered left or right side, respectively), a total of 9 initial guess adducts were possible: (i) three with the H atoms adopting the same adsorption state at the different "Mg–O_3" moieties (*i.e.*, 010–Mg1a-Mg1b, 010–Mg2a-Mg2b and 010–O1a-O1b); (ii) three derived from the combination of the 010–Mg1, 010–Mg2 and 010–O1 adsorption states at the different "Mg–O_3" moieties (*i.e.*, 010–O1a-Mg1b, 010–O1a-Mg2b and 010–Mg2a-Mg1b); and (iii) three more derived from the combination of 010–Mg1, 010–Mg2 and 010–O1 at the same "Mg–O_3" moiety (*i.e.*, 010–O1a-Mg1a, 010–O1a-Mg2a and 010–Mg2a-Mg1a). For all these di-adsorptions, the initial guess orbitals corresponded to a broken symmetry solution. Geometry optimizations resulted in 6 different complexes (see Figure 3.17). The initial 010–Mg2a-Mg1b and 010–Mg2a-Mg1a structures converged into the same adduct (structure 010–Mg2a-Mg1b of Figure 3.17) and the 010–O1a-Mg1b and 010–O1a-Mg1a complexes evolve toward the spontaneous H_2 formation (010–H_2 adduct, shown at the bottom of Figure 3.17).

Table 3.13 *B3LYP-D2* reaction energies (in kcal mol^{-1}) calculated at B1 and B2//B1 levels for the global H adsorption processes on Fo(010) to form the 010–Mg1a-Mg1b, 010–Mg2a-Mg1b, 010–Mg2a-Mg2b, 010–O1a-Mg2b, 010–O1a-Mg2a and 010–O1a-O1b complexes. Uncorrected (ΔE), BSSE corrected (ΔE^C) and zero-point energy corrected (ΔU_0^C) adsorption energies.*

Reaction	Level	ΔE	ΔE^C	ΔU_0^C
Fo(010) + 2H → 010–Mg1a-Mg1b	B1	-6.4	-3.8	-2.0
	B2//B1	-6.7	-5.6	-3.8
Fo(010) + 2H → 010–Mg2a-Mg1b	B1	-7.4	-5.0	-2.5
	B2//B1	-7.5	-6.6	-4.0
Fo(010) + 2H → 010–Mg2a-Mg2b	B1	-8.2	-6.1	-2.8
	B2//B1	-8.2	-7.4	-4.2
Fo(010) + 2H → 010–O1a-Mg2b	B1	-79.5	-75.5	-65.7
	B2//B1	-81.1	-80.6	-70.8
Fo(010) + 2H → 010–O1a-Mg2a	B1	-97.9	-93.9	-84.0
	B2//B1	-99.1	-97.5	-87.7
Fo(010) + 2H → 010–O1a-O1b	B1	-18.4	-12.7	-1.0
	B2//B1	-20.6	-18.1	-6.5
Fo(010) + 2H → 010–H_2	B1	-115.7	-113.5	-105.0
	B2//B1	-115.1	-114.4	-105.8

As one can see in Table 3.13, the 010–O1a-Mg2b and 010–O1–Mg2b complexes are the most stable ones (BSSE-corrected adsorption energies including ZPE-corrections, ΔU_0^C, being −70.8 and −87.7 kcal mol^{-1}, respectively). This is because these adducts contain both a hydride and a proton, which arise from the Mg–H and the Si–OH groups, respectively as first pointed out by Goumans *et al* [109]. These complexes are formed because in 010–O1 the unpaired electron is almost entirely localized on the bare Mg atom (see Table 3.11), thereby having a large propensity to receive the second H atom to form an Mg^+–H^- hydride. The larger stability of 010–O1a-Mg2a with respect to 010–O1a-Mg2b is due to the favourable electrostatic interaction between the two H atoms, respectively with a H^-/H^+ character due to the bond with Mg/O ions (Mulliken net charges of these H atoms are −0.33/+0.33|e|, respectively, see Appendix A). The 010–Mg1a-Mg1b, 010–Mg2a-Mg1b and 010–Mg2a-Mg2b adducts give ΔU_0^C values of about −4 kcal mol^{-1}, in which the spin densities are on the H atoms (with opposite signs, see Appendix A). For the 010–O1a-O1b complex, the adsorption of the second H atom is less favourable (ΔU_0^C = -6.5 kcal mol^{-1}) because of the formation of a surface geminal Si–$(OH)_2$ group resulted from the breaking of two Mg–O surface bonds (see structure 010–O1a-O1b of Figure 3.17). In this case, the spin densities are located on the bare Mg atoms with opposite signs, about −0.85/+0.85|e| (see Appendix A).

3.2.4. H_2 Formation

From the doubly H-adsorbed adducts, the recombination of the H ad-atoms to form a H_2 molecule has been studied. The B3LYP-D2* reaction energies are listed in Table 3.14 and energy profiles including ZPE-corrections with respect to the Fo(010) + 2H asymptote are shown in Figure 3.18 and Figure 3.19. The adsorption of H_2 on Fo(010) takes place through the outermost Mg atom (see 010–H_2 of Figure 3.17). In the complex, H_2 is weakly bound to the surface (ΔU_0 of -2.8 kcal mol^{-1}), with dispersion contributing to nearly 31%. Despite this weak interaction, the reaction energy for the H_2 formation is very large and negative (about −107 kcal mol^{-1}), in agreement with the high nascent energy associated with the H_2 molecule formation.

Table 3.14 *B3LYP-D2* reaction energies (in kcal mol^{-1}) calculated at B1 and B2//B1 levels for the H_2 formation from the 2H/Fo(010) complexes on Fo(010). Uncorrected (ΔE), BSSE corrected (ΔE^C) and zero-point energy corrected (ΔU_0^C) adsorption energies.*

Reaction	Level	ΔE	ΔE^C	ΔU_0^C
010–Mg2a-Mg1b → 010–H_2	B1	-108.3	-108.5	-102.5
	B2//B1	-107.6	-107.8	-101.8
010–Mg2a-Mg2b → 010–H_2	B1	-107.5	-107.4	-102.2
	B2//B1	-106.9	-107.0	-101.6
010–O1a-Mg2b → 010–H_2	B1	-36.2	-38.0	-39.3
	B2//B1	-34.0	-33.8	-35.0
010–O1a-Mg2a → 010–H_2	B1	-17.8	-19.6	-21.0
	B2//B1	-16.0	-16.9	-18.1
010–O1a-O1b → 010–H_2	B1	-97.3	-100.8	-104.0
	B2//B1	-94.5	-96.3	-99.3

Not surprisingly, the H_2 formation when the two H atoms are physisorbed on Fo(010) (*i.e.*, 010–Mg2a-Mg1b and 010–Mg2a-Mg2b) exhibits very large and negative reaction energies (around –102 kcal mol^{-1}, see Table 3.14) and very low energy barriers (less than 1 kcal mol^{-1}, see Figure 3.18) as this process envisages a radical–radical reaction, thus suggesting that the Langmuir–Hinshelwood mechanism is feasible. It is worth mentioning that any attempt to find a reaction from the 010–Mg1a-Mg1b complex failed, since the located transition structures collapsed on the 010–$TS_{Mg2a\text{-}Mg1b\rightarrow H2}$ structure (the same for the 010–Mg2a-Mg1b complex) meaning that, previous to the H_2 formation, a conversion of the 010–Mg1a-Mg1b complex into 010–Mg2a-Mg1b should take place.

The H_2 formation channels when at least one of the H atoms is chemisorbed were found to have lower reaction energies and higher energy barriers (see Table 3.14 and Figure 3.19, respectively) compared to those for the physisorbed states. However, from the 010–O1a-Mg2a adduct, the obtained reaction energy is –18.1 kcal mol^{-1} (the lowest one, see Table 3.14) and calculated energy barrier is 1.7 kcal mol^{-1} (see Figure 3.19b). This is because it is the most stable complex and the H recombination is between the neighbouring H^- and H^+ atoms belonging to the surface Mg–H and SiOH groups, respectively (*vide supra*). Despite the fact that the very same $H^-\cdots H^+$ coupling might occur for the 010–O1a-Mg2b, the reaction presents a reaction energy and energy barrier of –35.0 and 23 kcal mol^{-1},

respectively (see Table 3.14 and Figure 3.19a). This increment in the energy barrier is caused by the need of breaking the Mg–H bond in order to bring the two H atoms in close proximity. We have also checked whether the H of 010–O1a-Mg2b can first evolve towards 010–O1a-Mg2a (see $TS_{O1a–Mg2ba}$ of Figure 3.17) but a barrier as high as 18.3 kcal mol^{-1} is needed for this reaction, preventing any significant occurrence of this process. Finally, the H_2 formation from the 010–O1a-O1b complex yields a reaction energy of -99.3 kcal mol^{-1} (see Table 3.14) and exhibits the highest energy barrier (about 35 kcal mol^{-1}, see Figure 3.19c) since this recombination involves the coupling of two H^+ atoms that belong to the surface geminal $Si(OH)_2$ group.

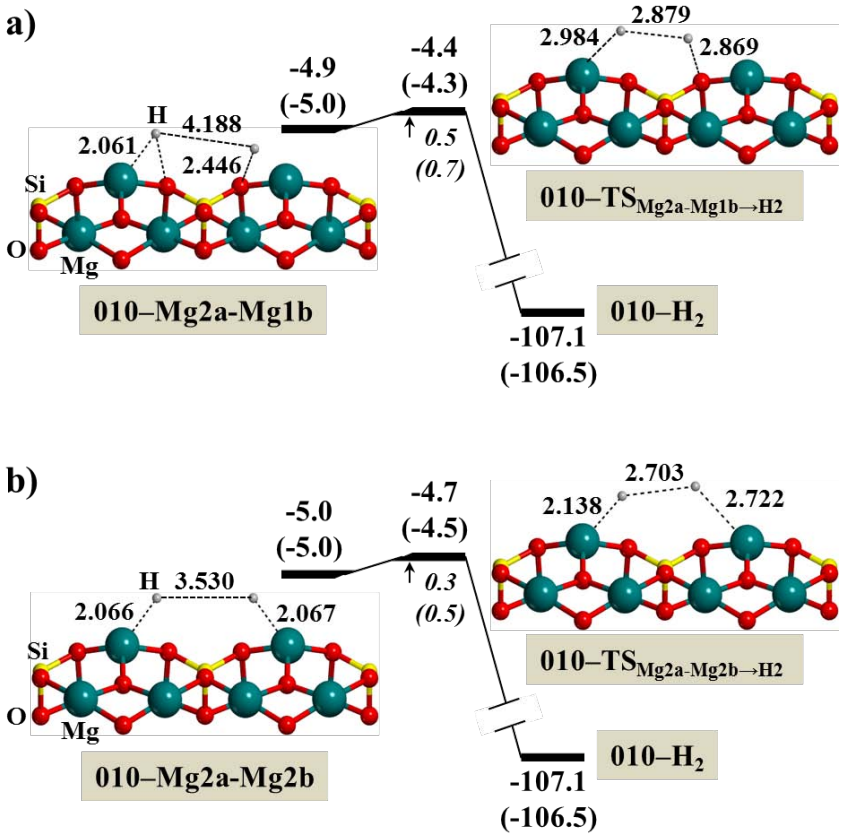

Figure 3.18 B3LYP-D2* energy profiles including zero-point energy corrections (in kcal mol^{-1}) for the recombination of two physisorbed H atoms to form H_2 on the (010) Mg_2SiO_4 surface model. Relative energies are referenced with respect to the Fo(010) + 2H zero-energy asymptote. Bare values calculated at B1; in parentheses at B2//B1.

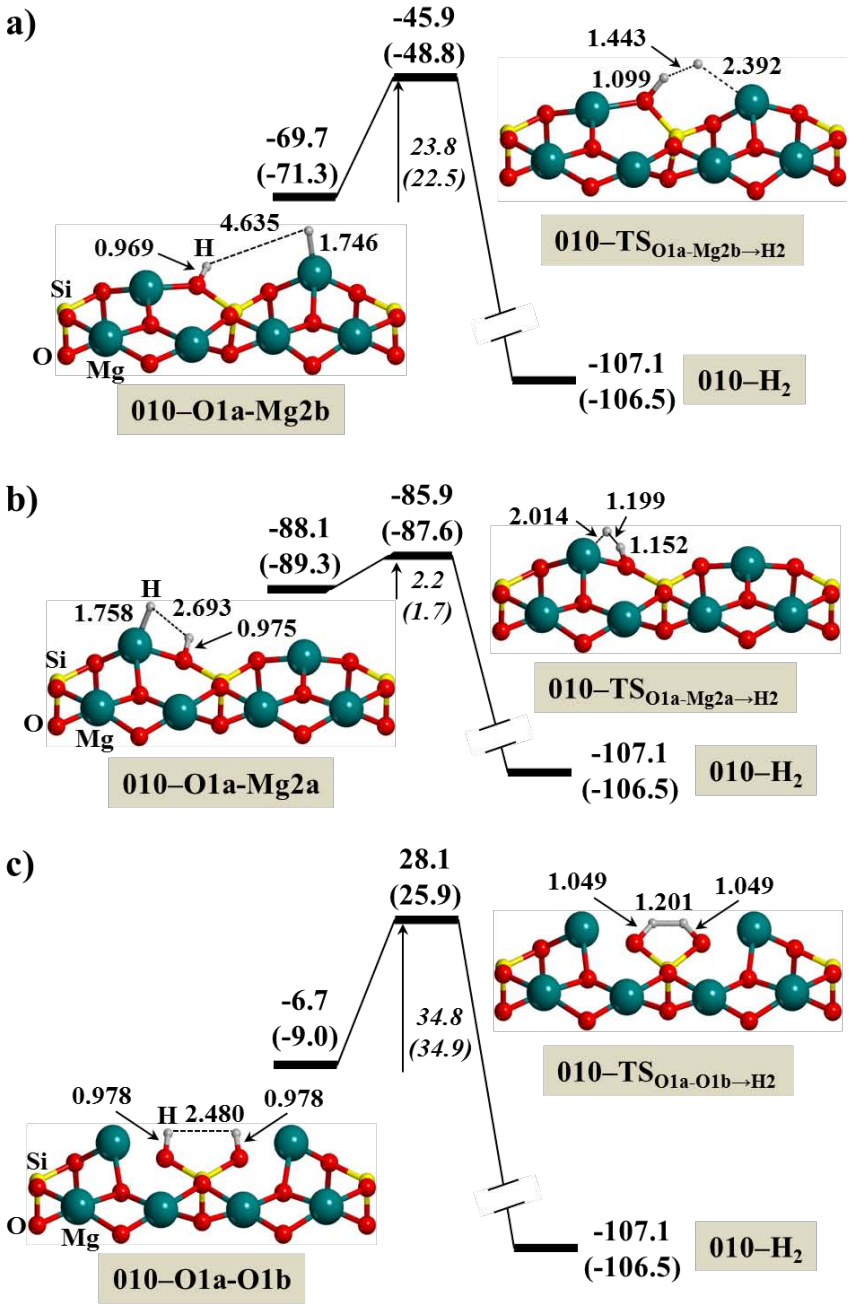

Figure 3.19 B3LYP-D2* energy profiles including zero-point energy corrections (in kcal mol^{-1}) for the recombination of two H atoms to form H_2 on the (010) Mg_2SiO_4 surface model when at least one H atom is chemisorbed. Relative energies are referenced with respect to the Fo(010) + 2H zero-energy asymptote. Bare values calculated at B1; in parentheses at B2//B1.

The present results are at variance from the data obtained by Goumans *et al.* [109], as they computed a much higher barrier of 11.1 kcal mol^{-1} for the same recombination process of the two chemisorbed H atoms. Compared to our value of 1.7 kcal mol^{-1} starting from the 010–O1a-Mg2a adduct, possible explanations for this difference may be their use of the embedded cluster approach, allowing more flexibility to the system, the absence of ZPE

corrections or the DFT method employed (mPWB1K functional). Comparison with barriers computed by Kerkeni and Bromley [105] is less straightforward as they adopted the $(MgO)_6(SiO_2)_3$ nanocluster, resulting in a rather large range of values spanning the 1.4–21.2 kcal mol^{-1} interval as a function of the H attachment sites. Nevertheless, our barrier is compatible with their smallest barrier value of 1.4 kcal mol^{-1} resulting from the H_2 formation starting from structure 4a of Ref. [105].

3.2.5. Final Remarks

On the crystalline (010) surface of Mg_2SiO_4 forsterite, H physisorption is barrierless and exclusively occurs either on the most exposed Mg ions (010–Mg1 and 010–Mg2), with a ZPE-corrected adsorption energy of about -2 kcal mol^{-1}. The kinetic barrier for the hydrogen atom jump between the physisorption sites (*i.e.*, 010–Mg1 → 010–Mg2) is 4.1 kcal mol^{-1}, implying that H diffusion is limited at the low temperatures found in the ISM and H can only displace on the surface through adsorption–desorption steps. The formation of the chemisorbed state 010–O1 is characterized by a ZPE-corrected adsorption energy of -9.0 kcal mol^{-1} and a kinetic barrier from 010–Mg2 of 6.4 kcal mol^{-1} at the oxygen site or through the direct interaction of the H atom of 6.0 kcal mol^{-1}, with spin density entirely located at the nearby Mg ion.

A second H atom can be chemisorbed on an already reacted Fo(010) (the 010–O1 case) to form the most stable product 010–O1a-Mg2a, which envisages a vicinal $Si–OH^{(+)}/^{(-)}H–Mg$ ion-pair interaction. The H_2 formation at Fo(010) adopting a Langmuir–Hinshelwood mechanism starts either from two physisorbed H atoms (010–Mg2a-Mg1b and 010–Mg2a-Mg2b complexes) with an almost negligible kinetic barrier of 0.5 kcal mol^{-1} through a radical–radical coupling driven reaction, or from two chemisorbed H atoms as in the 010–O1a-Mg2a adduct with a barrier of 1.7 kcal mol^{-1}.

3.3. Influence of Surface Morphology: H_2 Formation on (001) and (110) Mg_2SiO_4 Surfaces

The primary cleavage plane of forsterite is the (010) surface and, as reported above, the H_2 formation on this surface has been studied in detail. However, the crystal morphology of Mg_2SiO_4 presents other extended surfaces. It is therefore interesting to study the H_2 formation also on these other crystal faces, which may exhibit different chemical activity compared to the (010) surface. In this section, the H adsorption and H_2 formation on the (001) and (110) crystalline surfaces, which are less stable than the (010), is presented. Comparison of the results from all cases provides a more complete scenario to elucidate the H_2 formation in the ISM environment.

3.3.1. Adsorption of One H Atom

Different adsorption states of H atom on the (001) and (110) surfaces has been explored. We have characterized five different H/Fo(001) adducts, two in which the H atom is interacting with the uppermost Mg atom (001–Mg1 and 001–Mg2) and three in which the H atom interacts with the most exposed O atoms (001–O1, 001–O2 and 001–O3), thus forming a surface silanol (SiOH) group; and six different H/Fo(110) adducts, two in which the interaction takes place through the outermost Mg atoms (110–Mg1 and 110–Mg2) and four through O atoms (110–O1, 110–O2, 110–O3 and 110–O4), forming the corresponding SiOH surface groups. Figure 3.20 displays the B3LYP-D2*/B1 optimized adducts for all these adsorptions on Fo(001) and Fo(110) slab models.

Computed adsorption energies calculated at B2//B1 theory level are reported in Table 3.15. Energy values calculated with both B1 and B2//B1 basis sets for all the processes described in this section are reported in the Appendix A. According to that, the most stable adduct on Fo(001) is 001–O3. The largest adsorption energies (values of ΔU_0 between -48 and -33 kcal mol^{-1}) are exhibited by the O-interacting systems, followed by 001–Mg1 (-11.1 kcal mol^{-1}) and by 001–Mg2 (-2.7 kcal mol^{-1}). It is worth mentioning that in 001–Mg1 and 001–O3, the outermost Mg atom displaces laterally giving rise to a different surface atomic distribution in the edge-layers. The Mulliken spin density for 001–Mg1 and 001–Mg2 is almost entirely localized on the nearest O atoms (+0.92|e| and +0.94|e|, respectively),

whereas for 001–O1, 001–O2 and 001–O3 it is on the neighbouring outermost Mg atom (+0.93|e|, +0.93|e| and +0.91|e|, respectively), indicating a H^+ character of the H ad-atom. Appendix A also includes the whole set of net Mulliken charges and spin densities for all considered adducts. Spin density values, as well as the O–H and H–Mg distances, indicate that all adducts are chemisorbed states. This is in contrast to that observed for Fo(010) [247], for which several physisorbed states with spin density located at the H atom and O···H and Mg···H distances larger than 2.0 Å were localized.

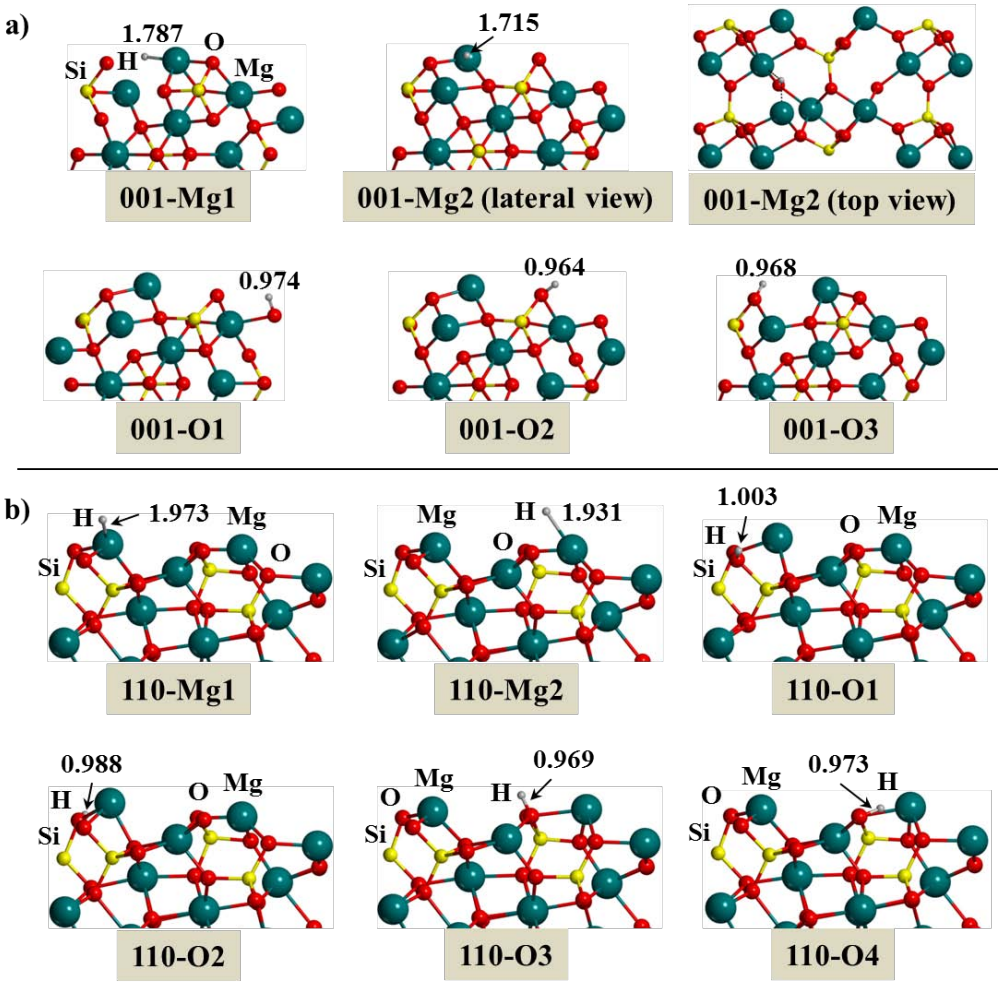

Figure 3.20 B3LYP-D2* optimized geometries of the different adducts resulting from the adsorption of one H atom (a) on the Fo(001) (001–Mg1, 001–Mg2, 001–O1, 001–O2 and 001–O3) and (b) on the Fo(110) (110–Mg1, 110–Mg2, 110–O1, 110–O2, 110–O3 and 110–O4). Bond distances in Å.

Physisorption resulted for all the Mg-interacting systems on Fo(110) (ΔU_0 = -3.8 and -5.8 kcal mol^{-1}, respectively, see Table 3.15), as the major fraction of the spin density is on the H atom (+0.64|e| and +0.61|e|, respectively) and the Mg–H distance (1.973 and 1.931 Å, respectively) is significantly larger than that determined for the chemisorbed 001–Mg1

(1.787 Å) and 001–Mg2 (1.715 Å) species. In contrast, chemisorption dominates the O-interacting systems (ΔU_0 = -30.6, -26.6, -27.4 and -41.2 kcal mol^{-1}, respectively) and the spin density basically lies on the adjacent Mg atoms (+0.92|e|, +0.93|e|, +0.91|e| and +0.85|e|, respectively).

Table 3.15 *B3LYP-D2* reaction energies (in kcal mol^{-1}) calculated at the B2//B1 level for the first H adsorption on Fo(001) to form the 001–Mg1, 001–Mg2, 001–O1, 001–O2 and 001–O3 adducts and on Fo(110) to form the 110–Mg1, 110–Mg2, 110–O1, 110–O2, 110–O3 and 110–O4 adducts. Uncorrected (ΔE) and zero-point energy corrected (ΔU_0) adsorption energy.*

Reaction	ΔE	ΔU_0
Fo(001) + H → 001–Mg1	-14.1	-11.1
Fo(001) + H → 001–Mg2	-6.7	-2.7
Fo(001) + H → 001–O1	-40.1	-33.0
Fo(001) + H → 001–O2	-51.5	-44.5
Fo(001) + H → 001–O3	-55.3	-48.4
Fo(110) + H → 110–Mg1	-6.0	-3.8
Fo(110) + H → 110–Mg2	-7.9	-5.8
Fo(110) + H → 110–O1	-37.0	-30.6
Fo(110) + H → 110–O2	-33.0	-26.6
Fo(110) + H → 110–O3	-34.0	-27.4
Fo(110) + H → 110–O4	-47.7	-41.2

Figure 3.21a shows the energy profile corresponding to the 001–Mg2 → 001–Mg1 → 001–O3 path (namely, from the less to the most stable adsorption sites). The first step involves the breaking of the Mg–O simultaneously associated with a rearrangement of the H atom on the Mg atom. The second step consists of an H jump from the Mg atom to the O atom. Figure 3.21b shows the energy profile for the H jumps that connect the different chemisorption states along the 001–O2 → 001–O1 → 001–O3 path. For this case, all jumps involve a synchronous O–H breaking/formation on the surface. The calculated energy barriers ($\Delta U_0^{\ddagger}$) of all these processes are significantly high (between 13.7 and 23.8 kcal mol^{-1}), due to the cleavage of chemical bonds and thus, these processes appear to be kinetically hindered at low temperatures. This means that, upon H adsorption, the systems will not evolve towards the most stable adsorption state and, accordingly, all the described adsorption states, if formed, are metastable in relation to H_2 formation.

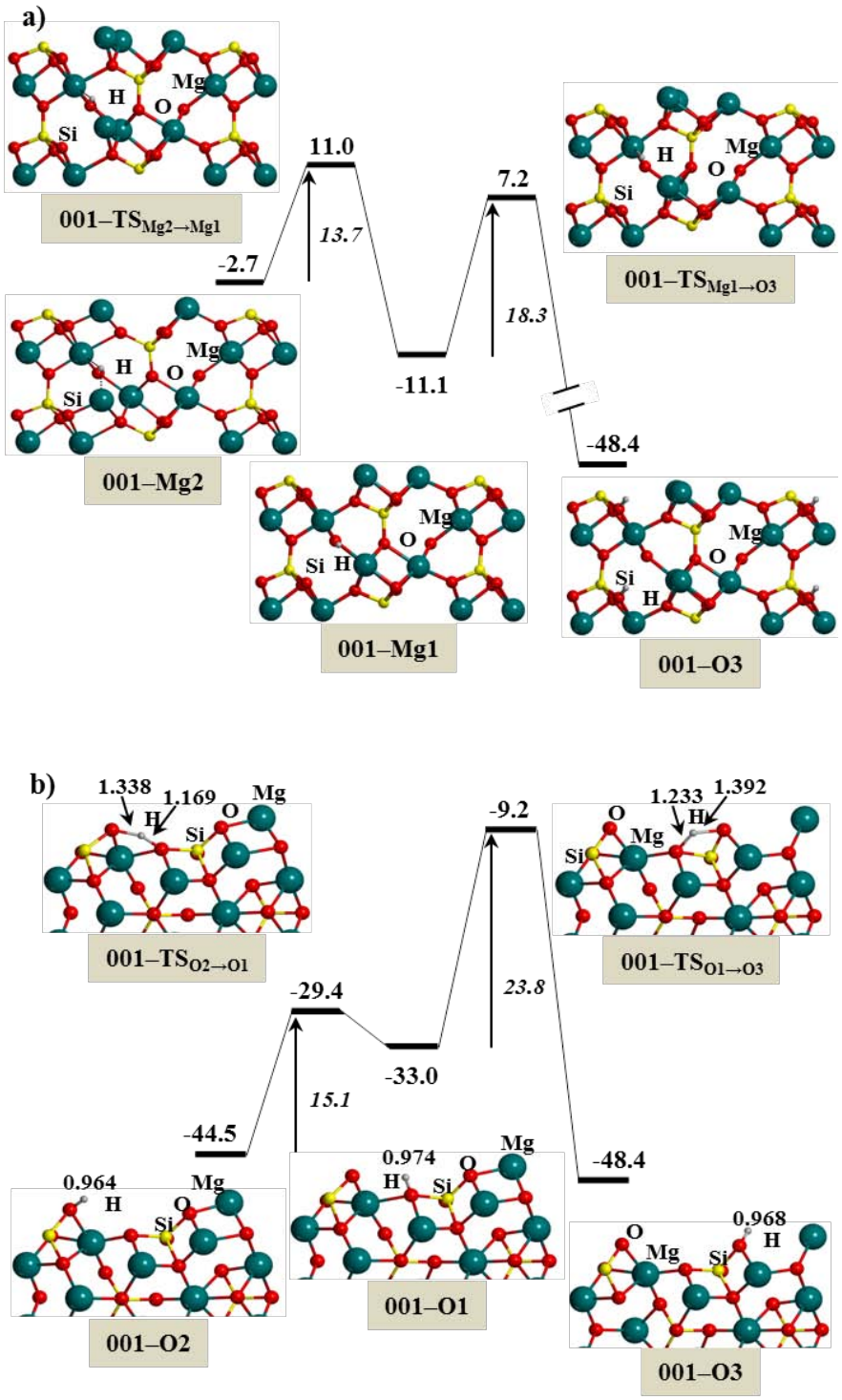

Figure 3.21 B3LYP-D2* energy profiles including ZPE corrections for the inter-conversion between the different adsorption states adopting a 001–Mg2 → 001–Mg1 → 001–O3 (a) and a 001–O2 → 001–O1 → 001–O3 (b) sequence calculated at B2//B1 (bond distances in Å and energies in kcal mol^{-1}). Relative energies are referenced with respect to the Fo(001) + H zero-energy asymptote. The unit cell of adducts has been shifted half of the cell parameter *b* to highlight the H-jumps.

Figure 3.22 shows the energy profile for the 110–Mg2 → 110–O4 path, which goes from the most stable physisorption state to the most stable chemisorption state. The process involves the simultaneous Mg–H breaking/O–H forming bonds. The energy barrier of this H jump is lower than those computed on Fo(001) because here the H atom is physisorbed.

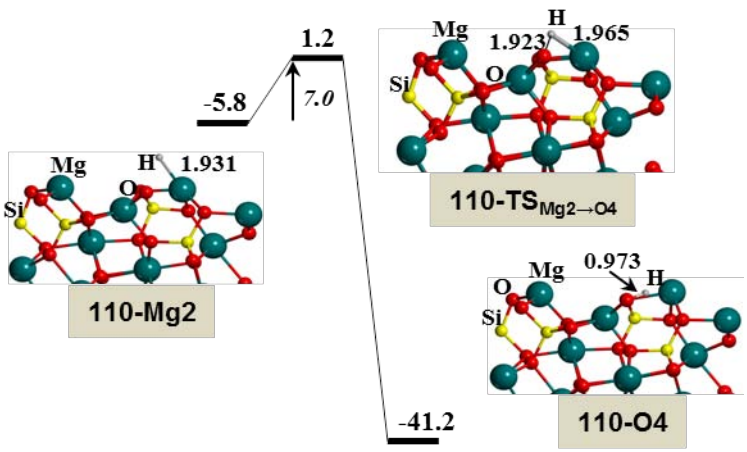

Figure 3.22 B3LYP-D2* energy profiles including ZPE corrections for the 110–Mg2 → 110–O4 inter-conversion path calculated at B2//B1 (bond distances in Å and energies in kcal mol^{-1}). Relative energies are referenced with respect to the Fo(110) + H zero-energy asymptote.

3.3.2. Adsorption of a Second H Atom

To simulate the formation of the H_2 molecule on Fo(001) through a Langmuir-Hinshelwood mechanism, the adsorption of a second H atom on the 001–Mg1, 001–Mg2, 001–O1, 001–O2 and 001–O3 adducts was also studied. We considered a total of 10 initial guess adducts by combining the different H/Fo(001) complexes: i) three derived from the combination of 001–Mg1 with the second H atom adsorbed on the three available O atoms (*i.e.*, 001–O1-Mg1, 001–O2-Mg1 and 001–O3-Mg1); ii) three derived from the combination of 001–Mg2 with the O atoms (*i.e.*, 001–O1-Mg2, 001–O2-Mg2 and 001–O3-Mg2); iii) three derived from the combination of the O-interacting adducts (*i.e.*, 001–O2-O1, 001–O3-O1 and 001–O3-O2); and iv) one derived from the combination of 001-Mg1 and 001-Mg2 (*i.e.*, 001–Mg1-Mg2). Geometry optimization of all these starting structures collapsed into 7 different complexes. For the sake of clarity, only the B3LYP-D2* optimized geometry of the most stable adduct for each type of double-adsorption (which are the most relevant ones) are shown in Figure 3.23a and the calculated total adsorption

energies in Table 3.16, that is, the reaction energy of Fo(001) + 2H → 2H/Fo(001). Appendix A reports the remaining complexes (both structure and adsorption energies) and adsorption energies of the second H atom from the H/Fo(001) complexes (*i.e.*, the reaction energy of H/Fo(001) + H → 2H/Fo(001)). The initial 001–O2-Mg1 collapsed to 001–O2-Mg2, the 001–O3-Mg2 complex evolved to 001–O3-Mg1 and 001–Mg1-Mg2 leads to the formation of H_2 because the two H atoms are adsorbed on the same Mg atom.

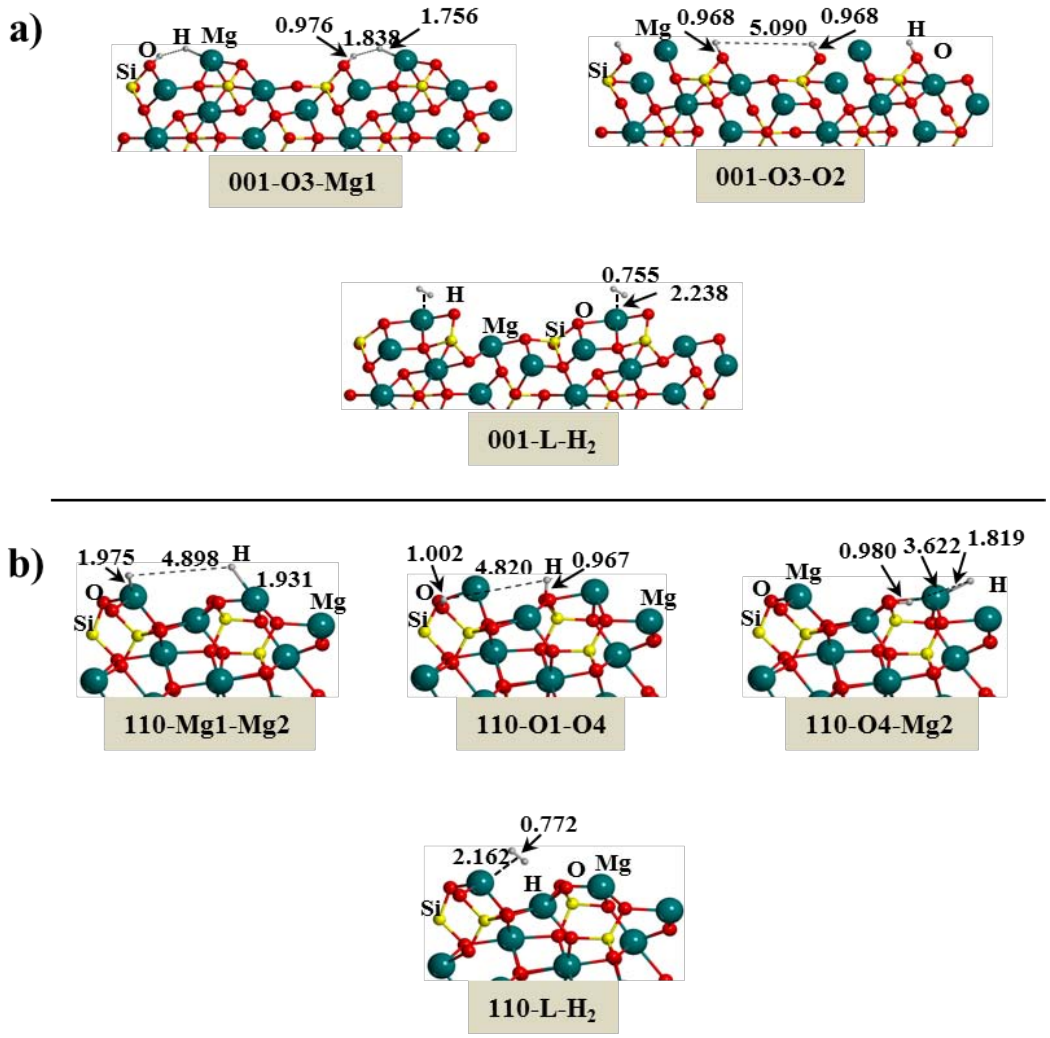

Figure 3.23 B3LYP-D2* optimized geometries of the different complexes resulting from the adsorption of two H atoms (a) on the Fo(001) (001–O3-Mg1, 001–O3-O2 and 001–L–H_2) and (b) on Fo(110) (110–Mg1-Mg2, 110–O1-O4, 110–O4-Mg2 and 110–L–H_2). Bond distances in Å (in Fo(001) case, the unit cell has been doubled to highlight the H–H interactions).

Table 3.16 *B3LYP-D2* reaction energies (in kcal mol^{-1}) calculated at the B2//B1 level for the global H adsorption processes on Fo(001) to form the 001–O3-O2, 001–O3-Mg1 and 001–L–H_2 complexes and on Fo(110) to form the 110–Mg1-Mg2, 110–O1-O4, 110–O4-Mg2 and 110–L–H_2 complexes. Uncorrected (ΔE) and zero-point energy corrected (ΔU_0) adsorption energy.*

Reaction	ΔE	ΔU_0
Fo(001) + 2H → 001–O3-O2	-84.3	-71.1
Fo(001) + 2H → 001–O3-Mg1	-137.9	-126.8
Fo(001) + 2H → 001–L-H_2	-116.2	-107.2
Fo(110) + 2H → 110–Mg1-Mg2	-13.2	-8.9
Fo(110) + 2H → 110–O1-O4	-82.5	-69.8
Fo(110) + 2H → 110–O4-Mg2	-130.7	-120.0
Fo(110) + 2H → 110–L-H_2	-118.4	-108.8

The most stable complex is that in which one H adsorbs on the Mg atom while the other adsorbs on the O atom; *i.e.*, 001–O3-Mg1 with calculated ΔU_0 of -126.8 kcal mol^{-1} (remaining complexes with the same motif lye between -105 and -120 kcal mol^{-1}). This large stability is due to the formation of both hydride (Mg–H) and an OH group (Si–OH). This complex is formed because in 001–O3 case (the others chemisorption states act equally) the unpaired electron is almost entirely localized on the bare Mg atom and, accordingly, prone to receive the second H atom to form Mg–H (Appendix A includes the whole set of net Mulliken charges for all considered complexes). Note that for these di-adsorption calculations, the initial guess orbitals corresponded to a broken symmetry solution, which collapsed to a singlet closed shell state. As a consequence, the two hydrogen atoms become chemisorbed at the surface, the one attached to Mg exhibiting an important hydride character whereas that attached to the oxygen behaving as a proton. Complexes of this kind were also identified in silicate nanoclusters [105] and in the (010) forsterite surfaces [109], [247]. Additionally, the high stability of 001–O3-Mg1 is due to a dihydrogen bond between the H^- and H^+ ad-atoms, which is confirmed by their Mulliken net charges (-0.35 and +0.35|e|, respectively). The adsorption energy for 001–O3-O2 is less favourable (ΔU_0 of -71.1 kcal mol^{-1}; remaining complexes presenting double chemisorption have values of -57.8 and -62.9 kcal mol^{-1}). This lower stability is due to the presence of two silanol (SiOH) groups, which forces the weakening/breaking of different Mg–O bonds. The positive Mulliken net charge of these H atoms (+0.35|e|) is coherent with the formation of an OH group.

For the Fo(110) surface, a total of 15 starting adducts were considered: i) one from the combination of the two Mg-interacting H/Fo(110) adducts (*i.e.*, 110–Mg1-Mg2); ii) eight structures derived from the combination of the two Mg-interacting H/Fo(110) with the four O-interacting ones (*i.e.*, 110–O1-Mg1, 110–O1-Mg2, 110–O2-Mg1, 110–O2-Mg2, 110–O3-Mg1, 110–O3-Mg2, 110–O4-Mg1 and 110–O4-Mg2); and iii) six structures combining the O-interacting H/Fo(110) complexes (*i.e.*, 110–O1-O2, 110–O1-O3, 110–O1-O4, 110–O2-O3, 110–O2-O4 and 110–O3-O4). All the proposed adducts were identified. Following the scheme proposed for the Fo(001), only the optimized geometry of the most stable adduct for each type of double-adsorption is shown in Figure 3.23b and the corresponding adsorption energies in Table 3.16. The remaining complexes (both structure and adsorption energies) and the adsorption energies of the second H atom from the H/Fo(110) complexes are reported in Appendix A.

As occurred for Fo(001), the most stable complex (110–O4-Mg2, ΔU_0 = -120.0 kcal mol^{-1}) has one H adsorbed on a Mg atom and the other on a O atom. In terms of relative stability, this complex is followed by others in which again the H atoms are simultaneously adsorbed on the Mg and O atoms (ΔU_0 between -95 – -107 kcal mol^{-1}), then by complexes in which the two H atoms are adsorbed on the O atoms (ΔU_0 between -50 – -70 kcal mol^{-1}), and finally by 110–Mg1-Mg2 (ΔU_0 = -8.9 kcal mol^{-1}) which is the less stable complex, as the two H atoms are physisorbed on the two outermost Mg atoms (see Appendix A).

3.3.3. H_2 Formation

The interaction of H_2 on Fo(001) gives a structure where molecular hydrogen is on the uppermost Mg atom (001–L-H_2, shown in Figure 3.23a). The calculated adsorption energy (ΔU_0 = -3.5 kcal mol^{-1}) indicates that H_2 molecule is very weakly bound to Fo(001) and dispersion contribution is nearly 65% of the adsorption energy (Appendix A includes the whole adsorption energies calculated at B1 and B2//B1). Despite this weak interaction, the reaction energy for the formation of H_2 along the Fo(001) + 2H → 001–L-H_2 channel is very large and negative (about -107 kcal mol^{-1}, see Table 3.16) because of the release of the H_2 formation energy. Table 3.17 reports the reaction energies for the H_2 formation from the 2H/Fo(001) complexes (in Appendix A the reaction energies at B1 and B2//B1 basis

set). Nevertheless, the reaction is unfavourable starting from the 001–O3-Mg1 complex, *i.e.* the 001–O3-Mg1 → 001–L-H_2 reaction energy is positive, resulting in an endoergic process. In contrast, the reaction is exoergic when it involves 001–O3-O2 complex. However, despite the exoergic character of this reaction, it exhibits very high-energy barriers, preventing any occurrence of the process, as it involves the recombination of two H atoms with a H^+ character and thus, H_2 formation requires an important electronic and structural reorganization. Similar situations were already found for the H_2 formation on Fo(010) [247], as it can be seen in Section 3.2. According to this, the H_2 formation is favourable when the two H atoms are either: i) physisorbed (weakly bound to the surfaces) and couple through a radical-radical process; or ii) chemisorbed leading to SiOH and Mg–H surface groups in close spatial proximity. For the present (001) surface, complexes with two physisorbed H atoms have not been identified, as all cases exhibit chemisorption. The only complex in which the reaction may exhibit a low energy barrier is the 001–O3-Mg1 as SiOH and Mg–H groups are in close spatial proximity to make a dihydrogen bond. However, as previously mentioned, this reaction is hampered by unfavourable reaction energy. Therefore, the Langmuir-Hinshelwood recombination of the H ad-atoms to form a H_2 molecule from the doubly H-adsorbed adducts does not seem feasible on Fo(001).

Table 3.17 *B3LYP-D2* reaction energies (in kcal mol^{-1}) calculated at the B2//B1 level for the H_2 formation from the 2H/Fo(001) complexes on Fo(001) and from the 2H/Fo(110) on Fo(110). Uncorrected (ΔE) and zero-point energy corrected (ΔU_0) adsorption energy.*

Reaction	ΔE	ΔU_0
001–O3–O2 → 001–L–H_2	-31.9	-36.1
001–O3–Mg1 → 001–L–H_2	21.7	19.6
110–Mg1–Mg2 → 110–L–H_2	-105.2	-99.9
110–O1–O4 → 110–L–H_2	-35.9	-39.1
110-O4-Mg2 → 110–L–H_2	12.4	11.2

We also modelled the formation of H_2 on the (001) forsterite surface through the Eley-Rideal mechanism by impinging an H atom to the 001–Mg1 adduct. We performed a constrained geometry optimization (a scan calculation), keeping the interatomic H···H distance fixed at specific values (simulating the approach of the incoming H atom) while optimizing the other internal coordinates. The energy variation along the scan calculation shows that, the shorter the interatomic distance, the lower the energy of the system,

indicating a barrierless process. To confirm this point, we fully relaxed the geometry of the system starting with an initial H···H distance of 3 Å and the system evolved into the spontaneous formation of H_2. Thus, provided a high enough H atom flux in the ISM condition, the calculations suggest that H_2 formation on the crystalline Fo(001) surface is favourable towards an Eley-Rideal mechanism. To better investigate on the feasibility of the Eley-Rideal mechanism, the time-independent quantum reactive scattering calculations to determine the vibrational distributions of product H_2 should be carried out. Interestingly, sensible results can already be obtained with calculations fixing the distances between hydrogen and the surface atom and the intermolecular H···H distance, as Clary and co-workers did for H_2 formation on graphite [52]. They proved that the total reaction probability is very close to 1 for H collision energy compatible to that available at very low temperature of the ISM. Also, the formed H_2 molecule leaved the surface in the second excited vibrational level. Due to the similarity with the present system we can roughly assume a similar behaviour also for the forsterite surfaces.

The adsorption of H_2 on Fo(110) takes place through the outermost Mg atoms (see 110–L-H_2 of Figure 3.23b). In the complex, H_2 is weakly bound to the surface (ΔU_0 of -5.1 kcal mol^{-1}), with dispersion contributing to nearly 35%. Table 3.17 shows the reaction energies for the formation of H_2 from the 2H/Fo(110) complexes shown in Figure 3.23b. The reaction considering 110–O4-Mg2 as the reactant (the most stable complex) is endoergic, whereas from the other complexes is exoergic. However, from 110–O1-O4, H_2 formation implies the recombination of two SiOH protons so that the energy barrier is expected to be significantly high. In contrast, as in 110–Mg1-Mg2 the two H atoms are physisorbed, the reaction is expected to be energetically feasible because it involves a radical-radical coupling. The calculated energy profile is shown in Figure 3.24 and, unexpectedly, rather than proceeding through a direct H recombination, it involves two steps. In the first step, H jumps from the Mg atom to an O atom, thus forming another and more stable complex (110–O3-Mg1, already identified as a 2H/Fo(110) complex, see Appendix A). In the second step, H recombination occurred from the 110–O3-Mg1 structure. The calculated energy barriers were found to be relatively low ($\Delta U_0^{\ddagger}$ = 0.4 and 1.2 kcal mol^{-1} for the first and second steps, respectively).

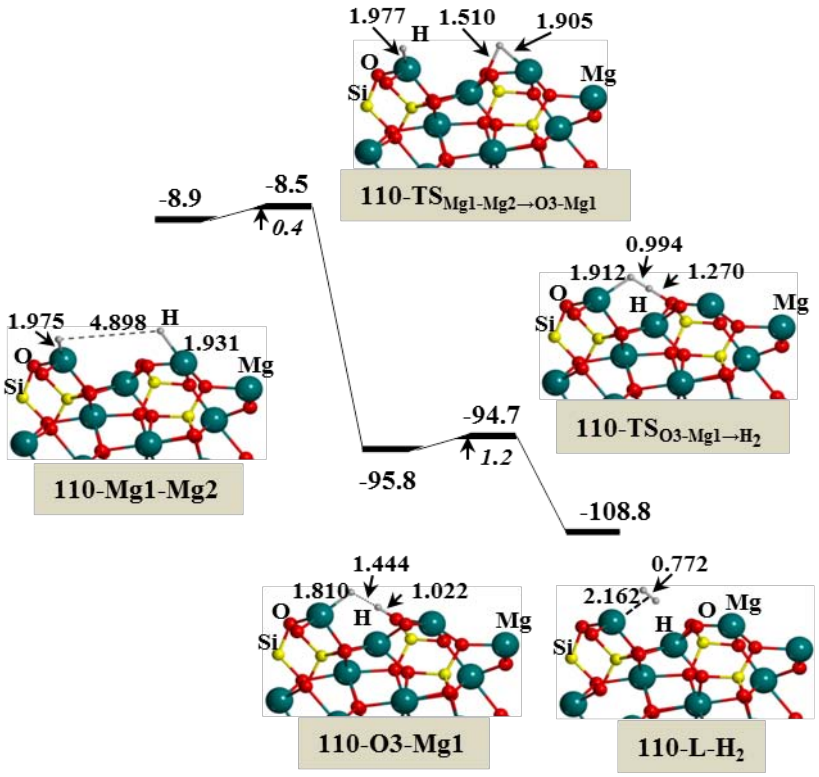

Figure 3.24 B3LYP-D2* energy profiles including ZPE corrections for the recombination of two H atoms to form H_2 calculated at B2//B1 (bond distances in Å and energies in kcal mol^{-1}). Relative energies are referenced with respect to the Fo(110) + 2H zero-energy asymptote.

As done for the Fo(001) surface, we computed the potential energy surface for an Eley-Rideal mechanism by vertically approaching a second H atom to the 110–Mg2 state. At an interatomic H···H distance close to 3.0 Å, the 110–Mg2 adduct spontaneously evolves to the 110–O3 one. In addition, when fully relaxing a system in which the 110–O3 adduct is initially separated by the second H atom by 3.5 Å formation of H_2 spontaneously occurred indicating a barrierless process.

3.3.4. Comparison with (010) Mg_2SiO_4 Surface

Hitherto, the adsorption of H atom and formation of H_2 on the (010), (001) and (110) surfaces of crystalline forsterite have been adressed. These surfaces have different surface energy, so insights on the role of crystal morphology on H_2 formation can be obtained. A first interesting datum is that, compared to the (010) surface, the (001) and (110) surfaces are more heterogeneous, exhibiting a higher number of potential adsorption sites, which

have all been addressed here. Quite obviously, the more negative the H adsorption energy, the higher the associated surface energy, thus showing a clear correlation. This is shown by the adsorption energy of the most stable singly H chemisorbed adducts on the (010), (001) and (110) faces (-10.3 kcal mol^{-1}, -48.4 kcal mol^{-1} and -41.2 kcal mol^{-1}, respectively) which are in line with the surface energy values. This also affects the diffusion behaviour of H atoms on these surfaces. H jumps on the (010) surface exhibit lower energy barriers (between 4–6 kcal mol^{-1}) compared to those on the (001) and (110) surfaces (between 7–23 kcal mol^{-1}), since H atom is largely adsorbed on these latter surfaces.

The different adsorption features between these Mg_2SiO_4 surfaces also have significant consequences on the H recombination to form H_2 through a Langmuir-Hinshelwood mechanism. On the (010) surface, two paths were identified as feasible [247], one based on a radical-radical H coupling and the other on a $H^+\cdots H^-$ recombination. In contrast, on the (001) surface, all reaction channels resulted to be energetically unfavourable, because the 2H/Fo(001) initial states are more stable than the H_2/Fo(001) final product, whereas for the (110) surface, only one favourable channel ($H^+\cdots H^-$ recombination) leading to the formation of H_2 has been elucidated. These results indicate that the larger instability of the (001) and (110) surfaces makes them very reactive towards H adsorption, with the consequence that the high stability of the formed complexes inhibits the formation of H_2. Investigation on the potential energy surface of H impinging on hydrogen pre-adsorbed on Fo(001) and Fo(110) suggest that the Eley-Rideal mechanism may become important due to the barrierless nature of the process. However, the low H density in diffuse clouds of the ISM decreases the probability of the ER mechanism and, consequently, the present results suggest that among these three crystalline faces, the (010) is the most active one as far as H_2 formation is concerned, through a LH mechanism.

Finally, the trend of the kinetics of the different H hopping and H recombination on the (010), (001) and (110) surfaces have been examined. To this end, the crossover temperature (T_X) for each surface process is calculated and the Arrhenius plots of $k^{SC\text{-}TST}$ are represented, considering that $\kappa(T) = 1$ above *T*x. Calculated T_X values, alongside the values of $\Delta U_0^{\ddagger}$ and $\nu^{\ddagger}$ used, are shown in Table 3.18 and the Arrhenius plots are represented in Figure 3.25 and Figure 3.26. It is worth mentioning that as the employed $\kappa(T)$ expression is stable to arbitrarily low temperatures, the Arrhenius plots were represented between 150 and 450 K. Lower temperatures have not been considered

because this will require more accurate treatments of tunnelling effects such as Feynman's path integral formalisms, as already done in H-based processes on carbonaceous surfaces [187], [190].

Table 3.18 *B3LYP-D2* zero-point energy corrected energy barriers ($\Delta U_0^{\ddagger}$, in kcal mol^{-1}) at the B2//B1 level, transition frequencies ($\nu^{\ddagger}$, in cm^{-1}) and tunnelling crossover temperatures (T_X, in K).*

	Reaction	$\Delta U_0^{\ddagger}$	$\nu^{\ddagger}$	T_X
Figure 3.15a	010–Mg1 → 010–Mg2	4.1	137	32
	010–Mg2 → 010–O1	6.4	1058	264
Figure 3.18b	010–Mg2a-Mg2b → 010–H_2	0.5	361	108
Figure 3.19b	010–O1a-Mg2a → 010–H_2	1.7	1110	320
Figure 3.21a	001–Mg2 → 001–Mg1	13.7	249	57
	001–Mg1 → 001–O3	18.3	946	220
Figure 3.21b	001–O2 → 001–O1	15.1	1048	245
	001–O1 → 001–O3	23.8	1560	365
Figure 3.22	110–Mg2 → 110–O4	7.0	500	117
Figure 3.24	110–Mg1-Mg2 → 110–O3-Mg1	0.4	626	278
	110–O3-Mg1 → 110–L-H_2	1.1	761	220

Previously, we must check what kind of expression to account for tunnelling contributions is the most appropriate to better describe the H diffusion and H_2 formation on the Mg_2SiO_4 surfaces. Thus, the four most relevant Fo(010) reactions have been studied with each of the three considered approximations to calculate the transmission coefficient $\kappa(T)$, presented previously in Section 2.6. The corresponding Arrhenius plots of $k^{\text{SC-TST}}$ are shown in Figure 3.25.

For the 010–Mg2 → 010–O1 case (Figure 3.25b), Wigner's correction overestimates the values of $\log_{10}(k^{\text{SC-TST}})$ with respect to the Skodje's and Fermann's approximations by around six orders of magnitude, because this correction works well only when $h\nu^{\ddagger}i \ll k_B T$ (at very low temperatures it fails) and depends only on the transition frequency $\nu^{\ddagger}$, whereas Skodje's and Fermann's approximations also accounts for the energy barrier $\Delta U_0^{\ddagger}$. These two latter corrections provide similar trends below T_x, but close to crossover temperature the Skodje's correction gives values of $\log_{10}(k^{\text{SC-TST}})$ one order of magnitude larger than calculated with the Fermann's correction. This is due to the inversion of the parameter that

governs $\kappa(T)$: at lower temperatures, β parameter is greater than α parameter and hence eq. (2.36) is employed, but close to T_x this trend changes and α is greater than β, so the estimation of κ is through eq. (2.35) and produces as a result this anomaly.

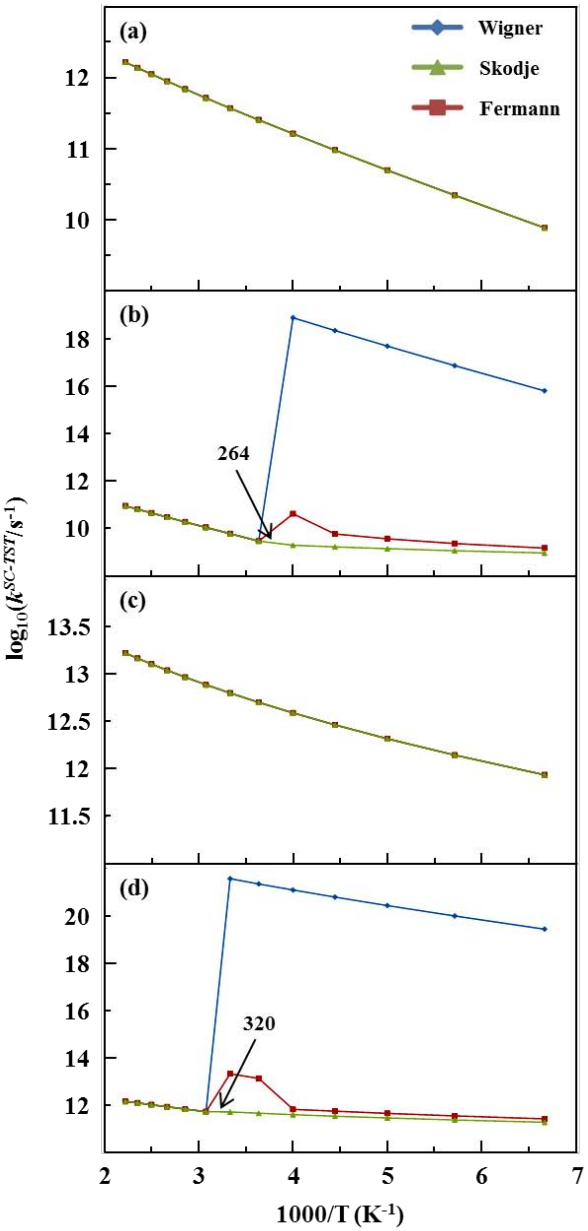

Figure 3.25 Arrhenius plots of $k^{\text{SC-TST}}$ between 150 and 450 K using the three considered approximations for $\kappa(T)$ and for the four most relevant Fo(010) reactions: 010–Mg1 → 010–Mg2 (a), 010–Mg2 → 010–O1 (b), 010–Mg2a-Mg2b → 010–H_2 (c) and 010–O1a-Mg2a → 010–H_2 (d). Crossover temperatures (T_X) are indicated for each reaction and above T_X, $\kappa(T) = 1$ is considered.

For the 010–O1a-Mg2a → 010–H_2 case (Figure 3.25d) similar trends are obtained. Wigner overestimates the values of $\log_{10}(k^{\text{SC-TST}})$ of about nine orders of magnitude with respect to Skodje's and Fermann's correction, and Skodje overestimates these values only close to

crossover temperature by around one order of magnitude. Therefore, Fermann's approximation to transmission coefficient $\kappa(T)$ seems to be the best choice to include tunnelling contributions at semi-classical level to the processes of H adsorption and H_2 formation studied.

In view of these results, a comprehensive analysis of the kinetic trends for the processes occurring on the (010), (001) and (110) surfaces is provided, computing $\kappa(T)$ with the Fermann's correction. On the (010) surface (Figure 3.26a), neither the 010–Mg1 → 010–Mg2 H hopping nor the 010–Mg2a-Mg2b → 010–H_2 H_2 formation (namely, those processes involving exclusively physisorbed H atoms) are affected by tunnelling, whose calculated T_X values are 32 and 108 K, respectively. Both processes are fast at the range of temperatures since the calculated $\log_{10}(k^{\text{SC-TST}})$ values are about 11 and 13, respectively, at 150 K. For the 010–Mg2 → 010–O1 H hopping (namely, the change of a physisorbed into a chemisorbed H atom), tunnelling effects seem to be significant due to the slope change at its crossover temperature ($T_X = 264\ K$), whereas for the 010–O1a-Mg2a → 010–H_2 H_2 formation (namely, the coupling involving a $H^+ \cdots H^-$ recombination) a small but appreciable slope change takes place at its crossover temperature ($T_X = 320\ K$), in which, moreover, the calculated $\log_{10}(k^{\text{SC-TST}})$ values indicate that the processes are fast (about 9 and 12, respectively, at 150 K).

For the processes on the (001) surface (Figure 3.26b), tunnelling contributions are expected to be significant in the range of the considered temperatures for the 001–Mg1 → 001–O3, 001–O2 → 001–O1 and 001–O1 → 001–O3 H hopping because the corresponding Arrhenius plots show a prominent slope change, which makes $\log_{10}(k^{\text{SC-TST}})$ values to remain relatively constant below T_X as occurs in regimes dominated by tunnelling. This is at variance with the 001–Mg2 → 001–Mg1 path ($T_X = 57\ K$) because it is not strictly an H jump but an Mg–O breaking followed by an H rearrangement on the Mg atom. However, the calculated $\log_{10}(k^{\text{SC-TST}})$ values are small at low temperatures (between 0 and -5 at 150 K), pointing out that these H jumps are kinetically hindered at the interstellar temperatures.

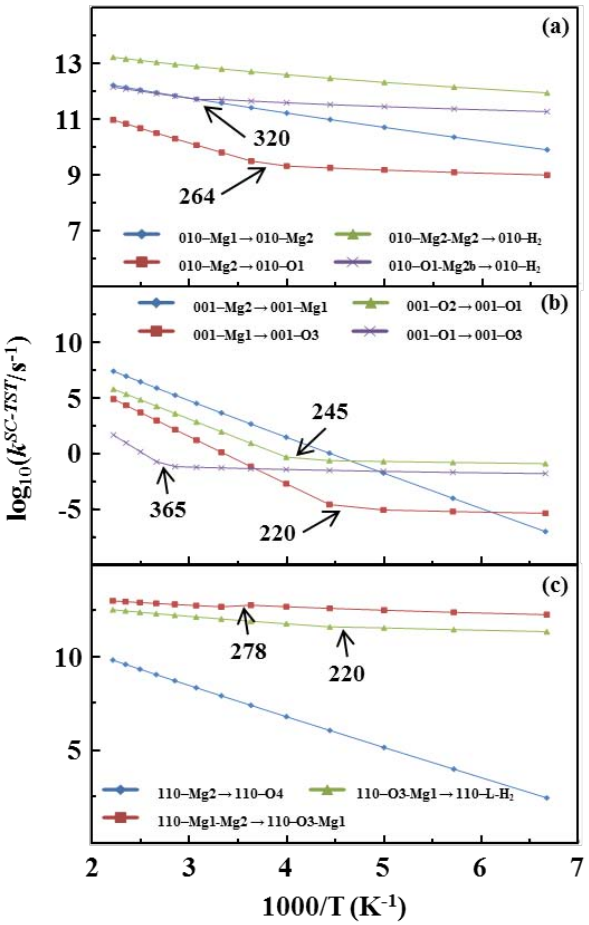

Figure 3.26 Arrhenius plots of $k^{\text{SC-TST}}$ between 150 and 450 K. Crossover temperatures (T_X) are indicated for each process on Fo(010) (a), Fo(001) (b) and Fo(110) (c). Above T_X, $\kappa(T) = 1$ is considered.

Finally, for the (110) surface (Figure 3.26c), it is found that the T_X for the 110–Mg2 → 110–O4 H hopping is about 120 K (see Table 3.18) and accordingly no slope change is observed in our Arrhenius plot. For the processes involved in the H_2 formation (*i.e.*, 110–Mg1-Mg2 → 110–O3-Mg2 and 110–O3-Mg1 → 110–L-H_2), although the calculated T_X are above 100 K (278 and 220 K, respectively), no considerable slope changes are observed, meaning that, regardless of tunnelling contributions, the H_2 formation reaction is fast (the calculated $\log_{10}(k^{\text{SC-TST}})$ are above 12.5 at the range of temperatures) because the corresponding energy barriers are very low ($\Delta U_0^{\neq}$ = 0.4 and 1.2 kcal mol^{-1}, respectively).

3.3.5. Final Remarks

On the crystalline (001) and (110) surfaces of Mg_2SiO_4 forsterite, while the hydrogen physisorption occurs essentially on the Mg atoms, different adsorption states envisage chemisorption occurring both on the Mg and on the O atoms. The calculated adsorption energies for the chemisorption states are large and significantly stronger than the (010) surface. The calculated energy profiles on the (001) and (110) faces indicate that the H jumps through different adsorption states are energetically more expensive in most of the calculated paths than on the (010) one due to the large hydrogen/surface interactions.

The most stable doubly H adsorbed complexes are those in which Mg–H and SiO–H surface groups are formed. On the most stable (010) surface, the H recombination processes to give H_2 from the doubly H adsorbed complexes occurs through a Langmuir-Hinshelwood mechanism. In contrast, on the (001) surface the process is endoergic because of the larger stability of the initial states, causing the final products to be more unstable. The (110) surface exhibits an intermediate character, as only one reactive channel leading to H_2 formation is energetically feasible at ISM conditions. The associated potential energy surface for the Eley-Rideal mechanism, in which an H atom impinges on a H pre-adsorbed forsterite surface, has also been computed. Due to the barrierless process occurring in these cases, the ER mechanism is expected to be efficient also at very low H collision energy estimated for the low temperature of the ISM region. Low H atom flux is nevertheless the most limiting factor for this mechanism to become relevant in the ISM.

Finally, represented Arrhenius plots between 450 and 150 K indicate that, at this range of temperatures, the H hopping processes on the (001) surfaces are kinetically hindered at low temperatures although tunnelling effects are predicted to be significant, whereas on the (110) surface, those processes involved in the H_2 formation are found to be fast irrespective of tunnelling contributions, and on the (010) surface, all the processes are fast, in which related to H_2 formation, the radicalradical H coupling does not exhibit tunnelling dependency, whereas the $H^+\cdots H^-$ recombination tunnelling effects allow this reaction to be fast at low temperatures.

3.4. Influence of Fe^{2+} Atoms: H_2 Formation on (010) $(Mg,Fe)_2SiO_4$ Surface

Present section addresses the question whether Fe^{2+} at the surface exert any positive or negative effect on the H_2 formation. As it was shown in Section 3.1, iron has a preference for the outermost positions of the surface, rather than more internal positions [245]. Moreover, the lowest energy spin state is the quintet one. Because of the complexity of the electronic structure of iron, the number of Fe atoms per unit cell of the surface model used here has been reduced to one (compared to the four shown by Fo_{75}^{top}). This slab surface model is denoted to as Ol(010) in reference to the (010) surface of olivine.

3.4.1. Calibration of the Functional

For the Mg-pure and Fe-containing olivine bulk and surfaces, the B3LYP functional was used (see Section 3.1). However, here H adsorption and the subsequent recombination is considered accordingly a previous calibration study to identify the functional that better describes the interactions between iron and the hydrogen atom.

To calibrate the method, a small cluster considering the first coordination sphere around Fe^{2+} atom was designed (the unsaturated O atoms were saturated with H atoms), resulting in a cluster model with a total of nine atoms. The calibration study was based on the adsorption of one H atom on the Fe cation employing different DFT methods. As mentioned, the lowest spin state of a Fe-containing olivine is the quintet one. Due to the inclusion of an unpaired electron coming from the H atom, the system can now lead to two spin states, sextet or quadruplet, *i.e.*, H having the spin up or down, respectively. The relative stability of these two states may be difficult to describe with DFT methods. Thus, Table 3.19 shows the energy difference between the two spin multiplicities for each method, computed with the GAUSSIAN09 package [248] from single-point energy calculations at the geometry of the designed cluster. The basis set used for oxygen and hydrogen atoms was a standard *6-31G(d,p)* Pople basis set and for iron atoms a Wachters basis set [249] with *f* functions for polarization [250].

Table 3.19 *Energy differences between different spin multiplicities (sextet and quartet) obtained for each method (in kcal mol^{-1}).*

Method	% of Exact Exchange	$E_{sextet} - E_{quartet}$
BLYP	0	-0.1
PBE	0	-2.2
TPSSh*	10	-6.7
B3LYP	20	-8.9
B3PW91	20	-10.6
B97H	21	-10.5
HSE06	25	-12.5
PBE0	25	-13.3
mPWB1K*	44	-18.8
BHLYP	50	-21.2
CCSD(T)	---	-17.0

* Exchange-correlation functionals not available in CRYSTAL code.

DFT results were compared to those provided by the CCSD(T) method, with an extended basis set of *aug-cc-pVTZ* [251] for O and H atoms and *Roos Augmented Triple Zeta ANO* [252] for Fe atoms. As it can be seen, in almost all cases the energy differences (defined as $E_{sextet} - E_{quartet}$) are negative, meaning that sextet is more stable than quartet and the system preferring a high-spin state in accordance with different studies [92]–[94]. Values of Table 3.19 also show a systematic correlation between the percentage of exact exchange of the functional and the $E_{sextet} - E_{quartet}$ values. That is, the larger the percentage of exact exchange, the larger the energy difference. This is because the inclusion of exchange exact tends to stabilize high-spin states. Comparing these results with those of the reference CCSD(T) method, GGA functionals present $E_{sextet} - E_{quartet}$ values largely different than the CCSD(T) one, exhibiting nearly degenerate spin states. However, hybrid functionals increase the stability of the sextet spin state with respect to the quartet one. Low percentage of exact exchange also give very different $E_{sextet} - E_{quartet}$ values (*e.g.*, for B3LYP is -8.9 kcal mol^{-1}), whereas for the hybrid functionals with more percentage of exact exchange, $E_{sextet} - E_{quartet}$ values are closer to the CCSD(T). Indeed, the functionals that better describe this system are PBE0, mPWB1K and BHLYP, with 25, 44 and 50 % of exact exchange, respectively. The mPWB1K functional is not implemented in the CRYSTAL09

code, so we finally decided to take the BHLYP functional (implemented in CRYSTAL) to calculate the H adsorption and H_2 formation on Ol(010) by means of periodic calculations.

3.4.2. Adsorption of One H Atom

BHLYP/B1 optimized adducts for the adsorption of one H atom on Ol(010) with the most stable sextet spin state is shown in Figure 3.27, and Table 3.20 and Table 3.21 report the corresponding computed adsorption energies and their net charges and electronic spin densities calculated at B2//B1 theory level, respectively. Energy values calculated with both B1 and B2//B1 basis sets and also the quartet spin multiplicity for all the processes described in this section are reported in the Appendix B. Four different H/Ol(010) adducts were characterized: one in which the H atom is interacting with the uppermost Fe atom (010–Fe1), two in which the H-atom interaction takes place through the most exposed O atoms (010–O1 and 010–O2), forming a silanol (Si–OH) group, and the last one in which the H atom interacts with the uppermost Mg atom (010–Mg1).

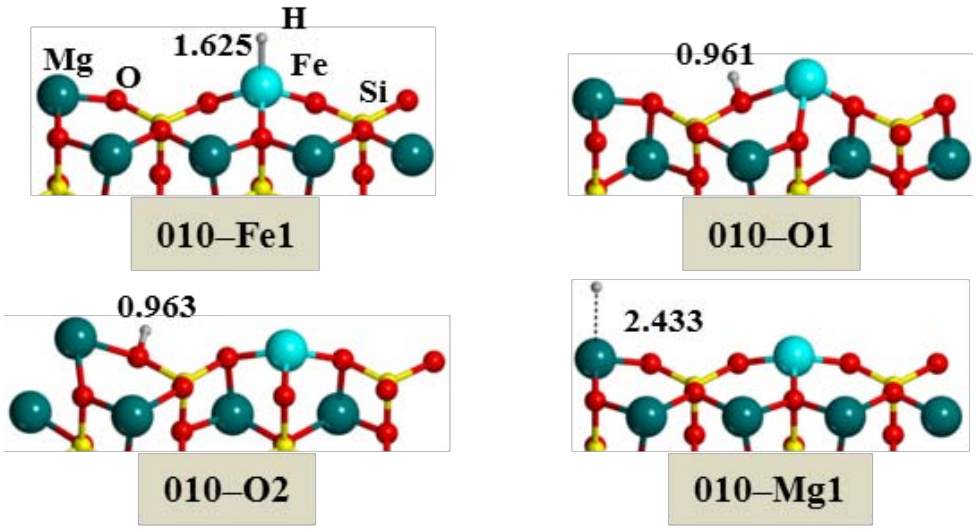

Figure 3.27 BHLYP optimized geometries of the different adducts resulting from the adsorption of one H atom on Ol(010) (010–Fe1, 010–O1, 010–O2 and 010–Mg1) at sextet spin state. Bond distances in Å.

Table 3.20 *BHLYP adsorption energies (in kcal mol^{-1}) calculated at the BHLYP/B2//BHLYP/B1 level for the first H adsorption processes on Ol(010) to form the 010–Fe1, 010–O1, 010–O2 and 010–Mg1 adducts. Pure potential adsorption energy (ΔE_{el}), estimate of the contribution of dispersion to the adsorption energy (ΔE_{D2}) and zero-point energy corrected (ΔU_0) adsorption energy.*

Reaction	ΔE_{el}	ΔE_{D2}*	$\Delta E_{el}+\Delta E_{D2}$	ΔU_0	$\Delta U_0+\Delta E_{D2}$
Ol(010) + H → 010–Fe1	-38.7	-1.4	-40.1	-34.3	-35.7
Ol(010) + H → 010–O1	-16.2	-1.3	-17.5	-9.4	-10.7
Ol(010) + H → 010–O2	-13.8	-2.7	-16.5	-7.3	-10.0
Ol(010) + H → 010–Mg1	-1.1	-0.8	-1.9	-0.2	-1.0

* Grimme's dispersion energy calculated with scaling factor to $s_6 = 1.0$.

According to the calculated adsorption energies (see Table 3.20), the most stable adduct is 010–Fe1 (ΔU_0 = -34.3 kcal mol^{-1}), in which the H atom interacts directly with the iron (Fe-interacting system). This is followed by the O-interacting 010–O1 and 010–O2 systems (ΔU_0 between -9 and -7 kcal mol^{-1}) and the Mg-interacting 001–Mg2 system (ΔU_0 = -0.2 kcal mol^{-1}). In order to estimate the magnitude of dispersion forces on the adsorption energy, the Grimme's correction for dispersion assuming a scaling factor of $S_6 = 1.0$ have been calculated (note that for BHLYP functional no scaling factor has been described) and is reported in Table 3.20. For 010–Mg1, its adsorption energy value, as well as the large Mg–H distance (2.433 Å) and the distribution of spin density (+0.96 on H and +3.90 on Fe), indicate this corresponds to a physisorption state. The rest of the adducts are chemisorpted states because, in addition to larger adsorption energies, the O-interacting systems have typical O–H distances (by around 0.96 Å) and the 010–Fe1 adduct has a Fe–H distance of 1.625 Å.

Table 3.21 *Net charges and electronic spin densities on the H, Fe and Mg atoms, and the sum of the spin density values of the O atoms closest to H, computed at B2//B1 level for the different singly-H adsorptions on Ol(010) at sextet spin state.*

	Charge				Spin			
	H	Fe	Mg	O	H	Fe	Mg	O
010–Fe1	-0.26	+1.35	+1.10	-1.18	0.19	4.58	0.00	0.23
010–O1	+0.32	+0.52	+1.11	-1.13	0.01	4.93	0.00	0.06
010–O2	+0.33	+1.20	+0.45	-1.13	0.01	3.93	0.95	0.11
010–Mg1	+0.06	+1.18	+1.02	-1.19	0.96	3.90	0.02	0.12

For the remaining adducts, the spin density on the adsorbed H atom is mainly zero, in agreement with their chemisorbed character. The spin density contribution depends on the chemisorbed state. That is, for 010–O2, the Mulliken spin density is on the outermost Mg atom (+0.95 on Mg and +3.93 on Fe), whereas for 010–O1 adduct, the spin density is on the Fe atom (+4.93). That is, upong interacting with the O atom, the spin density of H atom moves to the closest metal. On the other hand, and according to atomic charges, it seems that iron reduces its partial charge in the 010–O1 adduct, in agreement with the electron transferred from the adsorbed H atom to the Fe atom, which suggests that iron has undergone a partial reduction in its oxidation state (from +1.18|e| to +0.52|e|) and the H atom has a character of H^+ with a Mulliken charge of +0.32|e|. As iron has five unpaired electrons, it adopts a $4s^1 3d^6$ electronic configuration, in detriment of the $4s^0 3d^7$ configuration, which would imply a spin density of about +3.00. Note that the $4s^1 3d^6$ and $4s^0 3d^7$ electronic configuration of iron lye very close in energy, the former being the ground state. Different electronic reorganization is observed in the 010–Fe1 adduct. In this complex, the charge of the H atom is -0.26|e| so that it acquires a certain character of H^-, whereas the charge of iron increases (from +1.18|e| to +1.35|e|), thus indicating a partial oxidation of the Fe atom. The calculated spin density of iron is +4.58, which seems to indicate an electronic configuration close to $4s^0 3d^5$ to justify the almost five unpaired electrons.

Figure 3.28a shows the energy profile corresponding to the interconversion between the different adsorption states along the 010–Mg1 → 010–O2 → 010–O1 → 010–Fe1 path, which goes from the physisorption state to the most stable chemisorption state. The first step consists of an H jump from the Mg atom to the adjacent O atom, involving the simultaneous Mg–H breaking and O–H forming bonds. Then, the second step connects the two O-interacting chemisorption states, which involves a synchronous O–H breaking/formation on the surface. The calculated energy barrier ($\Delta U_0^{\ddagger}$) of this process is very high (39.7 kcal mol^{-1}), due to the cleavage of chemical bond, whereas the energy barrier of the first H jump is much lower (7.1 kcal mol^{-1}), because the H atom is physisorbed. Finally, the third step involves the hydrogen jump to reach the most stable 010–Fe1 adduct. In this case, the computed energy barrier is also significantly high (19.9 kcal mol^{-1}), because of the cleavage of a SiO–H surface silanol group.

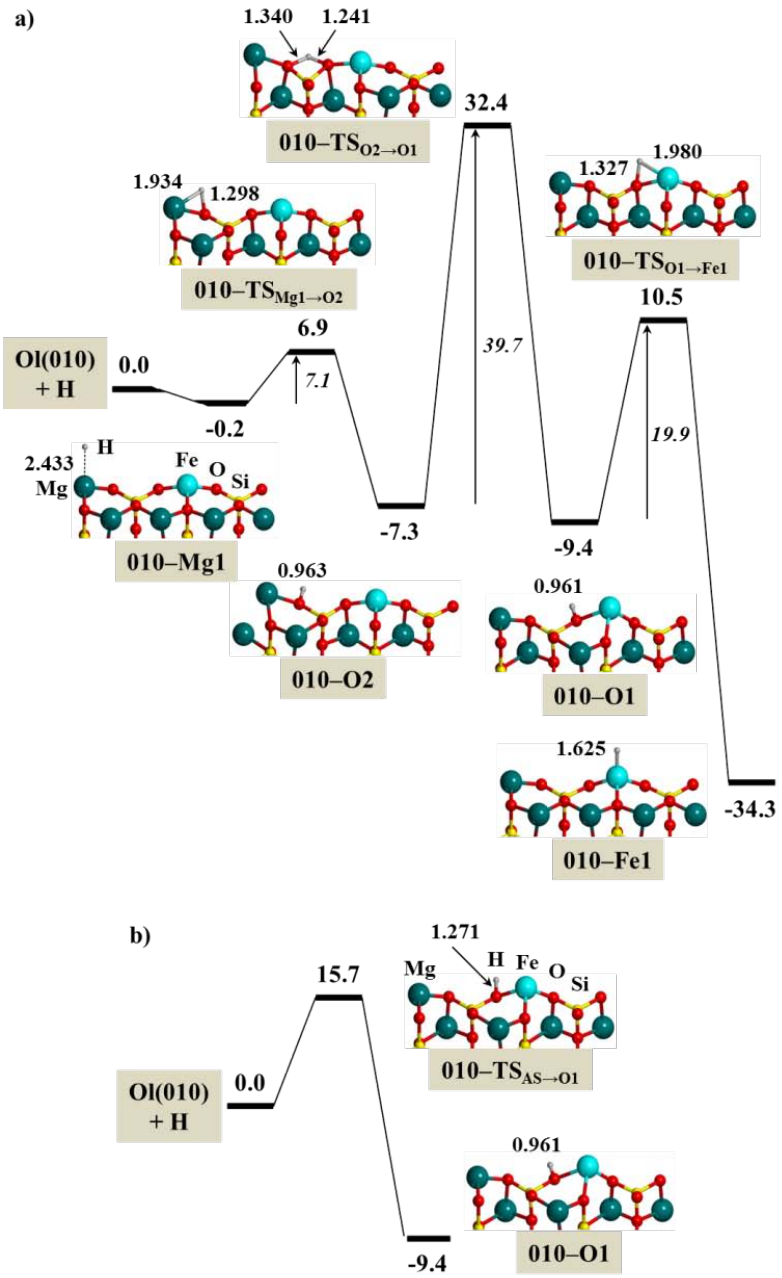

Figure 3.28 BHLYP energy profiles including ZPE corrections for the interconversion between the different adsorption states adopting a 010–Mg1 → 010–O2 → 010–O1 → 010–Fe1 sequence (a) and direct H adsorption to form 010–O1 (b) calculated at B2//B1 (bond distances in Å and energies in kcal mol^{-1}). Relative energies are referenced with respect to the Ol(010) + H zero-energy asymptote.

Following the same procedure developed in the Fo(010) surface, localization of transition structures connecting the Ol(010) + H asymptote with the adsorbed species was attempted. Whereas no transition structures have been found for 010–Mg1 and 010–Fe1 adsorptions, indicating that these adsorption processes are barrierless, a transition structure for 010–O1 was located. Figure 3.28b shows the energy profile for the direct H adsorption connecting

the Ol(010) + H asymptote with the most stable O-interacting 010–O1 chemisorption, displaying an energy barrier $\Delta U_0^{\ddagger}$ = 15.7 kcal mol^{-1}, very far from the value obtained on passing from 010–O2 to 010–O1 (see Figure 3.28a).

To sum up, the H jump process appears to be kinetically hindered at the low temperatures in the ISM, as it involves chemisorbed species. On the other hand, all the calculated transition structures in these processes are energetically higher than the Ol(010) + H asymptote, thus indicating that the jump from one adsorption site to another may take place through H desorption–adsorption steps rather than *via* surface diffusion.

3.4.3. Adsorption of a Second H Atom

To simulate the formation of the H_2 molecule on Ol(010) through a LH mechanism, the adsorption of a second H atom on the 010–Fe1, 010–O1, 010–O2 and 010–Mg1 adducts has been considered adopting a quintet spin state, which is more stable than the heptet one. A total of 8 initial guess adducts by combining the different H/Ol(010) complexes were taken into account: i) one derived from the combination of 010-Fe1 and 010-Mg1 (*i.e.*, 010–Fe1-Mg1); ii) two derived from the combination of 010–Fe1 with the second H atom adsorbed on the O atoms (*i.e.*, 010–Fe1-O1 and 010–Fe1-O2); iii) two derived from the combination of 010–Mg1 with the O atoms (*i.e.*, 010–O1-Mg1 and 010–O2-Mg1); and iv) three derived from the combination of the O-interacting adducts (*i.e.*, 010–O1-O1, 010–O1-O2 and 010–O2-O2). For the sake of clarity, only the optimized geometry of the most stable adducts for each type of double-adsorption with the quintet spin state is shown in Figure 3.29. The total adsorption energies computed as Ol(010) + 2H → 2H/Ol(010) are given in Table 3.22 and the net charge and electronic spin density values for the different doubly-H adsorptions are given in Table 3.23. Appendix B reports the remaining complexes (both structures and adsorption energies and also at the heptet spin state) and adsorption energies of the second H atom from the H/Ol(010) adducts, computed as H/Ol(010) + H → 2H/Ol(010).

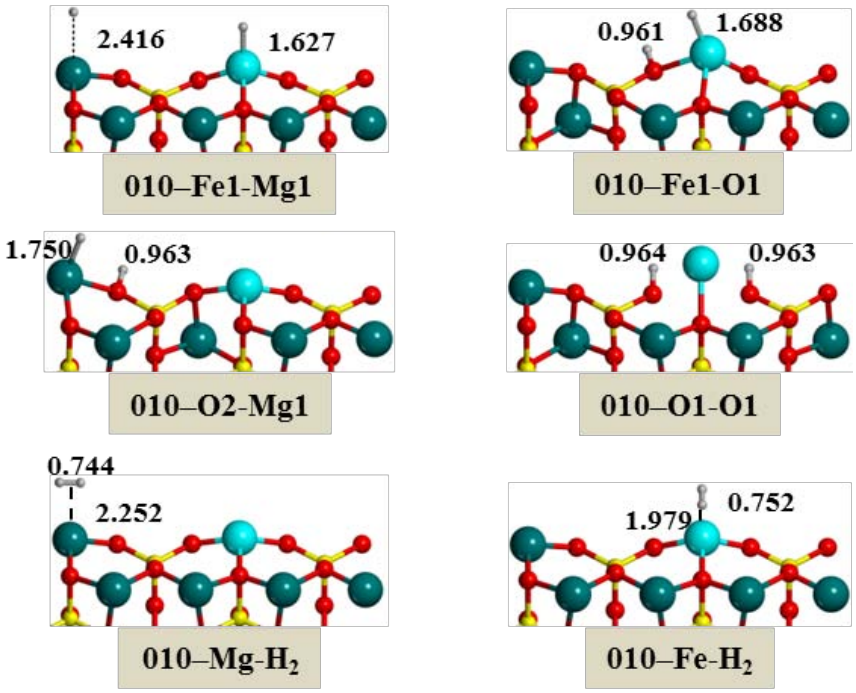

Figure 3.29 BHLYP optimized geometries of the different complexes resulting from the adsorption of two H atoms on Ol(010) (010–Fe1-Mg1, 010–O2-Mg1, 010–Fe1-O1, 010–O1-O1, 010–Mg-H_2 and 010–Fe–H_2) at quintet spin state. Bond distances in Å.

Table 3.22 *BHLYP reaction energies (in kcal mol^{-1}) calculated at the B2//B1 level for the global H adsorption processes on Ol(010) to form the 010–Fe1-Mg1, 010–O2-Mg1, 010–Fe1-O1, 010–O1-O1, 010–Mg-H_2 and 010–Fe–H_2 complexes. Pure potential adsorption energy (ΔE_{el}), estimate of the contribution of dispersion to the adsorption energy (ΔE_{D2}) and zero-point energy corrected (ΔU_0) adsorption energy.*

Reaction	ΔE_{el}	ΔE_{D2}*	$\Delta E_{el}+\Delta E_{D2}$	ΔU_0	$\Delta U_0+\Delta E_{D2}$
Ol(010) + 2H → 010–Fe1-Mg1	-41.2	-2.3	-43.5	-36.1	-38.4
Ol(010) + 2H → 010–Fe1-O1	-100.7	-2.6	-103.3	-90.0	-92.6
Ol(010) + 2H → 010–O2-Mg1	-95.3	-0.2	-95.5	-85.0	-85.2
Ol(010) + 2H → 010–O1-O1	-38.3	-1.3	-39.6	-25.2	-26.5
Ol(010) + 2H → 010–Mg-H_2	-111.7	-1.5	-113.2	-103.1	-104.6
Ol(010) + 2H → 010–Fe-H_2	-111.3	-1.5	-112.8	-101.8	-103.3

* Grimme's dispersion energy calculated with scaling factor to $s_6 = 1.0$.

The most stable complexes present one H atom adsorbed on the metal atom (Mg or Fe) while the other H atom is adsorbed on the neighbouring O atom; *i.e.*, 010–Fe1-O1 and 010–O2-Mg1, with ΔU_0 = -90.0 and -85.0 kcal mol^{-1}, respectively. These complexes are formed from a different route. As mentioned, the major fraction of spin density in 010–Fe1

is located on the Fe atom, thus partially oxidising iron. By adsorbing the second H atom on the O atom close to Fe atom (forming an O–H bond), the H atom transfers its electron to Fe atom, resulting in H^+ and a partial reduction of iron to its initial oxidation state (Appendix B includes the whole set of net Mulliken charges and spin densities for all considered complexes). On the other hand, the unpaired electron in the 010–O2 adduct is localized on the uppermost Mg atom and, accordingly, the second H atom is adsorbed on Mg to form Mg–H. Therefore, the large stability is due to the formation of both hydride (Mg–H or Fe–H) and proton (Si–OH) groups.

Table 3.23 *Net charges and electronic spin densities on the H, Fe and Mg atoms, and the sum of the spin density values of the O atoms closest to H, computed at B2//B1 level for the different doubly-H adsorptions on Ol(010) (H^{1st} and H^{2nd} denotes the first and second H position according to the nomenclature of the complex, respectively).*

	Charge					Spin				
	H^{1st}	H^{2nd}	Fe	Mg	O	H^{1st}	H^{2nd}	Fe	Mg	O
010–Fe1-Mg1	+0.07	-0.27	+1.35	+1.02	-1.18	-0.96	0.19	4.59	-0.03	0.21
010–Fe1-O1	+0.33	-0.43	+0.97	+1.11	-1.13	0.00	-0.04	4.00	0.00	0.04
010–Fe1-O2	+0.34	-0.23	+1.34	+0.46	-1.12	-0.01	0.20	4.57	-0.96	0.19
010–O1-Mg1	-0.31	+0.34	+1.20	+0.78	-1.13	0.00	0.00	3.91	0.00	0.08
010–O2-Mg1	-0.34	+0.34	+1.21	+0.79	-1.13	0.00	0.00	3.92	0.00	0.08
010–O1-O1	+0.29	+0.29	-0.13	+1.14	-1.05	-0.03	-0.03	4.06	0.00	0.00
010–O1-O2	+0.31	+0.29	+0.54	+0.47	-1.05	-0.03	0.03	4.88	-0.92	0.04
010–O2-O2	+0.30	+0.30	+1.22	-0.16	-1.05	0.00	0.00	3.92	0.00	0.08

Moreover, the larger stability of 010–Fe1-O1 and 010–O2-Mg1 with respect to the other complexes with this kind of hydride/proton character (ΔU_0 = -67.7 and -40.5 kcal mol^{-1}, see Appendix B), is due to the presence of the dihydrogen bond between the H^- and H^+ ad-atoms, which is confirmed by their net charges (+0.33 and –0.43|e|, and –0.34 and +0.34|e|, respectively). The intermediate adsorption energy of 010–Fe1-Mg1 (ΔU_0 = -36.1 kcal mol^{-1}) is mainly due to the high adsorption energy coming from 010–Fe1 adduct. The adsorption energy of 010–O1-O1 is the less favourable (ΔU_0 = -25.2 kcal mol^{-1}; remaining complexes presenting double O chemisorption have values of -13.3 and -6.5 kcal mol^{-1}, see Appendix B). This low stability is due to the presence of two silanol (SiOH) groups, which partially breaks two Mg–O surface bonds.

3.4.4. H_2 Formation

H_2 adsorbed on Ol(010) offers two structures: one in which the interaction is with the uppermost Mg atom (010–Mg-H_2) and the other on the Fe atom (010–Fe-H_2), which are shown in Figure 3.29. The computed adsorption energy at quintet spin state (ΔU_0 = -1.3 and ~0 kcal mol^{-1}, respectively) indicates they are very weakly bound $H_2\cdots$Ol(010) adducts (Appendix B includes the whole adsorption energies calculated at B1 and B2//B1). Regardless of this weak interaction, the reaction energy for the H_2 formation through Ol(010) + 2H → 010–M-H_2 (M = Mg or Fe) is very large and negative (about -103 kcal mol^{-1}, see Table 3.22). Table 3.24 shows the reaction energies for the H_2 formation from the 2H/Ol(010) complexes presented in Figure 3.29 (in Appendix B the reaction energies at B1 and B2//B1 basis set and at quintet and septet spin state). In all cases the reaction is favourable, *i.e.* the reaction energies are negative, resulting in exoergic processes. Despite the exoergic character of the 010–O1-O1 complex, the reaction is expected to exhibit very high-energy barriers because the recombination of two H atoms with an H^+ character (entailing a significant electronic and structural reorganization) prevents any occurrence of the process. Similar situations were already found for the H_2 formation on Fo(010) [247]. The reaction through the three other complexes shows significantly smaller energy-barrier processes, as either present the H^+ and H^- surface groups (010–Fe1-O1 and 010–O2-Mg1) or one H atom is physisorbed (010–Fe1-Mg1) so it can easily recombine with its H partner.

Table 3.24 *BHLYP reaction energies (in kcal mol^{-1}) calculated at the B2//B1 level for the H_2 formation from the 2H/Ol(010) complexes on Ol(010) at quintet spin state. Pure potential adsorption energy (ΔE_{el}), estimate of the contribution of dispersion to the adsorption energy (ΔE_{D2}) and zero-point energy corrected (ΔU_0) adsorption energy.*

Reaction	ΔE_{el}	ΔE_{D2}*	$\Delta E_{el}+\Delta E_{D2}$	ΔU_0	$\Delta U_0+\Delta E_{D2}$
010–Fe1-Mg1 → 010–Fe-H_2	-70.1	0.8	-69.3	-65.7	-64.9
010–O2-Mg1 → 010–Mg-H_2	-16.4	-1.2	-17.6	-18.1	-19.3
010–Fe1-O1 → 010–Fe-H_2	-10.6	+1.1	-9.5	-11.8	-10.7
010–O1-O1 → 010–Fe-H_2	-73.0	-0.2	-73.2	-76.6	-76.8

* Grimme's dispersion energy calculated with scaling factor to $s_6 = 1.0$.

The computed energy profiles are shown in Figure 3.30. The H_2 formation from 010–Fe1-Mg1 involves a radical–hydride reaction (+0.07 and -0.27|e| net charge and -0.94 and +0.19 spin density, respectively), and exhibits very large and negative reaction energy

(around -66 kcal mol^{-1}, see Table 3.24) and very low energy barrier (around 1 kcal mol^{-1}, see Figure 3.30a), thus suggesting that the LH mechanism is feasible.

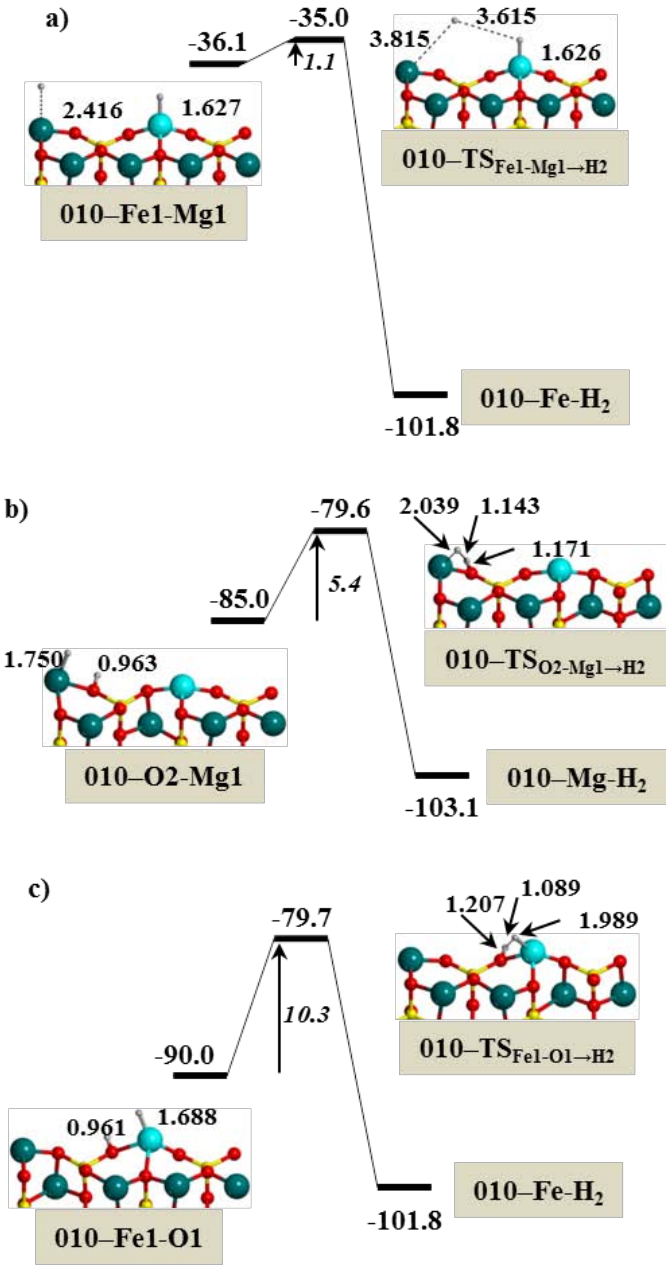

Figure 3.30 BHLYP energy profiles including ZPE corrections for the recombination of two H atoms to form H_2 on 010–Fe1-Mg1, 010–O2-Mg1 and 010–Fe1-O1 complexes calculated at B2//B1 (bond distances in Å and energies in kcal mol^{-1}). Relative energies are referenced with respect to the Ol(010) + 2H zero-energy asymptote.

H_2 formation from 010–O2-Mg1 and 010–Fe1-O1 (*i.e.*, those with O-chemisorbed states) were found to have less favourable reaction energies (-18.1 and -11.8 kcal mol^{-1}, see Table 3.24) and higher energy barriers (5.4 and 10.3 kcal mol^{-1}, see Figure 3.30b and Figure

3.30c). This is because they are the most stable complexes and H recombination is between neighbouring H^- and H^+ atoms belonging to the surface Mg–H or Fe–H and SiOH groups, respectively (*vide supra*), in which chemical bonds breakings are involved.

3.4.5. Comparison with (010) Mg_2SiO_4 Surface

H adsorption can occur either on the uppermost metal atoms (Mg or Fe) or on the most exposed surface oxygen atoms. According to the results obtained, H physisorption exclusively takes place on the outermost Mg ion, while adsorption on the O and Fe ions leads to chemisorbed states. The major difference between forsterite and Fe-containing surfaces is the larger adsorption energy when the H atom interacts directly with the Fe atom (010–Fe1 adduct, ΔU_0 ~ 34 kcal mol^{-1}), compared to the other singly H-adsorbed adducts ($\Delta U_0 \leq$ 10 kcal mol^{-1}). This is because Fe atom has an open-shell electronic structure, which makes the interaction with a radical species such as a hydrogen atom stronger than with Mg and O atoms. Thus, surface diffusion of hydrogen is limited at the ISM temperatures even more with the presence of iron in the silicate surface. Due to the high energy barriers for the H atom jumps through the different chemisorption sites ($\Delta U_0^{\ddagger}$ of 20 and 40 kcal mol^{-1}), H can only displace on the surface through adsorption–desorption steps, in line with the Mg-rich (010) forsterite surface.

The Langmuir-Hinshelwood recombination of the H ad-atoms to form a H_2 molecule from the doubly H-adsorbed adducts seems feasible on the Ol(010) surface. In order to find out what is the role of iron in the formation of molecular hydrogen, a comparison between forsterite and Fe-containing surfaces has been carried out. For a better comparison, the energy profiles corresponding to the H_2 formation on Ol(010) have been recalculated at the B3LYP level of theory, adopting the same methodology employed with Fo(010). Table 3.25 shows the potential energy barriers and reaction energies of those complexes which are homologous to both surfaces. Results from the reactions involving metal adsorbed H atoms (*i.e.*, those derived from 010–Mg2a-Mg2b and 010–Fe1-Mg1) show that the energy barriers are very similar on forsterite and on Fe-containing system ($\Delta E^{\ddagger}$ = 1.8 and 1.6 kcal mol^{-1}, respectively), whereas the reaction energies are significantly different, being much more negative on forsterite (ΔE = -105.8 and -67.5 kcal mol^{-1}, respectively), due to the

larger stability of 010–Fe1-Mg1 than 010–Mg2a-Mg2b as initial reactants. Despite these differences, for both systems the formation of H_2 through LH mechanism is favourable.

Table 3.25 *Energy barriers ($\Delta E^{\ddagger}$) and reaction energies (ΔE) (only the contribution to the electronic energy, in kcal mol^{-1}) for the H_2 formation on Ol(010), using the BHLYP and B3LYP functionals (at the BHLYP/B2//BHLYP/B1 and B3LYP/B2//B3LYP/B1 theory level, respectively) and on Fo(010)* [247], *using the B3LYP functional (at B3LYP/B2//B3LYP/B1 theory level).*

		$\Delta E^{\ddagger}$		ΔE	
Reaction	Surface	BHLYP	B3LYP	BHLYP	B3LYP
010–Mg2a-Mg2b → 010–H_2	Fo(010)	---	1.8	---	-105.8
010–Fe1-Mg1 → 010–Fe-H_2	Ol(010)	1.6	1.6	-70.1	-67.5
010–O1a-Mg2a → 010–H_2	Fo(010)	---	5.5	---	-14.8
010–O2-Mg1 → 010–Mg-H_2	Ol(010)	8.1	4.1	-16.4	-15.1
010–Fe1-O1 → 010–Fe-H_2	Ol(010)	13.2	10.4	-10.6	-13.4

Those reactions involving O-chemisorbed H atoms (010–O1a-Mg2a, 010–O2-Mg1 and 010–Fe1-O1) have very similar reaction energies, between -13 and -15 kcal mol^{-1}. As far as the reaction energy is concerned, differences can be observed. Comparing the 010–O2-Mg1 and 010–O1a-Mg2a complexes, in which both hydrogens are adsorbed onto a contiguous Mg and O atoms, the former presents an energy barrier 1.4 kcal mol^{-1} lower than the latter (4.1 and 5.5 kcal mol^{-1}, respectively), suggesting that iron (only present in the former) exerts a minor influence in the energy barrier when it acts as spectator. However, the energy barrier from 010–Fe1-O1 is significantly higher than 010–O1a-Mg2a (10.4 and 5.5 kcal mol^{-1}, respectively) because of the stronger Fe–H interaction compared to the Mg–H one. According to these results, if the H_2 formation takes place following a Langmuir-Hinshelwood mechanism through an O-chemisorbed H-atom coupling, the presence of iron hinders the process.

As a final point, the trend of the kinetics of the different H hopping and H recombination on the Fe-containing surface has been studied. For each surface process the crossover temperature (T_X) has been determined [182] and by means of Eyring's equation the Arrhenius plots of $k^{\text{SC-TST}}$ represented. Transmission coefficients have been estimated using the formula by Fermann and Auerbach [182] (above Tx, $\kappa(T) = 1$ is considered). Calculated T_X values, together with the values of $\Delta U_0^{\ddagger}$ and $\nu^{\ddagger}$ used, are shown in Table 3.26 and the Arrhenius plots between 150 and 450 K are represented in Figure 3.31.

Table 3.26 *BHLYP zero-point energy corrected energy barriers ($\Delta U_0^{\ddagger}$, in kcal mol^{-1}) at the B2//B1 level, transition frequencies ($\nu^{\ddagger}$, in cm^{-1}) and tunnelling crossover temperatures (T_X, in K) on Ol(010).*

	Reaction	$\Delta U_0^{\ddagger}$	$\nu^{\ddagger}$	T_X
Figure 3.28a	010–Mg1 → 010–O2	7.1	1272	308
Figure 3.28a	010–O2 → 010–O1	39.7	1795	417
Figure 3.28a	010–O1 → 010–Fe1	19.9	1284	300
Figure 3.28b	Ol(010) + H → 010–O1	15.7	2422	583
Figure 3.30a	010–Fe1-Mg1 → 010–Fe-H_2	1.1	82	19
Figure 3.30b	010–O2-Mg1 → 010–Mg-H_2	5.4	1405	350
Figure 3.30c	010–Fe1-O1 → 010–Fe-H_2	10.3	1445	346

For the processes related to the interconversion between the different H-adsorption sites on the Ol(010) surface (Figure 3.31a), tunnelling contributions are expected to be important in the range of the considered temperatures for the 010–Mg1 → 010–O2, 010–O2 → 010–O1 and 010–O1 → 010–Fe1 H hopping, whose calculated T_X values are 308, 417 and 300 K, respectively (see Table 3.26). Indeed, the corresponding Arrhenius plots show a notorious slope change below these T_x, in which $\log_{10}(k^{\text{SC-TST}})$ remain relatively constant as happens in regimes dominated by tunnelling. However, the processes have different rates at these range of temperatures since the calculated $\log_{10}(k^{\text{SC-TST}})$ values are clearly different, about 7, -8 and -2, respectively, at 150 K. Therefore, while the 010–Mg1 → 010–O2 process is fast, the 010–O2 → 010–O1 and 010–O1 → 010–Fe1 H jumps are kinetically hindered at the interstellar temperatures, in agreement also with the corresponding energy barriers ($\Delta U_0^{\neq}$ = 7.1, 39.7 and 19.9 kcal mol^{-1}, respectively). This is at variance with the Ol(010) + H → 010–O1 direct H-adsorption path (T_X = 583 K), where no slope change is observed because $T_X > [150, 450\ K]$. Although the corresponding energy barrier is rather high ($\Delta U_0^{\neq}$ = 15.7 kcal mol^{-1}), the process is fast (the calculated $\log_{10}(k^{\text{SC-TST}})$ between 6.5 and 7.5 at the range of temperatures).

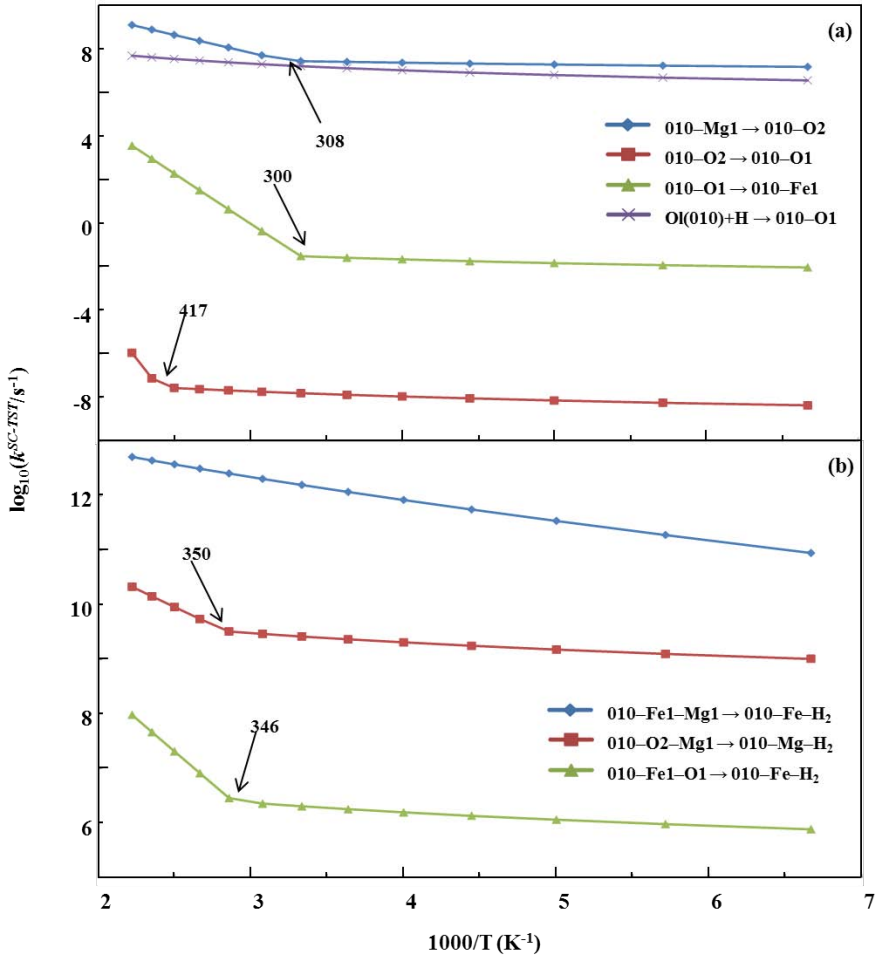

Figure 3.31 Arrhenius plots of $k^{\text{SC-TST}}$ between 150 and 450 K on Ol(010). Crossover temperatures (T_X) are indicated for each process in the interconversion between the different adsorption states (a) and in the recombination of two H atoms to form H_2 (b). Above T_X, $\kappa(T) = 1$ is considered.

For the processes related to H recombination to form H_2 on the Ol(010) surface (Figure 3.31b), it is found that the T_X for the 010–Fe1-Mg1 → 010–Fe-H_2 is about 19 K (see Table 3.26) and accordingly no slope change is observed in the Arrhenius plot, in line with the 010–Mg2a-Mg2b H recombination complex on Fo(010) (T_X = 108 K), which are not affected by tunnelling. For the rest of the processes implicated in the H_2 formation (*i.e.*, 010–O2-Mg1 → 010–Mg-H_2 and 010–Fe1-O1 → 010–Fe-H_2), tunnelling effects seem to be significant due to the slope change at its crossover temperature (T_X = 350 and 346 K, respectively), consistent also with the 010–O1a-Mg2a H recombination process on forsterite (T_X = 320 K). Nevertheless, the calculated $\log_{10}(k^{\text{SC-TST}})$ values of all H recombination complexes on the Fe-containing surface, although they indicate that the H_2 formation processes are fast, about 11, 9 and 6, respectively (at 150 K), in agreement with the corresponding energy barriers ($\Delta U_0^{\neq}$ = 1.1, 5.4 and 10.3 kcal mol^{-1}, respectively), they

are not as fast as on forsterite surfaces, with $\log_{10}(k^{SC\text{-}TST})$ values of 13 and 12 for the 010–Mg2a-Mg2b and 010–O1a-Mg2a H recombination processes, respectively, at 150 K. As a result, those reactions of H_2 formation occurring on forsterite, despite the relevance of tunnelling effects, are faster at 150 K than those reactions occurring on the Fe-containing system.

3.4.6. Final Remarks

In order to identify the functional that better describes the interactions between iron and the hydrogen atom, H adsorption and the subsequent recombination is considered accordingly a previous calibration study. In almost all DFT functionals, the sextet spin state is more stable than quartet, trend that is increased at larger percentage of exact exchange. Comparing those functionals with a percentage between 25 and 50 % have $E_{sextet} - E_{quartet}$ values in closer proximity to the reference CCSD(T) method. As a result, we finally decided to take the BHLYP as the funcional to calculate the H adsorption and subsequent recombination on Fe-containing systems.

On the Fe-containing (010) forsterite surface, H atom can interact with the uppermost Mg or Fe metal atoms or through the most exposed O atoms, forming a silanol (Si–OH) group. While on the Mg atom the H adsorption is clearly a physisorbed state, the rest of the adsorption are chemisorbed states due to the larger adsorption energies, the typical H distances and mainly the value of the spin density on the adsorbed H atom is zero. In the cases where the H atom is adsorbed closer to the Fe atom, the former acquires a character of proton or hydride and the latter undergoes a partial reduction or oxidation, respectively, according to atomic charges and spin densities. Because of the strongest chemisorbed states, the H diffusion is limited from the physisorption to the O-chemisorbed H jump process, whereas the rest of the chemisorbed H jumps processes have very high energy barriers for the ISM conditions.

For the doubly-H adsorption, the most stable complexes present one H atom adsorbed on the metal atom (Mg or Fe) while the other H atom is adsorbed on the neighbouring O atom, thus forming both hydride (Mg–H or Fe–H) and proton (Si–OH) groups. Additionally, the presence of the dihydrogen bond between hydride and proton adsorbed H atoms promotes

larger stabilities. However, these complexes envisage higher energy barriers than a less stable complex where one H atom is physisorbed. Whereas that the former ones are the most stable complexes and their H recombination requires chemical bonds breaking, the latter one involves a radical-hydride reaction.

To conclude, represented Arrhenius plots between 450 and 150 K indicate that tunnelling contributions are expected to be important in the range of the considered temperatures for the processes related to the H hopping. However, those processes with the highest energy barriers are kinetically hindered, that is, the interconversion between the chemisorbed states. For the processes related to the H recombination, tunnelling effects seem to be significant due to the slope change at its crossover temperature only for the doubly-H chemisorbed complexes, while the radical-hydride complex is not affected by tunnelling. Nevertheless, all the processes are fast in agreement with the corresponding energy barriers.

4. Conclusions

This thesis has focussed on understanding the adsorption of atomic hydrogen and the formation of molecular hydrogen on crystalline olivine surfaces. Specifically, we have used quantum mechanical calculations based on periodic density functional theory to provide a more complete scenario to elucidate how these processes in the ISM environment take place. With the presented results, answering a set of questions is aimed:

- What is the role of the silicates in the formation of molecular hydrogen?

In the gas phase, H_2 formation through the $2H \rightarrow H_2$ reaction is barrierless, while on silicate surfaces the process has energy barrier. Therefore, it seems that silicates do not act as catalysts but inhibit kinetically the reaction. However, in the gas phase the formed H_2 molecule cannot release its excess of energy and this induces its dissociation. The presence of silicates overcome this problem because they can act as third bodies that quickly absorb the nascent energy, hence avoiding H_2 dissociation. Silicates can also act as hydrogen collector, which is of paramount importance in scenarios such as the diffuse interstellar medium. Moreover, the strenghness of H interaction significantly affect the role of silicate. For chemisorbed H atoms, silicates act as H reservoirs because H_2 formation is relatively expensive; in contrast, for physisorbed H atoms, silicates act as platforms where the reactions can take place and H_2 formation occurs readily. As a result, the role of silicates is very important to nascent molecular hydrogen from atomic hydrogen by acting as third body and as H collector.

- How important is the different morphology of the crystal in the processes?

The crystallographic (010) face, the more stable and extended orientation of forsterite, has a very regular and homogeneous surface structure without almost any reconstructions, which results in low H adsorption energies compared to those obtained for the other studied (001) and (110) crystallographic faces. These two latter surfaces have more irregular morphologies, with major structural reconstructions, resulting in heterogeneity that causes stronger adsorption processes. On the (010) surface, two feasible paths were

identified, based on a radical-radical H coupling and on a $H^{+}\cdots H^{-}$ recombination. In contrast, on the (001) surface, all reaction paths resulted to be energetically unfavourable due to the larger di-adsorption energies, whereas for the (110) surface, only the $H^{+}\cdots H^{-}$ recombination path has been elucidated as favourable. These results may show the different chemical behaviour towards H adsorption and recombination as a function of surface morphology and stability.

- What is the effect of iron in the H_2 formation?

Iron has a similar role as the less stable forsterite surface. H interaction with iron is stronger than with the other atoms on the Fe-containing (010) surface. This indicates that Fe-containing silicates act as good reservoirs. Recombination involving Fe–H or Mg–H present similar energy barriers to Mg–H/Mg–H in forsterite, indicating that the formation of H_2 through this mechanism is favourable in the presence of iron. In contrast, reaction involving Fe–H/O–H presents higher energy barriers than reacting involving Mg–H/O–H in forsterite, probably because of the stronger Fe–H interaction than the Mg–H one. According to this, if the H_2 formation takes place following this mechanism through this path, the reaction is more expensive in terms of energy barriers.

- How important are tunnelling effects in the processes?

In general, tunnelling is important basically in processes dominated by chemisorbed states, in which bond breaking is expensive. In the case of H diffusion, jumps between Mg atoms in (010) and (001) forsterite surfaces and the jump from Mg atom to an O atom on the (110) surface, are processes where tunnelling seems to be irrelevant, whereas the other processes, which involve up to two chemisorbed atoms, are clearly governed by tunneling. Similars facts occur in the formation of H_2, only recombinations from H di-adsorptions on metal centers, in which at least one H atom is physisorbed, are not under the effects of tunnelling, while this is indeed the case of rest of the recombinations.

To sum up, two future prospects can be adressed as a result of the present thesis to study hydrogen adsorption and subsequent recombination. On one hand, on surfaces of amorphous silicates. Dust grains formed by crystalline silicates are present in the interstellar medium; however, many of them are present in an amorphous state due to shocks and impacts suffered. Therefore, once provided to the current situation clues about the formation of H_2 with this thesis, modeling an amorphous material and understanding the role of defects produced may help to understand the complexity of these phenomena.

On the other hand, on other silicate minerals. In this thesis only it has been considered the forsterite mineral as one of the most abundant crystalline silicates in the ISM, but other silicate minerals may provide additional information to these processes. One is the enstatite ($MgSiO_3$), the magnesium endmember of the pyroxene silicate mineral series. Enstatite is one of the few silicate minerals that have been observed in crystalline form outside our Solar System, particularly around evolved stars and Planetary Nebulae, and is thought to be one of the early stages for the formation of crystalline silicates in space. The other major family are phyllosilicate minerals, such as serpentine, clay minerals, mica and chlorite groups. They are found near some planetary surfaces and have been important to life and many theories of abiogenesis involve them. All phyllosilicate minerals are hydrated, with either water or hydroxyl groups attached, which gives a greater number of physisorption phenomena and therefore more likely to occur radical-radical coupling.

In any case, results are very sensitive both to the method of calculation and to the surface model used. In previous works, Kerkeni and Bromley [105] used the mPWB1K functional and a nanocluster surface model, and Goumans and coworkers [109] also used the same mPWB1K density functional method in an embedded cluster approach. In both cases different energy results were identified, mainly in the energy barriers. This is of significance because the energetic results provided by quantum chemical calculations can be used in numerical astrochemical models as input data. So, the sparce of energetic results can dramatically affect the predictions and trends provided by the numerical models.

5. References

[1] A. G. G. M. Tielens, “The Molecular Universe,” *Rev. Mod. Phys.*, vol. 85, no. 3, pp. 1021–1081, 2013.

[2] T. J. Millar and D. A. Williams, *Dust and Chemistry in Astronomy*, 1st ed. London: Institute of Physics, 1993.

[3] H. Y. McSween Jr. and G. R. Huss, *Cosmochemistry*. Cambridge University Press, 2010.

[4] J. E. Dyson and D. A. Williams, *The Physics of the Interstellar Medium*, 2nd ed. Bristol: Institute of Physics, 1997.

[5] T. P. Snow and B. J. McCall, “Diffuse Atomic and Molecular Clouds,” *Annu. Rev. Astron. Astrophys.*, vol. 44, no. 1, pp. 367–414, 2006.

[6] J. M. Dickey and R. W. Garwood, “The Mass Spectrum of Interstellar Clouds,” *Astrophys. J.*, vol. 341, pp. 201–207, 1989.

[7] P. Swings and L. Rosenfeld, “Considerations Regarding Interstellar Molecules,” *Astrophys. J.*, vol. 86, no. 4, pp. 483–486, 1937.

[8] H. Liszt and R. Lucas, “Comparative Chemistry of Diffuse Clouds - II. CN, HCN, HNC, CH3CH and N2H+,” *Astron. Astrophys.*, vol. 370, no. 2, pp. 576–585, 2001.

[9] J. P. Maier, N. M. Lakin, G. A. H. Walker, and D. A. Bohlender, “Detection of C3 in Diffuse Interstellar Clouds,” *Astrophys. J.*, vol. 553, no. 1, pp. 267–273, 2001.

[10] J. A. Thorburn, L. M. Hobbs, B. J. McCall, T. Oka, D. E. Welty, S. D. Friedman, T. P. Snow, P. Sonnentrucker, and D. G. York, “Some Diffuse Interstellar Bands Related to Interstellar C2 Molecules,” *Astrophys. J.*, vol. 584, no. 1, pp. 339–356, 2003.

[11] B. J. McCall, T. R. Geballe, K. H. Hinkle, and T. Oka, “Detection of H3+ in the Diffuse Interstellar Medium Toward Cygnus OB2 No. 12,” *Science (80-.).*, vol. 279, no. 5358, pp. 1910–1913, 1998.

[12] E. Herbst and E. F. van Dishoeck, “Complex Organic Interstellar Molecules,” *Annu. Rev. Astron. Astrophys.*, vol. 47, no. 1, pp. 427–480, 2009.

[13] A. G. G. M. Tielens, *The Physics and Chemistry of the Interstellar Medium*. Cambridge University Press, 2005.

[14] E. A. Bergin, P. F. Goldsmith, R. L. Snell, and W. D. Langer, “The Chemical Composition and Evolution of Giant Molecular Cloud Cores: A Comparison of Observation and Theory,” *Astrophys. J.*, vol. 482, no. 1, pp. 285–297, 1997.

[15] T. J. Millar, C. M. Leung, and E. Herbst, “How Abundant are Complex Interstellar Molecules?,” *Astron. Astrophys.*, vol. 183, pp. 109–117, 1987.

[16] T. I. Hasegawa, E. Herbst, and C. M. Leung, “Models of Gas-Grain Chemistry in Dense Interstellar Clouds with Complex Organic Molecules,” *Astrophys. J. Suppl. Ser.*, vol. 82, no. 1, pp. 167–195, 1992.

[17] A. Leger, M. Jura, and A. Omont, “Desorption from Interstellar Grains,” *Astron. Astrophys.*, vol. 144, no. 1, pp. 147–160, 1985.

[18] M. P. Collings, J. W. Dever, H. J. Fraser, M. R. S. McCoustra, and D. A. Williams, “Carbon Monoxide Entrapment in Interstellar Ice Analogs,” *Astrophys. J.*, vol. 583, no. 2, pp. 1058–1062, 2003.

[19] S. A. Sandford and L. J. Allamandola, “The Physical and Infrared Spectral Properties of CO2 in Astrophysical Ice Analogs,” *Astrophys. J.*, vol. 355, pp. 357–372, 1990.

[20] P. Caselli, E. Keto, L. Pagani, Y. Aikawa, U. A. Yıldız, F. F. S. van der Tak, M. Tafalla, E. A. Bergin, B. Nisini, C. Codella, E. F. van Dishoeck, R. Bachiller, A. Baudry, M. Benedettini, A. O. Benz, P. Bjerkeli, G. A. Blake, S. Bontemps, J. Braine, S. Bruderer, J. Cernicharo, F. Daniel, A. M. di Giorgio, C. Dominik, S. D. Doty, P. Encrenaz, M. Fich, A. Fuente, T. Gaier, T. Giannini, J. R. Goicoechea, T. de Graauw, F. Helmich, G. J. Herczeg, F. Herpin, M. R. Hogerheijde, B. Jackson, T. Jacq, H. Javadi, D. Johnstone, J. K. Jørgensen, D. Kester, L. E. Kristensen, W. Laauwen, B. Larsson, D. Lis, R. Liseau, W. Luinge, M. Marseille, C. McCoey, A. Megej, G. J. Melnick, D. A. Neufeld, M. Olberg, B. Parise, J. C. Pearson, R. Plume, C. Risacher, J. Santiago-García, P. Saraceno, R. Shipman, P. Siegel, T. A. van Kempen, R. Visser, S. F. Wampfler, and F. Wyrowski, “Water Vapor Toward Starless Cores: The Herschel View,” *Astron. Astrophys.*, vol. 521, p. L29, 2010.

[21] P. Hily-Blant, S. Maret, A. Bacmann, S. Bottinelli, B. Parise, E. Caux, A. Faure, E. A. Bergin, G. A. Blake, A. Castets, C. Ceccarelli, J. Cernicharo, A. Coutens, N. Crimier, K. Demyk, C. Dominik, M. Gerin, P. Hennebelle, T. Henning, C. Kahane, A. Klotz, G. J. Melnick, L. Pagani, P. Schilke, C. Vastel, V. Wakelam, A. Walters, A. Baudry, T. A. Bell, M. Benedettini, A. Boogert, S. Cabrit, P. Caselli, C. Codella, C. Comito, P. Encrenaz, E. Falgarone, A. Fuente, P. F. Goldsmith, F. Helmich, E. Herbst, T. Jacq, M. Kama, W. D. Langer, B. Lefloch, D. Lis, S. Lord, A. Lorenzani, D. A. Neufeld, B. Nisini, S. Pacheco, T. Phillips, M. Salez, P. Saraceno, K. Schuster, X. Tielens, F. F. S. van der Tak, M. H. D. van der Wiel, S. Viti, F. Wyrowski, and H. Yorke, “Nitrogen Hydrides in the Cold Envelope of IRAS 16293-2422,” *Astron. Astrophys.*, vol. 521, p. L52, 2010.

[22] D. A. Williams and S. Viti, “Recent Progress in Astrochemistry,” *Annu. Rep. Prog. Chem., Sect. C Phys. Chem.*, vol. 98, pp. 87–120, 2002.

[23] S. S. Prasad and S. P. Tarafdar, “UV Radiation Field Inside Dense Cluds: Its Possible Existence and Chemical Implications,” *Astrophys. J.*, vol. 267, pp. 603–609, 1983.

[24] R. Gredel, S. Lepp, A. Dalgarno, and E. Herbst, "Cosmic-Ray-Induced Photodissociation and Photoionization Rates of Interstellar Molecules," *Astrophys. J.*, vol. 347, pp. 289–293, 1989.

[25] E. A. Bergin, D. A. Neufeld, and G. J. Melnick, "Formation of Interstellar Ices behind Shock Waves," *Astrophys. J. Lett.*, vol. 510, no. 2, pp. L145–L148, 1999.

[26] S. D. Rodgers and S. B. Charnley, "Chemical Evolution in Protostellar Envelopes: Cocoon Chemistry," *Astrophys. J.*, vol. 585, no. 1, pp. 355–371, 2003.

[27] L. B. D'Hendecourt, L. J. Allamandola, and J. M. Greenberg, "Time Dependent Chemistry in Dense Molecular Clouds," *Astron. Astrophys.*, vol. 152, no. 1, pp. 130–150, 1985.

[28] K. Hiraoka, T. Sato, S. Sato, N. Sogoshi, T. Yokoyama, H. Takashima, and S. Kitagawa, "Formation of Formaldehyde by the Tunneling Reaction of H with Solid CO at 10 K Revisited," *Astrophys. J.*, vol. 577, no. 1, pp. 265–270, 2002.

[29] M. Allen and G. W. Robinson, "The Molecular Composition of Dense Interstellar Clouds," *Astrophys. J.*, vol. 212, pp. 396–415, 1977.

[30] D. M. Hudgins, S. A. Sandford, L. J. Allamandola, and A. G. G. M. Tielens, "Mid- and Far-Infrared Spectroscopy of Ices: Optical Constants and Integrated Absorbances," *Astrophys. J. Suppl. Ser.*, vol. 86, no. 2, pp. 713–870, 1993.

[31] A. Dalgarno, *H2 in Space*. Cambridge University Press, 2000.

[32] J. Tennyson, *Astronomical Spectroscopy*, Vol. 2. London: Imperial College Press, 2005.

[33] D. J. Hollenbach and E. E. Salpeter, "Surface Recombination of Hydrogen Molecules," *Astrophys. J.*, vol. 163, pp. 155–164, 1971.

[34] G. R. Carruthers, "Rocket Observation of Interstellar Molecular Hydrogen," *Astrophys. J.*, vol. 161, pp. L81–L85, 1970.

[35] M. Jura, "Interstellar Clouds Containing Optically Thin H2," *Astrophys. J.*, vol. 197, pp. 575–580, 1975.

[36] J. M. Shull and S. Beckwith, "Interstellar Molecular Hydrogen," *Annu. Rev. Astron. Astrophys.*, vol. 20, pp. 163–190, 1982.

[37] J. Fischer, T. R. Geballe, H. A. Smith, M. Simon, and J. W. V. Storey, "Molecular Hydrogen Line Emission in Seyfert Galactic Nuclei," *Astrophys. J.*, vol. 320, pp. 667–675, 1987.

[38] J. H. Black and A. Dalgarno, "Interstellar H2 - The Population of Excited Rotational States and the Infrared Response to Ultraviolet Radiation," *Astrophys. J.*, vol. 203, pp. 132–142, 1976.

[39] D. R. Flower, “The Rotational Excitation of H2 by H2,” *Mon. Not. R. Astron. Soc.*, vol. 297, no. 1, pp. 334–336, 1998.

[40] J. Le Bourlot, G. P. Des Forêts, and D. R. Flower, “The Cooling of Astrophysical Media by H2,” *Mon. Not. R. Astron. Soc.*, vol. 305, no. 4, pp. 802–810, 1999.

[41] J. Le Bourlot, G. P. Des Forêts, D. R. Flower, and S. Cabrit, “New Determinations of the Critical Velocities of C-type Shock Waves in Dense Molecular Clouds: Application to the Outflow Source in Orion,” *Mon. Not. R. Astron. Soc.*, vol. 332, no. 4, pp. 985–993, 2002.

[42] J. H. Black and E. F. van Dishoeck, “Fluorescent Excitation of Interstellar H2,” *Astrophys. J.*, vol. 322, pp. 412–449, 1987.

[43] A. Sternberg, “Ultraviolet Fluorescent Molecular Hydrogen Emission,” *Astrophys. J.*, vol. 347, pp. 863–874, 1989.

[44] D. J. Hollenbach and A. G. G. M. Tielens, “Photodissociation Regions in the Interstellar Medium of Galaxies,” *Rev. Mod. Phys.*, vol. 71, no. 1, pp. 173–230, 1999.

[45] P. R. Maloney, D. J. Hollenbach, and A. G. G. M. Tielens, “X-Ray-Irradiated Molecular Gas. I. Physical Processes and General Results,” *Astrophys. J.*, vol. 466, pp. 561–584, 1996.

[46] T. A. Bell, E. Roueff, S. Viti, and D. A. Williams, “Molecular Line Intensities as Measures of Cloud Masses - I. Sensitivity of CO Emissions to Physical Parameter Variations,” *Mon. Not. R. Astron. Soc.*, vol. 371, no. 4, pp. 1865–1872, 2006.

[47] G. R. Knapp and M. Jura, “Observations of CO Emission from Diffuse Interstellar Clouds,” *Astrophys. J.*, vol. 209, pp. 782–792, 1976.

[48] T. W. Hartquist and D. A. Williams, *The Chemically Controlled Cosmos*, 1st ed. Cambridge University Press, 1995.

[49] W. Duley and D. A. Williams, *Interstellar Chemistry*. London: Academic Press, 1984.

[50] R. J. Gould and E. E. Salpeter, “The Interstellar Abundance of the Hydrogen Molecule. I. Basic Processes,” *Astrophys. J.*, vol. 138, pp. 393–407, 1963.

[51] O. Biham, I. Furman, N. Katz, V. Pirronello, and G. Vidali, “H2 Formation on Interstellar Grains in Different Physical Regimes,” *Mon. Not. R. Astron. Soc.*, vol. 296, no. 4, pp. 869–872, 1998.

[52] A. J. Farebrother, A. J. H. M. Meijer, D. C. Clary, and A. J. Fisher, “Formation of Molecular Hydrogen on a Graphite Surface Via an Eley–Rideal Mechanism,” *Chem. Phys. Lett.*, vol. 319, no. 3–4, pp. 303–308, 2000.

[53] V. Pirronello, C. Liu, L. Shen, and G. Vidali, "Laboratory Synthesis of Molecular Hydrogen on Surfaces of Astrophysical Interest," *Astrophys. J. Lett.*, vol. 475, no. 1, pp. L69–L72, 1997.

[54] V. Pirronello, O. Biham, C. Liu, L. Shen, and G. Vidali, "Efficiency of Molecular Hydrogen Formation on Silicates," *Astrophys. J. Lett.*, vol. 483, no. 2, pp. L131–L134, 1997.

[55] G. Vidali, J. E. Roser, L. Ling, E. Congiu, G. Manicò, and V. Pirronello, "The Formation of Interstellar Molecules Via Reactions on Dust Grain Surfaces," *Faraday Discuss.*, vol. 133, pp. 125–135, 2006.

[56] J. E. Roser, G. Manicò, V. Pirronello, and G. Vidali, "Formation of Molecular Hydrogen on Amorphous Water Ice: Influence of Morphology and Ultraviolet Exposure," *Astrophys. J.*, vol. 581, no. 1, pp. 276–284, 2002.

[57] S. Cazaux and A. G. G. M. Tielens, "Molecular Hydrogen Formation in the Interstellar Medium," *Astrophys. J. Lett.*, vol. 575, no. 1, pp. L29–L32, 2002.

[58] S. Cazaux and A. G. G. M. Tielens, "H2 Formation on Grain Surfaces," *Astrophys. J.*, vol. 604, no. 1, pp. 222–237, 2004.

[59] E. Habart, M. Walmsley, L. Verstraete, S. Cazaux, R. Maiolino, P. Cox, F. Boulanger, and G. P. Des Forêts, "Molecular Hydrogen," *Space Sci. Rev.*, vol. 119, no. 1–4, pp. 71–91, 2005.

[60] A. J. H. M. Meijer, A. J. Farebrother, D. C. Clary, and A. J. Fisher, "Time-Dependent Quantum Mechanical Calculations on the Formation of Molecular Hydrogen on a Graphite Surface Via an Eley−Rideal Mechanism," *J. Phys. Chem. A*, vol. 105, no. 11, pp. 2173–2182, 2001.

[61] A. J. H. M. Meijer, A. J. Fisher, and D. C. Clary, "Surface Coverage Effects on the Formation of Molecular Hydrogen on a Graphite Surface Via an Eley−Rideal Mechanism," *J. Phys. Chem. A*, vol. 107, no. 50, pp. 10862–10871, 2003.

[62] S. Morisset, F. Aguillon, M. Sizun, and V. Sidis, "Wave-Packet Study of H2 Formation on a Graphite Surface through the Langmuir–Hinshelwood Mechanism," *J. Chem. Phys.*, vol. 122, no. 19, pp. 194702–194708, 2005.

[63] S. Morisset, F. Aguillon, M. Sizun, and V. Sidis, "Quantum Dynamics of H2 Formation on a Graphite Surface through the Langmuir Hinshelwood Mechanism," *J. Chem. Phys.*, vol. 121, no. 13, pp. 6493–6501, 2004.

[64] S. Morisset, F. Aguillon, M. Sizun, and V. Sidis, "The Dynamics of H2 Formation on a Graphite Surface at Low Temperature," *Phys. Chem. Chem. Phys.*, vol. 5, no. 3, pp. 506–513, 2003.

[65] S. Morisset, F. Aguillon, M. Sizun, and V. Sidis, “Quantum Wavepacket Investigation of Eley Rideal Formation of H2 on a Relaxing Graphite Surface,” *Chem. Phys. Lett.*, vol. 378, no. 5–6, pp. 615–621, 2003.

[66] M. Rutigliano, M. Cacciatore, and G. D. Billing, “Hydrogen Atom Recombination on Graphite at 10 K Via the Eley–Rideal Mechanism,” *Chem. Phys. Lett.*, vol. 340, no. 1–2, pp. 13–20, 2001.

[67] D. Bachellerie, M. Sizun, F. Aguillon, and V. Sidis, “Effects of a Nonrigid Graphene Surface on the LH Associative Desorption of H Atoms and on the Deexcitation of Nascent H2 Molecules Colliding with Model Walls of Carbonaceous Porous Material,” *J. Phys. Chem. A*, vol. 113, no. 1, pp. 108–117, 2008.

[68] D. Bachellerie, M. Sizun, F. Aguillon, D. Teillet-Billy, N. Rougeau, and V. Sidis, “Unrestricted Study of the Eley-Rideal Formation of H2 on Graphene Using a New Multidimensional Graphene-H-H Potential: Role of the Substrate,” *Phys. Chem. Chem. Phys.*, vol. 11, no. 15, pp. 2715–2729, 2009.

[69] D. Bachellerie, M. Sizun, D. Teillet-Billy, N. Rougeau, and V. Sidis, “Eley-Rideal Formation of H2 Involving One of Two para-Chemisorbed H Atoms on a Graphite Surface,” *Chem. Phys. Lett.*, vol. 448, no. 4–6, pp. 223–227, 2007.

[70] H. C. van de Hulst, “Scattering in a Planetary Atmosphere,” *Astrophys. J.*, vol. 107, pp. 220–246, 1948.

[71] W. H. McCrea and D. McNally, “The Formation of Population I Stars, Part II. The Formation of Molecular Hydrogen in Interstellar Matter,” *Mon. Not. R. Astron. Soc.*, vol. 121, no. 2, pp. 238–251, 1960.

[72] L. Spitzer and E. G. Zweibel, “Theory of H2 Rotational Excitation,” *Astrophys. J.*, vol. 191, pp. L127–L130, 1974.

[73] I. Langmuir, “The Mechanism of the Catalytic Action of Platinum in the Reactions 2Co + O2= 2Co2 and 2H2+ O2= 2H2O,” *Trans. Faraday Soc.*, vol. 17, pp. 621–654, 1922.

[74] C. N. Hinshelwood, “Annual Reports on the Progress of Chemistry,” *Annu. Res. London Chem. Soc.*, vol. 27, p. 11, 1930.

[75] D. D. Eley and E. K. Rideal, “Parahydrogen Conversion on Tungsten,” *Nature*, vol. 146, pp. 401–402, 1940.

[76] D. D. Eley, “The Interchange of Hydrogen in the Adsorbed Film on Tungsten,” *Proc. R. Soc. London A*, vol. 178, no. 975, pp. 452–464, 1941.

[77] J. Harris and B. Kasemo, “On Precursor Mechanisms for Surface Reactions,” *Surf. Sci.*, vol. 105, no. 2–3, pp. L281–L287, 1981.

[78] B. Kerkeni and D. C. Clary, "Quantum Dynamics Study of the Langmuir–Hinshelwood H + H Recombination Mechanism and H2 Formation on a Graphene Model Surface," *Chem. Phys.*, vol. 338, no. 1, pp. 1–10, 2007.

[79] D. J. Hollenbach and E. E. Salpeter, "Surface Adsorption of Light Atoms," *J. Chem. Phys.*, vol. 53, no. 1, pp. 79–86, 1970.

[80] E. Herbst, "Three Milieux for Interstellar Chemistry: Gas, Dust, and Ice," *Phys. Chem. Chem. Phys.*, vol. 16, no. 8, pp. 3344–3359, 2014.

[81] D. W. Martin, E. W. McDaniel, and M. L. Meeks, "On the Possible Occurence of H3+ in Interstellar Space," *Astrophys. J.*, vol. 134, pp. 1012–1013, 1961.

[82] B. T. Draine, "Interstellar Dust Grains," *Annu. Rev. Astron. Astrophys.*, vol. 41, no. 1, pp. 241–289, 2003.

[83] J. S. Mathis, W. Rumpl, and K. H. Nordsieck, "The Size Distribution of Interstellar Grains," *Astrophys. J.*, vol. 217, pp. 425–433, 1977.

[84] B. T. Draine, "Infrared Emission from Dust in Shocked Gas," *Astrophys. J.*, vol. 245, pp. 880–890, 1981.

[85] B. D. Savage and K. R. Sembach, "Interstellar Abundances from Absorption-Line Observations with the Hubble Space Telescope," *Annu. Rev. Astron. Astrophys.*, vol. 34, no. 1, pp. 279–329, 1996.

[86] J. H. Oort and H. C. van de Hulst, "Gas and Smoke in Interstellar Space," *Bull. Astron. Inst. Netherlands*, vol. 10, pp. 187–204, 1946.

[87] T. Henning, "Cosmic Silicates," *Annu. Rev. Astron. Astrophys.*, vol. 48, no. 1, pp. 21–46, 2010.

[88] F. Molster and C. Kemper, "Crystalline Silicates," *Space Sci. Rev.*, vol. 119, no. 1–4, pp. 3–28, 2005.

[89] R. M. Hazen, "Effects of Temperature and Pressure on the Crystal Structure of Forsterite," *Am. Mineral.*, vol. 61, no. 11–12, pp. 1280–1293, 1976.

[90] W. A. Deer, R. A. Howie, and J. Zussman, *Introduction to the Rock-Forming Minerals*. Longman, Harlow, UK, 1992.

[91] W. D. Nesse, *Introduction to Mineralogy*. New York: Oxford University Press, 2000.

[92] J. Badro, J.-P. Rueff, G. Vankó, G. Monaco, G. Fiquet, and F. Guyot, "Electronic Transitions in Perovskite: Possible Nonconvecting Layers in the Lower Mantle," *Science (80-.).*, vol. 305, no. 5682, pp. 383–386, 2004.

[93] T. Tsuchiya, R. M. Wentzcovitch, C. R. S. da Silva, and S. de Gironcoli, "Spin Transition in Magnesiowüstite in Earth's Lower Mantle," *Phys. Rev. Lett.*, vol. 96, no. 19, p. 198501, 2006.

[94] J. Rouquette, I. Kantor, C. A. McCammon, V. Dmitriev, and L. S. Dubrovinsky, "High-Pressure Studies of (Mg0.9Fe0.1)2SiO4 Olivine Using Raman Spectroscopy, X-ray Diffraction, and Mössbauer Spectroscopy," *Inorg. Chem.*, vol. 47, no. 7, pp. 2668–2673, 2008.

[95] A. C. Reber, S. Paranthaman, P. A. Clayborne, S. N. Khanna, and A. W. Castleman, "From SiO Molecules to Silicates in Circumstellar Space: Atomic Structures, Growth Patterns, and Optical Signatures of SinOm Clusters," *ACS Nano*, vol. 2, no. 8, pp. 1729–1737, 2008.

[96] T. P. M. Goumans and S. T. Bromley, "Efficient Nucleation of Stardust Silicates Via Heteromolecular Homogeneous Condensation," *Mon. Not. R. Astron. Soc.*, vol. 420, no. 4, pp. 3344–3349, 2012.

[97] N. H. de Leeuw, S. C. Parker, C. R. A. Catlow, and G. D. Price, "Proton-Containing Defects at Forsterite {010} Tilt Grain Boundaries and Stepped," *Am. Mineral.*, vol. 85, no. 9, pp. 1143–1154, 2000.

[98] N. H. de Leeuw, "Density Functional Theory Calculations of Hydrogen-Containing Defects in Forsterite, Periclase, and α-Quartz," *J. Phys. Chem. B*, vol. 105, no. 40, pp. 9747–9754, 2001.

[99] Y. Noël, M. Catti, P. D'Arco, and R. Dovesi, "The Vibrational Frequencies of Forsterite Mg2SiO4: an All-Electron Ab Initio Study with the CRYSTAL Code," *Phys. Chem. Miner.*, vol. 33, no. 6, pp. 383–393, 2006.

[100] M. de La Pierre, R. Orlando, L. Maschio, K. Doll, P. Ugliengo, and R. Dovesi, "Performance of Six Functionals (LDA, PBE, PBESOL, B3LYP, PBE0, and WC1LYP) in the Simulation of Vibrational and Dielectric Properties of Crystalline Compounds. The Case of Forsterite Mg2SiO4," *J. Comput. Chem.*, vol. 32, no. 9, pp. 1775–1784, 2011.

[101] G. W. Watson, P. M. Oliver, and S. C. Parker, "Computer Simulation of the Structure and Stability of Forsterite Surfaces," *Phys. Chem. Miner.*, vol. 25, no. 1, pp. 70–78, 1997.

[102] N. H. de Leeuw, S. C. Parker, C. R. A. Catlow, and G. D. Price, "Modelling the Effect of Water on the Surface Structure and Stability of Forsterite," *Phys. Chem. Miner.*, vol. 27, no. 5, pp. 332–341, 2000.

[103] M. Bruno, F. R. Massaro, M. Prencipe, R. Demichelis, M. de La Pierre, and F. Nestola, "Ab Initio Calculations of the Main Crystal Surfaces of Forsterite (Mg2SiO4): A Preliminary Study to Understand the Nature of Geochemical Processes at the Olivine Interface," *J. Phys. Chem. C*, vol. 118, no. 5, pp. 2498–2506, 2014.

[104] S. Casolo, G. F. Tantardini, and R. Martinazzo, “Insights into H2 Formation in Space from Ab Initio Molecular Dynamics,” *Proc. Natl. Acad. Sci.*, vol. 110, no. 17, pp. 6674–6677, 2013.

[105] B. Kerkeni and S. T. Bromley, “Competing Mechanisms of Catalytic H2 Formation and Dissociation on Ultrasmall Silicate Nanocluster Dust Grains,” *Mon. Not. R. Astron. Soc.*, vol. 435, no. 2, pp. 1486–1492, 2013.

[106] T. P. M. Goumans and S. T. Bromley, “Hydrogen and Oxygen Adsorption on a Nanosilicate – a Quantum Chemical Study,” *Mon. Not. R. Astron. Soc.*, vol. 414, no. 2, pp. 1285–1291, 2011.

[107] S. Garcia-Gil, D. Teillet-Billy, N. Rougeau, and V. Sidis, “H Atom Adsorption on a Silicate Surface: The (010) Surface of Forsterite,” *J. Phys. Chem. C*, vol. 117, no. 24, pp. 12612–12621, 2013.

[108] C. A. Downing, B. Ahmady, C. R. A. Catlow, and N. H. de Leeuw, “The Interaction of Hydrogen with the {010} Surfaces of Mg and Fe Olivine as Models for Interstellar Dust Grains: a Density Functional Theory Study,” *Philos. Trans. R. Soc. A*, vol. 371, no. 1994, p. 20110592, 2013.

[109] T. P. M. Goumans, C. R. A. Catlow, and W. A. Brown, “Formation of H2 on an Olivine Surface: a Computational Study,” *Mon. Not. R. Astron. Soc.*, vol. 393, no. 4, pp. 1403–1407, 2009.

[110] A. D’Ercole, E. Giamello, C. Pisani, and L. Ojamäe, “Embedded-Cluster Study of Hydrogen Interaction with an Oxygen Vacancy at the Magnesium Oxide Surface,” *J. Phys. Chem. B*, vol. 103, no. 19, pp. 3872–3876, 1999.

[111] H.-Y. T. Chen, L. Giordano, and G. Pacchioni, “From Heterolytic to Homolytic H2 Dissociation on Nanostructured MgO(001) Films As a Function of the Metal Support,” *J. Phys. Chem. C*, vol. 117, no. 20, pp. 10623–10629, 2013.

[112] M. Cococcioni, A. Dal Corso, and S. de Gironcoli, “Structural, Electronic, and Magnetic Properties of Fe2SiO4 Fayalite: Comparison of LDA and GGA Results,” *Phys. Rev. B*, vol. 67, no. 9, p. 094106, 2003.

[113] W. Lottermoser, S.-U. Weber, M. Grodzicki, A. Kirfel, and G. Amthauer, “A Semi-Quantitative Approach to Derive the Electric Field Gradient, Applied to Synthetic Fayalite, α-Fe2SiO4: A Reappraisal,” *Eur. J. Mineral.*, vol. 24, no. 5, pp. 791–797, 2012.

[114] Y. Noël, M. de La Pierre, L. Maschio, M. Rérat, C. M. Zicovich-Wilson, and R. Dovesi, “Electronic Structure, Dielectric Properties and Infrared Vibrational Spectrum of Fayalite: An Ab Initio Simulation with an All-Electron Gaussian Basis Set and the B3LYP Functional,” *Int. J. Quantum Chem.*, vol. 112, no. 9, pp. 2098–2108, 2012.

[115] Y. G. Yu, V. L. Vinograd, B. Winkler, and R. M. Wentzcovitch, "Phase Equilibria of (Mg,Fe)2SiO4 at the Earth's Upper Mantle Conditions from First-Principles Studies," *Phys. Earth Planet. Inter.*, vol. 217, pp. 36–47, 2013.

[116] J. W. Stucki, K. Lee, L. Zhang, and R. A. Larson, "Effects of Iron Oxidation States on the Surface and Structural Properties of Smectites," *Pure Appl. Chem.*, vol. 74, no. 11, pp. 2145–2158, 2002.

[117] P. Komadel, J. Madejová, and J. Bujdák, "Preparation and Properties of Reduced-Change Smectites - A Review," *Clays Clay Miner.*, vol. 53, no. 4, pp. 313–334, 2005.

[118] J. W. Stucki, D. C. Golden, and C. B. Roth, "Effects of Reduction and Reoxidation of Structural Iron on the Surface Charge and Dissolution of Dioctahedral Smectites," *Clays Clay Miner.*, vol. 32, no. 5, pp. 350–356, 1984.

[119] J. W. Stucki, P. F. Low, C. B. Roth, and D. C. Golden, "Effects of Oxidation State of Octahedral Iron on Clay Swelling," *Clays Clay Miner.*, vol. 32, no. 5, pp. 357–362, 1984.

[120] M. Born and R. Oppenheimer, "Zur Quantentheorie der Molekeln," *Ann. Phys.*, vol. 389, no. 20, pp. 457–484, 1927.

[121] A. Szabo and N. Ostlund, *Modern Quantum Chemistry*. New York: Dover Publications, Inc., 1996.

[122] F. Jensen, *Introduction to Computational Chemistry*. Wiley, 2006.

[123] C. J. Cramer, *Essentials of Computational Chemistry: Theories and Models*. John Wiley & Sons, Inc., 2004.

[124] C. C. J. Roothaan, "New Developments in Molecular Orbital Theory," *Rev. Mod. Phys.*, vol. 23, no. 2, pp. 69–89, 1951.

[125] G. G. Hall, "The Molecular Orbital Theory of Chemical Valency. VIII. A Method of Calculating Ionization Potentials," *Proc. R. Soc. London A Math. Phys. Eng. Sci.*, vol. 205, no. 1083, pp. 541–552, 1951.

[126] P. Saxe, H. F. Schaefer III, and N. C. Handy, "Exact Solution (Within a Double-Zeta Basis Set) of the Schrodinger Electronic Equation for Water," *Chem. Phys. Lett.*, vol. 79, no. 2, pp. 202–204, 1981.

[127] K. F. Freed, "Many-Body Theories of the Electronic Structure of Atoms and Molecules," *Annu. Rev. Phys. Chem.*, vol. 22, pp. 313–346, 1971.

[128] R. J. Bartlett, "Many-Body Perturbation Theory and Coupled Cluster Theory for Electron Correlation in Molecules," *Annu. Rev. Phys. Chem.*, vol. 32, pp. 359–401, 1981.

[129] M. R. Hoffmann and H. F. Schaefer III, "A Full Coupled-Cluster Singles, Doubles, and Triples Model for the Description of Electron Correlation," *Adv. Quantum Chem.*, vol. 18, pp. 207–279, 1986.

[130] K. Raghavachari, G. W. Trucks, J. A. Pople, and M. Head-Gordon, "A Fifth-Order Perturbation Comparison of Electron Correlation Theories," *Chem. Phys. Lett.*, vol. 157, no. 6, pp. 479–483, 1989.

[131] K. Raghavachari and J. B. Anderson, "Electron Correlation Effects in Molecules," *J. Phys. Chem.*, vol. 100, no. 31, pp. 12960–12973, 1996.

[132] G. E. Scuseria and H. F. Schaefer III, "Is Coupled Cluster Singles and Doubles (CCSD) more Computationally Intensive than Quadratic Configuration Interaction (QCISD)?," *J. Chem. Phys.*, vol. 90, no. 7, pp. 3700–3703, 1989.

[133] R. G. Parr and W. Yang, *Density Functional Theory of Atoms and Molecules*. New York: Oxford University Press, 1989.

[134] K. Burke, "Perspective on Density Functional Theory," *J. Chem. Phys.*, vol. 136, no. 15, p. 150901, 2012.

[135] L. H. Thomas, "The Calculation of Atomic Fields," *Math. Proc. Cambridge Philos. Soc.*, vol. 23, no. 5, pp. 542–548, 1927.

[136] E. Fermi, "Eine statistische Methode zur Bestimmung einiger Eigenschaften des Atoms und ihre Anwendung auf die Theorie des periodischen Systems der Elemente," *Zeitschrift für Phys.*, vol. 48, no. 1–2, pp. 73–79, 1928.

[137] J. C. Slater, "A Generalized Self-Consistent Field Method," *Phys. Rev.*, vol. 91, no. 3, pp. 528–530, 1953.

[138] W. Kohn, "Electronic Structure of Matter-Wave Functions and Density Functionals," *Rev. Mod. Phys.*, vol. 71, no. 5, pp. 1253–1266, 1999.

[139] P. Hohenberg and W. Kohn, "Inhomogeneous Electron Gas," *Phys. Rev.*, vol. 136, no. 3B, pp. B864–B871, 1964.

[140] W. Kohn and L. J. Sham, "Self-Consistent Equations Including Exchange and Correlation Effects," *Phys. Rev.*, vol. 140, no. 4A, pp. A1133–A1138, 1965.

[141] R. M. Martin, *Electronic Structure. Basic Theory and Practical Methods*. Cambridge University Press, 2005.

[142] W. Koch and M. C. Holthausen, *A Chemist's Guide to Density Functional Theory*, 2nd ed. WILEY-VCH Verlag, 2001.

[143] P. A. M. Dirac, "Note on Exchange Phenomena in the Thomas Atom," *Math. Proc. Cambridge Philos. Soc.*, vol. 26, no. 3, pp. 376–385, 1930.

[144] S. H. Vosko, L. Wilk, and M. Nusair, "Accurate Spin-Dependent Electron Liquid Correlation Energies for Local Spin Density Calculations: A Critical Analysis," *Can. J. Phys.*, vol. 58, no. 8, pp. 1200–1211, 1980.

[145] D. M. Ceperley and B. J. Alder, "Ground State of the Electron Gas by a Stochastic Method," *Phys. Rev. Lett.*, vol. 45, no. 7, pp. 566–569, 1980.

[146] J. C. Slater, "A Simplification of the Hartree-Fock Method," *Phys. Rev.*, vol. 81, no. 3, pp. 385–390, 1951.

[147] A. D. Becke, "Density Functional Calculations of Molecular Bond Energies," *J. Chem. Phys.*, vol. 84, no. 8, pp. 4524–4529, 1986.

[148] A. D. Becke, "Density-Functional Exchange-Energy Approximation with Correct Asymptotic-Behavior," *Phys. Rev. A*, vol. 38, no. 6, pp. 3098–3100, 1988.

[149] J. P. Perdew, "Density-Functional Approximation for the Correlation Energy of the Inhomogeneous Electron Gas," *Phys. Rev. B*, vol. 33, no. 12, pp. 8822–8824, 1986.

[150] C. Lee, W. Yang, and R. G. Parr, "Development of the Colle-Salvetti Correlation-Energy Formula into a Functional of the Electron Density," *Phys. Rev. B*, vol. 37, no. 2, pp. 785–789, 1988.

[151] J. P. Perdew, M. Ernzerhof, and K. Burke, "Rationale for Mixing Exact Exchange with Density Functional Approximations," *J. Chem. Phys.*, vol. 105, no. 22, pp. 9982–9985, 1996.

[152] K. Burke, M. Ernzerhof, and J. P. Perdew, "The Adiabatic Connection Method: a Non-Empirical Hybrid," *Chem. Phys. Lett.*, vol. 265, no. 1–2, pp. 115–120, 1997.

[153] C. Adamo and V. Barone, "Toward Reliable Density Functional Methods without Adjustable Parameters: The PBE0 Model," *J. Chem. Phys.*, vol. 110, no. 13, pp. 6158–6170, 1999.

[154] Y. Zhao and D. G. Truhlar, "The M06 Suite of Density Functionals for Main Group Thermochemistry, Thermochemical Kinetics, Noncovalent Interactions, Excited States, and Transition Elements: Two New Functionals and Systematic Testing of Four M06-Class Functionals and 12 other Function," *Theor. Chem. Acc.*, vol. 120, no. 1–3, pp. 215–241, 2008.

[155] S. Grimme, "Semiempirical GGA-Type Density Functional Constructed with a Long-Range Dispersion Correction," *J. Comput. Chem.*, vol. 27, no. 15, pp. 1787–1799, 2006.

[156] M. Sodupe, J. Bertran, L. Rodríguez-Santiago, and E. J. Baerends, "Ground State of the (H2O)2+ Radical Cation: DFT versus Post-Hartree−Fock Methods," *J. Phys. Chem. A*, vol. 103, no. 1, pp. 166–170, 1999.

[157] J. Poater, M. Solà, A. Rimola, L. Rodríguez-Santiago, and M. Sodupe, "Ground and Low-Lying States of Cu2+−H2O. A Difficult Case for Density Functional Methods," *J. Phys. Chem. A*, vol. 108, no. 28, pp. 6072–6078, 2004.

[158] F. Starrost and E. A. Carter, "Modeling the Full Monty: Baring the Nature of Surfaces Across Time and Space," *Surf. Sci.*, vol. 500, no. 1–3, pp. 323–346, 2002.

[159] M. Svensson, S. Humbel, R. D. J. Froese, T. Matsubara, S. Sieber, and K. Morokuma, "ONIOM: A Multilayered Integrated MO + MM Method for Geometry Optimizations and Single Point Energy Predictions. A Test for Diels−Alder Reactions and Pt(P(t-Bu)3)2 + H2 Oxidative Addition," *J. Phys. Chem.*, vol. 100, no. 50, pp. 19357–19363, 1996.

[160] T. Vreven and K. Morokuma, "On the Application of the IMOMO (Integrated Molecular Orbital + Molecular Orbital) Method," *J. Comput. Chem.*, vol. 21, no. 16, pp. 1419–1432, 2000.

[161] F. Maseras and K. Morokuma, "IMOMM: A New Integrated Ab Initio + Molecular Mechanics Geometry Optimization Scheme of Equilibrium Structures and Transition States," *J. Comput. Chem.*, vol. 16, no. 9, pp. 1170–1179, 1995.

[162] M. Sierka and J. Sauer, "Finding Transition Structures in Extended Systems: A Strategy Based on a Combined Quantum Mechanics–Empirical Valence Bond Approach," *J. Chem. Phys.*, vol. 112, no. 16, pp. 6983–6996, 2000.

[163] U. Eichler, C. M. Kölmel, and J. Sauer, "Combining Ab Initio Techniques with Analytical Potential Functions for Structure Predictions of Large Systems: Method and Application to Crystalline Silica Polymorphs," *J. Comput. Chem.*, vol. 18, no. 4, pp. 463–477, 1997.

[164] C. Pisani, "Ab-Initio Approaches to the Quantum-Mechanical Treatment of Periodic Systems," in *Quantum-Mechanical Ab-Initio Calculation of the Properties of Crystalline Materials*, vol. 67, C. Pisani, Ed. Springer Berlin Heidelberg, 1996, pp. 47–75.

[165] N. W. Ashcroft and N. D. Mermin, *Solid State Physics*. Saunders, 1976.

[166] F. Bloch, "Über die Quantenmechanik der Elektronen in Kristallgittern," *Zeitschrift für Phys.*, vol. 52, no. 7–8, pp. 555–600, 1929.

[167] R. Dovesi, B. Civalleri, C. Roetti, V. R. Saunders, and R. Orlando, "Ab Initio Quantum Simulation in Solid State Chemistry," in *Reviews in Computational Chemistry*, New York: John Wiley & Sons, Inc., 2005.

[168] H. J. Monkhorst and J. D. Pack, "Special Points for Brillouin-Zone Integrations," *Phys. Rev. B*, vol. 13, no. 12, pp. 5188–5192, 1976.

[169] D. S. Sholl and J. A. Steckel, *Density Functional Theory: A Practical Introduction*. John Wiley & Sons, Inc., 2009.

[170] R. Dovesi, V. R. Saunders, C. Roetti, R. Orlando, C. M. Zicovich-Wilson, F. Pascale, B. Civalleri, K. Doll, N. M. Harrison, I. J. Bush, P. D'Arco, and M. Llunell, *CRYSTAL09 User's Manual*. Torino: University of Torino, 2010.

[171] Y. Zhao and D. G. Truhlar, "Density Functionals for Noncovalent Interaction Energies of Biological Importance," *J. Chem. Theory Comput.*, vol. 3, no. 1, pp. 289–300, 2007.

[172] M. C. Payne, M. P. Teter, D. C. Allan, T. A. Arias, and J. D. Joannopoulos, "Iterative Minimization Techniques for Ab Initio Total-Energy Calculations: Molecular Dynamics and Conjugate Gradients," *Rev. Mod. Phys.*, vol. 64, no. 4, pp. 1045–1097, 1992.

[173] J. VandeVondele, M. Krack, F. Mohamed, M. Parrinello, T. Chassaing, and J. Hutter, "Quickstep: Fast and Accurate Density Functional Calculations Using a Mixed Gaussian and Plane Waves Approach," *Comput. Phys. Commun.*, vol. 167, no. 2, pp. 103–128, 2005.

[174] M. E. Tuckerman, *Statistical Mechanics: Theory and Molecular Simulation*. New York: Oxford University Press, 2010.

[175] R. Car and M. Parrinello, "Unified Approach for Molecular Dynamics and Density-Functional Theory," *Phys. Rev. Lett.*, vol. 55, no. 22, pp. 2471–2474, 1985.

[176] S. Nosé, "A Unified Formulation of the Constant Temperature Molecular Dynamics Methods," *J. Chem. Phys.*, vol. 81, no. 1, pp. 511–519, 1984.

[177] W. G. Hoover, "Canonical Dynamics: Equilibrium Phase-Space Distributions," *Phys. Rev. A*, vol. 31, no. 3, pp. 1695–1697, 1985.

[178] G. J. Martyna, M. L. Klein, and M. E. Tuckerman, "Nosé–Hoover Chains: The Canonical Ensemble Via Continuous Dynamics," *J. Chem. Phys.*, vol. 97, no. 4, pp. 2635–2643, 1992.

[179] C. Chipot and A. Pohorille, *Free Energy Calculations*. New York: Springer-Verlag, 2007.

[180] J. G. Kirkwood, "Statistical Mechanics of Fluid Mixtures," *J. Chem. Phys.*, vol. 3, no. 5, pp. 300–313, 1935.

[181] V. I. Goldanskii, "Facts and Hypotheses of Molecular Chemical Tunnelling," *Nature*, vol. 279, no. 5709, pp. 109–115, 1979.

[182] J. T. Fermann and S. Auerbach, "Modeling Proton Mobility in Acidic Zeolite Clusters: II. Room Temperature Tunneling Effects from Semiclassical Rate Theory," *J. Chem. Phys.*, vol. 112, no. 15, pp. 6787–6794, 2000.

[183] D. G. Truhlar and B. C. Garrett, "Variational Transition State Theory," *Annu. Rev. Phys. Chem.*, vol. 35, pp. 159–189, 1984.

[184] E. Wigner, "Concerning the Excess of Potential Barriers in Chemical Reactions," *Zeitschrift für Phys. Chemie*, vol. 19, no. 2–3, pp. 203–216, 1932.

[185] R. T. Skodje and D. G. Truhlar, "Parabolic Tunneling Calculations," *J. Phys. Chem.*, vol. 85, no. 6, pp. 624–628, 1981.

[186] T. P. M. Goumans and S. Andersson, "Tunnelling in the O + CO Reaction," *Mon. Not. R. Astron. Soc.*, vol. 406, no. 4, pp. 2213–2217, 2010.

[187] T. P. M. Goumans and J. Kästner, "Hydrogen-Atom Tunneling Could Contribute to H2 Formation in Space," *Angew. Chemie Int. Ed.*, vol. 49, no. 40, pp. 7350–7352, 2010.

[188] S. Andersson, T. P. M. Goumans, and A. Arnaldsson, "Tunneling in Hydrogen and Deuterium Atom Addition to CO at Low Temperatures," *Chem. Phys. Lett.*, vol. 513, no. 1–3, pp. 31–36, 2011.

[189] T. P. M. Goumans, "Isotope Effects for Formaldehyde plus Hydrogen Addition and Abstraction Reactions: Rate Calculations Including Tunnelling," *Mon. Not. R. Astron. Soc.*, vol. 413, no. 4, pp. 2615–2620, 2011.

[190] T. P. M. Goumans, "Hydrogen Chemisorption on Polycyclic Aromatic Hydrocarbons Via Tunnelling," *Mon. Not. R. Astron. Soc.*, vol. 415, no. 4, pp. 3129–3134, 2011.

[191] T. P. M. Goumans and J. Kästner, "Deuterium Enrichment of Interstellar Methanol Explained by Atom Tunneling," *J. Phys. Chem. A*, vol. 115, no. 39, pp. 10767–10774, 2011.

[192] S. Andersson, G. Nyman, A. Arnaldsson, U. Manthe, and H. Jónsson, "Comparison of Quantum Dynamics and Quantum Transition State Theory Estimates of the H + CH4 Reaction Rate†," *J. Phys. Chem. A*, vol. 113, no. 16, pp. 4468–4478, 2009.

[193] W. H. Miller, "Semiclassical Limit of Quantum Mechanical Transition State Theory for Nonseparable Systems," *J. Chem. Phys.*, vol. 62, no. 5, pp. 1899–1906, 1975.

[194] I. Affleck, "Quantum-Statistical Metastability," *Phys. Rev. Lett.*, vol. 46, no. 6, pp. 388–391, 1981.

[195] J. B. Rommel, T. P. M. Goumans, and J. Kästner, "Locating Instantons in Many Degrees of Freedom," *J. Chem. Theory Comput.*, vol. 7, no. 3, pp. 690–698, 2011.

[196] R. Dovesi, R. Orlando, B. Civalleri, C. Roetti, V. R. Saunders, and C. M. Zicovich-Wilson, "CRYSTAL: A Computational Tool for the Ab Initio Study of the Electronic Properties of Crystals," *Zeitschrift für Krist.*, vol. 220, no. 5–6, pp. 571–573, 2004.

[197] C. Pisani, R. Dovesi, and C. Roetti, *Hartree-Fock Ab Initio Treatment of Crystalline Systems*. Berlin: Springer-Verlag, 1988.

[198] A. D. Becke, “Density-Functional Thermochemistry. III. The Role of Exact Exchange,” *J. Chem. Phys.*, vol. 98, no. 7, pp. 5648–5652, 1993.

[199] B. Civalleri, C. M. Zicovich-Wilson, L. Valenzano, and P. Ugliengo, “B3LYP Augmented with an Empirical Dispersion Term (B3LYP-D*) as Applied to Molecular Crystals,” *CrystEngComm*, vol. 10, no. 4, pp. 405–410, 2008.

[200] A. D. Boese and J. Sauer, “Accurate Adsorption Energies of Small Molecules on Oxide Surfaces: CO-MgO(001),” *Phys. Chem. Chem. Phys.*, vol. 15, no. 39, pp. 16481–16493, 2013.

[201] P. Ugliengo and A. Damin, “Are Dispersive Forces Relevant for CO Adsorption on the MgO (001) Surface?,” *Chem. Phys. Lett.*, vol. 366, no. 5–6, pp. 683–690, 2002.

[202] B. Civalleri, L. Maschio, P. Ugliengo, and C. M. Zicovich-Wilson, “Role of Dispersive Interactions in the CO Adsorption on MgO (001): Periodic B3LYP Calculations Augmented with an Empirical Dispersion Term,” *Phys. Chem. Chem. Phys.*, vol. 12, no. 24, pp. 6382–6386, 2010.

[203] J. P. Perdew, K. Burke, and M. Ernzerhof, “Generalized Gradient Approximation Made Simple,” *Phys. Rev. Lett.*, vol. 77, no. 18, pp. 3865–3868, 1996.

[204] A. D. Becke, “A New Mixing of Hartree-Fock and Local Density-Functional Theories,” *J. Chem. Phys.*, vol. 98, no. 2, pp. 1372–1377, 1993.

[205] A. Rimola, C. M. Zicovich-Wilson, R. Dovesi, and P. Ugliengo, “Search and Characterization of Transition State Structures in Crystalline Systems Using Valence Coordinates,” *J. Chem. Theory Comput.*, vol. 6, no. 4, pp. 1341–1350, 2010.

[206] M. de La Pierre, C. Carteret, R. Orlando, and R. Dovesi, “Use of Ab Initio Methods for the Interpretation of the Experimental IR Reflectance Spectra of Crystalline Compounds,” *J. Comput. Chem.*, vol. 34, no. 17, pp. 1476–1485, 2013.

[207] A. Schäfer, H. Horn, and R. Ahlrichs, “Fully Optimized Contracted Gaussian Basis Sets for Atoms Li to Kr,” *J. Chem. Phys.*, vol. 97, no. 4, pp. 2571–2577, 1992.

[208] F. Pascale, S. Tosoni, C. M. Zicovich-Wilson, P. Ugliengo, R. Orlando, and R. Dovesi, “Vibrational Spectrum of Brucite, Mg(OH)2: A Periodic Ab Initio Quantum Mechanical Calculation Including OH Anharmonicity,” *Chem. Phys. Lett.*, vol. 396, no. 4–6, pp. 308–315, 2004.

[209] K. Doll, “Implementation of Analytical Hartree–Fock Gradients for Periodic Systems,” *Comput. Phys. Commun.*, vol. 137, no. 1, pp. 74–88, 2001.

[210] C. G. Broyden, “The Convergence of a Class of Double-Rank Minimization Algorithms. I: General Considerations,” *J. Inst. Math. its Appl.*, vol. 6, no. 1, pp. 76–90, 1970.

[211] R. Fletcher, "A New Approach to Variable Metric Algorithms," *Comput. J.*, vol. 13, no. 3, pp. 317–322, 1970.

[212] D. Goldfarb, "A Family of Variable-Metric Methods Derived by Variational Means," *Math. Comput.*, vol. 24, no. 109, pp. 23–26, 1970.

[213] D. F. Shanno, "Conditioning of Quasi-Newton Methods for Function Minimization," *Math. Comput.*, vol. 24, no. 111, pp. 647–656, 1970.

[214] B. Civalleri, P. D'Arco, R. Orlando, V. R. Saunders, and R. Dovesi, "Hartree-Fock Geometry Optimisation of Periodic Systems with the CRYSTAL Code," *Chem. Phys. Lett.*, vol. 348, no. 1–2, pp. 131–138, 2001.

[215] M. Corno, C. Busco, V. Bolis, S. Tosoni, and P. Ugliengo, "Water Adsorption on the Stoichiometric (001) and (010) Surfaces of Hydroxyapatite: A Periodic B3LYP Study," *Langmuir*, vol. 25, no. 4, pp. 2188–2198, 2009.

[216] F. Pascale, C. M. Zicovich-Wilson, F. López Gejo, B. Civalleri, R. Orlando, and R. Dovesi, "The Calculation of the Vibrational Frequencies of Crystalline Compounds and its Implementation in the CRYSTAL Code," *J. Comput. Chem.*, vol. 25, no. 6, pp. 888–897, 2004.

[217] C. M. Zicovich-Wilson, R. Dovesi, and V. R. Saunders, "A General Method to Obtain Well Localized Wannier Functions for Composite Energy Bands in Linear Combination of Atomic Orbital Periodic Calculations," *J. Chem. Phys.*, vol. 115, no. 21, pp. 9708–9719, 2001.

[218] C. M. Zicovich-Wilson, F. J. Torres, F. Pascale, L. Valenzano, R. Orlando, and R. Dovesi, "Ab Initio Simulation of the IR Spectra of Pyrope, Grossular, and Andradite," *J. Comput. Chem.*, vol. 29, no. 13, pp. 2268–2278, 2008.

[219] C. M. Zicovich-Wilson, A. Bert, C. Roetti, R. Dovesi, and V. R. Saunders, "Characterization of the Electronic Structure of Crystalline Compounds through their Localized Wannier Functions," *J. Chem. Phys.*, vol. 116, no. 3, pp. 1120–1127, 2002.

[220] C. M. Zicovich-Wilson, F. Pascale, C. Roetti, V. R. Saunders, R. Orlando, and R. Dovesi, "Calculation of the Vibration Frequencies of α-Quartz: The Effect of Hamiltonian and Basis Set," *J. Comput. Chem.*, vol. 25, no. 15, pp. 1873–1881, 2004.

[221] M. Ferrero, M. Rérat, R. Orlando, and R. Dovesi, "The Calculation of Static Polarizabilities of 1-3D Periodic Compounds. The Implementation in the Crystal Code," *J. Comput. Chem.*, vol. 29, no. 9, pp. 1450–1459, 2008.

[222] M. Ferrero, M. Rérat, R. Orlando, and R. Dovesi, "Coupled Perturbed Hartree-Fock for Periodic Systems: The role of Symmetry and Related Computational Aspects," *J. Chem. Phys.*, vol. 128, no. 1, p. 14110, 2008.

[223] M. Ferrero, M. Rérat, B. Kirtman, and R. Dovesi, "Calculation of First and Second Static Hyperpolarizabilities of One- to Three-Dimensional Periodic Compounds. Implementation in the CRYSTAL Code," *J. Chem. Phys.*, vol. 129, no. 24, p. 244110, 2008.

[224] M. Ferrero, B. Civalleri, M. Rérat, R. Orlando, and R. Dovesi, "The Calculation of the Static First and Second Susceptibilities of Crystalline Urea: A Comparison of Hartree–Fock and Density Functional Theory Results Obtained with the Periodic Coupled Perturbed Hartree–Fock/Kohn–Sham Scheme," *J. Chem. Phys.*, vol. 131, no. 21, p. 214704, 2009.

[225] S. Dall'Olio, R. Dovesi, and R. Resta, "Spontaneous Polarization as a Berry Phase of the Hartree-Fock Wave Function: The Case of KNbO3," *Phys. Rev. B*, vol. 56, no. 16, pp. 10105–10114, 1997.

[226] P. Baranek, C. M. Zicovich-Wilson, C. Roetti, R. Orlando, and R. Dovesi, "Well Localized Crystalline Orbitals Obtained from Bloch Functions: The Case of KNbO3," *Phys. Rev. B*, vol. 64, no. 12, p. 125102, 2001.

[227] Y. Noël, C. M. Zicovich-Wilson, B. Civalleri, P. D'Arco, and R. Dovesi, "Polarization Properties of ZnO and BeO: An Ab Initio Study through the Berry Phase and Wannier Functions Approaches," *Phys. Rev. B*, vol. 65, no. 1, p. 14111, 2001.

[228] A. M. Ferrari, L. Valenzano, A. Meyer, R. Orlando, and R. Dovesi, "Quantum-Mechanical Ab Initio Simulation of the Raman and IR Spectra of Fe3Al2Si3O12 Almandine," *J. Phys. Chem. A*, vol. 113, no. 42, pp. 11289–11294, 2009.

[229] L. Maschio, M. Ferrabone, A. Meyer, J. Garza, and R. Dovesi, "The Infrared Spectrum of Spessartine: An Ab Initio All Electron Simulation with Five Different Functionals (LDA, PBE, PBESOL, B3LYP and PBE0)," *Chem. Phys. Lett.*, vol. 501, no. 4–6, pp. 612–618, 2011.

[230] R. Dovesi, M. de La Pierre, A. M. Ferrari, F. Pascale, L. Maschio, and C. M. Zicovich-Wilson, "The IR Vibrational Properties of Six Members of the Garnet Family: A Quantum Mechanical Ab Initio Study," *Am. Mineral.*, vol. 96, no. 11–12, pp. 1787–1798, 2011.

[231] G. Henkelman, B. P. Uberuaga, and H. Jónsson, "A Climbing Image Nudged Elastic Band Method for Finding Saddle Points and Minimum Energy Paths," *J. Chem. Phys.*, vol. 113, no. 22, pp. 9901–9904, 2000.

[232] G. J. Martyna and M. E. Tuckerman, "A Reciprocal Space Based Method for Treating Long Range Interactions in Ab Initio and Force-Field-Based Calculations in Clusters," *J. Chem. Phys.*, vol. 110, no. 6, pp. 2810–2821, 1999.

[233] J. L. Servoin and B. Piriou, "Infrared Reflectivity and Raman Scattering of Mg2SiO4 Single Crystal," *Phys. Status Solidi B*, vol. 55, no. 2, pp. 677–686, 1973.

[234] K. Iishi, "Lattice Dynamics of Forsterite," *Am. Mineral.*, vol. 63, no. 11–12, pp. 1198–1208, 1978.

[235] A. M. Hofmeister, "Single-Crystal Absorption and Reflection Infrared Spectroscopy of Forsterite and Fayalite," *Phys. Chem. Miner.*, vol. 14, no. 6, pp. 499–513, 1987.

[236] B. Reynard, "Single-Crystal Infrared Reflectivity of Pure Mg2SiO2 Forsterite and (Mg0.86,Fe0.14)2SiO4 Olivine," *Phys. Chem. Miner.*, vol. 18, no. 1, pp. 19–25, 1991.

[237] A. Chopelas, "Single Crystal Raman Spectra of Forsterite, Fayalite, and Monticellite," *Am. Mineral.*, vol. 76, no. 7–8, pp. 1101–1109, 1991.

[238] B. A. Kolesov and C. A. Geiger, "A Raman Spectroscopic Study of Fe–Mg Olivines," *Phys. Chem. Miner.*, vol. 31, no. 3, pp. 142–154, 2004.

[239] H. Suto, H. Sogawa, S. Tachibana, C. Koike, H. Karoji, A. Tsuchiyama, H. Chihara, K. Mizutani, J. Akedo, K. Ogiso, T. Fukui, and S. Ohara, "Low-Temperature Single Crystal Reflection Spectra of Forsterite," *Mon. Not. R. Astron. Soc.*, vol. 370, no. 4, pp. 1599–1606, 2006.

[240] R. D. Shannon and M. A. Subramanian, "Dielectric Constants of Chrysoberyl, Spinel, Phenacite, and Forsterite and the Oxide Additivity Rule," *Phys. Chem. Miner.*, vol. 16, no. 8, pp. 747–751, 1989.

[241] J. Decius and R. Hexter, *Molecular Vibrations in Crystals*. New York: McGraw-Hill, 1977.

[242] M. F. Hochella Jr., "Atomic Structure, Microtopography, Composition and Reactivity of Mineral Surfaces," in *Mineral-Water Interface Geochemistry*, P. H. Ribbe, Ed. Washington, DC: Reviews in Mineralogy: Mineralogical Society of America, 1990, pp. 87–132.

[243] N. H. de Leeuw, F. M. Higgins, and S. C. Parker, "Modeling the Surface Structure and Stability of α-Quartz," *J. Phys. Chem. B*, vol. 103, no. 8, pp. 1270–1277, 1999.

[244] H. Suto, C. Koike, H. Sogawa, A. Tsuchiyama, H. Chihara, and K. Mizutani, "Infrared Spectra of Fayalite Crystal," *Astron. Astrophys.*, vol. 389, no. 2, pp. 568–571, 2002.

[245] J. Navarro-Ruiz, P. Ugliengo, A. Rimola, and M. Sodupe, "B3LYP Periodic Study of the Physicochemical Properties of the Nonpolar (010) Mg-Pure and Fe-Containing Olivine Surfaces," *J. Phys. Chem. A*, vol. 118, no. 31, pp. 5866–5875, 2014.

[246] N. Katz, I. Furman, O. Biham, V. Pirronello, and G. Vidali, "Molecular Hydrogen Formation on Astrophysically Relevant Surfaces," *Astrophys. J.*, vol. 522, no. 1, pp. 305–312, 1999.

[247] J. Navarro-Ruiz, M. Sodupe, P. Ugliengo, and A. Rimola, "Interstellar H Adsorption and H2 Formation on the Crystalline (010) Forsterite Surface: A B3LYP-D2* Periodic Study," *Phys. Chem. Chem. Phys.*, vol. 16, no. 33, pp. 17447–17457, 2014.

[248] M. J. Frisch, G. W. Trucks, H. B. Schlegel, G. E. Scuseria, M. A. Robb, J. R. Cheeseman, G. Scalmani, V. Barone, B. Mennucci, G. A. Petersson, H. Nakatsuji, M. Caricato, X. Li, H. P. Hratchian, A. F. Izmaylov, J. Bloino, G. Zheng, J. L. Sonnenberg, M. Hada, M. Ehara, K. Toyota, R. Fukuda, J. Hasegawa, M. Ishida, T. Nakajima, Y. Honda, O. Kitao, H. Nakai, T. Vreven, J. Montgomery, J. A., J. E. Peralta, F. Ogliaro, M. Bearpark, J. J. Heyd, E. Brothers, K. N. Kudin, V. N. Staroverov, R. Kobayashi, J. Normand, K. Raghavachari, A. Rendell, J. C. Burant, S. S. Iyengar, J. Tomasi, M. Cossi, N. Rega, J. M. Millam, M. Klene, J. E. Knox, J. B. Cross, V. Bakken, C. Adamo, J. Jaramillo, R. Gomperts, R. E. Stratmann, O. Yazyev, A. J. Austin, R. Cammi, C. Pomelli, J. W. Ochterski, R. L. Martin, K. Morokuma, V. G. Zakrzewski, G. A. Voth, P. Salvador, J. J. Dannenberg, S. Dapprich, A. D. Daniels, Ö. Farkas, J. B. Foresman, J. V. Ortiz, J. Cioslowski, and D. J. Fox, *Gaussian 09, Revision D.01*. Gaussian, Inc., Wallingford CT, 2009.

[249] A. J. H. Wachters, "Gaussian Basis Set for Molecular Wavefunctions Containing Third-Row Atoms," *J. Chem. Phys.*, vol. 52, no. 3, pp. 1033–1036, 1970.

[250] C. W. Bauschlicher, S. R. Langhoff, H. Partridge, and L. A. Barnes, "Theoretical Studies of the First- and Second-Row Transition-Metal Methyls and their Positive Ions," *J. Chem. Phys.*, vol. 91, no. 4, pp. 2399–2411, 1989.

[251] T. H. Dunning, "Gaussian Basis Sets for Use in Correlated Molecular Calculations. I. The Atoms Boron through Neon and Hydrogen," *J. Chem. Phys.*, vol. 90, no. 2, pp. 1007–1023, 1989.

[252] R. Pou-Amérigo, M. Merchán, I. Nebot-Gil, P.-O. Widmark, and B. O. Roos, "Density Matrix Averaged Atomic Natural Orbital (ANO) Basis Sets for Correlated Molecular Wave Functions," *Theor. Chim. Acta*, vol. 92, no. 3, pp. 149–181, 1995.

Appendix A. Further Details on H Adsorption and H_2 Formation on (010), (001) and (110) Mg_2SiO_4 Surfaces

Further details on the calculations of the reaction energies for the adsorption of the second H atom on Fo(010) and for the adsorption of one and two H atom on Fo(001) and Fo(110).

A.1. Adsorption of a Second H Atom on Fo(010)

Table A.1 *Net charges and electronic spin densities on the H atoms, on the Mg atom closest to H, and the sum of the spin density values of the O atoms closest to H, computed at B2//B1 level for the different doubly-H adsorptions on Fo(010) (H^{1st} and H^{2nd} denotes the first and second H position according to the nomenclature of the complex, respectively, and Mg^a and Mg^b denotes the position of Mg depending on whether it is left or right on the surface, respectively).*

	Charge				
	H^{1st}	H^{2nd}	Mg^a	Mg^b	O
010–Mg1a-Mg1b	+0.01	+0.01	+0.96	+0.96	-1.10
010–Mg2a-Mg1b	-0.02	+0.02	+0.93	+0.97	-1.08
010–Mg2a-Mg2b	-0.01	-0.01	+0.93	+0.93	-1.07
010–O1a-Mg2b	+0.33	-0.29	+1.00	+0.71	-1.04
010–O1a-Mg2a	+0.33	-0.33	+0.74	+1.01	-1.08
010–O1a-O1b	+0.29	+0.29	+0.44	+0.44	-0.97
	Spin				
	H^{1st}	H^{2nd}	Mg^a	Mg^b	O
010–Mg1a-Mg1b	0.88	-0.88	0.03	-0.03	0.00
010–Mg2a-Mg1b	0.74	-0.89	0.06	-0.03	0.14
010–Mg2a-Mg2b	0.75	-0.75	0.06	-0.06	0.00
010–O1a-Mg2b	0.00	0.00	0.00	0.00	0.00
010–O1a-Mg2a	0.00	0.00	0.00	0.00	0.00
010–O1a-O1b	0.04	-0.04	0.85	-0.85	0.00

Table A.2 *B3LYP-D2* reaction energies calculated at B3LYP-D2*/B1 and B3LYP-D2*/B2//B3LYP-D2*/B1 for the second H atom on Fo(010) from the H/Fo(010) adducts. Uncorrected (ΔE), BSSE corrected (ΔE^C) and zero-point energy corrected (ΔU_0^C) adsorption energies (values in kcal mol^{-1}).*

	ΔE		ΔE^C		ΔU_0^C	
Reaction	B1	B2//B1	B1	B2//B1	B1	B2//B1
010–Mg1 + H → 010–Mg1a-Mg1b	-3.1	-3.4	-1.9	-2.9	-1.2	-2.2
010–Mg2 + H → 010–Mg2a-Mg1b	-3.1	-3.2	-1.8	-2.8	-1.0	-1.9
010–Mg2 + H → 010–Mg2a-Mg2b	-3.9	-3.9	-2.9	-3.6	-1.3	-2.1
010–O1 + H → 010–O1a-Mg2b	-63.9	-64.4	-63.0	-65.2	-59.6	-61.8
010–O1 + H → 010–O1a-Mg2a	-82.3	-82.4	-81.4	-82.1	-77.9	-78.7
010–O1 + H → 010–O1a-O1b	-2.8	-3.9	-0.2	-2.7	+5.1	+2.5

A.2. Adsorption of One H Atom on Fo(001) and Fo(110)

Table A.3 *B3LYP-D2* reaction energies calculated at the B3LYP-D2*/B1 and B3LYP-D2*/B2//B3LYP-D2*/B1 level for the first H adsorption process on Fo(001) to form the H/Fo(001) adducts and on Fo(110) to form the H/Fo(110) adducts. Uncorrected (ΔE) and zero-point energy corrected (ΔU_0) adsorption energy (values in kcal mol^{-1}).*

	ΔE		ΔU_0	
Reaction	B1	B2//B1	B1	B2//B1
Fo(001) + H → 001–Mg1	-17.1	-14.1	-14.1	-11.1
Fo(001) + H → 001–Mg2	-12.0	-6.7	-8.1	-2.7
Fo(001) + H → 001–O1	-41.6	-40.1	-34.5	-33.0
Fo(001) + H → 001–O2	-53.7	-51.5	-46.7	-44.5
Fo(001) + H → 001–O3	-56.7	-55.3	-49.8	-48.4
Fo(110) + H → 110–Mg1	-6.3	-6.0	-4.0	-3.8
Fo(110) + H → 110–Mg2	-8.3	-7.9	-6.2	-5.8
Fo(110) + H → 110–O1	-37.8	-37.0	-31.4	-30.6
Fo(110) + H → 110–O2	-34.5	-33.0	-28.1	-26.6
Fo(110) + H → 110–O3	-34.8	-34.0	-28.2	-27.4
Fo(110) + H → 110–O4	-49.3	-47.7	-42.8	-41.2

Table A.4 *Net charges and electronic spin densities on the H atom, on the Mg atom closest to H, and the sum of the spin density values of the O atoms closest to H, computed at B2//B1 level for the different singly-H adsorptions on Fo(001) and Fo(110).*

	Charge			Spin		
	H	Mg	O	H	Mg	O
001–Mg1	-0.36	+0.69	-0.64	0.07	0.00	0.93
001–Mg2	-0.34	+0.72	-1.09	0.06	0.00	0.94
001–O1	+0.35	+0.33	-0.86	0.00	0.93	0.07
001–O2	+0.31	+0.32	-0.74	0.00	0.93	0.07
001–O3	+0.27	+0.30	-0.80	0.03	0.91	0.06
110–Mg1	0.00	+0.87	-0.94	0.64	0.14	0.22
110–Mg2	-0.04	+0.83	-0.94	0.61	0.08	0.31
110–O1	+0.38	+0.53	-0.85	0.00	0.92	0.08
110–O2	+0.35	+0.59	-0.78	0.03	0.93	0.04
110–O3	+0.29	+0.57	-0.80	0.01	0.91	0.08
110–O4	+0.31	+0.47	-0.78	0.01	0.85	0.14

A.3. Adsorption of a Second H Atom on Fo(001) and Fo(110)

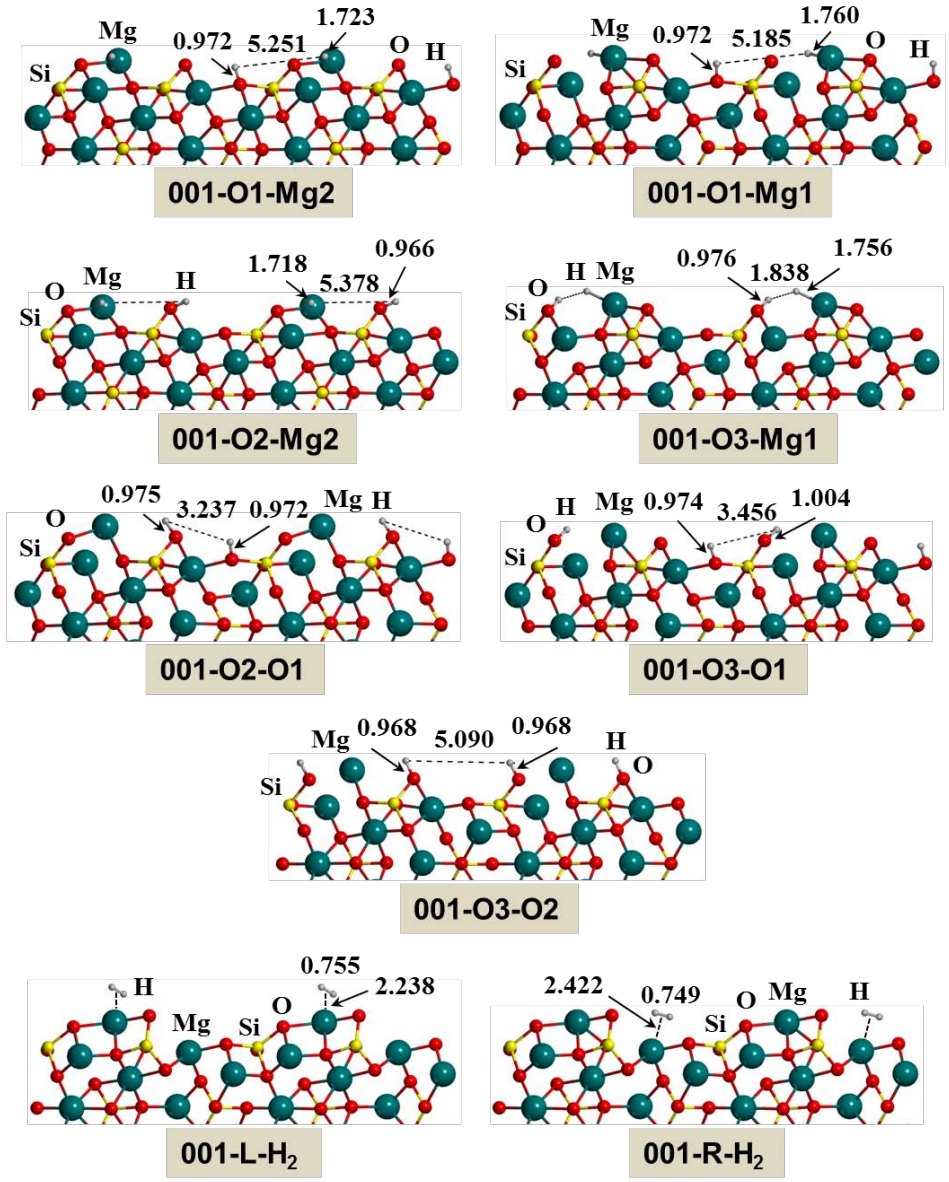

Figure A.1 B3LYP-D2* optimized geometries of the different complexes resulting from the adsorption of two H atoms on Fo(001) (001–O1-Mg2, 001–O1-Mg1, 001–O2-Mg2, 001–O3-Mg1, 001–O2-O1, 001–O3-O1, 001–O3-O2, 001–L-H_2 and 001–R-H_2). Bond distances in Å.

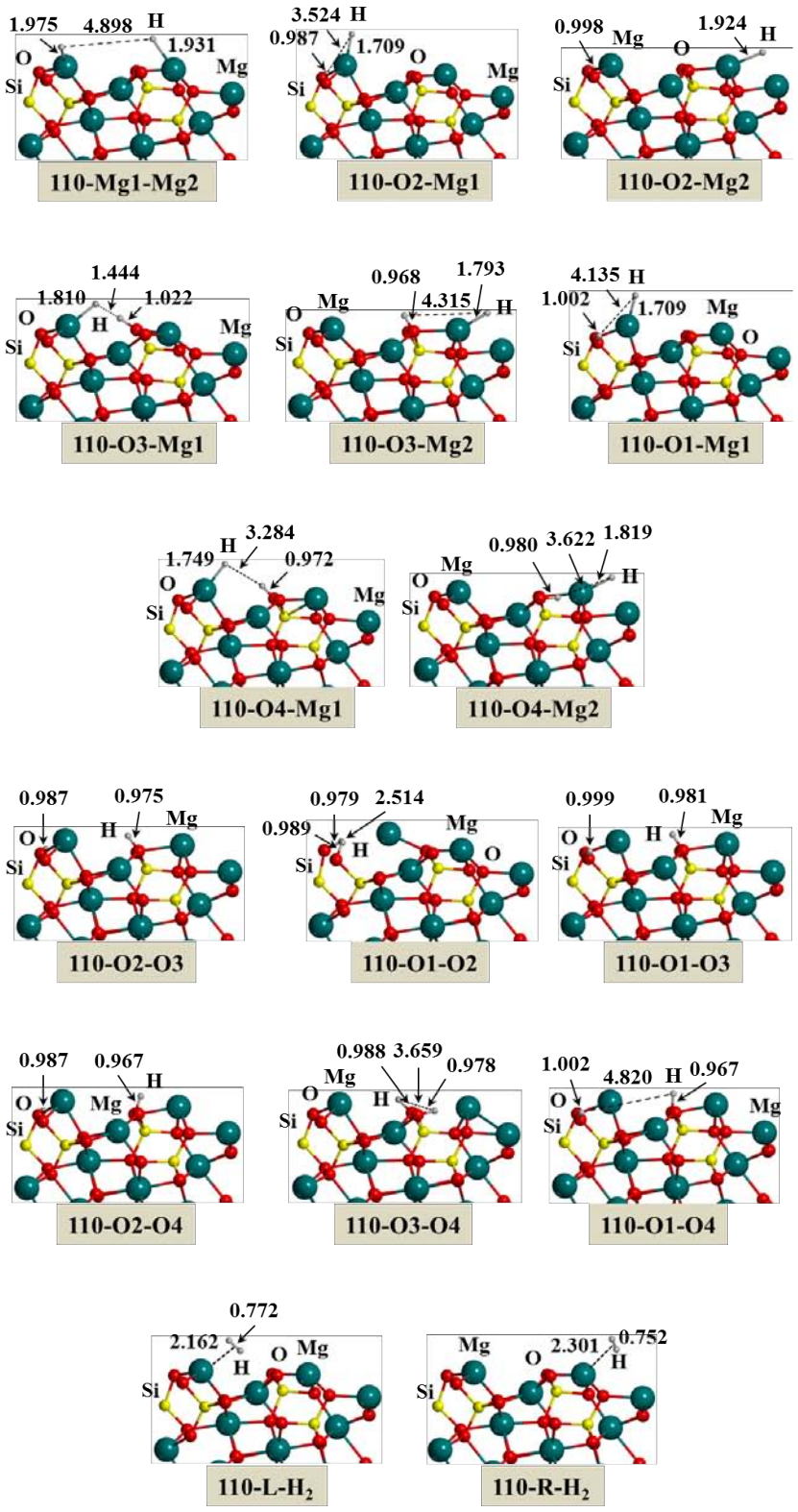

Figure A.2 B3LYP-D2* optimized geometries of the different complexes resulting from the adsorption of two H atoms on Fo(110) (110–Mg1-Mg2, 110–O2-Mg1, 110–O2-Mg2, 110–O3-Mg1, 110–O3-Mg2, 110–O1-Mg1, 110–O4-Mg1, 110–O4-Mg2, 110–O2-O3, 110–O1-O2, 110–O1-O3, 110–O2-O4, 110–O3-O4, 110–O1-O4, 110–L-H_2 and 110–R-H_2). Bond distances in Å.

Table A.5 *B3LYP-D2* reaction energies calculated at B3LYP-D2*/B1 and B3LYP-D2*/B2//B3LYP-D2*/B1 for the H recombination process on Fo(001) to form the 2H/Fo(001) and H_2/Fo(001) complexes and on Fo(110) to form the 2H/Fo(110) and H_2/Fo(110) complexes. Uncorrected (ΔE) and zero-point energy corrected (ΔU_0) adsorption energy (values in kcal mol^{-1}).*

	ΔE		ΔU_0	
Reaction	B1	B2//B1	B1	B2//B1
Fo(001) + 2H → 001–O1-Mg2	-125.7	-122.7	-113.8	-110.9
Fo(001) + 2H → 001–O1-Mg1	-118.4	-116.2	-107.1	-104.9
Fo(001) + 2H → 001–O2-Mg2	-135.7	-131.6	-124.1	-120.0
Fo(001) + 2H → 001–O3-Mg1	-140.9	-137.9	-129.8	-126.8
Fo(001) + 2H → 001–O2-O1	-79.4	-76.5	-65.8	-62.9
Fo(001) + 2H → 001–O3-O1	-72.1	-70.6	-59.3	-57.8
Fo(001) + 2H → 001–O3-O2	-88.2	-84.3	-75.0	-71.1
Fo(001) + 2H → 001–L-H_2	-117.7	-116.2	-108.7	-107.2
Fo(001) + 2H → 001–R-H_2	-116.8	-114.4	-108.1	-105.7
Fo(110) + 2H → 110–Mg1-Mg2	-14.2	-13.2	-9.9	-8.9
Fo(110) + 2H → 110–O2-Mg1	-112.3	-110.6	-102.3	-100.6
Fo(110) + 2H → 110–O2-Mg2	-105.1	-106.1	-94.8	-95.8
Fo(110) + 2H → 110–O3-Mg1	-93.6	-106.4	-83.0	-95.8
Fo(110) + 2H → 110–O3-Mg2	-115.9	-115.9	-105.4	-105.5
Fo(110) + 2H → 110–O1-Mg1	-114.6	-113.3	-104.6	-103.4
Fo(110) + 2H → 110–O4-Mg1	-119.9	-117.3	-109.7	-107.1
Fo(110) + 2H → 110–O4-Mg2	-132.2	-130.7	-121.5	-120.0
Fo(110) + 2H → 110–O2-O3	-74.7	-73.1	-61.7	-60.1
Fo(110) + 2H → 110–O1-O2	-62.2	-61.6	-50.5	-49.9
Fo(110) + 2H → 110–O1-O3	-75.3	-73.5	-62.2	-60.5
Fo(110) + 2H → 110–O2-O4	-84.3	-82.1	-71.5	-69.3
Fo(110) + 2H → 110–O3-O4	-74.2	-71.3	-61.4	-58.5
Fo(110) + 2H → 110–O1-O4	-84.8	-82.5	-72.1	-69.8
Fo(110) + 2H → 110–L-H_2	-119.8	-118.4	-110.3	-108.8
Fo(110) + 2H → 110–R-H_2	-115.4	-114.3	-106.9	-105.8

Table A.6 *Net charges and electronic spin densities on the H atoms, on the Mg atom closest to H, and the sum of the spin density values of the O atoms closest to H, computed at B2//B1 level for the different doubly-H adsorptions on Fo(001) and Fo(110) (H^{1st} and H^{2nd} denotes the first and second H position according to the nomenclature of the complex, respectively, and Mg^a and Mg^b denotes the position of Mg depending on whether it is left or right on the surface, respectively).*

	Charge					Spin				
	H^{1st}	H^{2nd}	Mg^a	Mg^b	O	H^{1st}	H^{2nd}	Mg^a	Mg^b	O
001–O1-Mg2	+0.34	-0.36	+0.73	---	-0.96	0.00	0.00	0.00	---	0.00
001–O1-Mg1	+0.33	-0.40	+0.71	---	-0.96	0.00	0.00	0.00	---	0.00
001–O2-Mg2	+0.31	-0.35	+0.71	---	-0.98	0.00	0.00	0.00	---	0.00
001–O3-Mg1	+0.28	-0.36	+0.64	---	-0.96	0.00	0.00	0.00	---	0.00
001–O2-O1	+0.29	+0.34	-0.29	---	-0.90	0.00	0.00	0.00	---	0.00
001–O3-O1	+0.28	+0.35	-0.23	---	-0.88	0.00	0.00	0.00	---	0.00
001–O3-O2	+0.30	+0.28	-0.31	---	-0.87	0.00	0.00	0.00	---	0.00
110–Mg1-Mg2	+0.00	-0.03	+0.86	+0.86	-0.96	0.66	-0.62	0.14	-0.10	-0.05
110–O2-Mg1	+0.35	-0.26	+0.85	+0.85	-0.96	-0.02	0.08	-0.08	0.00	0.02
110–O2-Mg2	+0.35	-0.39	+1.02	+1.02	-0.98	0.00	0.00	0.00	0.00	0.00
110–O3-Mg1	+0.28	-0.36	+0.71	+0.71	-0.96	0.00	0.00	0.00	0.00	-0.05
110–O3-Mg2	+0.29	-0.34	+0.94	+0.94	-0.94	0.00	0.00	0.00	0.00	-0.05
110–O1-Mg1	+0.37	-0.25	+0.86	+0.86	-0.97	0.00	0.00	0.02	0.00	0.00
110–O4-Mg1	+0.34	-0.32	+0.88	+0.88	-0.94	0.00	0.00	0.00	0.00	0.00
110–O4-Mg2	+0.33	-0.34	+0.93	+0.93	-0.95	0.00	0.00	0.00	0.00	0.00
110–O2-O3	+0.35	+0.30	+0.54	+0.54	-0.90	0.00	-0.02	-0.86	0.75	-0.01
110–O1-O2	+0.27	+0.25	+0.45	+0.45	-0.88	0.00	0.00	0.00	0.00	0.00
110–O1-O3	+0.37	+0.29	+0.56	+0.56	-0.90	0.00	-0.04	-0.87	0.79	-0.02
110–O2-O4	+0.35	+0.29	+0.50	+0.50	-0.90	0.00	-0.01	0.88	-0.77	0.01
110–O3-O4	+0.26	+0.33	+0.51	+0.51	-0.88	0.09	0.00	0.77	-0.85	0.01
110–O1-O4	+0.38	+0.29	+0.51	+0.51	-0.91	0.00	0.00	0.89	-0.82	0.01

Table A.7 *B3LYP-D2* reaction energies calculated at B3LYP-D2*/B1 and B3LYP-D2*/B2//B3LYP-D2*/B1 for the second H atom on Fo(001) from the H/Fo(001) adducts and on Fo(110) from the H/Fo(110) adducts. Uncorrected (ΔE) and zero-point energy corrected (ΔU_0) adsorption energy (values in kcal mol^{-1}).*

	ΔE		ΔU_0	
Reaction	B1	B2//B1	B1	B2//B1
001–O1 + H → 001–O1-Mg2	-84.1	-82.6	-79.4	-77.9
001–O1 + H → 001–O1-Mg1	-76.8	-76.1	-72.7	-71.9
001–O2 + H → 001–O2-Mg2	-82.0	-80.1	-77.4	-75.5
001–O3 + H → 001–O3-Mg1	-84.2	-82.7	-80.0	-78.5
001–O2 + H → 001–O2-O1	-25.7	-25.0	-19.1	-18.4
001–O3 + H → 001–O3-O1	-15.4	-15.3	-9.5	-9.4
001–O3 + H → 001–O3-O2	-31.5	-29.1	-25.2	-22.8
110–Mg2 + H → 110–Mg1-Mg2	-5.9	-5.4	-3.7	-3.1
110–O2 + H → 110–O2-Mg1	-77.8	-77.6	-74.3	-74.0
110–O2 + H → 110–O2-Mg2	-70.7	-73.1	-66.8	-69.2
110–O3 + H → 110–O3-Mg1	-58.8	-72.4	-54.8	-68.4
110–O3 + H → 110–O3-Mg2	-81.1	-81.9	-77.3	-78.0
110–O1 + H → 110–O1-Mg1	-76.8	-76.3	-73.2	-72.8
110–O4 + H → 110–O4-Mg1	-70.7	-69.6	-67.0	-65.9
110–O4 + H → 110–O4-Mg2	-83.0	-83.0	-78.8	-78.9
110–O3 + H → 110–O2-O3	-40.0	-39.1	-33.5	-32.6
110–O1 + H → 110–O1-O2	-24.4	-24.6	-19.1	-19.3
110–O1 + H → 110–O1-O3	-37.5	-36.5	-30.8	-29.8
110–O4 + H → 110–O2-O4	-35.0	-34.4	-28.7	-28.1
110–O4 + H → 110–O3-O4	-24.9	-23.6	-18.7	-17.4
110–O4 + H → 110–O1-O4	-35.5	-34.8	-29.3	-28.6

A.4. H_2 Formation on Fo(001) and Fo(110)

Table A.8 *B3LYP-D2* reaction energies calculated at B3LYP-D2*/B1 and B3LYP-D2*/B2//B3LYP-D2*/B1 for the H_2 formation on Fo(001) from the 2H/Fo(001) complexes and on Fo(110) from the 2H/Fo(110) complexes. Uncorrected (ΔE) and zero-point energy corrected (ΔU_0) adsorption energy (values in kcal mol^{-1}).*

	ΔE		ΔU_0	
Reaction	B1	B2//B1	B1	B2//B1
001–O1-Mg2 → 001–L-H_2	8.0	6.5	5.1	3.7
001–O1-Mg1 → 001–L-H_2	0.7	0.0	-1.6	-2.3
001–O2-Mg2 → 001–L-H_2	18.0	15.4	15.4	12.8
001–O3-Mg1 → 001–L-H_2	23.2	21.7	21.1	19.6
001–O2-O1 → 001–L-H_2	-38.3	-39.7	-42.9	-44.3
001–O3-O1 → 001–L-H_2	-45.6	-45.6	-49.4	-49.4
001–O3-O2 → 001–L-H_2	-29.5	-31.9	-33.7	-36.1
110–Mg1–Mg2 → 110–L-H_2	-105.6	-105.1	-100.4	-99.9
110–O2–Mg1 → 110–L-H_2	-7.5	-7.8	-7.9	-8.3
110–O2–Mg2 → 110–L-H_2	-14.6	-12.2	-15.4	-13.0
110–O3–Mg1 → 110–L-H_2	-26.2	-12.0	-27.3	-13.0
110–O3–Mg2 → 110–L-H_2	-3.9	-2.5	-4.8	-3.4
110–O1–Mg1 → 110–L-H_2	-5.2	-5.1	-5.6	-5.5
110–O4–Mg1 → 110–L-H_2	0.1	-1.1	-0.5	-1.8
110–O4–Mg2 → 110–L-H_2	12.4	12.4	11.3	11.2
110–O2–O3 → 110–L-H_2	-45.0	-45.2	-48.6	-48.8
110–O1–O2 → 110–L-H_2	-57.6	-56.8	-59.7	-59.0
110–O1–O3 → 110–L-H_2	-44.5	-44.9	-48.0	-48.4
110–O2–O4 → 110–L-H_2	-35.5	-36.3	-38.8	-39.6
110–O3–O4 → 110–L-H_2	-45.6	-47.1	-48.8	-50.3
110–O1–O4 → 110–L-H_2	-35.0	-35.9	-38.2	-39.1

Table A.9 *B3LYP-D2* adsorption energies calculated at B3LYP-D2*/B1 and B3LYP-D2*/B2//B3LYP-D2*/B1 of the H_2 molecule on Fo(001) and Fo(110). Uncorrected (ΔE) and zero-point energy corrected (ΔU_0) adsorption energy (values in kcal mol^{-1}).*

	ΔE		ΔU_0	
Reaction	B1	B2//B1	B1	B2//B1
Fo(001) + H_2 → 001–L-H_2	-7.7	-6.2	-5.0	-3.5
Fo(001) + H_2 → 001–R-H_2	-6.8	-4.3	-4.4	-2.0
Fo(110) + H_2 → 110–L-H_2	-9.7	-8.3	-6.6	-5.1
Fo(110) + H_2 → 110–R-H_2	-5.3	-4.2	-3.2	-2.1

Appendix B. Further Details on Influence of Fe^{2+} Atoms: H_2 Formation on (010) $(Mg,Fe)_2SiO_4$ Surface

Further details on the calculations of the reaction energies at different spin multiplicities for the adsorption of one and two H atom on Ol(010).

B.1. Adsorption of One H Atom on Ol(010)

Regarding the spin multiplicity of Fe^{2+} atom (d^6, four unpaired electrons), the incoming H atom can adsorb on the surface with an up or down spin state, leading to a sextet or quartet global spin multiplicity, respectively. Table B.1 shows the adsorption energies of the different H/Ol(010) adducts for the sextet and quartet spin multiplicity and Table B.2 presents their net charges and spin densities. As it mentioned in Section 5.3.2.1 of Chapter 5, sextet is more stable than quartet for a cluster model, trend that is reproduced using periodic calculations. However, not all adducts accomplish this trend, the closer the H atom of the Fe atom is located, the larger the energy difference between the two spin states. The most clearly cases are the 010–Fe1 and 010–O1 adducts, where the H atom is interacting directly or closer on the metal atom, respectively, being around 24 and 7 kcal mol^{-1} more stable the sextet (five unpaired electrons) than the quartet (three unpaired electrons) spin state, respectively (values of $\Delta\Delta U_0$ at B2//B1, see Table B.1, and for the values of spin densities see Table B.2). On the other hand, adsorption energies of remain two H-adsorbed adducts (*i.e.*, 010–O2 and 010–Mg1) as a function of the spin density are identical and thus independent of the spin multiplicity, according to the distance at which the H atom of the Fe atom is placed.

Table B.1 *BHLYP reaction energies calculated at the BHLYP/B1 and BHLYP/B2//BHLYP/B1 level for the first H adsorption process on Ol(010) to form the H/Ol(010) adducts. Uncorrected (ΔE) and zero-point energy corrected (ΔU_0) adsorption energy (values in kcal mol^{-1}).*

		ΔE		ΔU_0	
Reaction	M_S	B1	B2//B1	B1	B2//B1
Ol(010) + H → 010–Fe1	6	-44.2	-38.7	-39.9	-34.3
	4	-18.3	-14.6	-13.8	-10.1
Ol(010) + H → 010–O1	6	-15.0	-16.2	-8.1	-9.4
	4	-9.1	-9.2	-2.2	-2.4
Ol(010) + H → 010–O2	6	-13.8	-13.8	-7.3	-7.3
	4	-13.8	-13.8	-7.1	-7.1
Ol(010) + H → 010–Mg1	6	-1.8	-1.1	-0.9	-0.2
	4	-1.8	-1.1	-0.9	-0.3

Table B.2 *Net charges and electronic spin densities on the H, Fe and Mg atoms, and the sum of the spin density values of the O atoms closest to H, computed at B2//B1 level for the different singly-H adsorptions on Ol(010).*

		Charge				Spin			
	M_S	H	Fe	Mg	O	H	Fe	Mg	O
010–Fe1	6	-0.26	+1.35	+1.10	-1.18	0.19	4.58	0.00	0.23
010–Fe1	4	-0.05	+1.14	+1.11	-1.18	-0.53	3.49	0.00	0.04
010–O1	6	+0.32	+0.52	+1.11	-1.13	0.01	4.93	0.00	0.06
010–O1	4	+0.32	+0.51	+1.12	-1.13	-0.02	2.99	0.00	0.03
010–O2	6	+0.33	+1.20	+0.45	-1.13	0.01	3.93	0.95	0.11
010–O2	4	+0.33	+1.21	+0.45	-1.13	-0.01	3.90	-0.95	0.06
010–Mg1	6	+0.06	+1.18	+1.02	-1.19	0.96	3.90	0.02	0.12
010–Mg1	4	+0.06	+1.18	+1.02	-1.19	-0.96	3.92	-0.02	0.07

B.2. Adsorption of a Second H Atom on Ol(010)

Figure B.1 illustrates the overall doubly-H-adsorbed complexes on Ol(010) at quintet spin state, derived from the most stable sextet singly-H-adsorbed adducts.

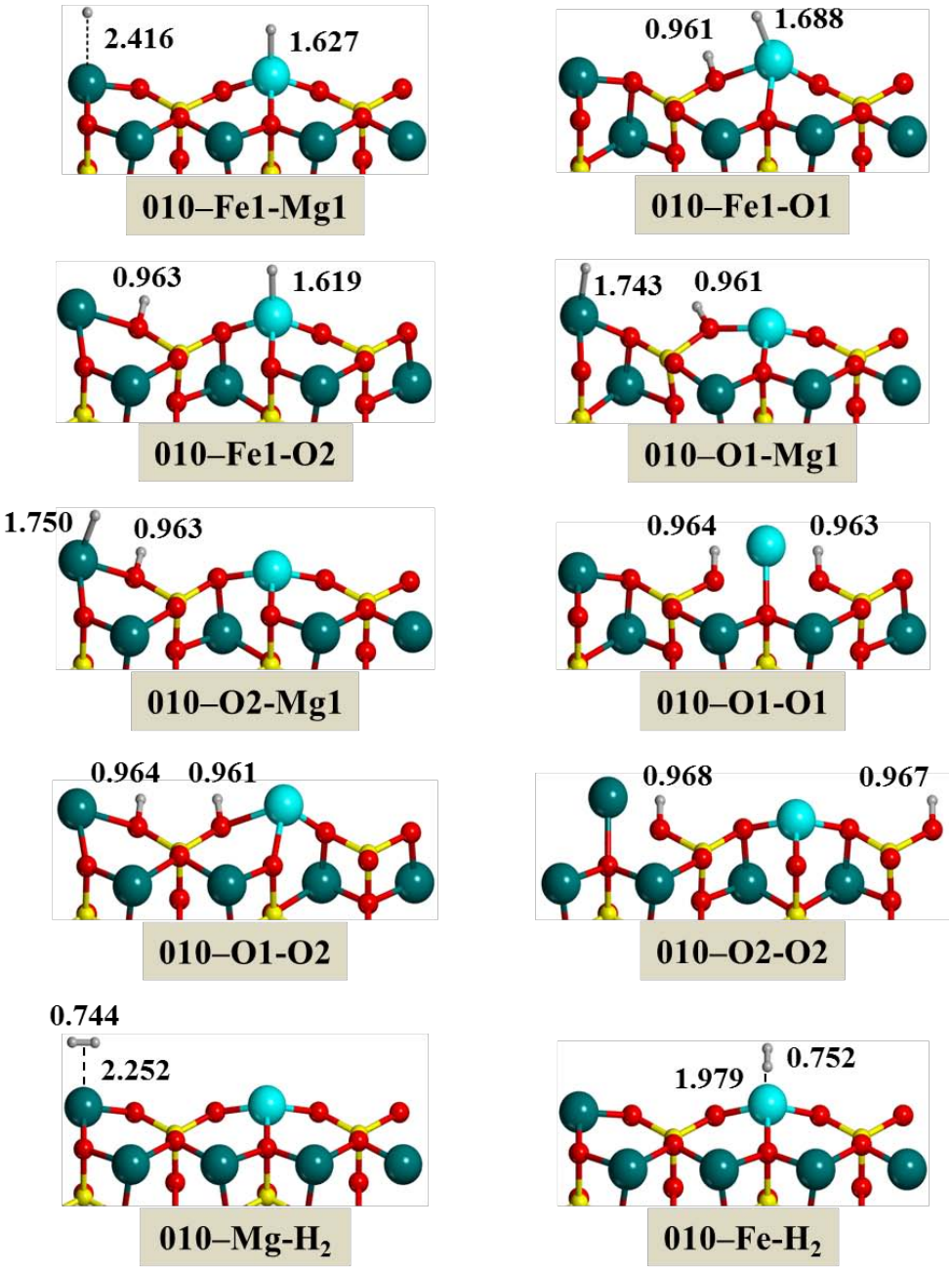

Figure B.1 BHLYP optimized geometries of the different complexes resulting from the adsorption of two H atoms on Ol(010) at quintet spin multiplicity (010–Fe1-Mg1, 010–Fe1-O1, 010–Fe1-O2, 010–O1-Mg1, 010–O2-Mg1, 010–O1-O1, 010–O1-O2, 010–O2-O2, 010–Mg-H_2 and 010–Fe-H_2). Bond distances in Å.

In order to investigate the influence of adsorb two H atoms on the surface by considering different spin densities, all the quintet spin state doubly-H-adsorbed complexes have also been computed at septet spin state. Table B.3 shows the adsorption energies of the different 2H/Ol(010) species for the two spin multiplicities studied and Table B.4 presents the corresponding net charges and spin densities. In this case, the 010–Fe1-Mg1 and 010–Fe1-O2 complexes are the only two complexes with no changes in their adsorption energies, neither quintet nor septet spin state. After that, complexes with double O-chemisorption (*i.e.*, 010–O1-O1, 010–O1-O2 and 010–O2-O2) have smaller differences between the adsorption energies, less than 10 kcal mol^{-1}. And finally, 010–Fe1-O1, 010–O1-Mg1 and 010–O2-Mg1 complexes have the larger $\Delta\Delta U_0$ differences, around 70 kcal mol^{-1}. Contrary to what happens with the singly-H adsorptions, one of the main factors making adsorption energies so different may be the distance between the two adsorbed hydrogen atoms, due to the electronic interaction between two electrons of parallel or antiparallel spins. This would explain why the 010–Fe1-Mg1 and 010–Fe1-O2 complexes have no alterations between their adsorption energies, finding the two H atoms away from each other, why the 010–O1-O1, 010–O1-O2 and 010–O2-O2 complexes, doubly O-chemisorbed, have slight differences in their energy adsorption and why the 010–Fe1-O1 and 010–O2-Mg1 complexes have the maximum energy differences, since the H···H distance is short and the electronic interaction is higher. Finally, 010–O1-Mg1 complex has a dihydrogen distance large enough to present no energy difference between its two spin states, but the existence of one of the two adsorbed H atoms in an O atom adjacent to the Fe atom, as happened with the singly-H adsorptions, incomes differences between adsorption energies.

Table B.3 *BHLYP reaction energies calculated at BHLYP/B1 and BHLYP/B2//BHLYP/B1 for the H recombination process on Ol(010) to form the 2H/Ol(010) and H_2/Ol(010) complexes at quintet and septet spin multiplicity. Uncorrected (ΔE) and zero-point energy corrected (ΔU_0) adsorption energy (values in kcal mol^{-1}).*

		ΔE		ΔU_0	
Reaction	M_S	B1	B2//B1	B1	B2//B1
Ol(010) + 2H → 010–Fe1-Mg1	5	-46.3	-41.2	-41.2	-36.1
	7	-46.3	-40.9	-41.3	-36.0
Ol(010) + 2H → 010–Fe1-O1	5	-100.1	-100.7	-89.4	-90.0
	7	-21.1	-31.0	-10.5	-20.4
Ol(010) + 2H → 010–Fe1-O2	5	-55.5	-51.2	-44.8	-40.5
	7	-55.5	-51.2	-44.9	-40.5
Ol(010) + 2H → 010–O1-Mg1	5	-76.8	-77.8	-66.7	-67.7
	7	-13.3	-13.0	-3.5	-3.3
Ol(010) + 2H → 010–O2-Mg1	5	-96.2	-95.3	-85.9	-85.0
	7	-33.6	-31.0	-23.8	-21.3
Ol(010) + 2H → 010–O1-O1	5	-35.2	-38.3	-22.1	-25.2
	7	-26.9	-31.1	-13.4	-17.6
Ol(010) + 2H → 010–O1-O2	5	-15.8	-19.3	-2.9	-6.5
	7	-15.4	-18.1	-2.7	-5.4
Ol(010) + 2H → 010–O2-O2	5	-27.4	-26.0	-14.7	-13.3
	7	-24.5	-25.8	-11.1	-12.3
Ol(010) + 2H → 010–Mg-H_2	5	-112.4	-111.7	-103.8	-103.1
Ol(010) + 2H → 010–Fe-H_2	5	-112.2	-111.3	-102.6	-101.8

Table B.4 *Net charges and electronic spin densities on the H, Fe and Mg atoms, and the sum of the spin density values of the O atoms closest to H, computed at B2//B1 level for the different doubly-H adsorptions on Ol(010) (H^{1st} and H^{2nd} denotes the first and second H position according to the nomenclature of the complex, respectively).*

		Charge					Spin				
	M_S	H^{1st}	H^{2nd}	Fe	Mg	O	H^{1st}	H^{2nd}	Fe	Mg	O
010–Fe1-Mg1	5	+0.07	-0.27	+1.35	+1.02	-1.18	-0.96	0.19	4.59	-0.03	0.21
	7	+0.07	-0.27	+1.35	+1.02	-1.18	0.95	0.19	4.56	0.03	0.25
010–Fe1-O1	5	+0.33	-0.43	+0.97	+1.11	-1.13	0.00	-0.04	4.00	0.00	0.04
	7	+0.35	-0.21	+1.30	+0.47	-1.11	0.00	0.21	4.59	0.96	0.24
010–Fe1-O2	5	+0.34	-0.23	+1.34	+0.46	-1.12	-0.01	0.20	4.57	-0.96	0.19
	7	+0.33	-0.23	+1.34	+0.46	-1.12	0.01	0.20	4.58	0.96	0.25
010–O1-Mg1	5	-0.31	+0.34	+1.20	+0.78	-1.13	0.00	0.00	3.91	0.00	0.08
	7	-0.29	+0.35	+1.01	+0.77	-1.10	0.00	0.00	5.71	0.00	0.29
010–O2-Mg1	5	-0.34	+0.34	+1.21	+0.79	-1.13	0.00	0.00	3.92	0.00	0.08
	7	-0.32	+0.35	+1.01	+0.78	-1.11	0.00	0.00	5.72	0.00	0.29
010–O1-O1	5	+0.29	+0.29	-0.13	+1.14	-1.05	-0.03	-0.03	4.06	0.00	0.00
	7	+0.35	+0.35	+0.54	+0.47	-1.06	0.00	0.00	5.00	0.95	0.06
010–O1-O2	5	+0.31	+0.29	+0.54	+0.47	-1.05	-0.03	0.03	4.88	-0.92	0.04
	7	+0.31	+0.29	+0.54	+0.47	-1.05	0.03	0.03	4.93	0.92	0.09
010–O2-O2	5	+0.30	+0.30	+1.22	-0.16	-1.05	0.00	0.00	3.92	0.00	0.08
	7	+0.35	+0.35	+0.53	+0.45	-1.06	0.00	0.00	4.96	0.97	0.07

Table B.5 shows the reaction corresponding to the formation energies computed from the H/Ol(010) adducts. It is clear that complexes with the largest variations in adsorption energies depending on their spin state (*i.e.*, 010–Fe1-O1, 010–O1-Mg1 and 010–O2-Mg1, see Table B.3) have the largest formation energies with a quintet spin state (values between -56 and -78 kcal mol^{-1}). In contrast, two of them (*i.e.*, 010–Fe1-O1 and 010–O1-Mg1) have, for septet spin state, positive formation energies, which indicate endothermic processes (14 and 6 kcal mol^{-1}, respectively). The remaining species (*i.e.*, 010–Fe1-Mg1, 010–Fe1-O2, 010–O2-Mg1, 010–O1-O1, 010–O1-O2 and 010–O2-O2) have negative formation energies irrespective of their spin state.

Table B.5 *BHLYP reaction energies calculated at BHLYP/B1 and BHLYP/B2//BHLYP/B1 for the second H atom on Ol(010) from the H/Ol(010) adducts at sextet spin multiplicity. Uncorrected (ΔE) and zero-point energy corrected (ΔU_0) adsorption energy (values in kcal mol^{-1}).*

		ΔE		ΔU_0	
Reaction	M_S	B1	B2//B1	B1	B2//B1
010–Fe1 + H → 010–Fe1-Mg1	5	-2.1	-2.5	-1.3	-1.8
	7	-2.1	-2.2	-1.4	-1.7
010–Fe1 + H → 010–Fe1-O1	5	-55.9	-62.0	-49.5	-55.7
	7	23.1	7.7	29.4	13.9
010–Fe1 + H → 010–Fe1-O2	5	-11.3	-12.5	-4.9	-6.2
	7	-11.3	-12.5	-5.0	-6.2
010–O1 + H → 010–O1-Mg1	5	-61.8	-61.6	-58.6	-58.3
	7	1.7	3.2	4.6	6.1
010–O2 + H → 010–O2-Mg1	5	-82.4	-81.5	-78.6	-77.7
	7	-19.8	-17.2	-16.5	-14.0
010–O1 + H → 010–O1-O1	5	-20.2	-22.1	-14.0	-15.8
	7	-11.9	-14.9	-5.3	-8.2
010–O1 + H → 010–O1-O2	5	-0.8	-3.1	5.2	2.9
	7	-0.4	-1.9	5.4	4.0
010–O2 + H → 010–O2-O2	5	-13.6	-12.2	-7.4	-6.0
	7	-10.7	-12.0	-3.8	-5.0

B.3. H_2 Formation on Ol(010)

Table B.6 illustrates the reaction energies corresponding to the H_2 formation computed from the 2H/Ol(010) complexes. As it can be seen, all the complexes have larger reaction energies in the septet than in the quintet spin state, except the 010–Fe1-Mg1 one, which has the same irrespective the spin state. This trend is in agreement with the fact that the complexes with highest multiplicities possess in most cases the lowest adsorption energies (see Table B.3). Nevertheless, all the reaction energies are negative, which means that at least all these processes are favourable thermodynamically.

Table B.6 *BHLYP reaction energies calculated at BHLYP/B1 and BHLYP/B2//BHLYP/B1 for the H_2 formation on Ol(010) from the 2H/Ol(010) complexes. Uncorrected (ΔE) and zero-point energy corrected (ΔU_0) adsorption energy (values in kcal mol^{-1}).*

		ΔE		ΔU_0	
Reaction	M_S	B1	B2//B1	B1	B2//B1
010–Fe1-Mg1 → 010–Fe-H_2	5	-65.9	-70.1	-61.4	-65.7
	7	-65.9	-70.4	-61.3	-65.8
010–O2-Mg1 → 010–Mg-H_2	5	-16.2	-16.4	-17.9	-18.1
	7	-78.8	-80.7	-80.0	-81.8
010–Fe1-O1 → 010–Fe-H_2	5	-12.1	-10.6	-13.2	-11.8
	7	-91.1	-80.3	-92.1	-81.4
010–O1-O1 → 010–Fe-H_2	5	-77.0	-73.0	-80.5	-76.6
	7	-85.3	-80.2	-89.2	-84.2

Table B.7 *BHLYP adsorption energies calculated at BHLYP/B1 and BHLYP/B2//BHLYP/B1 of the H_2 molecule on Ol(010). Uncorrected (ΔE) and zero-point energy corrected (ΔU_0) adsorption energy (values in kcal mol^{-1}).*

	ΔE		ΔU_0	
Reaction	B1	B2//B1	B1	B2//B1
Ol(010) + H_2 → 010–Mg-H_2	-4.1	-3.4	-2.0	-1.3
Ol(010) + H_2 → 010–Fe-H_2	-3.9	-3.0	-0.8	0.0